STRUCTURAL THERMOMECHANICAL MODELS FOR SHAPE MEMORY ALLOY COMPONENTS

A Dissertation

by

ASHWIN RAO

Submitted to the Office of Graduate and Professional Studies of
Texas A&M University
in partial fulfillment of the requirements for the degree of

DOCTOR OF PHILOSOPHY

Chair of Committee,	Arun R. Srinivasa
Co-Chair of Committee,	Junuthula N. Reddy
Committee Members,	Terry S. Creasy
	Wayne N.P. Hung
	Ramesh Talreja
Head of Department,	Andreas A. Polycarpou

May 2014

Major Subject: Mechanical Engineering

ABSTRACT

Thermally responsive shape memory alloys (SMA) demonstrate interesting properties like shape memory effect (SME) and superelasticity (SE). SMA components in the form of wires, springs and beams typically exhibit complex, nonlinear hysteretic responses and are subjected to tension, torsion or bending loading conditions.

Traditionally, simple strength of materials based models/tools have driven engineering designs for centuries, even as more sophisticated models existed for design with conventional materials. In light of this, an effort to develop *strength of materials* type modeling approach that can capture complex hysteretic SMA responses under different loading conditions is undertaken. The key idea here is of *separating the thermoelastic and the dissipative part of the hysteretic response by using a Gibbs potential and thermodynamic principles*. The dissipative part of the response is later accounted for by a discrete Preisach model. The models are constructed using experimentally measurable quantities (like torque–twist, bending moment–curvature etc.), since the SMA components subjected to torsion and bending experience an inhomogeneous non-linear stress distribution across the specimen cross-section. Such an approach enables simulation of complex temperature dependent superelastic responses including those with multiple internal loops.

The second aspect of this work deals with the durability of the material which is of critical importance with increasing use of SMA components in different engineering applications. Conventional S-N curves, Goodman diagrams etc. that capture only the mechanical loading aspects are not adequate to capture complex thermomechanical coupling seen in SMAs. Hence, a novel concept of *driving force amplitude v/s number of cycles* equivalent to thermodynamical driving force for onset of

phase transformations is proposed which simultaneously captures both mechanical and thermal loading in a single framework.

Recognizing the paucity of experimental data on functional degradation of SMAs (especially SMA springs), a custom designed thermomechanical fatigue test rig is used to perform user defined repeated thermomechanical tests on SMA springs. The data from these tests serve both to calibrate the model and establish *thermodynamic driving force and extent of phase transformation relationships* for SMA springs. A drop in driving force amplitude would suggest material losing its ability to undergo phase transformations which directly corresponds to a loss in the functionality/smartness of SMA component. This would allow designers to set appropriate driving force thresholds as a guideline for analyzing functional life of SMA components.

DEDICATION

To my parents, who raised me,

Raghavendra Rao and Jayashree R Rao

ACKNOWLEDGEMENTS

As this dissertation signifies the culmination of close to three decades of learning, I begin by acknowledging my parents Raghavendra Rao and Jayashree R Rao who raised me, motivated me and guided me through all ups and downs of my life. Without their help and support, I would not be writing this dissertation.

I would then like to thank my "boss/advisor/chair" Dr Arun Srinivasa for providing me with an opportunity to work on the NSF CMMI smart materials project. He came into my academic life with his bold, outspoken perspectives on mechanics and maths that shook my foundations. I really appreciate his time and guidance throughout the course of my stay at Texas A&M. Dr Srinivasa with his unique teaching philosophies is a role model for many aspiring educators like us. I would then like to thank "co-chair/advisor" Dr J.N.Reddy for all his help and support. His meticulous attention to details and his research/teaching philosophies have helped me develop as a researcher. I feel like to have won a lottery having Dr Srinivasa and Dr Reddy as my advisors.

I would like to thank my committee members Dr T.Creasy & Dr Hung for allowing us to use their laboratory facilities for much of the experimental work reported in this dissertation. Special thanks to Dr R. Talreja for sharing all his knowledge on fatigue and probing me with insightful questions throughout my dissertation.

I would like specially thank Dr Vidyashankar Burvalla from GE for many useful discussion on SMA during my visits to India and over several phone-calls/emails. Without his timely inputs, much of the experimental work wouldn't be possible.

I would like to acknowledge Dr Annie Ruimi from Texas A&M at Qatar for inviting me to Qatar and providing me with an opportunity to use their micro-torsion test rig. The experimental data acquired here forms a significant part of this

dissertation. I would also like to thank Shoaib and Roba for their support during my fortnight's stay at Doha.

I appreciate the help from Jace Curtis from T&M Instruments for his guidance for selection of various instruments for the test rig. I thank Holley Toschlog (support staff in MEEN) for all her patience and help while ordering various parts of the test rig.

A special mention for all my friends (alphabetically) Ajay, Alagappan, Arun, Biren, Feifei, Ginu, Gene, Harsha, Jason, Jayadurga, Jayavel, Jessica, Karthik, Krishnendu, Nitin, Pawan, Pradeep, Pratanu, Pritha, Sandeep, Sarthak, Shravani, Shishir, Shriram, Shrinidhi, Srikrishna, Swapnil, Venkat, Vinayak, Vinu and others for making my stay at Texas A&M a truly memorable one. Many of them have been generous with their time and support when I needed them.

I would like to specially thank my room-mate Krishna Kamath with whom I have had many discussions on research, movies, sports, politics, food and what not over my entire PhD journey. Shreyas also deserves a special mention for all the fun times we had over at my place. Almost every significant experience I have had as a graduate student has been shared with Krishna and Shreyas.

Special thanks to Dr Cheryl Page, Dr Robin Autenreith and Dr Butler Purry for providing me with an opportunity to participate in the E3 RET - Enrichment Experiences in Engineering Program. It was a wonderful experience to spend time off research with all the high school teachers over four summers.

Finally, thanks to GE Global Research, JFWTC, Bangalore for inviting me on a 4 month internship experience in my final year. Special thanks to Material Mechanics Laboratory team members Debdutt, Suresh, Swapnil, Vidyashankar, Yaranal and other for making this experience a truly enjoyable one.

TABLE OF CONTENTS

LIST OF FIGURES

FIGURE Page

LIST OF TABLES

TABLE Page

1. INTRODUCTION

1.1 Smart Materials : An Overview

Metals and alloys have played a significant role as structural materials for centuries [1]. Engineers have designed components and selected alloys by employing the classical engineering approach of understanding the macroscopic properties of the material and selecting the appropriate one to match the desired functionality based on the application [2]. With advancements in material science and increasing space, logistical limitations, replacing multi-component, multi-material systems with "active materials, multifunctional composites etc." that can achieve the same multiple functionalities, is now an attractive alternative [2, 3]. With such materials, researchers have began investigating how the microstructure of the material itself can be used to generate the required functionality for different applications and construct the system by themselves [3, 4]. Mamoda [3] in her recent review of future materials discusses some application ideas with such materials like "a smart solar panel that can change its orientation automatically during the day depending on sun's position ; a smart shock absorber that can alter its damping ability based on the road profile ; morphable wings and blades for aircraft maneuvering during flight ; a coating that changes color on demand" being a few to list.

Smart materials are a subgroup of such active/multifunctional materials that have shown an unique ability of recognizing a non-mechanical external stimuli from its surrounding environment and reversibly respond to the same [2]. Such materials can judge the magnitude of this external stimuli (signal) and react with an optimal response by either changing its physical or mechanical properties (generally macroscopic shape change) [2, 3, 5]. The non-mechanical stimuli could be in the form of

changes in temperature, magnetic field, electric potential, light intensity, moisture, changes in pH (chemical stimuli) etc. [6]. Figure 1.1 illustrates the various possible couplings between the the input signal (i.e magnitude of external stimuli) that the material is exposed to and its corresponding physical response for the same. With such materials, integration of multiple functions like actuation, sensing and control into a single structure using one or more smart material constituents is seen as a possibility (see figures 1.2 and 1.3 for illustrations) [4, 7]. These materials particularly have the potential to completely revolutionize the design of a wide variety of devices in applications ranging in areas from biomedical, automotive, aerospace, civil engineering to energy harvesting [8].

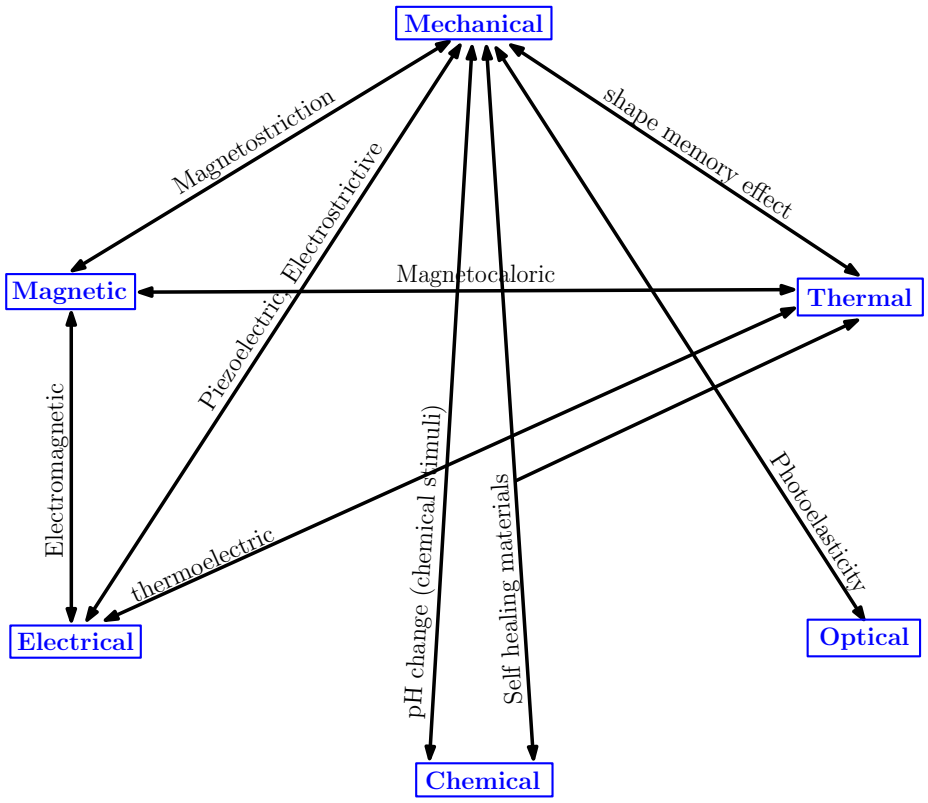

Figure 1.1: Smart materials can involve multi-physics coupling based on the external stimuli it is subjected to which results in changes of physical/mechanical properties i.e macroscopic shape change in most cases (adapted from fig 14 [9], [10]).

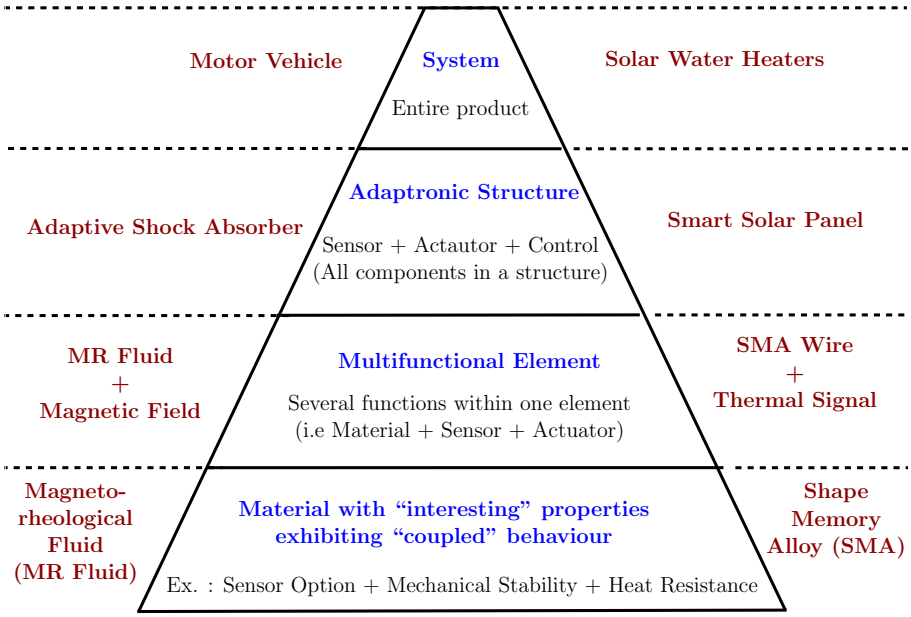

Figure 1.2: Integration of multiple functions like actuation, sensing and control into a single structure using one or more smart material constituents (adapted from figure 1.2 [4])

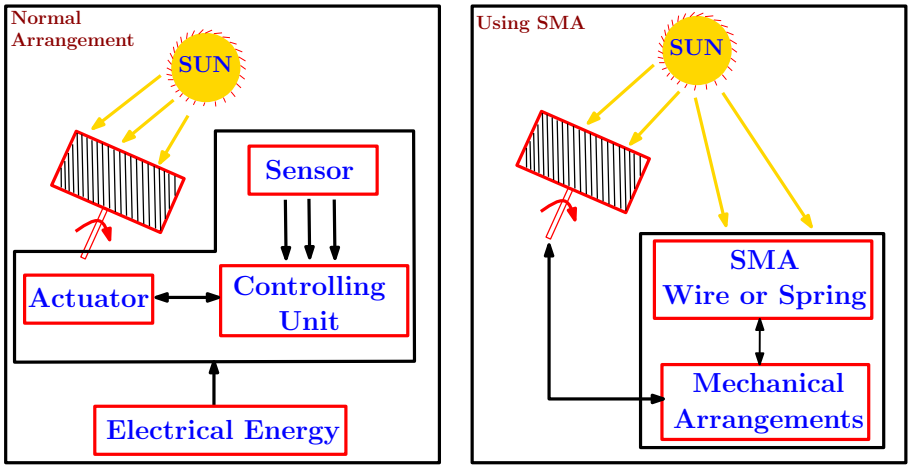

Figure 1.3: Comparing the number of working elements with existing sun tracking system (left) v/s number of working elements for a proposed smart sun tracking system (right) using SMA components that play the role of actuator & sensor simultaneously. (adapted from figure 1 and 2 [7])

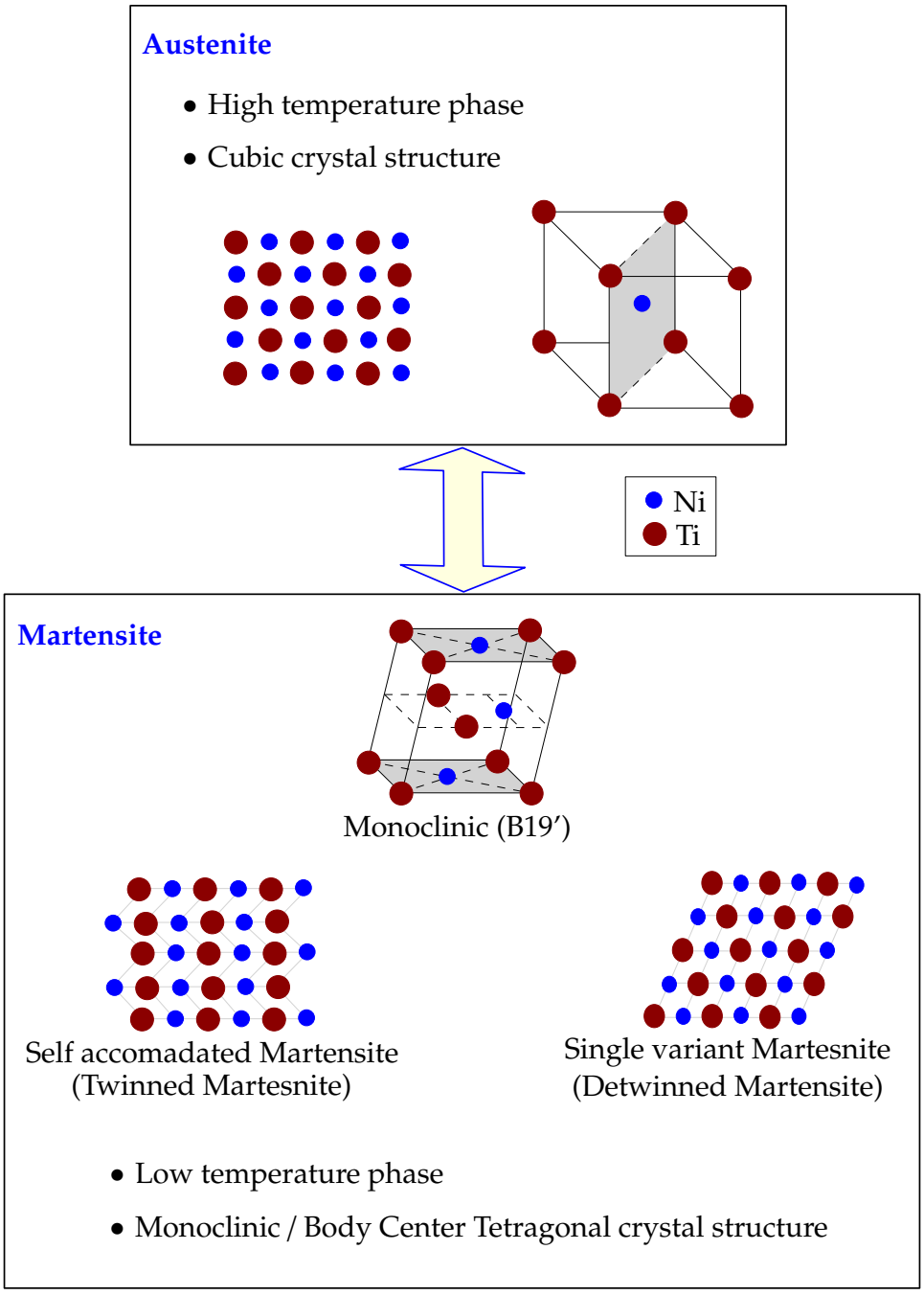

Figure 1.4: The underlying microstructural changes in shape memory alloys during thermoelastic phase transformations occur between a stable high temperature austenitic phase and low temperature martensitic phase. The non-cubic martensite phase can exist in different orientations or variants (adapted from [1], figure 2 [11]).

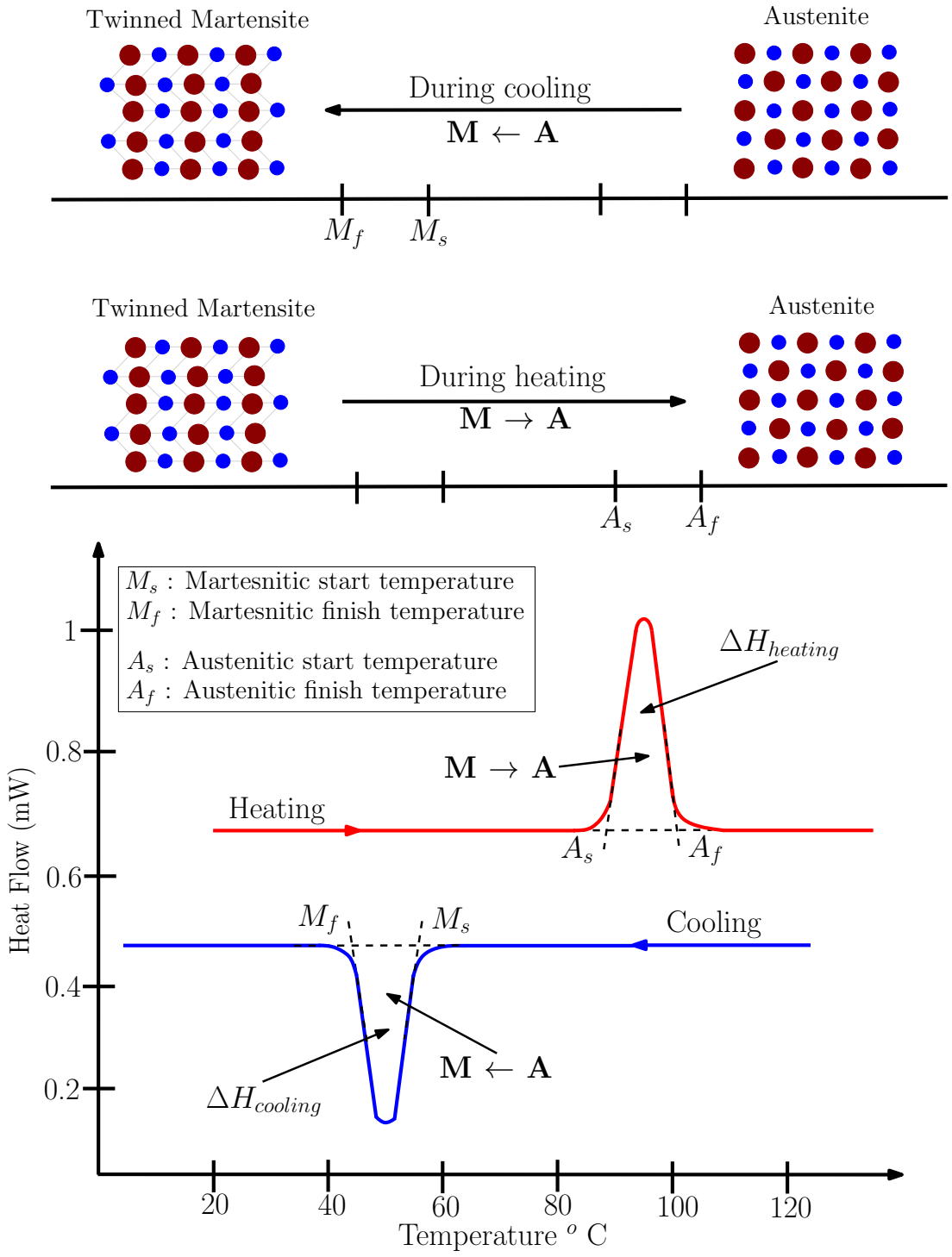

Figure 1.5: Schematic showing crystal structures of twinned martensite and austenite along with associated forward and backward transformation cases. Transformation temperatures martensitic start (M_s), martensitic finish (M_f), austenitic start (A_s) and austenitic finish (A_f) are obtained from a standard DSC test as per ASTM standard F2004-05R10 (adapted from [1, 12]).

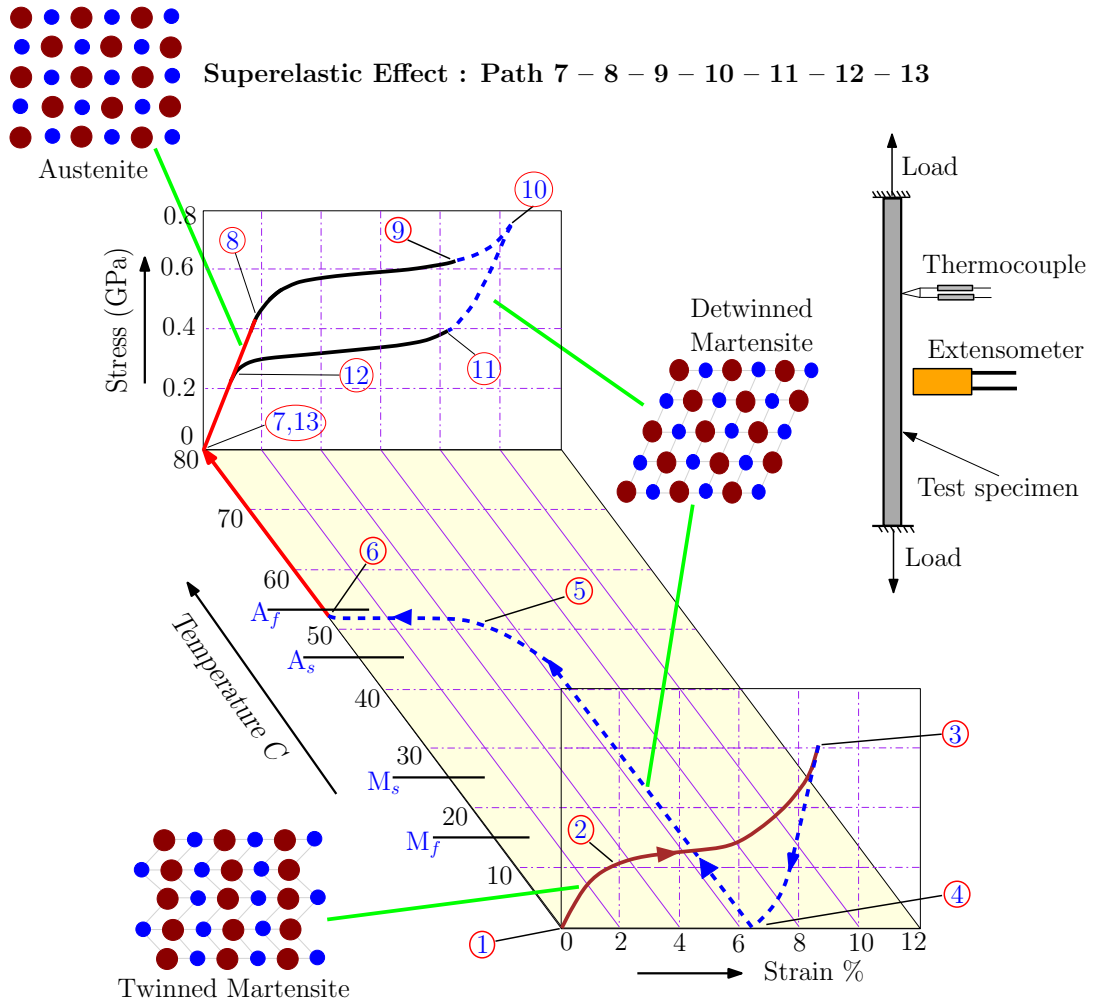

Figure 1.6: Thermomechanical experiment showing shape memory effect (path 1 – 5) and superelastic effects (path 6 – 11). A description of these states is discussed in section 1.2.1. These reversible effects are manifestations of solid-solid phase transformations between a stable high temperature austenitic phase and low temperature martensitic phase (adapted from figure 6 [11]).

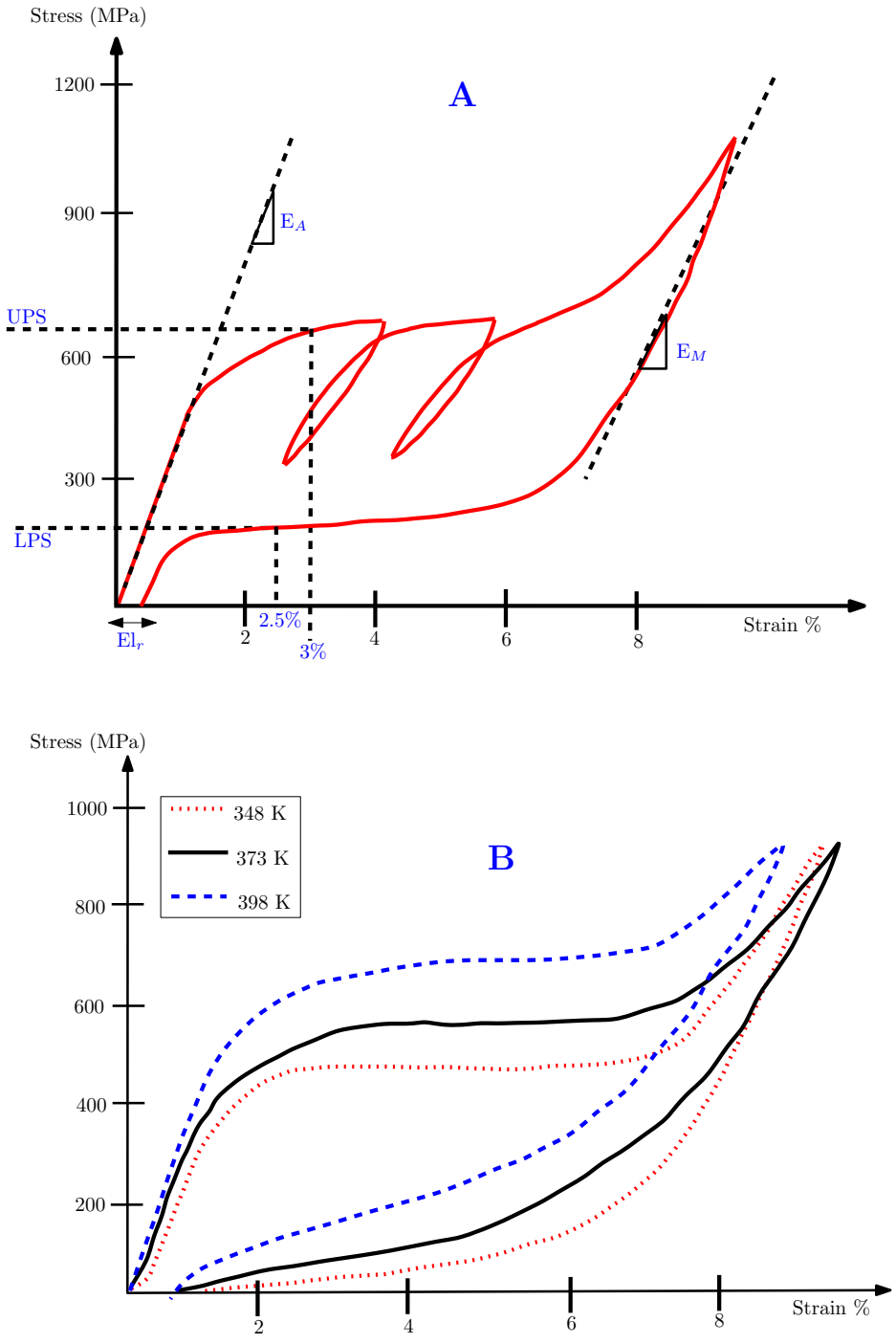

Figure 1.7: **(A)** shows a typical superelastic response with internal loops of a NiTi SMA with some salient features like upper plateau strength (UPS), lower plateau strength (LPS), residual elongation (El_r) highlighted as reported in ASTM standard F2516-07$^{\varepsilon}$ [13]. In addition, the austentic and martensitic moduli E_A and E_M are shown. **(B)** shows the temperature dependence of the superelastic response at three different temperatures.

1.2 Shape Memory Alloys : Temperature Induced Phase Transformations

In shape memory alloys (SMA), functionalities arise from their underlying microstructural changes when subjected to external non-mechanical stimuli like temperature or magnetic field changes [14]. In thermally responsive SMAs, the reversible solid-solid diffusionless thermoelastic phase transformations between a stable high temperature austenitic phase and low temperature martensitic phase are responsible for them to demonstrate interesting phenomenon like **shape memory effect (SME)** and **superelasticity (SE)**. The austentic phase has a cubic crystal structure as compared to the martensitic phase which has either tetragonal, orthorhombic or monoclinic structures as shown in 1.4 [15]. The transformations are a result of shear lattice distortions (twinning) rather than long range diffusion of atoms [1, 16]. The martensitic phase can have different orientations (variants) and can exist as twinned martensite formed by combination of "self-accommodated martensite variants" or as a "detwinnned/reoriented martensite" with a specific variant being dominant [1,16]. The phase transformations occur over some characteristic transformation temperatures namely martensitic start (M_s), martensitic finish (M_f), austenitic start (A_s) and austenitic finish (A_f). ASTM standard F2004-05R10 [12] discusses the details of measuring these transformation temperatures using a *differential scanning calorimetry (DSC)* test for a NiTi SMA. A schematic of crystal structures of twinned martensite, austenite and associated transformation temperatures are shown in figure 1.5.

1.2.1 Shape Memory Effect and Superelasticity/Pseudoelasticity

The ability of SMA to return to a predetermined shape on heating is referred to as the **shape memory effect (SME)**. As shown in path 1–5 in figure 1.6, upon external loading, self accommodated martenstic twins are detwinned into more stress preferred martensite variants typically associated with large ($\sim$8%) macro-

scopic strains [17]. Upon unloading, large residual inelastic strains are observed which are recovered upon heating to temperatures above A_f unlike in conventional materials. During heating, the low symmetric martensitic phase (M) is transformed back to stable austentic phase (A) thus resulting is complete strain recovery and thus demonstrating shape memory effect [17]. On cooling below M_s in absence to external loads, austentite transforms back to self-accommodating variants of martensite.

Martensitic transformations purely due to mechanical loading in the austensitc phase is also a possibility with SMA. The capability to recover large strains ($\sim$8%) and associated large stress–strain hysteresis due to mechanical loading-unloading under isothermal conditions is referred to as **superelastic/pseudoelastic effect (SE)** [17]. These effects are observed at temperatures greater than A_f as shown by path 6–11 in figure 1.6. ASTM standard F2516-07$^{\varepsilon 2}$ [13] discusses a standard test method for a tension test on NiTi superleastic materials. This standard also discusses details on some of the salient features (see figure 1.7) to be noted in a typical superelastic response like :

- **Upper plateau strength (UPS)**: The stress at 3% strain during loading of the sample
- **Lower plateau strength (LPS)**: The stress at 2.5% strain during unloading of sample after loading to 6%
- **Residual Elongation ($\mathbf{El}_r$)** : The difference between strains at a stress of 7 MPa during loading and unloading operations.
- **Uniform Elongation** : Elongation determined at maximum force sustained by specimen prior to necking or fracture or both.

In addition, the hysteretic area, large plateau strains (in order of 6 – 8%), and

moduli differences between the austentic and martensitic phases are some of the other important characteristics of a superelastic response of SMA (see figure 1.7). The SE response is also sensitive to the external stimuli i.e operating temperature as shown in figure 1.7B. The hysteretic behavior primarily makes SMA a excellent damping material.

1.3 Review of SMA Applications

The ability of SMA to reversibly respond to external temperature changes and change their physical/mechanical properties have enabled them to find many applications. SMAs can be used both as sensors and actuators where they can sense the changes in external stimuli and monitor certain desired functions [18]. The unique characteristics of SME and SE have made SMAs the material system of choice in applications ranging from sensing and control, vibration damping, biomedical, automotive and aerospace areas [8, 18–21]. A review of many SMA devices in use (or being developed) across many engineering applications is detailed in the following sections below.

1.3.1 Biomedical Applications

NiTi SMAs have found many biomedical applications due to their excellent biocompatibility. Clinical studies have shown that Nickel on its own is quite toxic and any contact with nickel can lead to various medical complications [22]. However, in case of intermetallic NiTi alloys, the bonding between Ni and Ti is quite strong (like in ceramic materials) as compared to the Nickel bonding in steel and other materials [23]. Further, the commercial NiTi alloys uses a passive TiO_2 (titanium oxide) layer coating on its outer surface that prevents any nickel leakage as it acts as a physical and chemical barrier in preventing Ni oxidation [23, 24]. The TiO_2 layer is harmless to human body and provides high resistance towards corrosion of

Ti alloys [22]. Many clinical studies have shown minimal Nickel contamination due to use of NiTi SMAs and thus showing good biocompatibility [24].

In addition, NiTi SMA's show excellent MRI compatibility, kink resistance, corrosion resistance and substantial moduli differences between austenitic and martensitic phases. All of these properties make SMAs a good choice for many biomedical applications like "drug delivery systems, self-expanding stents, stent delivery systems, implantable devices, catheters, guide-wires, atrial occlusion devices and thrombectomy devices" [22–29]. In most of these biomedical applications, transformation temperatures of the SMA are programmed such that the A_f is below the body temperature [28]. The superelastic SMA components are cooled to their martensitic state (i.e below M_f) and deformed to a temporary shape for easy insertion. Upon deployment at the right location in the body, the SMA device is heated above A_f (i.e austenitic state) where the NiTi component recovers back to its original shape and performs the necessary function as desired. Some specific examples are discussed below to illustrate this point.

SMA springs, wires and braces in many orthodontic applications are designed in the LPS region so that they can deliver relatively constant forces over large activation strokes as shown in figure 1.8. Their ability to deliver constant forces are commonly employed for space closure and tooth movement in many orthodontic applications [30–32]. Further, based on various test results, researchers have suggested that SMAs provide superior spring-back properties, large recoverable strains thus making them better alternatives when compared against its counterparts like stainless steel, β-Ti, Co-Cr for medical applications [33–35]. Though the stainless steel counterparts can deliver higher forces, however their force delivery rapidly decays over time as compared to SMA springs for relatively long activation ranges as shown in figure 1.8 [36,37]. In many of these dental applications, by choosing suitable wire diameters

of SMA, the required force can be varied based on application [38].

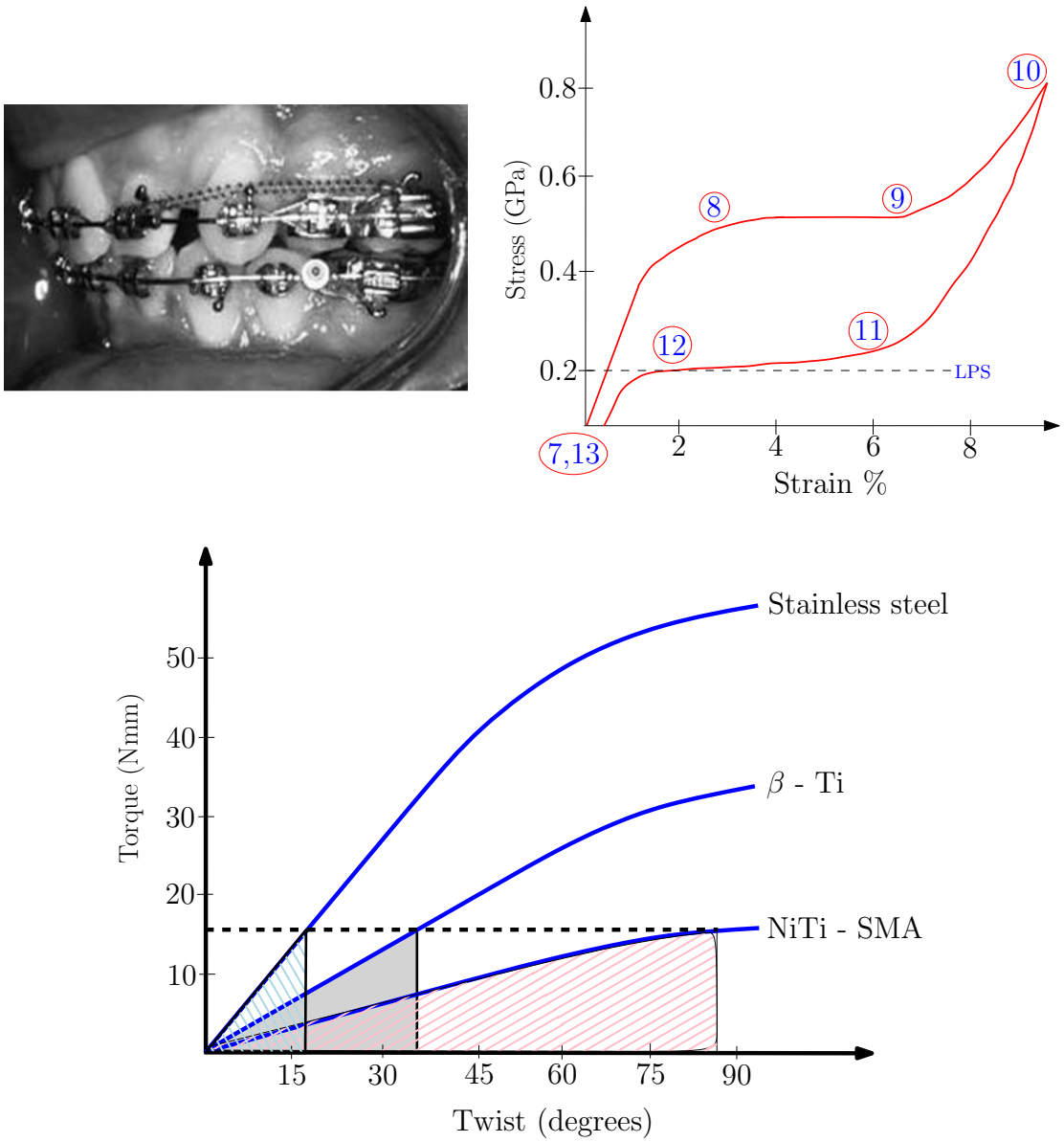

Figure 1.8: Figure shows a SMA torsional helical spring used for tooth movement, space closure in orthodontic applications. The idea here is to design the spring at the LPS so that it can deliver relatively constant forces over large strokes (photograph reproduced from figure 1 [39]. Comparison graph adapted from figure 1 [35]).

SMAs have found applications in many "minimal invasive surgery applications" as they can easily pass through convoluted paths and reach various parts of human body [23]. NiTi wires, tubes that demonstrate good kink resistance are used to maneuver complex paths and still remain in its original shape at the time of delivery [23]. These applications indicate the use of SMA like a "metallic rubberband" without the component loosing its shape. Superelastic SMA devices in their austenitic state provide high resistance to deformation/kinks and keeping them in desired shape without any permanent deformation even under considerable loads.

SMAs are used in the neurosurgical field as coils, stents or microguidewires mainly to treat cerebral aneurysms [40]. To prevent aneurysm rupture, coils are positioned into the aneurysm to facilitate "clotting or thrombotic reaction within the aneurysm" [40]. The superelastic effects of SMA are utilized here which allows large deformations and prevent crushing of the coil. Microguidewires made of NiTi are employed for stent positioning due to superior kink resistance and flexibility [24, 40]. Similarly, with the goal of trapping blood clots and dissolving them, many cardiovascular devices have been developed to tackle pulmonary embolism and one of the first SMA filter called "Simon Filter" was developed [22, 41].

Self expanding stents named in the honour of dentist C.T. Stent find applications in cardiovascular applications with the goal of preventing collapse of blood vessels [22, 25]. Stents are shape set in their deployed configuration (generally expanded diameter in its austenitic state) and then compressed into a catheter at lower temperatures below M_f. Stents employed in arteries may be subjected to continuously varying external pressures and collapsing or crushing of deployed stents could result in serious medical complications [24, 26]. SMA stents with their superior flexibility and spring back properties prevent the stents from collapsing when compared to its counterparts [24]. The stents are designed to work in the LPS region such that even

higher external pressures does not allow them to transform to their martensitic phase as the difference between plateau stresses are quite significant. This ensures that the stents are in their austenitic state without undergoing any permanent deformation under constant external pressures at all times during their deployment.

SMA spacers have found applications in many orthopaedic applications with the intention of applying constant forces on fractured bones to accelerate the bone healing process [22]. The spacers (sometimes addressed to as staples) in its opened (deformed) shape are deployed at the site and then heated so that the SMA in its austentic shape can apply the required compressive forces to facilitate rebuilding fracture bones [22, 27].

All of these unique features makes the use of SMA components a feasible option in many biomedical application with many of them already having FDA® approvals [42].

1.3.2 Civil Engineering Applications

In many civil engineering applications, large SMA wires, ropes, springs and beams are being used as damping elements in bridges, buildings and also in seismic resisting systems due to their excellent energy dissipation and recentering capabilities [20, 43–46]. Figures 1.10 and 1.11 shows different SMA reinforcements commonly used for energy dissipation in civil engineering structures.

In seismically active areas, buildings and bridges can be prone to damage due to lateral displacements during an earthquake event [47]. Building earthquake resistant structures have been an intense area of interest lately and study of SMA rebars as possible reinforcements in this pursuit has received significant attention (see figure 1.10) [45, 47]. The use of SMA components as reinforcements in reinforced concrete (RC) have performed better in confining lateral column displacements even at higher

amplitudes of dynamic loading (i.e simulating large earthquake events) compared with their counterparts like steel-RC columns [47].

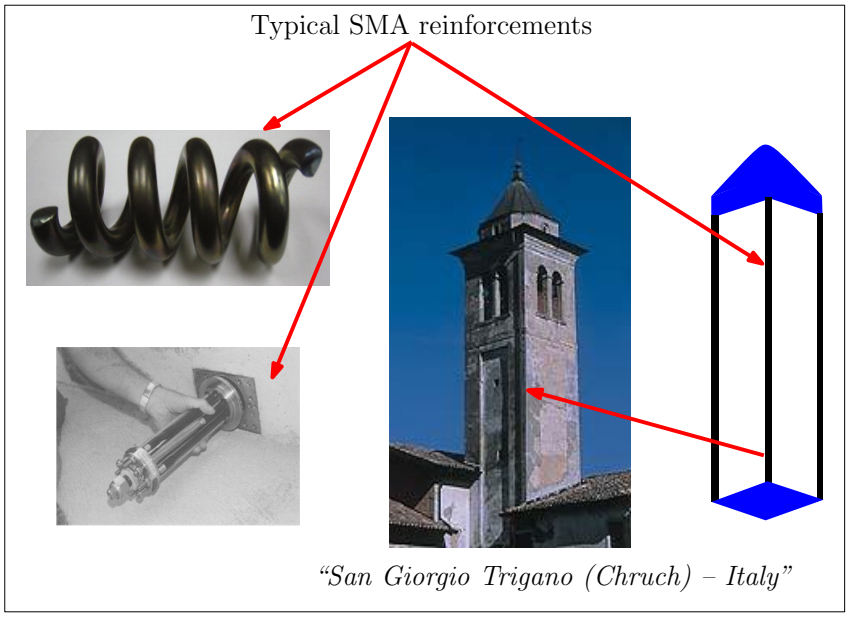

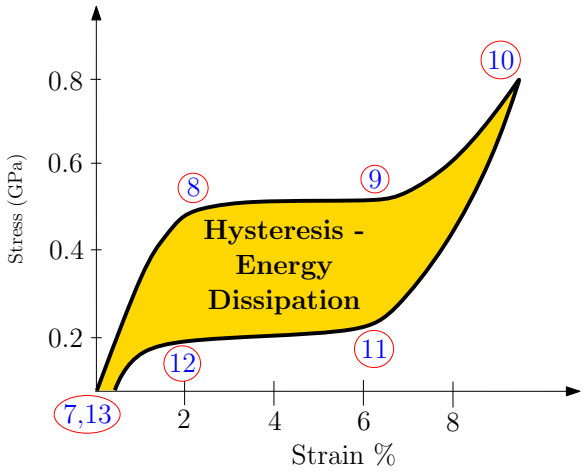

Figure 1.9: Figures some SMA reinforcements in many civil structures for recentering and damping applications. The large loading–unloading hysteresis (shaded region under the entire stress–strain curve) associated with superelastic responses in SMA makes them a very efficient energy dissipation system. (photographs reproduced from [20, 48]).

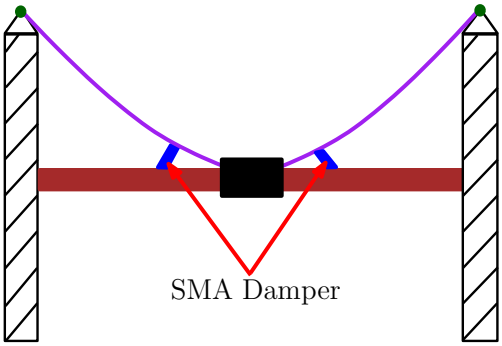

SMA Damper for Cable Bridge

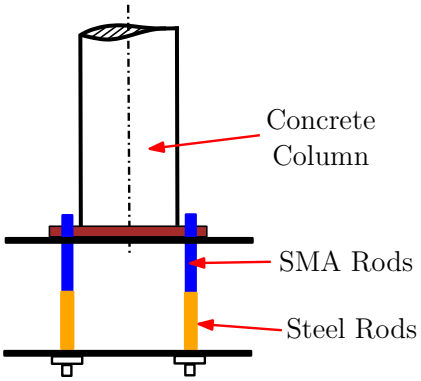

SMA Anchorage for Column

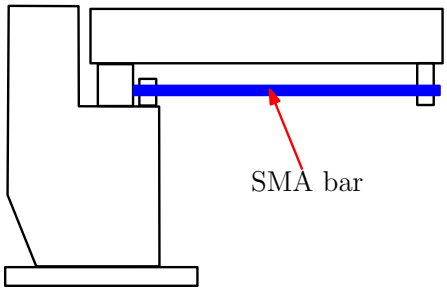

SMA Restrainer

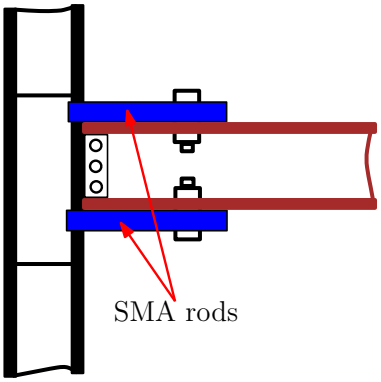

SMA Connector

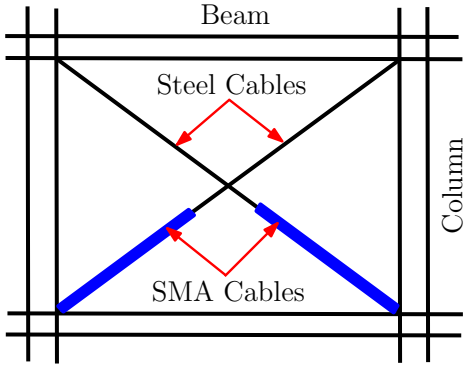

SMA braces for frame structure

Figure 1.10: Various use of SMA components as energy dissipation devices/dampers for simply supported cable bridges, anchorages and connectors for columns, braces for framed structures. (figures adapted from [20, 48]).

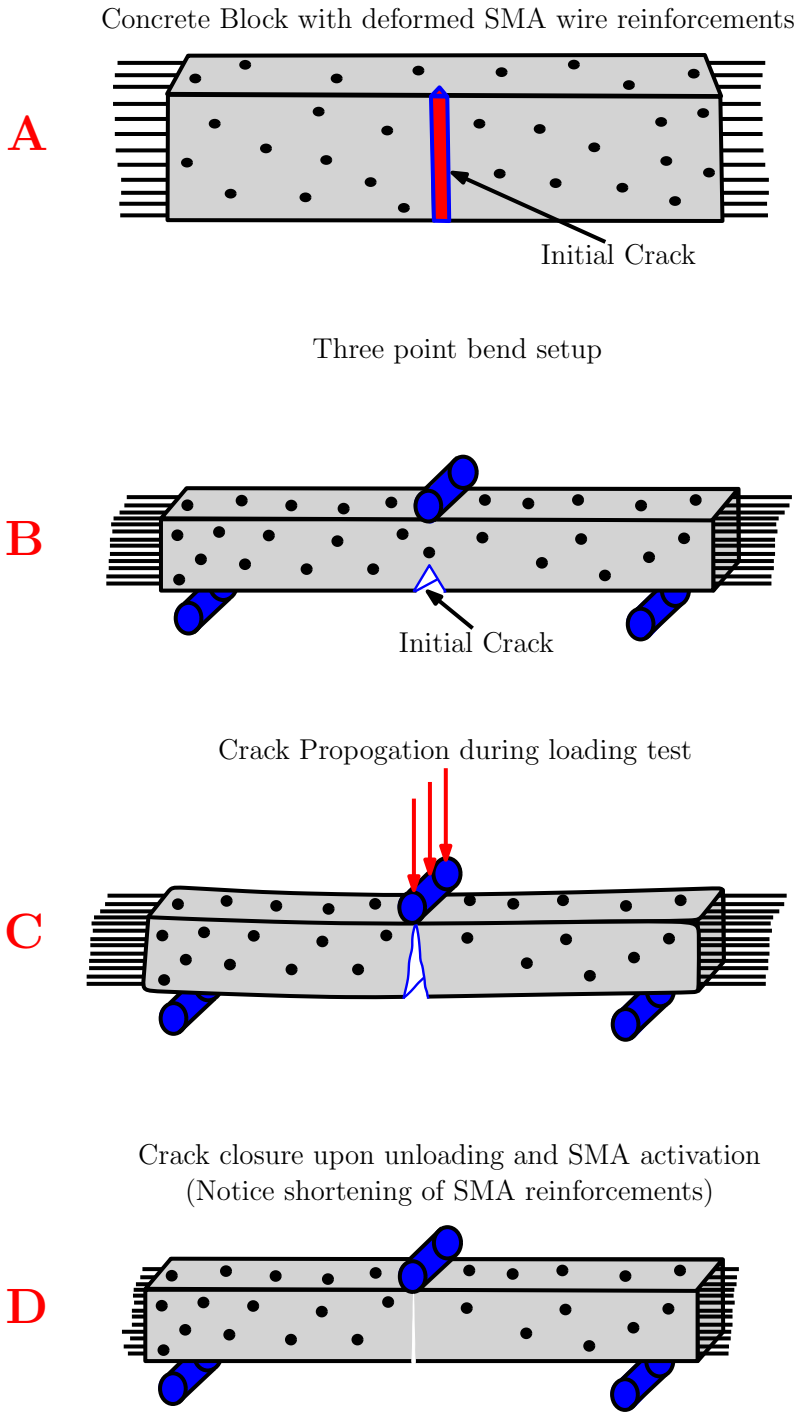

Figure 1.11: (A) - Some pretensioned SMA reinforcements in a concrete block with an initial crack. (B) shows a classic 3-point bend setup. (C) shows the crack propagation during loading. (D) shows the crack closure upon unloading and activating (heating) SMA reinforcements. The SMA wires shorten causing the crack to close (figures adapted from [20, 49]).

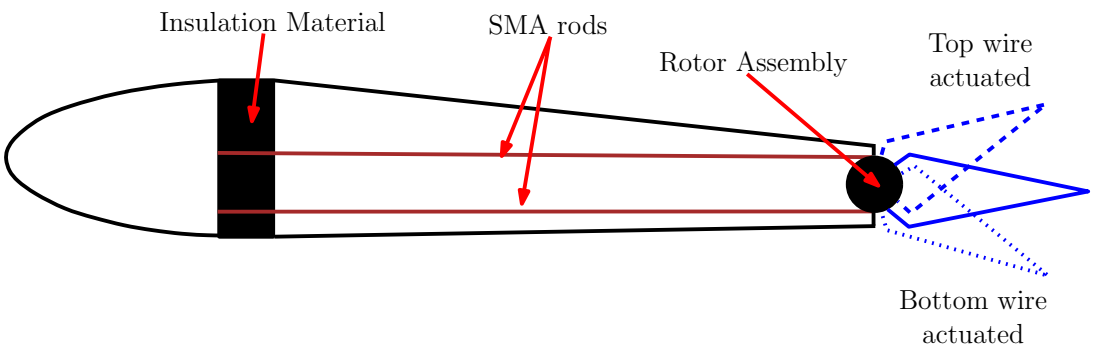

Figure 1.12: The use of pre-twisted SMA rods to torsionally actuate blade tabs between two angular positions is a possibility by differentially heating of top and lower SMA rods. This way the angular positioning of "trailing edge tab of a helicopter rotor" can be adjusted and thus allowing for user in-flight tracking of its position (figure adapted from [50]).

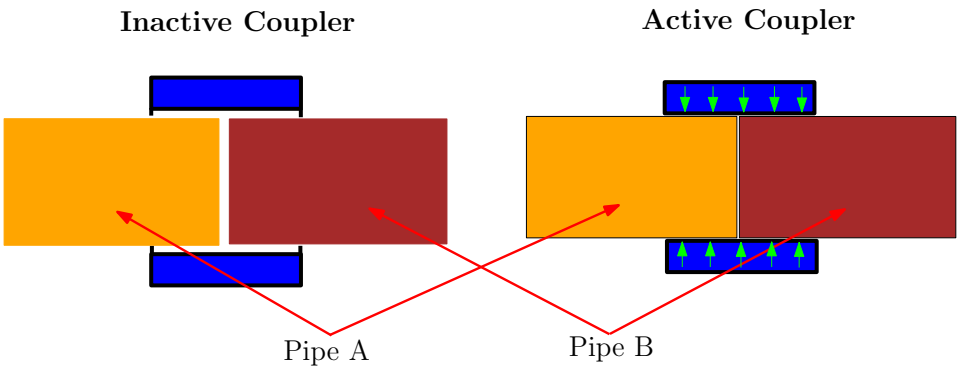

Figure 1.13: SMAs can be used as couplers that can substitute socket welds or compression fittings in aerospace, civil, oil exploration industries. The idea is to deform the couplers in its martensitic state to larger diameters for easy sliding along the pipes and then heated to temperatures above A_f to hold the ends of pipes firmly with appropriate compressive forces. (figure adapted from [51, 52])

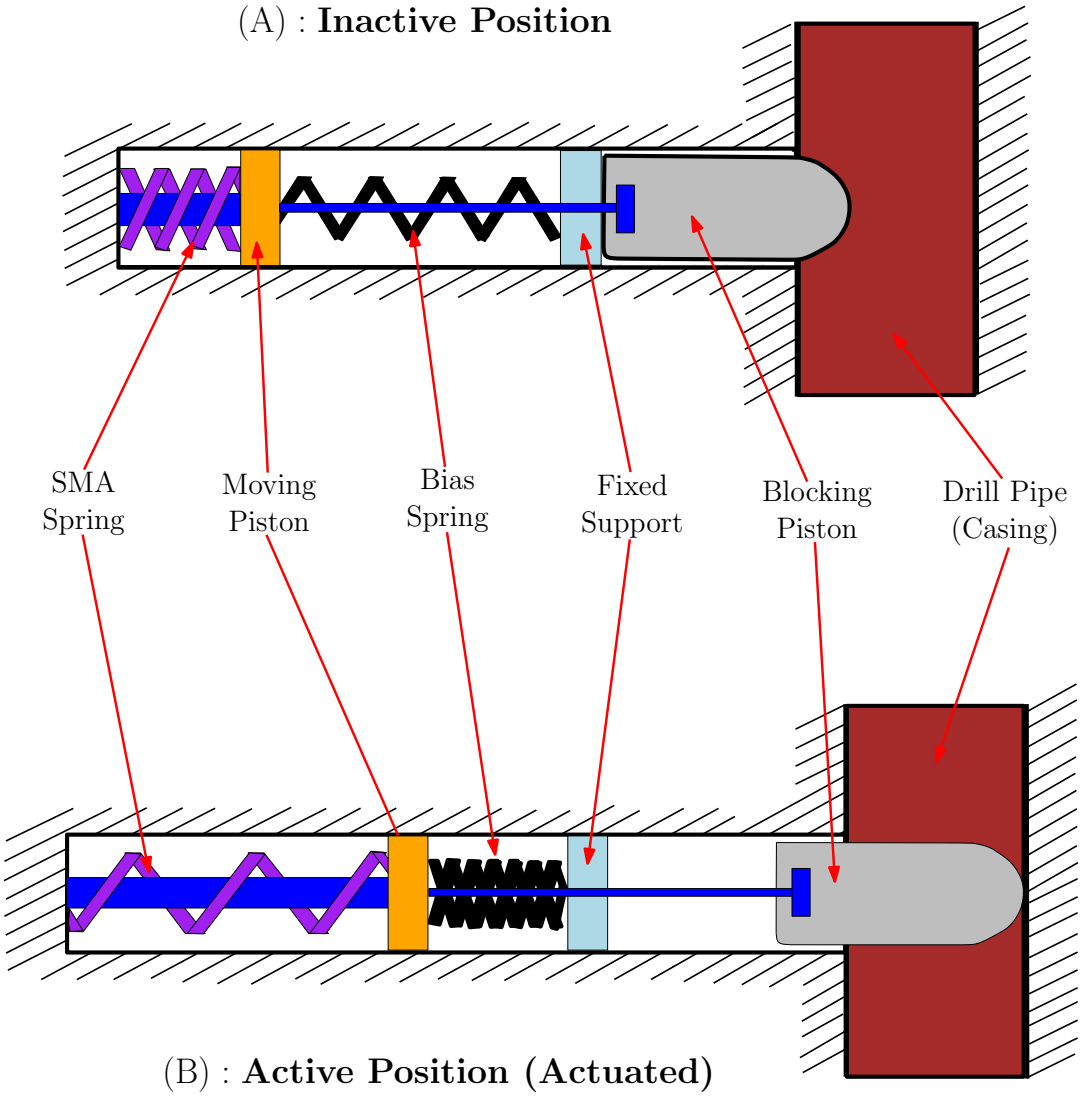

Figure 1.14: A combination of SMA springs and bias springs are employed to actuate pistons in "blowout preventer's" that either block or unblock drill pipes. (A) shows the the inactive position of blocking piston where the bias springs keeps the SMA spring compressed at lower temperatures (i.e below M_f). (B) shows the SMA spring in its austenitic state (at higher temperatures i.e above A_f) overpowers the bias spring forces and actuates the blocking piston to prevent any flow in drill pipe to prevent any accidents. (figure adapted from [52])

With superior damping capacity and ability to deliver large plateau strains at relatively constant stresses, SMAs make excellent candidates for recentering applications in the form of bracings or dampers [47]. Many different types of SMA braces for framed structures have been designed for energy dissipation devices (see figure 1.10) [20]. In many cases, bundles of pre-tensioned superelastic SMA wires are used as reinforcements have been employed for re-centering braces [20]. In addition, SMA's have also been effective contenders as beam–column or column–foundation joints in many retrofit structures as the large plateau strains in SE can be used to provide desired clamping forces to hold the members together [47]. This helps in controlling relative hinge displacements when used as restrainers [47]. By connecting the bearings and bridge deck with superelastic bars, the "position stability" of simply supported bridges could be improved (see figure 1.10) [48, 53].

If a SMA reinforcement in its martensitic form is deformed (also referred to as pretensioning) and embedded in concrete and then electrically activated such that it reaches temperatures above A_f, sufficient constraining forces can be generated as the SMA tries to recover back to its original shape [47,53]. The extent of prestressing can be increased or decreased by controlling the amount of initial deformation of SMA reinforcement [47]. To illustrate this point, Mo and co-workers looked at developing a "smart concrete structure" that can potentially "self heal" after a damaging earthquake event [49]. In their study, as shown in figure 1.11, a concrete block with many reinforced SMA ropes was considered [49]. The SMA reinforcements were initially predeformed (pre-tensioning) in their martensitic state (i.e below their M_f) and reinforced in the concrete block with an initial crack as shown in figure 1.11. On a test bench, dynamic 3-point bend tests were conducted which resulted in crack propogation with increasing loads/frequencies mimicking a damaging earthquake event. The cracked structure is then unloaded and the SMA ropes were activated by heating

them above their A_f. Upon heating, the SMA ropes transform back to austenite and shorten in length back to its original shape. This results in large recovery forces that results in crack closure (crack healing) as the concrete structures are pulled inwards and thus minimizing the chances of building collapse after an earthquake event. Many such "self-restoration" options have been proposed with almost complete crack closure upon recentering [20]. On similar lines, many active confinement techniques where concrete columns are helically wrapped with SMA bands that can provide necessary tensioning upon heating have also been proposed [48].

In one of the first reported retrofit applications using SMA devices, the San Giorgio chruch in Italy used bundles of SMA wires to refurbish the church structure after an earthquake event [45,54]. As shown in figure 1.9, SMA devices were arranged in series in order to limit the forces to the masonary under the required limits and further seismic analysis were performed to analyze the performance of SMA devices [45, 54].

However, given the size of civil engineering structures, the use of NiTi SMA components have been limited due to high initial material and processing costs [48]. Going forward, developing more cheaper copper or iron based SMAs that could replace NiTi SMA components without compromising material performance would greatly benefit the civil engineering community as they potentially use many more *smart structures with active control capabilities*. Developing such copper or iron based SMAs and further understanding their underlying microstructural changes that influence their functionality is still an active area of research [28].

1.3.3 Aerospace and Automotive Applications

SMA components are used as thermal actuators in different temperature regimes depending on the kind of applications in automotive industry [8]. The use of SMA

actuators are finding applications in many pre-commercialized concepts like smart automotive lighting systems, fuel management, climate control, mirrors adjustments, locking systems, suspension adjustments etc. [8, 55, 56]. Similarly, SMA cables, beams, torque tubes are used in tailoring inlet geometry and orientation, increase/decrease fan nozzle in various aerospace applications [18, 50, 57, 58].

In some aircraft applications, smart SMA couplings have shown the possibility of substitute socket welds or compression fittings [51]. As shown in figure 1.13, at temperatures below M_f, the couplings are expanded to a larger diameter such that it can easily slide through the pipes to be fastened [51]. Once the SMA coupling transforms back to austenite (i.e above A_f which is generally programmed to be lower than room temperature), it shrinks to its original dimension and thus securely holding the pipe ends as the SMA coupling enforces sufficient compressive forces [51].

Chopra [50] reviews many possible applications of using smart materials in aerospace systems. For example, adjusting the "trailing edge tab of a helicopter rotor for in-flight tracking" using SMA components is one of the key proposed ideas [50]. Pre-twisted SMA rods to torsionally actuate blade tabs between two angular positions is possibility by differentially actuating the SMA rods as shown in figure 1.12. By heating the upper rod, the SMA rod shortens and causes the rotor assembly to actuate in one direction. By heating the lower rod, the SMA rod enables the rotor assembly to actuate in a different direction. The actuation of the rotor assembly in different directions causes the trailing edge to occupy multiple angular positions during flight maneuver. The SMA rods clearly perform both sensing and actuating functions and thereby reducing the use of separate working elements for sensors and actuators to perform the same task.

On similar lines, "Chevrons" in aircraft engines are employed for flow mixing and their configurations can be altered by using SMA beams based on changes in flow

temperature (normally temperature changes with different altitudes) [18]. At low altitudes and speeds, with higher engine temperatures, the chevrons fold inward for improved gas mixing and thus lowering noise [18]. These chevrons relax to a different configuration at lower temperatures (i.e at higher altitudes and speeds) to improve engine performance [18].

1.3.4 Other Applications

Oil and gas industry uses many hydraulic and electrohydraulic systems along with additional signal conditioning components which makes the overall system quite bulky [52]. Many SMA components along with bias systems have been considered to replace these traditional hydraulic and electrohydraulic systems [52]. As shown in figure 1.14, a combination of SMA and steel bias springs were employed to actuate pistons in "blowout preventer's" that either block or unblock drill pipes [52]. With reference to figure 1.14, position (A) indicates the inactive position of the blocking piston at lower temperatures (i.e below M_f) where the bias spring keeps the SMA spring compressed and thus allowing free flow through the drill pipes during operation. At higher temperatures (i.e above A_f), the SMA spring in its austenitic state overpowers the bias spring forces and actuates the blocking piston to block any flow in drill pipe to prevent any blowout situation.

Due to NiTi alloys excellent corrosion resistance properties, many underwater couplers/connector applications are considered [52]. SMA springs are cryogenically cooled to temperatures below M_f so that they can easily be deformed into a temporary shape for deployment (generally expanded to larger diameter for easy deployment) [52]. On exposure to actual operating temperatures (above A_f) they can revert back to austenitic phase and tightly hold the pipe ends [52]. The couplers in their austenitic state can provide the required compressive forces to hold the pipe ends in

place. On similar lines, some smart couplings have also been tested for submarine applications and underwater gas pipelines as shown in figure 1.13. Such couplings are easy to work with as it does not require any initial pipe surface preparation or subsequent welding or safety hazards [51].

SMA compression springs along with bias steel springs are finding applications in sprinkler systems that can automatically turn on or off based on the water temperature [28]. Ni-Ti-Cu springs are finding applications in thermostats, electrical circuit breakers where for example door positions in an self cleaning oven are monitored using SMA components [28]. NiTi discs located between electrical contacts in Lithium ion batteries can be used to break the circuits at critical temperatures [28].

Jeya Ganesh and co-workers have attempted to design a simple "sun tracking mechanism (SSTM)" to illustrate the dual sensing and actuating capability of SMA components [7]. The solar receptor position is automatically changed over the course of the days by using the solar radiation to actuate the SMA springs [7]. As described in figure 1.3, the use of such smart SMA springs considerably reduces the number of working elements as compared against a convectional sun tracking system that employs separate sensor and actuator for providing system level response [7].

1.4 Review of Modeling Approaches and Their Limitations

As discussed with various applications in section 1.3, SMAs are mainly used in the form of wires, bars, springs and beams that are subjected to primary modes of deformation like tension, torsion or bending loading conditions. In order to design and realize the vision of creating novel, potentially useful applications using SMA, it is imperative to understand and model the material response under these primary loading cases at the component level. Due to the complex nature of SMA response (see figure 1.6), model development for these materials have been addressed in a

number of different perspectives that are suited for different purposes. As shown in figure 1.15, several microscopic and macroscopic models have been developed to capture the complex SMA responses, identifying underlying mechanisms in phase transformations and explaining their underlying physics [59].

The microscopic models (mostly crystal plasticity based) focus on the micro-scale features of phase transformation to understand the basic underlying physical mechanisms that are inherent to these material systems. Several models were developed in order to understated micro-scale features, such as nucleation, interface motion, twin growth, etc [60, 61]. The phase volume fractions are not considered as a-priori internal variables but are a resultant of consequences of interface movements among different phases. Such models are useful in understanding fundamental phenomenon but posses limitations in terms of their applications towards predicting macroscopic responses useful for designing SMA components for many engineering applications [62, 63].

A brief review of some important macroscopic modeling approaches (by no means exhaustive) under different loading conditions is covered in the following sections as it is an uphill task to cover the entire gamut of available models for SMA. Section 1.4.1 reviews some important modeling approaches and their shortcomings in capturing responses under tensile loading. In sections 1.4.2 and 1.4.3, a more detailed discussion on extension of modeling approaches highlighted in section 1.4.1 for simulating responses under torsion and bending loading conditions would be discussed along with their limitations.

1.4.1 Tension Response of SMA

Two main approaches in macroscopic modeling SMA response can be broadly classified into models analogous to elastoplasticity and those analogous to magnetic

hysteresis/ ferromagnetic domain wall models [64, 65].

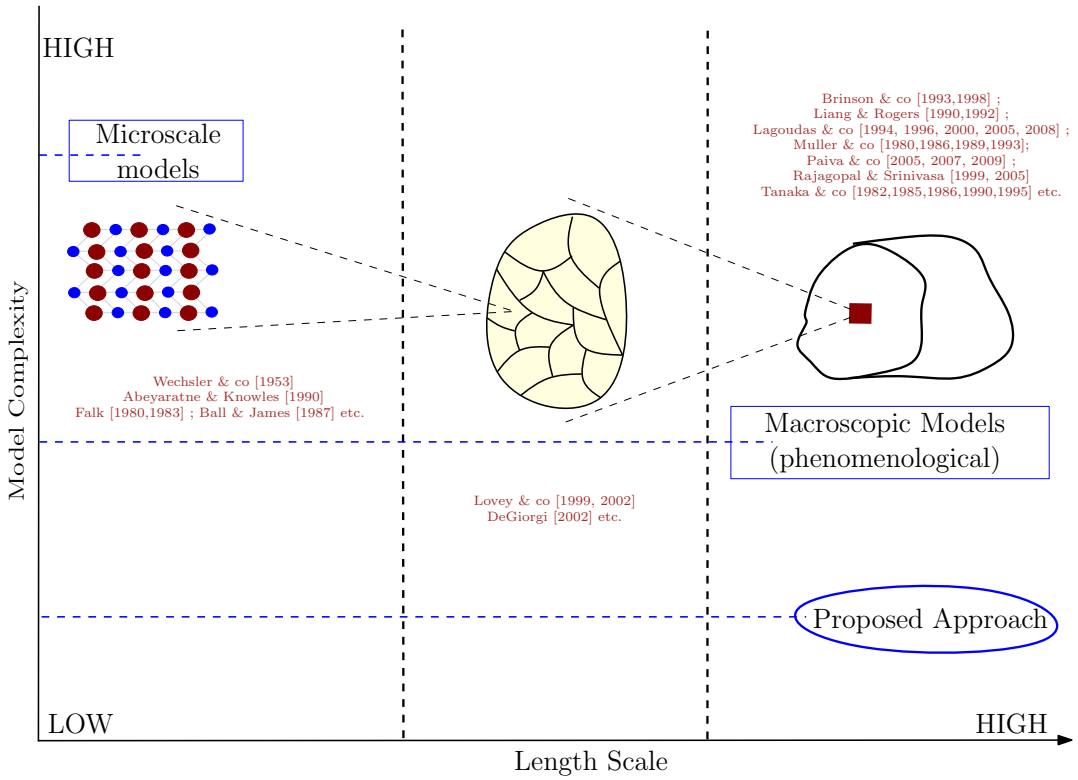

Figure 1.15: An overview of different modeling approaches along length scales. This dissertation focuses on the macroscopic structural models for SMA components that are computationally inexpensive and implementable directly at the component level.

The plasticity based approach assumes phase transformations similar to plastic flow with flow rules, yield conditions, normality conditions developed for phase transformations [59,64]. Tanaka and his co-workers [66–70] have presented an approach for thermoplastic materials with martensite volume fraction being the only scalar internal variable and constructing evolution equation of the martensitic volume fraction that can be reduced to a transformation state equation relating it with other state

variables like stress, strain, temperature. In their work, the energy balance equation and Clausius–Duhem inequality in the reference X-coordinate are expressed as shown in equation set 1.1.

$$\begin{aligned} \rho\dot{U} - \sigma L + \frac{\partial q_{sur}}{\partial X} - \rho q = 0 \\ \rho\dot{\eta} - \rho\left(\frac{q}{T}\right) + \frac{\partial}{\partial X}\left(\frac{q_{sur}}{T}\right) \geqslant 0 \end{aligned} \tag{1.1}$$

where ρ is the density in the current deformed configurations, σ being the Cauchy stress, U and q_{sur} the internal energy density and the heat flux from the surroundings and T, q and η are the temperature, internal heat generation and entropy density respectively. With an assumption that Helmholtz free energy ψ is a function of state variables strain($\bar{\varepsilon}$), temperature(T) and martensite volume fraction(ξ), equation sets 1.1 are reduced to a new form of Clausius–Duhem inequality given by equation 1.2 where $\boldsymbol{f}$ is the deformation gradient, $\bar{\sigma}$ is Piola–Kirchoff stress, η is entropy, ρ_o is the density in reference configurations. Further, an exponential form for the relation of martensite fraction and temperature during phase transformations is assumed as shown in equation 1.3 where, A_a, A_m, B_a and B_m are material constants in terms of transition transformation temperatures A_s, A_f, M_s and M_f respectively.

$$\left(\bar{\sigma} - \rho_o\frac{\partial\psi}{\partial\bar{\varepsilon}}\right)\dot{\bar{\varepsilon}} - \rho_o\left(\eta + \frac{\partial\psi}{\partial T}\right)\dot{T} - \left(\frac{\partial\psi}{\partial\bar{\xi}}\right)\dot{\xi} - \left(\frac{1}{\rho_o T}\right)\left(\frac{\rho}{\rho_o}\right) q\boldsymbol{f^{-1}}\frac{\partial T}{\partial X} \geqslant 0 \tag{1.2}$$

$$\begin{aligned} \xi_{M\to A} &= \exp[A_a(T - A_s) + B_a\sigma] \\ \xi_{A\to M} &= 1 - \exp[A_m(T - M_s) + B_m\sigma] \end{aligned} \tag{1.3}$$

$$\begin{aligned} \xi_{M\to A} &= \frac{1}{2}\left[cos\left(\frac{\pi}{A_f - A_s}(T - A_s)\right) + 1\right] \\ \xi_{A\to M} &= \frac{1}{2}\left[cos\left(\frac{\pi}{M_s - M_f}(T - M_f)\right) + 1\right] \end{aligned} \tag{1.4}$$

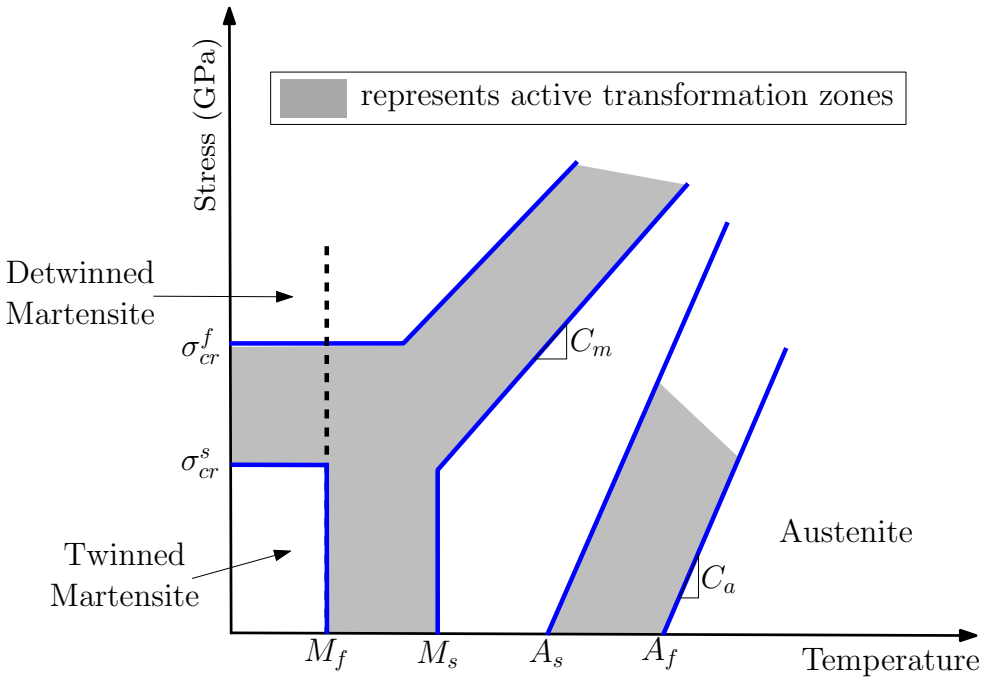

Figure 1.16: Figure shows a typical stress – temperature diagram used for some elastoplasticity approaches. Figure also indicates critical stresses (σ^s_{cr} and σ^f_{cr}), transformation temperatures (M_s, M_f, A_s and A_f) and slopes of various transformation lines/regions (C_m & C_a) used as inputs for model formulation. (adapted from [59,71])

Liang and Rogers [72,73], Brinson and co-workers [74,75] have extended Tanaka's approaches [70] by introducing transformation state equations describing transformation hardening effect using a stress–temperature phase diagram. In each active zone of the stress–temperature phase diagram (see figure 1.16), evolution functions for capturing the extent of martensite fraction are defined [59, 71]. Further, a constitutive relationship describing the thermomechancial response that uses the martensite evolution function must be established. The common evolution functions used are either polynomial, exponential or trigonometric in nature [59]. For example, Liang and Rogers [72] assume a cosine function as shown in equation 1.4 to describe martensite volume fraction–temperature (ξ–T) relation as against the exponential form chosen

by Tanaka and co-workers [72, 73]. Brinson and co-workers [74] further separate the martensite fraction internal variable into temperature and stress induced parts. Limitations of such phase diagram based approaches are summarized below :

- Such models require information on critical stresses governing formation of stress induced martensite, transformation temperatures and slopes of various transformation lines/regions in a stress–temperature phase diagram as inputs (as shown in figure 1.16) [71, 76]. These transition points like critical stresses and stress–temperature phase diagram slopes must be determined for every temperature and are not evident from a standard experimental stress–strain or stress–temperature response especially at different temperatures as the responses tend to show hardening or softening effects (see figure 1.7 for illustrations) [71, 76]. This makes it hard to derive necessary material and model parameters and implement such models for engineering cases as they are heavily dependent on such experimental information.

- The available models haven't shown the capability of capturing internal loops or temperature dependence observed in superelastic responses (see response in figure 1.7 for illustrations) which are quite critical for control system applications [76]. These models have only been used to approximately capture outer loop responses. Capturing internal loops and temperature dependence of responses are important from an application standpoint as in many applications not the entire the response is considered and only a partial internal loop might be of significance for design purposes [76]. If one need to capture responses at different temperatures then the model parameters must be recomputed thus making it cumbersome for implementation for various applications [76].

Lagoudas et al. [77], in an effort to study the effective thermomechanical response

of active fibrous composites with SMA fibers have generalized the one-dimensional formulation developed by Sato and Tanaka [70]. Abeyaratne and Knowles [78] in an attempt to describe austentite-martensite interfaces propose a differential type evolution equation for martensitic volume fraction by constructing a Helmholtz potential consisting of kinetic and nucleation criterion's (refer equations 31–35 in [78]). Auricchio and co-workers [79, 80] used two independent martensite volume fractions one denoting multiple variant martensite fraction and the other a single variant martenite fraction and developed expressions for their productions respectively (refer equation sets 14, 16 and 17 in [79]). Renicki and co-workers [81, 82], Leclercq and Lexcellent, [83] have developed a thermodynamical model (phenomenological) to simulate superleastic effects by constructing free energy potentials with martensitic volume fraction as a internal state variable. Boyd and Lagoudas [84], Qidwai and Lagoudas [85] have developed models by constructing free energy potentials for a 3-D case. In their approach, inelastic strains due to phase transformation are accounted for as additional internal state variables in addition to orientation of martensitic phase in order to account for non-proportional loading and combined isotropic and kinematic transformation hardening [84]. The Gibbs free energy for a polycrystalline SMA in their work is given by equation 1.5, where $\mathbb{S}$, α, c, s_0 and u_o are the effective compliance tensor, effective thermal expansion coefficient tensor, effective specific heat, effective specific entropy, and effective internal energy at the reference state respectively [84–86].

$$\begin{aligned} G(\sigma, T, \varepsilon^t, \xi) = & -\frac{1}{2\rho}\sigma : \mathbb{S} : \sigma - \frac{1}{\rho}\sigma : \left[\alpha(T - T_o) + \varepsilon^t\right] \\ & + c\left[(T - T_o) - T\ln\left(\frac{T}{T_o}\right)\right] - s_o T + u_o + \frac{1}{\rho}\boldsymbol{f}(\boldsymbol{\xi}) \end{aligned} \tag{1.5}$$

The symbols σ and T_o in equation 1.5 denote the Cauchy stress tensor and reference

temperature. The effective material properties denoted in equation 1.5 are assumed to vary with martensite volume fraction(ξ) as shown in 1.6. The hardening function $\boldsymbol{f(\xi)}$ is a polynomial that captures the transformation-induced strain hardening in the SMA materials for (A $\rightarrow$ M) and (M $\rightarrow$ A) transformation cases as shown in equation 1.7 where ρb^A, ρb^M, μ_1 and μ_2 are material constants for transformation strain hardening. It must be pointed out that the term $\boldsymbol{f(\xi)}$ in equation 1.5 is actually a function of $\dot{\xi}$ and not ξ as shown in equation 1.7 which makes the Gibbs potential internally inconsistent as it is now a function of $\dot{\xi}$ and not ξ (see equation 1.5).

$$\begin{aligned} \mathbb{S} = \mathbb{S}^{\boldsymbol{A}} + \xi\Delta\mathbb{S}, \quad \alpha = \alpha^A + \xi\Delta\alpha, \quad c = c^A + \xi\Delta c, \\ s_o = s_o^A + \xi\Delta s_o, \quad u_o = u_o^A + \xi\Delta u_o \end{aligned} \tag{1.6}$$

$$\boldsymbol{f(\xi)} = \begin{cases} \frac{1}{2}\rho b^M \xi^2 + (\mu_1 + \mu_2)\xi, & \dot{\xi} > 0, \text{ For transformation (A} \rightarrow \text{M)} \\ \frac{1}{2}\rho b^A \xi^2 + (\mu_1 - \mu_2)\xi, & \dot{\xi} < 0, \text{ For transformation (M} \rightarrow \text{A)} \end{cases} \tag{1.7}$$

Khandelwal and Buravalla [59] have summarized several such approaches formulated on a similar platform in table 1 and 2 of their work where they review various modeling approaches for SMA.

In general, with such elastoplasticity approaches, the evolution equations are generally obtained either by considering transformation micromechanims or generally by matching experimental results directly and further constructing a free energy potential and using a "dissipation postulate" in conjunction with second law of thermodynamics (as seen in equation 1.2) [59, 87, 88]. Also, the martenite volume fraction is generally used as internal state variables to describe the average measure of geometry of microstructures and different mathematical functions (polynomials, exponential, trignometric) are used to describe smooth transition (as seen in equations 1.3, 1.4, 1.6) [59,87,88]. In some cases the internal variable (martensite volume

fraction) are separated into temperature-induced and stress induced parts [74]. Such elastoplasticity based approaches have the following limitations :

- Though these models have firm thermodynamic foundations, such strategies become extremely cumbersome for identification of material and model parameters from experimental data as the identification is mostly heuristic. Incorporating temperature effects and accounting for internal loops is cumbersome as many of material parameters and functions must be recomputed for simulating these effects (For example, see table 1 in [84–86, 89] for the number of material parameters needed for model verification) [64].

- A close perusal of the 3-D constitutive models developed, reveals that, in actuality, these approaches just use the one dimensional data and use a von-Mises equivalent stress approach due to lack of a full three dimensional data on SMAs [90]. Given the fact that such an approach (originally based on experimental observations of steel) does not even work well for aluminum, it is hard to justify their use in SMA given their complex thermomechanical response [90].

- Further, if such models are used to simulate a simple bar or wire response then one needs to simulate a full 3-D model or use a reduced 3-D model for analyzing specific cases thus making them hard to implement for actual design cases at the component level.

However, phase transformations in SMA are more akin to domain wall switching in magnetism rather than crystallographic slip. The whole SMA structure can be imagined as a collection of many such domains with each of them discretely switching states based on the external impetus (i.e switching between austenite – martensite variant or between martensite variants in case of SMA). The macroscopic responses

of SMA hysteresis are quite similar to those observed in ferromagnetic materials with the only key difference being that there is a distinct elastic response observed in SMA before switching states during phase transformation event (see figure 1.17 for illustrations). Thus, in case of models analogous to magnetic hysteresis, the hysteresis associated with SMA responses are compared to magnetic hysteresis and modeled using Preisach models [72, 91–100].

The Preisach model was first introduced by Ferenc(Franz)Preisach in 1935 to study hysteresis in magnetic materials published first with a German academic journal [101]. Mayergoyz in his book "Mathematical Models of hysteresis" [102] discusses the notion of substituting a smooth hysteresis curve with a series of steps. Each step referred to as a "hysteron" is characterized by three characteristic parameters namely the "On" condition, "Off" condition and "height of the step" [103, 104].

Considering a set of "hysterons or units of hysteresis" $\hat{\boldsymbol{\gamma}}_{\boldsymbol{PQ}}$, each of which can be represented as a non-ideal switch on the input-output diagram as shown in figure 1.18. The "switch on" and "switch off" values are P and Q respectively with the assumption that $P > Q$ [104]. The outputs of the hysteron is assigned as $\hat{\gamma}_{PQ}\mathrm{u(t)} = +1$ and $\hat{\gamma}_{PQ}\mathrm{u(t)} = -1$ for "On" and "Off" states respectively. Paths a–b–c–d–e and e–d–f–b–a are taken for cases when input values increase or decrease respectively (see figure 1.18) [104].

$$f(t) = \iint\limits_{P \geqslant Q} \mu(P, Q)\hat{\gamma}_{PQ}[u(t)]\, dP\, dQ \tag{1.8}$$

Equation 1.8 is a representation for infinite set of hysterons with $\mu(P, Q)$ being the weight functions. Preisach models have been used for simulating hysteresis primarily in two ways i.e either temperature–strain hysteresis or stress–strain hysteresis [104].

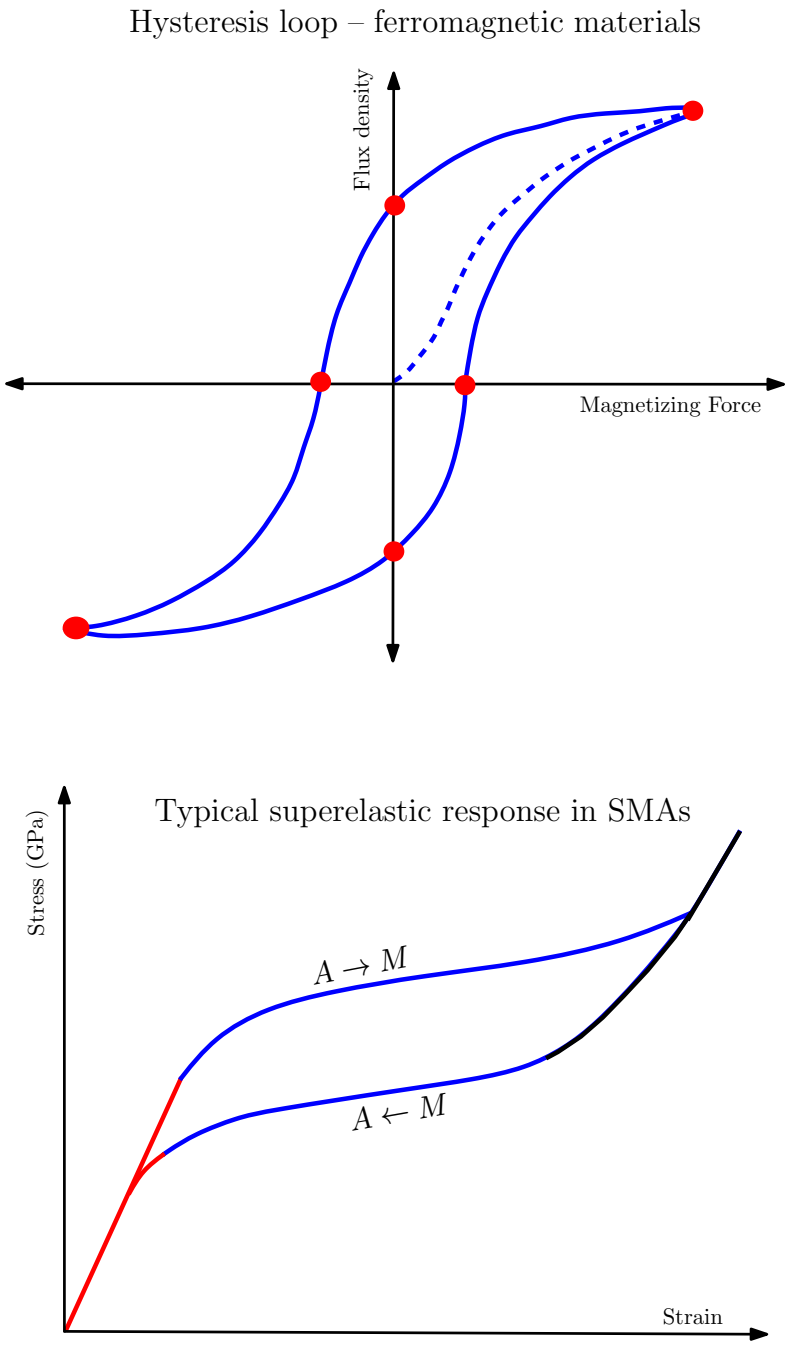

Figure 1.17: Figure shows similarity between hysteresis associated ferromagnetic materials and those associated with superelastic response of SMA. The distinct difference between the two is the elastic response observed in SMA before switching states during phase transformation event (i.e the intial & final elastic parts).

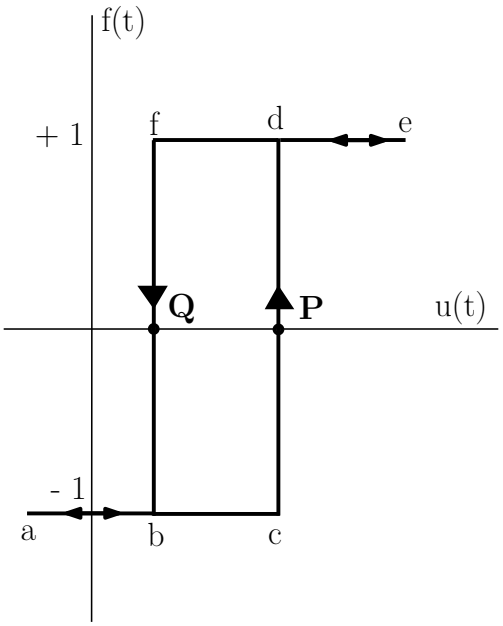

Figure 1.18: A hysteron defined in a classical Preisach model with P and Q being the switching values with the arrows directions corresponding to allowable paths.

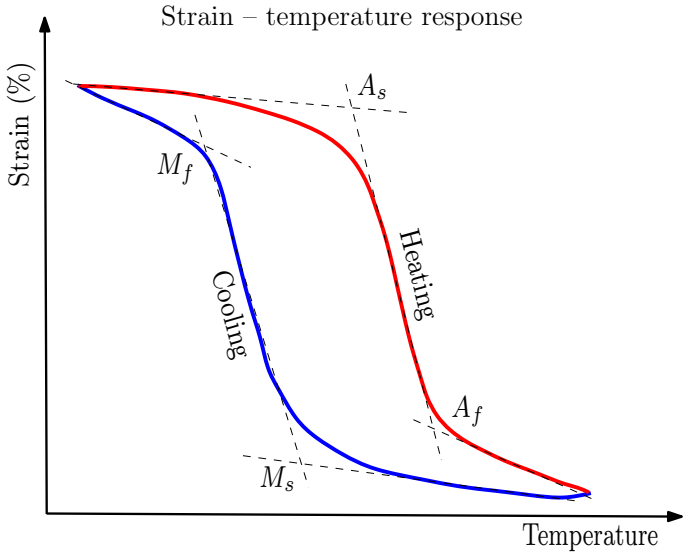

Figure 1.19: Figure shows a typical strain – temperature response used in Preisach modeling

A brief review of some important Preisach approaches is taken up below. Bo and Lagoudas [99] have discussed a number of models like Duhem-Madelong model, Preisach model and K–P type models used to simulate hysteretic behaviour of SMA's [104]. The integral type Preisach model was employed to simulate major and minor hysteresis loops for a temperature–strain data (see figure 1.19 for a typical strain – temperature plot). A distribution function $\mu(T_P, T_Q)$ for the martensite volume fraction $\xi[T]$ is a function of temperature history where T_P and T_Q are the hysteron parameters for hysteron $\hat{\gamma}_{PQ}$ [104]. An expression for total volume fraction is given by equation 1.9 below.

$$\xi[T] = \iint\limits_{T_P \geqslant T_Q} \mu(T_P, T_Q)\hat{\gamma}_{PQ}[T]\, dT_P\, dT_Q \tag{1.9}$$

Bo and Lagoudas [99] also discussed the disadvantages of using a Preisach model to simulate hysteresis modeling due to inability of capturing effects due to training/hysteresis stabilization, internal loops and different loading paths [104].

Ortin [97] presented a model for SMA to capture stress–strain hysteresis using the integral preisach approach with the applied stress being the forcing variable and strain being the output variable (both stress and strain variables are functions of time) [104]. Strain $\varepsilon(t)$ is expressed with $\mu(P, Q)$ being the weight function as an integral over all hysterons $\hat{\gamma}_{PQ}$ as shown in equation 1.10 below [104].

$$\varepsilon(t) = \iint\limits_{P \geqslant Q} \mu(P, Q)\hat{\gamma}_{PQ}[\sigma(t)]\, dP\, dQ \tag{1.10}$$

The currently available Preisach models for SMA are purely mechanical and phenomenological in nature and tend to capture the stress–strain [97] or temperature–strain responses [99] as shown in figures 1.17 and 1.19 respectively. Though most

Preisach models are purely empirical, they show good capability of simulating complex SMA responses quite accurately and are very versatile. However, some limitations of the existing Preisach approaches for SMA are summarized below :

- All of the present Preisach approaches followed in the literature generally have no thermodynamic base [64]. Hence, simulating temperature dependent complex superelastic responses with multiple internal loops (as shown in figure 1.7) are difficult to capture with such Preisach models as both the forward and backward transformation functions need extensive modifications as functions of temperature [104].

- Further, the superelastic responses varies with different SMA material systems like NiTi or CuZnAl and some SE responses show a really flat plateau or a non-hardening/ softening response i.e negative slope in the plateau regions of SE response (see figure 3(a) from [105]). Capturing such flat plateaus in a stress–strain response is critical in design of many medical applications [64,99].

- It must be also noted that such attempts of mimicking hysteresis using the infinite set of hysterons is computationally expensive and inversion of these models is not easy [64].

A setup of using a finite set of hysterons like a "Discrete Preisach Model" (used in this work) will be discussed later in section 4. The advantages of such an approach will become clear shortly.

1.4.2 Torsional Response of SMA

In many of the applications discussed in section 1.3, SMA components like springs, torsional tubes etc. undergo repeated torsional loading and unloading cycles and hence capturing their hysteretic response is critical. Experimental evidences also

suggest that the superelastic response is sensitive to temperature fluctuations which results in force/ stress variations [39, 106].

In one of the first efforts towards modeling hysteretic response of SMA members under torsion, Tobushi et al. [107] used Tanaka's constitutive model [68] to analyze axially loaded helical springs by assuming each segment is under pure torsion [107]. They treated the springs to be perfectly plastic and derived the constitutive relations by neglecting hardening/softening responses during phase transformation [107]. The main equation governing stress-strain-temperature in their work is shown in 1.11a with G, θ and $|\Omega/G|$ representing the shear modulus of elasticity, the thermoelastic constant and transformation strain respectively [107]. The form of martensite volume fraction–temperature relationship shown in equation 1.11b is similar to equation 1.3 discussed earlier [107].

$$\dot{\tau} = G\dot{\gamma} + \theta\dot{T} + \Omega\dot{\xi} \tag{1.11a}$$

$$\begin{aligned} \xi_{A\to M} &= 1 - \exp[b_A C_M (M_s - T) + b_M \tau] \\ \xi_{M\to A} &= \exp[b_A C_A (A_s - T) + b_A \tau] \end{aligned} \tag{1.11b}$$

Though, these assumptions greatly simplify the solution, however experimental evidence show that the hardening response cannot be neglected in SMA responses for polycrystalline SMA [108]. It is also difficult to incorporate temperature effects in the superelastic response by using such an approach.

Mirzaeifar et al. [109] in their work considered analysis of circular SMA bars subjected to pure torsion. They reduce three dimensional constitutive equations developed by Boyd and Lagoudas [84] and Qidwai and Lagoudas [85] for the case of pure torsion and thus deriving explicit relationship for shear stress. The equations 1.5, 1.6 and 1.7 are reduced for a 1-D case where the stress, strain and transformation tensors are chosen as shown in equation 1.12. They divide the wire cross section into

three zones - an inner austentitc core, a transition region and an outer martensitic layer (see figure 1.20) to derive relations for each of the divided regions under different twist angles by integrating state variables across the three zones (expression 25 & 26 in [109]). They further extend this idea in their sequel work to study SMA helical springs by considering the spring both as straight SMA bars and curved SMA bars (to include curvature effects) subjected to torsional loading [108]. Chapman et al. also reduce the 3D model developed by Boyd and Lagoudas [84] and Qidwai and Lagoudas [85] to predict torsional response with an implementation in Abaqus for a FE simulation [110]. A similar approach of reducing multidimensional constitutive relation developed by Liang and Rogers [72, 73] was taken up by the same authors, where they develop a 1-D shear stress and strain relation for designing SMA springs (see expression (1) in [111, 112] and equation 1.4 discussed earlier).

$$\sigma = \begin{bmatrix} 0 & 0 & 0 \\ 0 & 0 & \tau_{\theta z} \\ 0 & \tau_{\theta z} & 0 \end{bmatrix}; \ \varepsilon = \begin{bmatrix} 0 & 0 & 0 \\ 0 & 0 & \varepsilon_{\theta z} \\ 0 & \varepsilon_{\theta z} & 0 \end{bmatrix}; \ \varepsilon^t = \begin{bmatrix} 0 & 0 & 0 \\ 0 & 0 & \varepsilon^t_{\theta z} \\ 0 & \varepsilon^t_{\theta z} & 0 \end{bmatrix} \tag{1.12}$$

Such strategies are extremely cumbersome for identification of material and model parameters from experimental data and incorporating temperature changes (table 1 in [108–110] lists the number of material parameters needed for model verification). Furthermore, these approaches just use the one dimensional data and use a von-Mises equivalent stress approach due to lack of a full three dimensional data on SMAs. Aguiar et al. [113] in their work simplify the 1-D constitutive model developed by Paiva et al. [114] & Savi and Paiva [115] by replacing the corresponding terms for normal stress, strains and elastic modulus by its counterparts shear stress, shear strains and shear modulus respectively (expression 1–4 in [113]). The authors discuss

three different representations for shear stress and martensitic volume fractions and they assume the shear stress distribution and the volume fraction to be uniform across the wire cross section when the SMA spring is subjected to torsion (i.e "homogeneous phase transformation") [113].

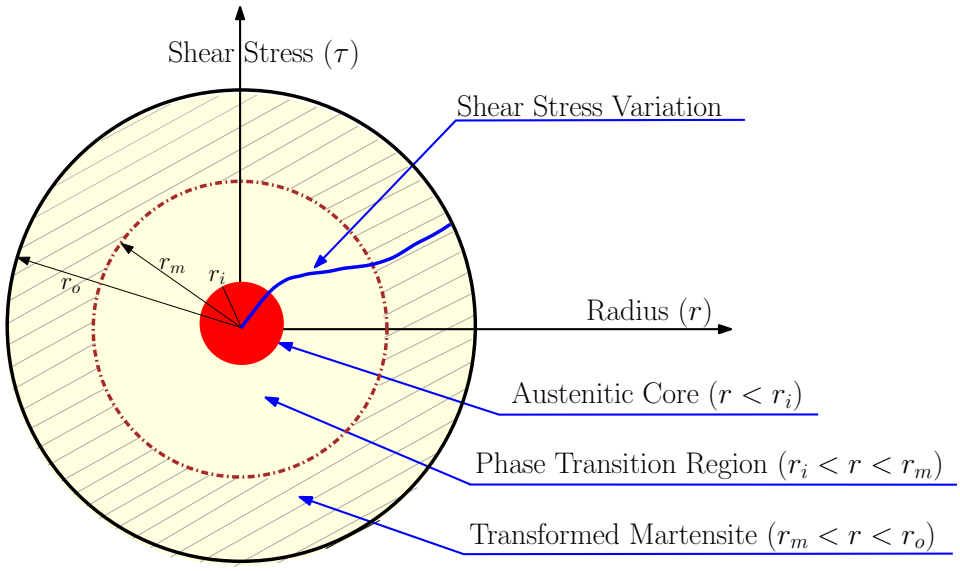

Figure 1.20: Non linear shear stress distribution across the wire cross-section under torsional loading with an inner austentic core, a phase transition region and an outer transformed martensitic layer [109].

Modeling strategies of either using the von-Mises equivalent stress approach or the assumption that phase transformations are homogeneous across the wire are not completely realistic as the phase transformation front gradually moves from the outer fibers towards the neutral axis as the wire twists under torsion and its location is not known a-priori [107–109]. They can be possibly determined only if the prior deformation history is known. Further, the shear strain tends to zero at the core of the specimen cross-section as the wire twists [113]. This implies that the

possibility of having a fully transformed case can only be possible if the angle of twist asymptotically reaches infinity [116]. A schematic in figure 1.20 shows the three zones - an inner austentitc core, a transition region and an outer martensitic layer. The untransformed austentic core at the center might exist even for the maximum possible twist due to really small shear strains. Figure 1.20 also depicts the non-linear shear stress variation across the wire cross-section. All of these suggest that the transition across the wire cross-section is not homogeneous and cannot be accounted for easily by just averaging or integrating certain state variables in constitutive relations across the wire cross sections.

1.4.3 Bending Response of SMA

In some applications discussed in section 1.3, SMA's are used under bending mode and thus efforts in understanding "moment v/s curvature/deflection" responses has been of keen interest with the medical community. Experimental results for Force v/s mid-span deflection for a 3-point bend test conducted on wires and slender beams have been reported widely by the medical community (see results in [33,34,117–130]). Most of the available experimental results from the medical community are using 3-point bend tests. Thus, Berg [131], Rejzner et al. [132] conducted experiments for a case of pure bending v/s curvature using custom designed experimental rigs. Wick et al. [133] have also reported experimental results by comparing responses for 3-point bending, pure bending and tension loading cases (see figure 4 in [133]). Considering the importance of predicting the bending response with its associated hysteresis, some efforts towards modeling their complex response were undertaken.

Rejzner et al. [132] used the model developed by Raniecki et al. ([134]) to solve rate-type kinetic equations that takes into account tension-compression asymmetry along with a non-linear differential equation describing neutral plane motion for

a symmetric cross-section. Marfia et al. [135] analysed a case of laminated SMA beams based on small-deformation Euler-Bernoulli theory. They explored a "mixture rule type approach" to determine martensite volume fractions and also established evolution equations for martensite and austentite phase production [135]. They extend this approach with Timoshenko beam theory to account for transverse shear and a layerwise approach which assumes constant shear deformation in beam cross-section. Axial force, bending moment and shear forces are derived as integrals of corresponding stress resultant expressions [135].

Atanacković and Achenbach [136], Eshghinejad and Elahinia [137] use an approach of dividing the phase transformation event into 3 different regions (elastic austentitc zone, a phase-transition region and an outer martensitic zone). Explicit relationships for bending moment are established upon integration of stress resultant expressions under loading and unloading events [136, 137].

Mirzaeifar et al. [138] in their recent work reduce the three dimensional constitutive equations developed by Boyd and Lagoudas [84], Qidwai and Lagoudas [85] for a pure bending case. They consider two different transformation functions to account for tension-compression asymmetry and these constitutive relationships are reduced to appropriate forms to study SE effects. Closed form expressions for bending moment and curvature are analyzed analytically from these stress resultant expressions.

In all of the above mentioned approaches, expressions for bending moments are obtained by integrating explicit stress resultant equations established (in many cases reducing complex 3-D constitutive equations for a special tension–compression 1-D case). However, for a case of pure bending, as the wire/beam bends, the phase transformation front moves from the outer fiber towards the neutral axis (parallel to neutral axis) [139]. Again, as noted earlier in case of torsional loading, the variation of the extent of transformation across the cross-section is not smooth and cannot

be determined by easily integrating certain state variables in constitutive relations across the specimen cross sections [90]. They can be possibly determined only if the prior deformation history is known. Further, due to lack of full three-dimensional experimental data and tension–compression asymmetry, the approach of deriving moment-curvature relationships from stress resultants gets quite complicated. In addition, parameter identification in reduced 3-D models gets cumbersome due to lack of experimental data [90].

Auricchio and Sacco [140] developed a thermomechanical model to capture tension-bending superelastic response under small deformation theory assumptions that plane sections remain plane in both unreformed and deformed configurations [140]. However, axial forces and moments again are obtained from stress resultants by integration.

Purohit and Bhattacharya [141] developed a strain energy relation that is a function of axial stretch, the average shear, and the curvature with the assumption the the beam is purely elastic [141]. They further assume that the phase transformation front moves perpendicular and not parallel to the neutral axis [141]. This is contrary to the physical intuition of the way the transformation front moves across the cross-section (i.e parallel to neutral axis). This point has been discussed in detail by Rajagopal and Srinivasa [139] in their work where they develop finite deformation model for SMA beams. Rajagopal and Srinivasa [139] in their work assume a form for Helmholtz potential/unit mass with the assumption that the elastic constants of martensite and austenite are the same and don't vary with operating temperature. However, experimental evidences (3-point and pure bending experimental results) have illustrated that the superleastic responses are sensitive to temperature fluctuations and thus resulting in force variations for the same amount of deflection/curvature (see experimental results in [123, 127, 129]).

1.5 Designer's Need

Given the complex nonlinear nature of SMA responses and the importance of understanding their coupled thermomechanical responses, some important concerns for researchers designing SMA components for various applications are :

1. Is it possible to develop thermodynamically consistent models for different loading cases applicable directly at component level?

2. Can one capture both shape memory and superelastic effects at the component level?

3. Can one capture effects of external stimuli – changes in operating temperature?

4. How is the material performance under repeated thermomechanical cycling?

5. Can one capture effects of loading rate ?

6. How easily can SMA components be attached to other materials – joining issues?

1.6 Problem Formulation : Motivation, Hypothesis and Scope

The currently available modeling approaches as reviewed in the previous sections 1.4 for different loading cases are developed primarily to capture the phenomenological aspects of SMA response. A close perusal of the available 3-D constitutive models developed, reveals that, in actuality, these approaches just use the one dimensional data and use a von-Mises equivalent stress approach due to lack of a full three dimensional data on SMAs as discussed earlier in sections 1.4.2 and 1.4.3. Given the fact that such an approach (originally based on experimental observations of steel) does not even work well for aluminum, it is hard to justify their use for SMA given

their complex thermomechanical response. The present modeling approaches currently followed are quite complex and require many material parameters for model verification. For example, to simulate a simple spring or wire response one needs to simulate a full 3-D model or use a reduced 3-D model for analyzing specific cases thus making them hard to implement for actual design cases. The material parameter identification is heuristic and there is no automated scheme for identifying them. Experimental results have suggested that the effect of external non-mechanical stimuli (i.e operating temperature in this case) plays a significant role with the mechanical response of these materials (as shown in figure 1.7). Further, it is important for the models to accurately capture partially transformed cases (i.e internal loops [1]) as the entire response might not be utilized always and only a portion of the entire response or internal loop might be of significance to designers. It is important for the models to capture responses that include these external stimuli effects along with the complex hysteric, large deformation phenomenons observed with SMAs.

Considering the designer's needs listed in section 1.5 and with the available literature, there is no unified framework for modeling responses of SMA components under various loading conditions, operating temperatures and extent of transformation. Developing a rational approach for constructing thermomechanical models for SMA components under various loading conditions would play a pivotal role for design of such devices from the structural and control systems standpoint.

The hypothesis is that one can develop structural mechanics models for SMA using thermodynamic principles and discrete Preisach models applied directly at the component level.

[1]Internal loop is a result of intermediate loading and unloading prior to complete transformation that result in smaller hysteretic responses which closely mimic the outer fully transformed loop. The area of these smaller hysteretic loops depends on the extent of the loading and unloading level that the component is subjected to in applications well with the transformation region (plateau region) [59].

In this work, developing "structural thermomechanical models for shape memory alloy components like wires, springs and beams" subjected to tension, torsion and bending loading conditions will be addressed. It is intended to formulate the model directly based on experimentally measurable quantities like tensile force–extension (stress – strain), torque – angle of twist or bending moment – curvature [2] rather than solving for non-homogeneous stress and strains across the wire cross-section and then integrating the same especially for bending and torsion loading conditions. Further, correlating the model parameters with experimental results under different loading conditions would be a key deliverable of this work.

Traditionally, simple strength of materials based models and tools have driven engineering designs for centuries, even as more sophisticated models existed for design with conventional materials. As these theories of beams and rods have shown that these approaches are extremely useful for designers as they can faithfully simulate the response with a minimum computations as compared against a full 3-D model formulation. However, pure elasticity theories (i.e mechanical loading) alone cannot capture the entire thermoelastic response irrespective of the complexity in the assumed form for stored energy functions [139]. The main advancement of the present modeling technique from a purely mechanical theory is the incorporation of thermal response by means of combining thermodynamic principles with Preisach model in simulating responses of superelastic SMA wires, beams and springs [64, 102, 103].

[2]Under tensile loading case, models can be developed directly using stress–strain relationships as the entire crosssection can be assumed to be uniformly loaded and the phase transformation front moves along the loading axis. Thus, one can integrate stress–strain relationships to obtain axial force–extension relationships in pure tension loading case. However, this idea of integrating stress resultants under torsion or bending loading cases is cumbersome, as in case of SMAs, the phase transformation front moves radially inwards from outer fiber to core as SMA component twists under torsion. Similarly, in bending, the phase transformation front moves from the outer fiber inwards towards the neutral axis (i.e parallel to neutral axis). Thus, models in torsion and bending are developed directly using experimentally measurable quantities i.e torque – angle of twist or bending moment – curvature relationships respectively.

Following Doraiswamy et al. [64], the key idea here would be in **separating the thermoelastic and the disspiative part of the hysteretic response with a Gibbs potential based formulation** which includes both thermal and mechanical loading in the same framework. The dissipative part is then handled by a **discrete Preisach model**. As pointed out earlier, phase transformations are more akin to domain switching in magnetism rather than crystallographic slip and hence a Preisach model is more appropriate here. The whole SMA structure can be imagined as a collection of many such domains with each of them switching based on the external impetus. Such an approach combines the physics and elegance of the thermodynamic based approach with the algorithmic efficiency/simplicity of the Preisach model and thus providing an effective way in predicting complex SMA responses.

The advantages of such a thermodynamic Preisach approach are [64, 104]:

- It is not necessary to use different approaches for stress and temperature driven phase changes as observed with SMA response.
- There is a greater connection with the thermodynamics of the response and an added capability of simulating both load and displacement controlled experiments in a single modeling framework.
- Ability to simulate complex superelastic responses with multiple internal loops and having an improved treatment of temperature dependence associated with superelastic responses (as shown in figure 1.7) without the requirement of recomputing any model parameters.
- Some SMA superleastic responses showing a really flat plateau or a non-hardening/ softening response (i.e negative slope) can also be simulated with this approach without any modifications to the model.

- An approximate response prediction could be beneficial for design purposes but a more precise prediction is essential from the control systems standpoint. With the use of a discrete Preisach model, one can do a approximate or a precise prediction by controlling the use of number of Preisach elements This way one doesn't have to choose different functions for simulating approximate or fine predictions and thus saving computational time.

- All three loading cases viz. tension, torsion and bending responses can be simulated with a similar approach. The model parameters in each loading case can be calibrated using a single stress–strain, torque–twist or moment–curvature plot depending on the chosen loading condition.

The efficacy of the model in directly predicting torque – angle of twist or bending moment – curvature response directly could play a vital role in designing SMA components like wires, springs and beams for various engineering applications. Capturing complex temperature dependent hysteretic responses with minimum computations could help designers immensely in studying component response under different conditions.

1.7 Objectives

The main objectives of this work are listed below :

1. Development of a two-species model to capture superelastic effects under tension, torsion and bending loading cases for SMA components like wires, bars, springs and beams.

2. Considering the technological importance of SMA components under torsional loading, a three species model to capture both superelastic and shape memory effects for a complete torsion loading case for SMA components like wires,

springs and beams is proposed. This approach could facilitate designers for actuator development.

3. Tackle another aspect of SMA response, namely their functional degradation. Apart from undergoing conventional mechanical fatigue/degradation, SMAs also undergo loss in their phase transformation ability, leading to a loss in functionality/smartness. A custom designed special test rig is used to perform cyclic thermomechanical experiments on SMA springs. Using the test data, a novel modeling framework to combine both mechanical and thermal loading response is proposed wherein a thermodynamic driving force is used to capture the functional life of SMA components.

1.8 Dissertation Organization

The remaining sections of this dissertation are organized as follows

- Section 2 : Experiments performed on NiTi SMA wires and springs at Texas A&M University (College Station & Qatar campuses) are presented.
- Section 3 : By using thermodynamics principles and a two species Gibbs potential, the thermoelastic and the dissipative part of superelastic response are separated to obtain expressions for thermodynamic driving force for phase transformations and the volume fraction of martensite (for tension, torsion and bending loading cases).
- Section 4 : A common discrete Preisach model used to handle the dissipative part (different driving force and volume fraction relationships) of response under different loading conditions is presented.
- Section 5 : A three species model that extends the proposed modeling approach of separating the thermoelastic and the dissipative part of response to simulate

both the shape memory and superelastic responses is discussed. The model captures the complete torsional response of SMA components like wires, rods and springs.

- Section 6 : The simulation protocol and identification of various model parameters arising from the thermodynamical framework for all proposed models in Sections 3 and 5 are detailed.

- Section 7 : The model simulations and predictions under different loading conditions are compared with the experimental data in this Section.

- Section 8 : The proposed model in Sections 3 are extended to develop a concept of "driving force amplitude v/s no of cycles" that could be used to analyze functional degradation of SMA components. A custom designed thermomechanical fatigue test rig is used to execute user defined repeated thermomechanical tests on SMA components.

- Section 9 : Concluding remarks and summary

- Section 10 : Some recommendations for future work to tackle other SMA related issues.

2. EXPERIMENTS ON SMA COMPONENTS – WIRES AND SPRINGS *

This section discusses the various experiments conducted on SMA components like wires and springs under different loading conditions at Texas A&M University (College Station & Qatar campuses). These experiments would provide an insight in understanding component level responses under different load cases and operating conditions. These experimental results would also be used later for model calibration and evaluating model predictions under different cases. Section 2.1 discusses experiments on SMA wires under pure tension. Section 2.2 discusses experiments on commercial SMA springs under torsion. Section 2.3 discusses experiments on SMA wires subjected to high degrees of twist.

2.1 SMA Wires Under Tension : Test Methodology and Results

2.1.1 Material and Experimental Set-up

NiTi wires (martensitic at room temperature) of 0.75 mm dia with a composition in element weight% (Ni-54.5, Balance Ti, trace elements < 0.25) were obtained from Images SI Inc (www.imagesco.com) with a listed transformation temperature of 323 K.

An Instron 5567 series uniaxial tensile testing machine was used to carry out cyclic loading experiments at various temperatures on SMA wires. The temperature control was through an Instron SFL heatwave environmental chamber (model: 3119-506 Heatwave 240) (A in figure 2.1) used for maintaining precise air temperature

*Reprinted with permission from "Combining Thermodynamic Principles with Preisach models for superelastic SMA Wires" by Doraiswamy, Rao and Srinivasa, *Smart Materials and Structures*, 20, 085032, 2011 [64], Copyright [2014] by IOP.

Reprinted with permission from "A two species thermodynamic Preisach model for the torsional response of SMA wires and springs under superelastic conditions" by Rao and Srinivasa, *International Journal of Solids and Structures*, 50, 887–898, 2013 [90], Copyright [2014] by Elsevier Limited.

throughout the length of the experiment. A 2716 series mechanical wedge action grips (B in figure 2.1) were used to hold the wire specimens. All the tests were conducted after the environmental chamber equilibrated at the desired temperature. The chamber employed two Inconel sheathed 3 mm diameter type K thermocouples with online temperature display on the control panel. In addition to this, external thermocouples were used to monitor the wire temperature.

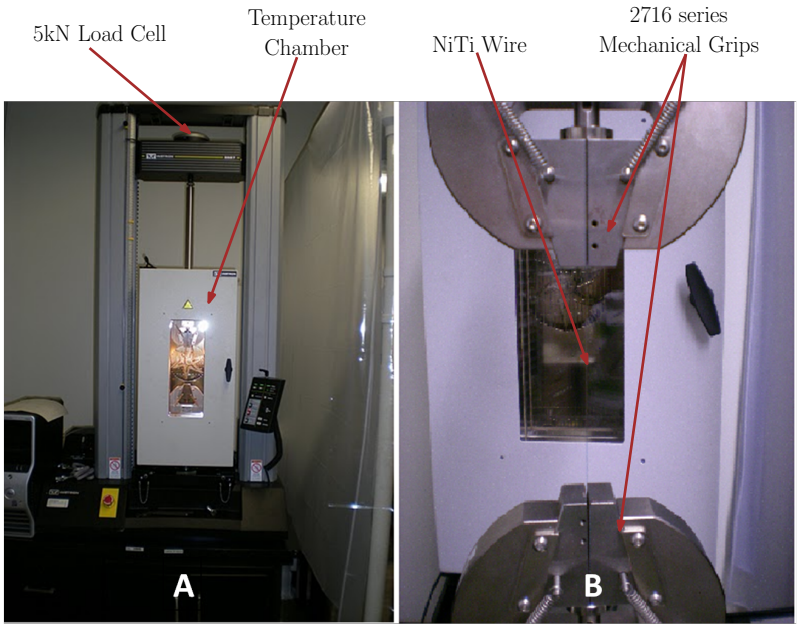

Figure 2.1: Experimental setup showing Instron uniaxial tensile testing machine with a temperature chamber and mounting of a NiTi wire between mechanical wedge grips

2.1.2 Test Methodology

Rate controlled uniaxial tension tests were conducted on SMA wires with the test purpose of achieving 3 internal loops during the loading cycle at temperatures 348, 373 and 398 K. Force and extension were the parameters monitored and recorded as a function of time using Instron's customized Bluehill 2.0 software with the help

of in built 5 kN capacity load cell and the crosshead displacement respectively. The initial gauge length of 120 mm and a displacement rate of 3 mm/min were selected for all specimen samples tested.

The loading - unloading profiles were achieved as explained below and the load profile is illustrated in figure 2.2.

1. **Block 1** - Crosshead displacement up to 5 mm and unload to 3 mm (internal Loop 1)

2. **Block 2** - Crosshead displacement up to 7 mm and unload to 5 mm (internal Loop 2)

3. **Block 3** - Crosshead displacement up to 9 mm and unload to 7 mm (internal Loop 3)

4. **Block 4** - Loading up to 400 N and unload to 0.1 N

In all of these cases, it was ensured that the maximum tensile force did not exceed 400 N. Four trials were conducted under each test condition to ensure repeatability (refer figure 2.3a).

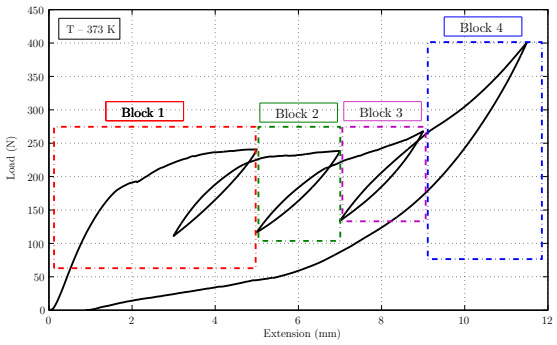

Figure 2.2: Load extension curve (at 373K) used to achieve 3 internal loops during the loading cycle of an uniaxial tension test on a NiTi wire with each block representing intermediate loading and unloading cycles.

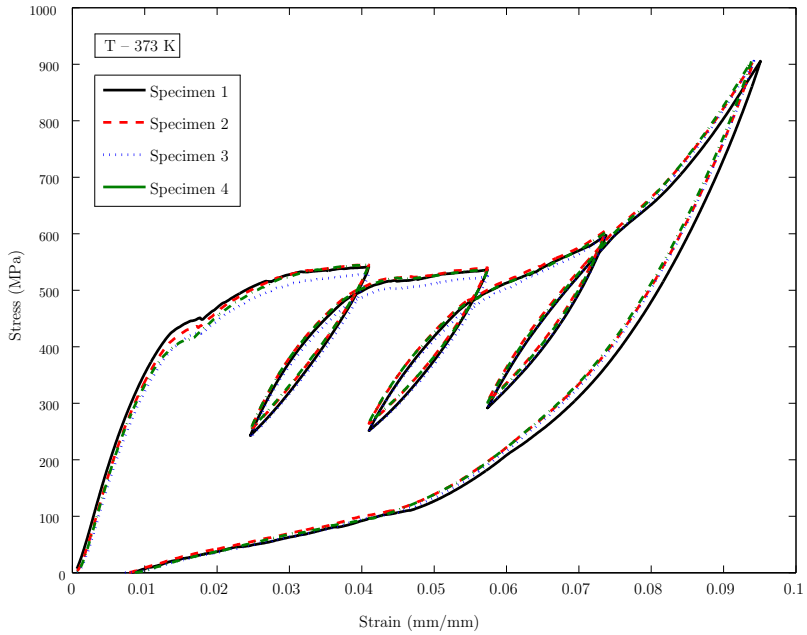

(a) Isothermal stress–strain curves at 373 K for a NiTi wire with four different trials to show stabilization and repeatability of experiments

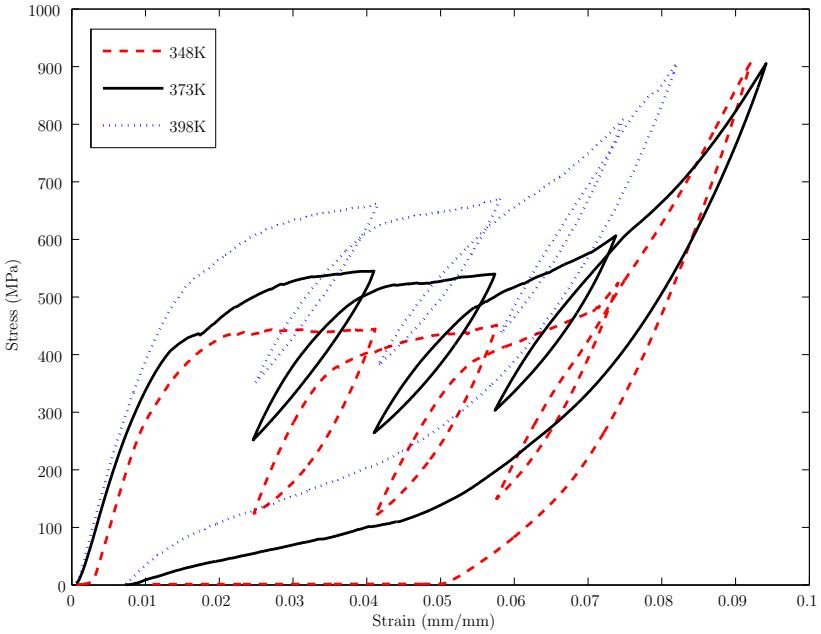

(b) Stress–strain response for a single specimen at three different temperatures 348, 373 and 398 K

Figure 2.3: Results of uniaxial tension tests conducted on NiTi wire at temperatures 348, 373 and 398 K using a loading–unloading profile illustrated in 2.2 with 3 mm/min displacement rate for all cases.

2.1.3 Results and Discussions

The isothermal stress–strain curves for different temperatures are illustrated in figure 2.3. In all cases considered here, the results presented are for the stabilized loops and thus initial gauge length was adjusted to account for hysteresis stabilization. As seen in figure 2.3b, there is a residual strain of about 5% observed on unloading for 348 K trial. This residual strain can be attributed to plastic deformation of martensite at higher stress levels (far greater than upper plateau stress) and incomplete recovery of some pockets of the specimen back to austenite upon unloading [142]. This would also explain the discrepancies between the initial austenitic slope during loading cycle and "partially transformed austenitic" slope during the unloading cycle as observed in figure 2.3b. A more detailed discussion on this can be found here [142], [143]. For tests conducted at 373 and 398 K, almost complete recovery of applied deformation was observed and thus demonstrating near perfect superelasticity.

2.2 SMA Springs Under Torsion : Test Methodology and Results

2.2.1 Material and Experimental Set-up

NiTi springs (martensitic at room temperature) with composition details in element weight % (Ni-55.91, Balance Ti, trace elements < 0.25) were obtained from Images SI Inc. The listed transformation temperature (A_f) as reported by the supplier is in the range of 318-328 K. The spring specifications are as follows.

- Mean coil diameter of the spring "D_m" = 6 mm
- Wire diameter "d" = 0.75 mm
- Spring Index "C" = 8

- Number of active coils "n" = 20.

An Instron 5567 series uniaxial tensile testing machine was used to carry out cyclic loading experiments at various temperatures on SMA springs. The temperature control was through an Instron SFL heatwave environmental chamber (Model: 3119-506 Heatwave 240) used for maintaining precise air temperature throughout the length of the experiment (see figure 2.4). A 2716 series mechanical wedge-action grips were used to hold the wire specimens. The grips with additional hooks were used to hold the extension springs inside the temperature chamber as shown in figure 2.4. All the tests were conducted after the environmental chamber equilibrated at the desired temperature. The chamber employed two Inconel sheathed 3 mm diameter type K thermocouples with online temperature display on the control panel. In addition to this, external thermocouples were used to monitor the wire temperature.

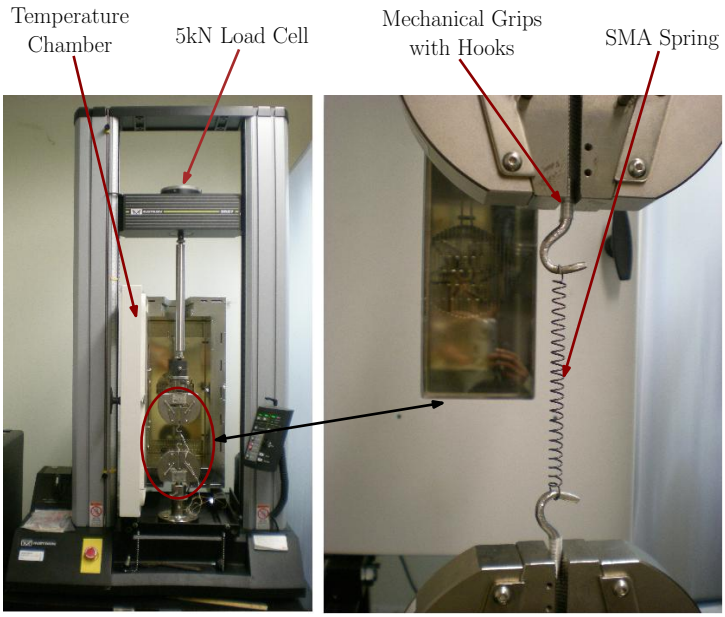

Figure 2.4: Experimental set-up showing Instron uniaxial tensile testing machine with a temperature chamber and mounting of a SMA Spring wire between mechanical wedge grips and hooks

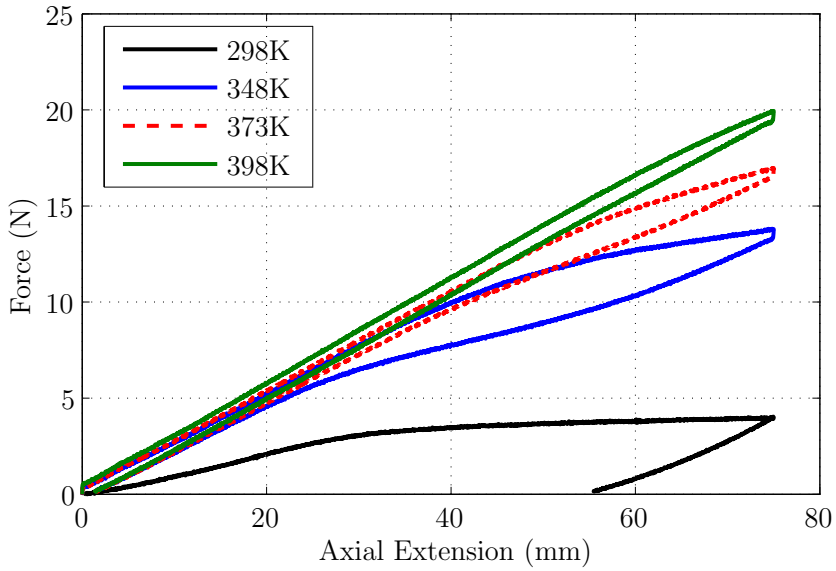

(a) Isothermal force versus axial extension results as measured using the Instron setup shown in figure 2.4

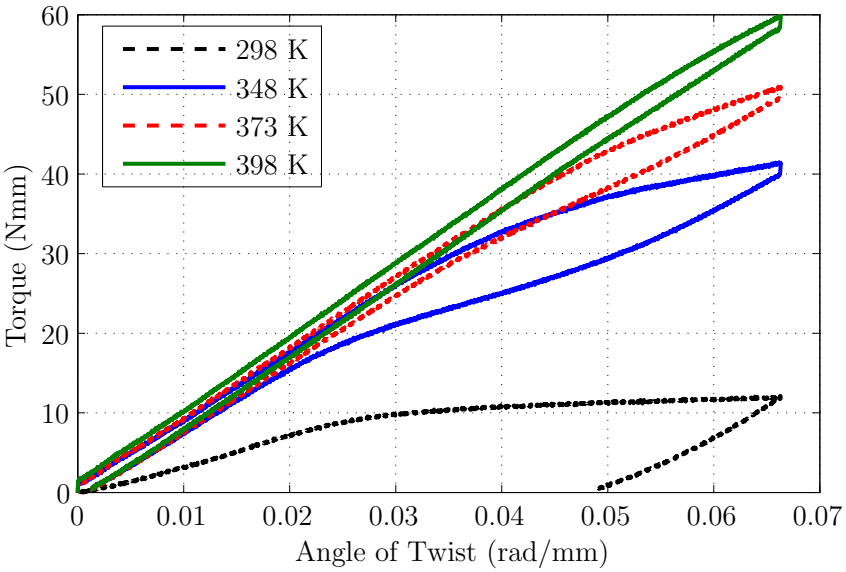

(b) Force versus axial extension of spring converted to torque versus angle of twist using equations 2.1 and 2.2

Figure 2.5: Results of tests conducted on NiTi SMA springs at temperatures 298, 348, 373 and 398 K with 15 mm/min displacement rate for all cases. The results for 348, 373 and 398 K show superelastic response of SMA springs. The extent of transformation in each high temperature trial is different when compared against the same maximum spring elongation (75 mm) or corresponding twist.

2.2.2 Test Methodology

Rate controlled uniaxial tests were conducted on the extension springs that were subjected to a axial displacement of 75 mm and then unloaded back. A constant displacement rate of 15 mm/min was employed throughout the length of the experiment. Force (P) and spring extension (δ) data were monitored and recorded as a function of time using Instron's customized Bluehill 2.0 software with the help of in-built 5kN capacity load cell and the crosshead displacement respectively.
The torque applied on the spring can be computed using the expression

$$T = P\left(\frac{D_m}{2}\right) \tag{2.1}$$

Assuming that the angle of twist is uniform over the entire length of the active coils and ignoring curvature effects, the angle of twist per unit length (ϕ) can be evaluated in terms of the spring displacement as

$$\phi = \frac{2\delta}{\pi D_m^2 n} \tag{2.2}$$

The above results (equations 2.1 and 2.2) are independent of each other with the former being purely kinetic and the latter being purely geometrical in nature. No constitutive theory relating the torque to the angle of twist is necessary for these results to be established.

The tests were performed at room temperature (298 K) to simulate shape memory effect and three other temperatures above A_f viz. 348, 373 and 398 K to observe superelastic behavior of SMA springs. Four trials were conducted under each test condition to ensure repeatability of results.

2.2.3 Results and Discussions

The force - extension results of the SMA spring as obtained from the Instron machine for different temperatures are illustrated in figure 2.5a. The corresponding torque–angle of twist results using equations 2.1 and 2.2 are shown in figure 2.5b. As seen in figure 2.5a, for 298 K trial, there is a residual elongation of about 50 mm observed upon unloading which can be recovered completely upon heating to a temperature above A_f. In the trials pertaining to higher temperatures 348, 373 and 398 K, the spring is austenitic at the start of the test and demonstrates near perfect pseudoelasticity with the complete recovery of applied deformation. In each of these cases, the springs are partially transformed to stress induced martensite (SIM) and the extent of transformation from austenite to SIM is different in each temperature trial. This is due to the fact that the higher the temperature above A_f, the higher is the critical stress required for transformation and thus lesser is the transformation from austenite to SIM when compared against the same maximum deformation (75 mm) of the spring. It can also be observed from figure 2.5a that the stiffness increases and the hysteresis area decreases with the increase in the working temperature above A_f.

2.3 SMA Wires Under Torsion : Test Methodology and Results

SMA components like wires, tubes, rods and springs during service could be subjected to load reversals before complete transformation is achieved which could result in partial or complex hysteretic internal loops either during the loading or unloading stage of the response [59]. Capturing such internal loops responses are important from an application standpoint as in many cases not the entire the response is necessary and only a partial internal loop might be of significance to designers [22, 28]. Most of the available literature has been on understanding a simple loading and

unloading case at different extent of twists. The reported literature in understanding partial or complex internal loop responses have been investigated under tension loading cases (see figure 4 in [144], figure 2,4a and 4b in [145], figure 6 in [146], figure 12 in [147], figure 6 in [148], figure 3 in [149], figure 3 in [150], figure 4 and 7 in [151], figure 5 in [152], figure 2,3 and 4 in [153], figure 6 in [154], figure 1 in [155] etc. for some illustrations under tension loading case). However, in all of the reported literature the study of internal loops (both under loading and unloading stages of the response) under torsional loading is not addressed.

In this part, an effort to understand the partial and fully transformed cases with internal loops under both during loading and unloading stages of SMA wires under torsion was undertaken. An Instron micro torsion test is used to conduct different experimental test cases to better understand the responses of superelastic SMA wires subjected to torsional loading. Such a study allows designers to get an idea of material response under complex loading and unloading situations in actual applications (especially the shape of inner loops compared to outer/major loops). Such experiments also allows designers to get an insight into behaviour of internal loops and analyze "return point memory (RPM) or sink point memory (SPM)" aspects of torsional response (see figure 8 in [59] for such an illustrations under tension loading). RPM and SPM provides important information on the ability of SMA components to return back to its original unloading point upon completion of a smaller hysteretic loop and is of particular importance to designers. SMA components showing "good RPM/SPM characteristics" is a desirable feature that indicates minimal residual/irreversible deformations after repeated complete or partial transformations.

2.3.1 Material and Experimental Set-up

Superelastic NiTi wires of diameter 0.58 and 0.89 mm were obtained from Small Parts. The wires were straight annealed in the as received condition from the supplier.

An Instron® micro torsion MT series machine was used to carry out cyclic twisting–untwisting (loading–unloading) experiments at room temperature (298 K) on the wire samples. Figure 2.6 shows the experimental set-up used along with the grip and specimen mounting details. The test setup uses a 22.5 Nm torque cell and a guide rail arrangement for gage length adjustment. Torque and twist were the parameters continuously monitored as a function of time throughout the test using the PARTNER® software supplied by Instron®. The destructive test option in this software allows the user to develop custom designed test protocols where one can customize user defined loading and unloading levels by creating various "test zones" thus allowing programming of customized internal loop responses.

2.3.2 Test Methodology

Wire samples of 60 mm gage length were cut from the as received superelastic SMA wires. The samples were fixed between the collet grip assemblies such that the wire be under minimal pre-tension between the grips. However, the pre-tension in the wire was not measured and its effects were neglected for this study (i.e. the wires were assumed to be under pure torsion). All the tests were twist/displacement controlled with a twisting rate of 2^o/s and a maximum twist of 1800^o. All the tests were conducted in the clockwise direction and under torsional loading, the direction of twisting is insignificant since responses are symmetric in nature (see figure 3 and 4 in [116] for illustrations). To ensure repeatability, a minimum of four runs for each test case were conducted.

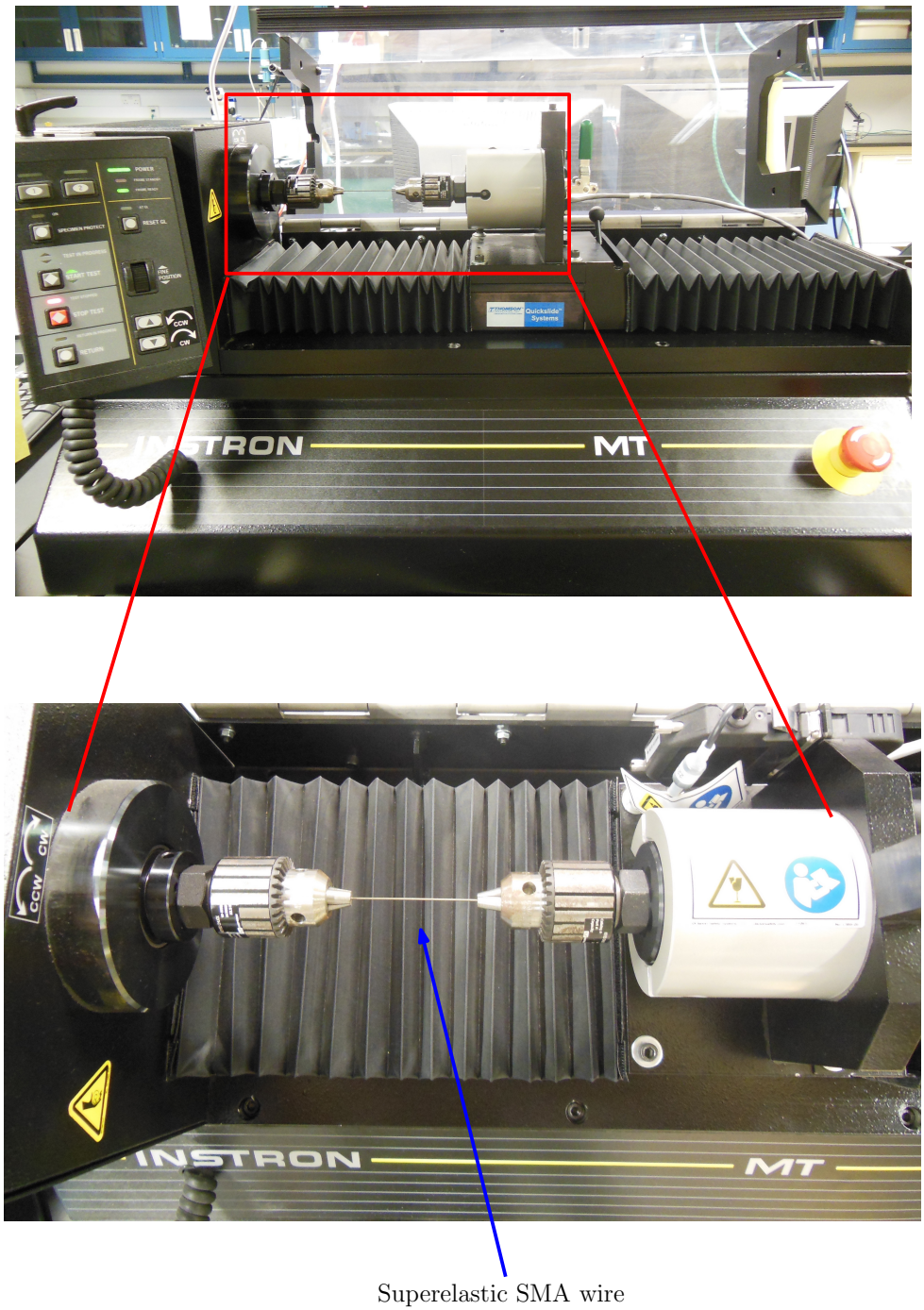

Figure 2.6: Experimental setup showing micro-torsion MT series machine with superelastic SMA wire specimen mounted between collet grips.

2.3.3 Experimental Runs

In the subsequent sections several different cases of internal loops under both loading and unloading stages of the response are discussed.

2.3.3.1 Simple loading and unloading

The procedure to obtain the response of a typical superelastic torsional loading and unloading case consisted of the two steps shown in figure 2.7a

- Zone 1 : Twist upto 1800^o twist (Loading cycle)
- Zone 2 : Untwist back to 0^o twist (Unloading cycle)

Data recorded when the input is a triangular force function (i.e. twist vs time) is shown on figure 2.7b and shows that the material response exhibits a non-linear behavior especially during the phase transformation event. The complete response (i.e. torque vs twist) is shown on figure 2.7c and shows near perfect superelasticity with almost negligible residual deformation upon unloading with a well defined plateau stresses [1] and elastic deformation of stress induced martensite (SIM). The torsional response is similar to a classic pseudoelastic tension response.

The test protocol was reapplied on samples subjected to 1500^o, 1350^o, 900^o and 600^o twist as shown in figure 2.8a. The corresponding twist vs time, torque vs time and torque vs twist responses overlap on each other (figure 2.8 which demonstrate good agreement and test repeatability.

[1] Plateau stresses are some of the salient features associated with a typical superelastic response under tension loading case as discussed in the ASTM standard F2516-07$^{\varepsilon 2}$ [13] for superelastic NiTi materials. The standard defines two plateau stresses – an **upper plateau strength (UPS)** which is the stress value at 3% strain during loading of the sample and a **lower plateau strength (LPS)** which is the stress value at 2.5% strain during unloading of sample after has been loaded up to 6% strain.

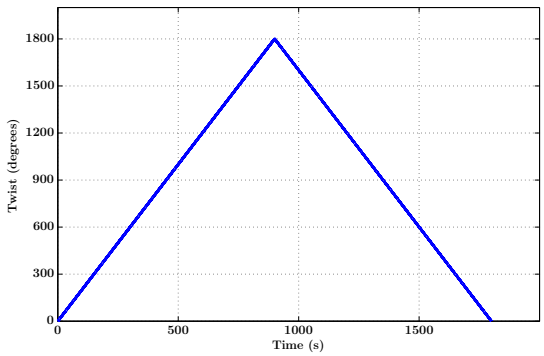

(a) Twist versus time plot

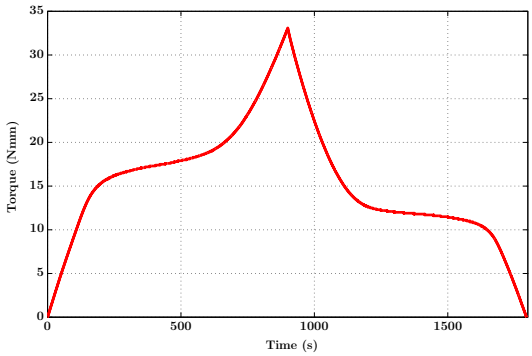

(b) Torque versus time plot

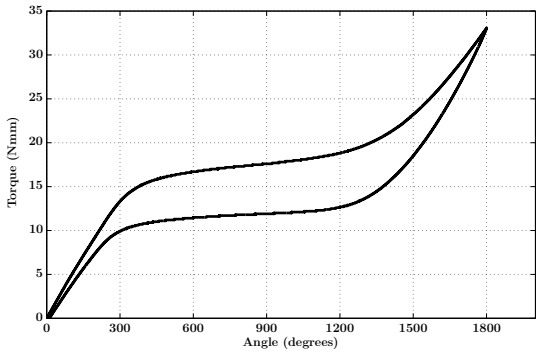

(c) Torque versus twist plot

Figure 2.7: Figures shows the twist versus time ; torque versus time and torque versus twist responses for a simple loading and unloading test upto 1800^o maximum twist.

2.3.3.2 Three internal loops during loading cycle

The procedure to obtain a material response with multiple internal loops (i.e the case of three internal loops was chosen as indicative of the phenomena) during the loading cycle consisted in the following steps as shown in figure 2.9a

- Zone 1 : Twist upto 600^o twist (Loading cycle)
- Zone 2 : Untwist back to 300^o twist (Unloading cycle)
- Zone 3 : Twist upto 900^o twist (Loading cycle)

- Zone 4 : Untwist back to 600^o twist (Unloading cycle)
- Zone 5 : Twist upto 1200^o twist (Loading cycle)
- Zone 6 : Untwist back to 900^o twist (Unloading cycle)
- Zone 7 : Twist upto 1800^o twist (Loading cycle)
- Zone 8 : Untwist back to 0^o twist (Unloading cycle)

The data recorded for this test run is shown in figure 2.9b. The torque–twist response 2.9c exhibits three internal loops (during the loading cycle) and shows almost perfect RPM. The austenitic and martensitic slopes of the internal loops follow the same trend as that of the outer loops.

2.3.3.3 Comparing an internal loop during loading and unloading cycle

Comparison of an internal loop during loading and unloading cycle was possible using the following protocol shown in figure 2.10a

- Zone 1 : Twist upto 900^o twist (Loading cycle)
- Zone 2 : Untwist back to 400^o twist (Unloading cycle)
- Zone 3 : Twist upto 1800^o twist (Loading cycle)
- Zone 4 : Untwist back to 800^o twist (Unloading cycle)
- Zone 5 : Twist upto 1300^o twist (Loading cycle)
- Zone 6 : Untwist back to 0^o twist (Unloading cycle)

Recorded data for this test run with triangular twist controlled forcing function as input is shown in figure 2.10b. For the non-linear torque–twist response shown in figure 2.10c, the internal loop during loading and unloading never intersects the outer

loop. In both loops, one can observe near perfect RPM with no residual elongation upon complete unloading.

2.3.3.4 Multiple internal loop during loading and unloading cycle

A test case to investigate multiple internal loops during loading and unloading cycles are programmed as described below and shown in figure 2.11a

- Zone 1 : Twist upto 500^o twist (Loading cycle)
- Zone 2 : Untwist back to 350^o twist (Unloading cycle)
- Zone 3 : Twist upto 800^o twist (Loading cycle)
- Zone 4 : Untwist back to 650^o twist (Unloading cycle)
- Zone 5 : Twist upto 1100^o twist (Loading cycle)
- Zone 6 : Untwist back to 950^o twist (Unloading cycle)
- Zone 7 : Twist upto 1400^o twist (Loading cycle)
- Zone 8 : Untwist back to 1250^o twist (Unloading cycle)
- Zone 9 : Twist upto 1800^o twist (Loading cycle)
- Zone 10 : Untwist back to 1100^o twist (Unloading cycle)
- Zone 11 : Twist upto 1250^o twist (Loading cycle)
- Zone 12 : Untwist back to 800^o twist (Unloading cycle)
- Zone 13 : Twist upto 950^o twist (Loading cycle)
- Zone 14 : Untwist back to 500^o twist (Unloading cycle)

- Zone 15 : Twist upto 650^o twist (Loading cycle)
- Zone 16 : Untwist back to 0^o twist (Unloading cycle)

The corresponding torque data recorded as a function of time is shown in figure 2.11b. The complete torque–twist response is shown in figure 2.11c. All the small internal loops under loading and unloading regimes show near perfect RPM with slopes similar to the austentic and martensitic slopes of the outer loops.

2.3.3.5 Complex loops during loading cycle

A complex loading scenario was investigated with the following protocol shown in figure 2.12a

- Zone 1 : Twist upto 1300^o twist (Loading cycle)
- Zone 2 : Untwist back to 400^o twist (Unloading cycle)
- Zone 3 : Twist upto 1100^o twist (Loading cycle)
- Zone 4 : Untwist back to 600^o twist (Unloading cycle)
- Zone 5 : Twist upto 900^o twist (Loading cycle)
- Zone 6 : Untwist back to 800^o twist (Unloading cycle)
- Zone 7 : Twist upto 1800^o twist (Loading cycle)
- Zone 8 : Untwist back to 0^o twist (Unloading cycle)

Data recorded for this case is shown in figure 2.12b. The complex loop response exhibited on the torque–twist plot 2.12c shows that the partially transformed case (internal loops) follows the trend of the fully transformed case (outer loop). The internal loops never intersect the outer loops regardless of the extent of loading and

unloading points selected with the transformation regime (i.e. the plateau stress levels).

2.3.3.6 Complex loops during unloading cycle

Similarly to above, the behavior of the response of a material subjected to a complex unloading case was recorded using the following protocol shown in figure 2.13a

- Zone 1 : Twist upto 1800^o twist (Loading cycle)
- Zone 2 : Untwist back to 400^o twist (Unloading cycle)
- Zone 3 : Twist upto 1300^o twist (Loading cycle)
- Zone 4 : Untwist back to 600^o twist (Unloading cycle)
- Zone 5 : Twist upto 1100^o twist (Loading cycle)
- Zone 6 : Untwist back to 800^o twist (Unloading cycle)
- Zone 7 : Twist upto 900^o twist (Loading cycle)
- Zone 8 : Untwist back to 0^o twist (Unloading cycle)

Data recorded for this case is shown in figure 2.13b. The complete torque–twist response is shown on figure 2.13c. The complex loops closely mimic the outer loop response but never intersect the outer loop. A good RPM was observed in this case too.

2.3.3.7 Complex loops during loading and unloading cycle

A test case to investigate a complex internal loop during unloading cycle was programmed as described below and shown in figure 2.14a

- Zone 1 : Twist upto 900^o twist (Loading cycle)
- Zone 2 : Untwist back to 400^o twist (Unloading cycle)
- Zone 3 : Twist upto 800^o twist (Loading cycle)
- Zone 4 : Untwist back to 500^o twist (Unloading cycle)
- Zone 5 : Twist upto 700^o twist (Loading cycle)
- Zone 6 : Untwist back to 600^o twist (Unloading cycle)
- Zone 7 : Twist upto 1800^o twist (Loading cycle)
- Zone 8 : Untwist back to 800^o twist (Unloading cycle)
- Zone 9 : Twist upto 1300^o twist (Loading cycle)
- Zone 10 : Untwist back to 900^o twist (Unloading cycle)
- Zone 11 : Twist upto 1200^o twist (Loading cycle)
- Zone 12 : Untwist back to 1000^o twist (Unloading cycle)
- Zone 13 : Twist upto 1100^o twist (Loading cycle)
- Zone 14 : Untwist back to 0^o twist (Unloading cycle)

The corresponding torque data recorded as a function of time is shown in figure 2.14b. The complete torque–twist response is shown in figure 2.14c.

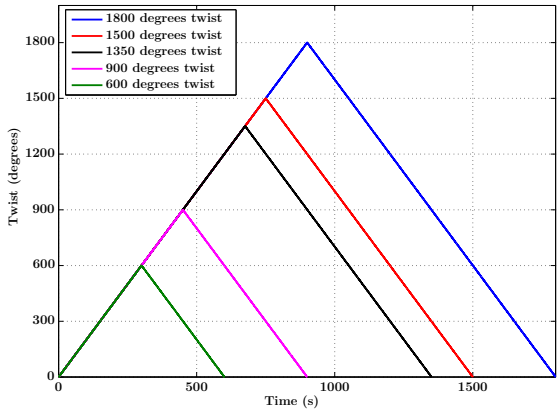

(a) Twist versus time plot

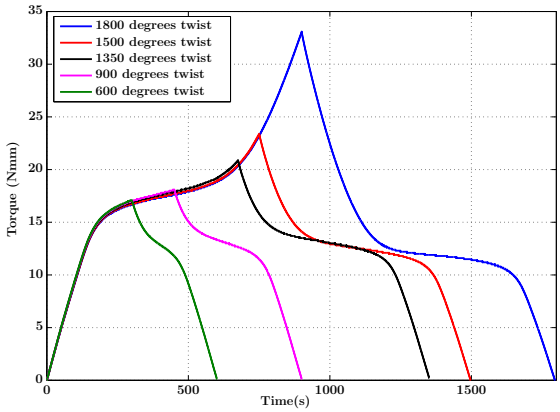

(b) Torque versus time plot

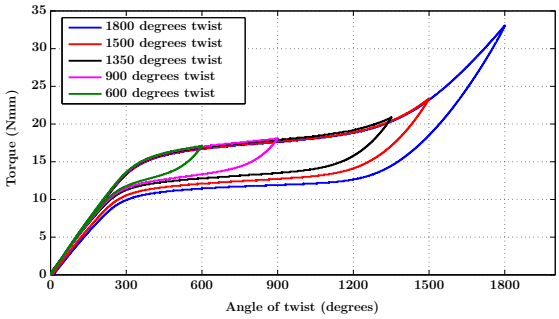

(c) Torque versus twist plot

Figure 2.8: Figures shows the twist versus time ; torque versus time and torque versus twist responses responses for a simple loading and unloading tests with different unloading points of 1500^o, 1350^o, 900^o and 600^o maximum twists overlapped on each other and compared against the 1800^o twist. All the individual tests were different trials performed on different test specimens demonstrating good agreement and test repeatability.

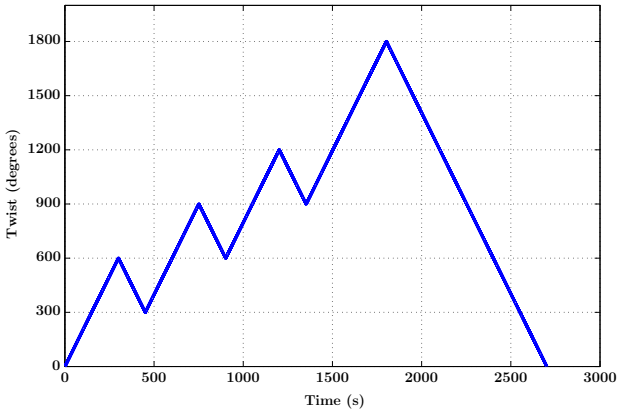

(a) Twist versus time plot

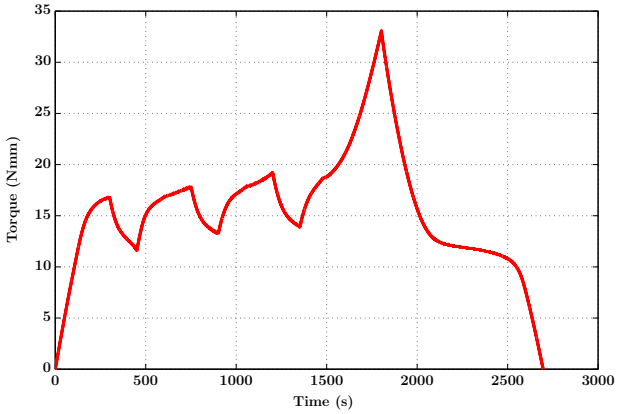

(b) Torque versus time plot

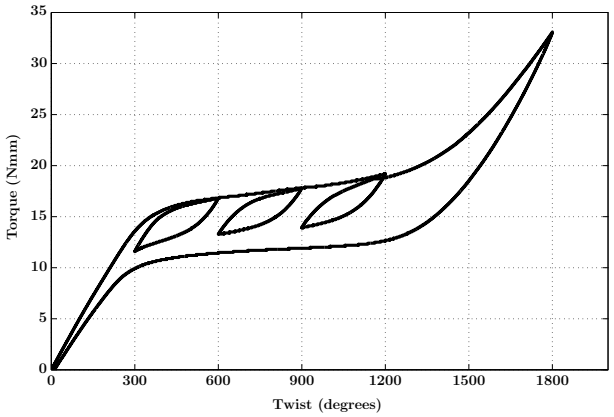

(c) Torque versus twist plot

Figure 2.9: Experimental data showing the twist versus time ; torque versus time and torque versus twist responses for test upto 1800^o maximum twist with three internal loops during the loading cycle.

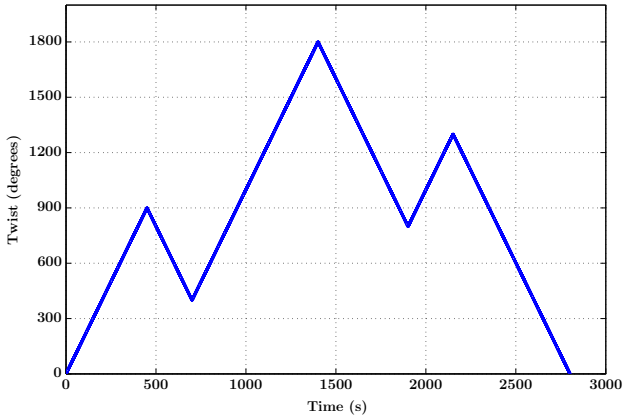

(a) Twist versus time plot

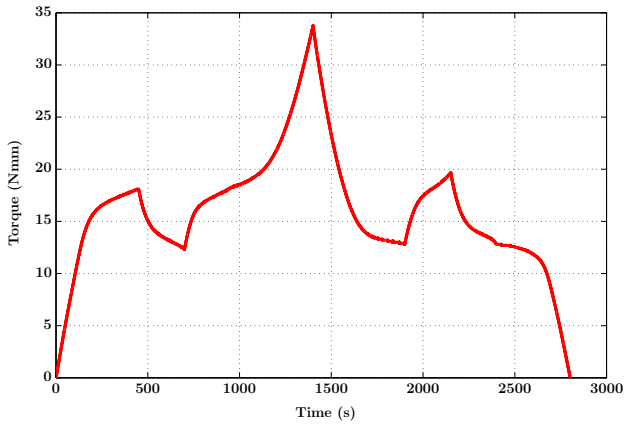

(b) Torque versus time plot

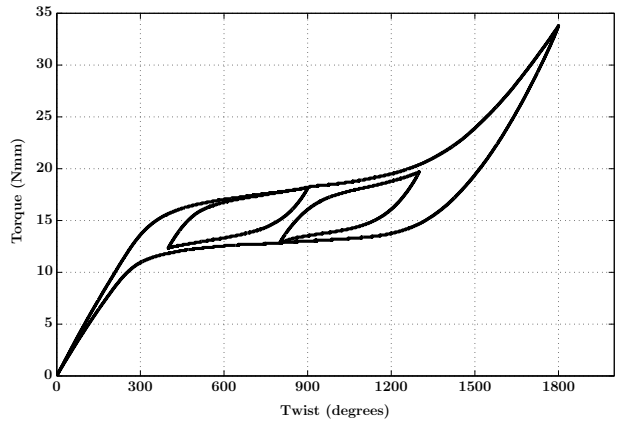

(c) Torque versus twist plot

Figure 2.10: Figures shows the twist versus time ; torque versus time and torque versus twist responses for test upto 1800^o maximum twist for comparing internal loops during loading and unloading cycle.

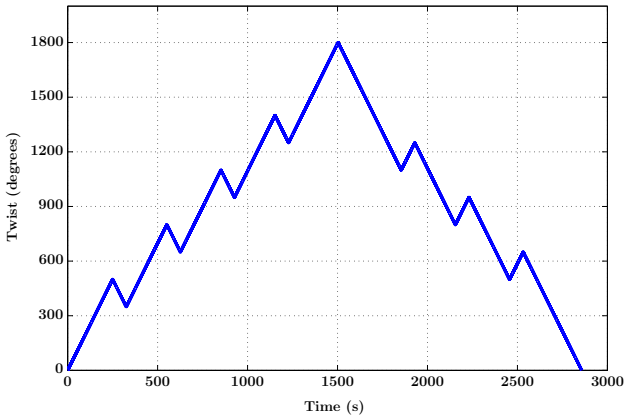

(a) Twist versus time plot

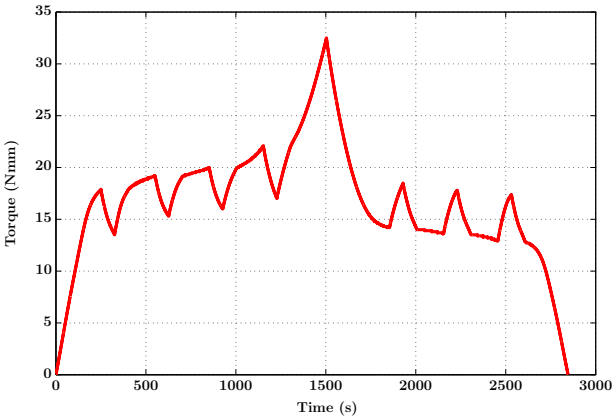

(b) Torque versus time plot

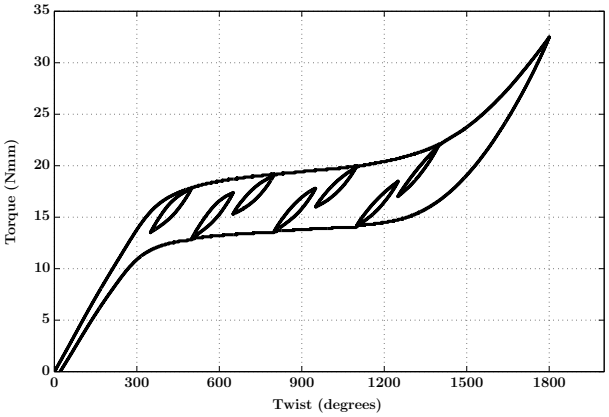

(c) Torque versus twist plot

Figure 2.11: Figures shows the twist versus time ; torque versus time and torque versus twist responses for test upto 1800^o maximum twist with multiple internal loops during loading and unloading.

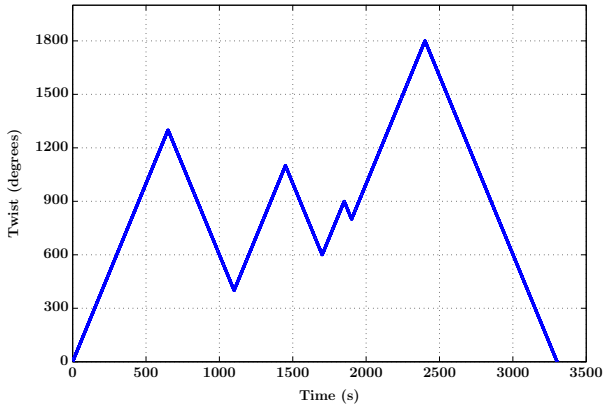

(a) Twist versus time plot

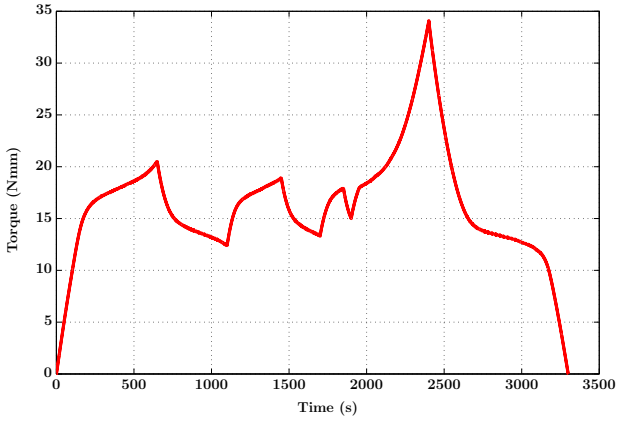

(b) Torque versus time plot

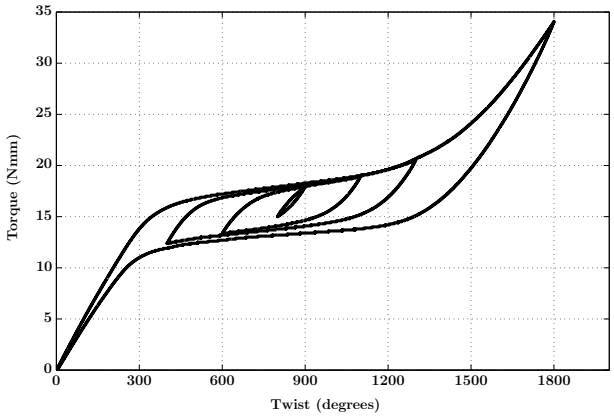

(c) Torque versus twist plot

Figure 2.12: Figures shows the twist versus time ; torque versus time and torque versus twist responses for test upto 1800^o maximum twist with a complex internal loops during loading cycle.

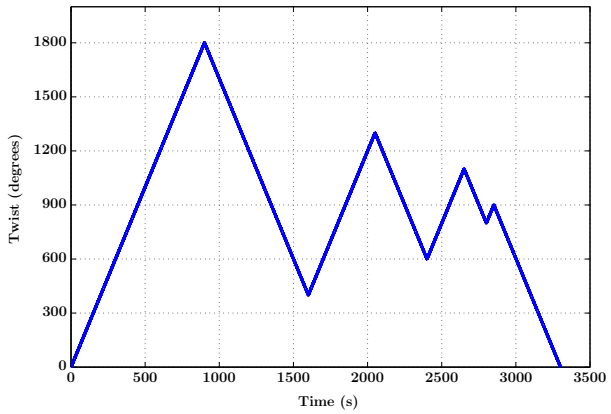

(a) Twist versus time plot

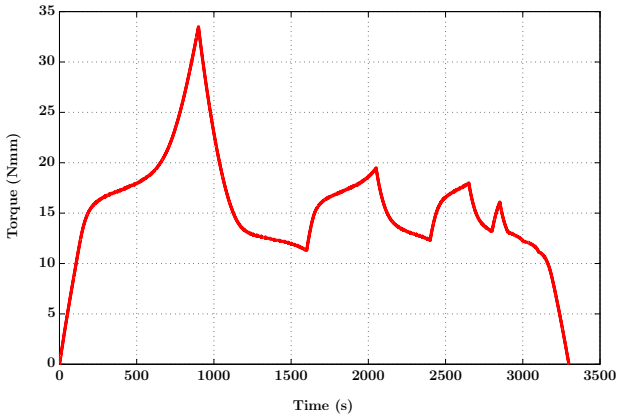

(b) Torque versus time plot

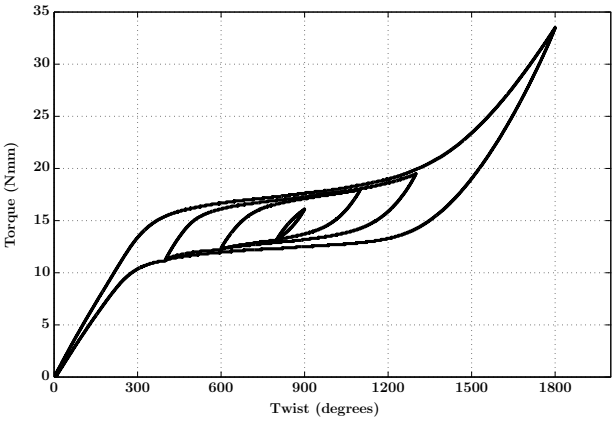

(c) Torque versus twist plot

Figure 2.13: Figures shows the twist versus time ; torque versus time and torque versus twist responses for test upto 1800^o maximum twist with a complex internal loops during unloading cycle.

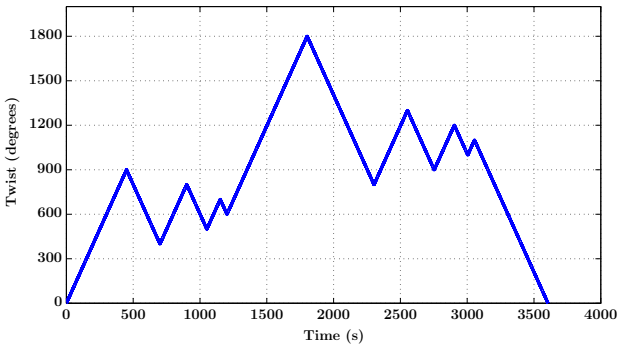

(a) Twist versus time plot

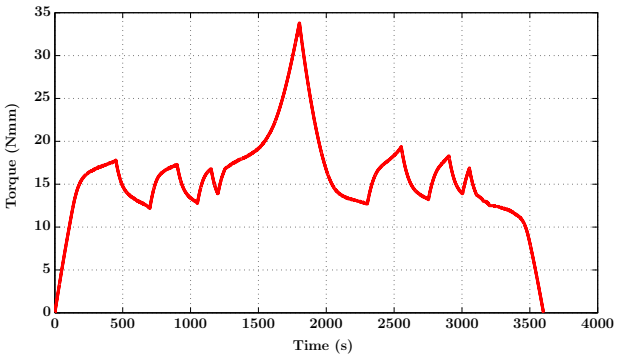

(b) Torque versus time plot

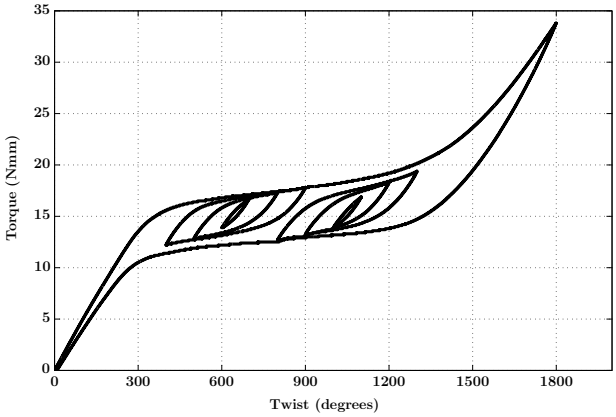

(c) Torque versus twist plot

Figure 2.14: Figures shows the twist versus time ; torque versus time and torque versus twist responses for test upto 1800^o maximum twist with a complex internal loops during both loading and unloading cycles.

3. MODEL DEVELOPMENT - TWO SPECIES *

In this section, the development of structural thermomechanical models for shape memory alloy components like wires, springs and beams subjected to either tension, torsion or bending loading conditions under superelastic conditions is discussed. Following Doraiswamy et al. [64], the key idea here would be in separating the thermoelastic and the dissipative part of the hysteretic response with a Gibbs potential based formulation. The hysteretic part of the response is then handled by a discrete Preisach model (to be discussed in section 4). As noted earlier, phase transformations are more akin to domain switching in magnetism rather than crystallographic slip, hence the whole SMA structure can be imagined as a collection of many such domains with each of them switching positions based on the external impetus. In this two species model, the two domains/phases considered are austenite and detwinned martensite. It is assumed that during a superelastic response, all the austenite transforms to one variant of martensite during $A \rightarrow M$ transformation and similarly all of the martensite switches back to austenite during the reverse $M \rightarrow A$ transformation.

A Gibbs potential per unit volume (inspired from [64, 65]) which is assumed to be a function of the stress (σ) or torque (T) or bending–moment (M) depending on the loading condition, operating temperature (θ) and the extent of transformation (ξ) i.e volume fraction of detwinned martensite formed during phase transition. The Gibbs potential is assumed to be composed of (refer equation 3.1) :

*Reprinted with permission from "Combining Thermodynamic Principles with Preisach models for superelastic SMA Wires" by Doraiswamy, Rao and Srinivasa, *Smart Materials and Structures*, 20, 085032, 2011 [64], Copyright [2014] by IOP.

Reprinted with permission from "A two species thermodynamic Preisach model for the torsional response of SMA wires and springs under superelastic conditions" by Rao and Srinivasa, *International Journal of Solids and Structures*, 50, 887–898, 2013 [90], Copyright [2014] by Elsevier Limited

1. a linear combination of the strain energy for the two species/phases,

2. an interaction term between the two phases,

3. a term related to the heat capacity difference between the two phases and

4. a term relating to the heat capacity of the austenite.

Specifically the Gibbs potential energy per unit reference volume is assumed to be of the form,

$$\boldsymbol{\mathcal{G}} = \overbrace{-\left(\xi U_M^* + (1-\xi)U_A^*\right)}^{1} + \overbrace{B\xi(\xi-1)}^{2} + \overbrace{(1-\xi)(a+b\theta)}^{3} - \overbrace{C\theta(1-\log\theta)}^{4} \qquad (3.1)$$

where,

- ξ is the martensite volume fraction,
- U_M^* & U_A^* are the stored energy function chosen based on the loading conditions for detwinned martensite and austenitic phases respectively,
- B, a and b are constants,
- θ is the temperature and
- C is the specific heat

In the following sections, a thermodynamical framework commonly employed for modeling phase transforming materials (as discussed in literature review under section 1.4.1) is employed with an appropriate choice of U_M^* and U_A^* based on the type of loading.

3.1 Tensile Loading Case : Model Development

Following Doraiswamy et al. [64], consider a NiTi SMA wire with an initial cross-sectional area A and initial gauge length of L_0 along the X-axis. If the wire is subjected to a tensile load of F along its axis, then the axial referential stress is obtained using $\sigma = \frac{F}{A}$. Assuming uniform deformation under quasi-static loading conditions, strain in the SMA wire is given by $\varepsilon = \frac{L-L_0}{L_0}$ with "L" being the current(deformed) length of the wire. A typical displacement-controlled experiment result is shown in figure 2.2.

For a tension loading case $U_M^* = \left(\frac{\sigma^2}{2E_M}\right)$ and $U_A^* = \left(\frac{\sigma^2}{2E_A}\right)$ respectively. Specifically the Gibbs potential energy per unit reference volume is assumed to be of the form,

$$\boldsymbol{\mathcal{G}_{ten}} = \overbrace{-\left(\frac{\xi_{ten}\sigma^2}{2E_M} + \frac{(1-\xi_{ten})\sigma^2}{2E_A}\right)}^{1} + \overbrace{B\xi_{ten}(\xi_{ten}-1)}^{2} + \overbrace{(1-\xi_{ten})(a+b\theta)}^{3} - \overbrace{C\theta(1-\log\theta)}^{4} \tag{3.2}$$

where,

- ξ_{ten} is the martensite volume fraction,
- σ is the stress,
- E_M and E_A are the martensitic and austentic moduli respectively
- B, a and b are constants,
- θ is the temperature and
- C is the specific heat

The constant B represents the interaction energy between the austenite and martensite phases while b is the entropy difference between the austenite and marten-

site phases respectively (see equation 3.4 below). Constant "a" is the internal energy difference between the austenite and martensite phases at 0 K (see equation 3.6 below). It is evident from the experimental evidences that in many tension tests indicate that the platue stress in a superelastic response scales linearly with the temperature and a linear assumption ($a + b\theta$ terms in the model) is one of the simplest ways to capture the temperature dependence of superelastic responses in SMA (see experimental results – 2.3b, figure 7 in [72], figure 12 in [147], figure 85 in [156], figure 16 in [142], figure 3 in [105] etc. for illustrations). The method to identify the above parameters would be described later in section 6.5.

3.1.1 Macroscopic Driving Force for Phase Transformation – Tension Loading Case

From classical thermodynamics, the entropy is given by,

$$\eta = -\frac{\partial \boldsymbol{\mathcal{G}_{ten}}}{\partial \theta} = -C \ln \theta - (1 - \xi_{ten}) b \tag{3.3}$$

Using above,

$$\left.\begin{aligned} \eta|_{(\xi_{ten}=1)} &= -C \ln \theta \\ \eta|_{(\xi_{ten}=0)} &= -C \ln \theta - b \end{aligned}\right\} \Longrightarrow b = \Delta\eta = \eta|_{(\xi=1)} - \eta|_{(\xi=0)} \tag{3.4}$$

thus, "b" is the entropy difference between the austenite and martensite states. The internal energy, $\exists$, is given by,

$$\begin{aligned} \exists = \boldsymbol{\mathcal{G}_{ten}} + \theta\eta = \boldsymbol{\mathcal{G}_{ten}} - \theta \frac{\partial \boldsymbol{\mathcal{G}_{ten}}}{\partial \theta} = -\left(\frac{\xi_{ten}\sigma^2}{2E_M} + \frac{(1 - \xi_{ten})\sigma^2}{2E_A} \right) + \\ B\xi_{ten}(\xi_{ten} - 1) + (1 - \xi_{ten})a - C\theta \end{aligned} \tag{3.5}$$

Using above,

$$\left.\begin{aligned} \exists_A = \exists|_{(\xi_{ten}=0,\sigma=0,\theta=0)} &= a \\ \exists_M = \exists|_{(\xi_{ten}=1,\sigma=0,\theta=0)} &= 0 \end{aligned}\right\} \Longrightarrow a = \exists_A - \exists_M \tag{3.6}$$

From the above, the parameter "a" is the internal energy difference between the two phases at 0 K.

From the Gibbs potential, the elastic strain is given by,

$$\varepsilon_e = -\frac{\partial \boldsymbol{\mathcal{G}_{ten}}}{\partial \sigma} = \frac{\xi_{ten}\sigma}{E_M} + \frac{(1-\xi ten)\sigma}{E_A} \tag{3.7}$$

Also, the Helmholtz potential ψ, is related to Gibbs potential $\boldsymbol{\mathcal{G}_{ten}}$, by,

$$\psi = \boldsymbol{\mathcal{G}_{ten}} - \sigma\frac{\partial \boldsymbol{\mathcal{G}_{ten}}}{\partial \sigma} \tag{3.8}$$

The difference between the rate of external working ($\sigma\dot{\varepsilon}$) and the rate of change of the Helmholtz potential keeping the temperature fixed ($\dot{\psi}|_\theta$), must be equal to the macroscopic inelastic power (P_{ten}^{inel}). In other words,

$$P_{ten}^{inel} = \sigma\dot{\varepsilon} - \dot{\psi}|_\theta \tag{3.9}$$

Using equations 3.7, 3.8 and simplifying the above,

$$\sigma(\dot{\varepsilon} - \dot{\varepsilon}_e) - \frac{\partial \boldsymbol{\mathcal{G}_{ten}}}{\partial \xi_{ten}}\dot{\xi_{ten}} = P_{ten}^{inel} \tag{3.10}$$

From equation 3.10, it is observed that there are two contributions to the inelastic power, one from the shape change that occurs due to phase transition ($\sigma(\dot{\varepsilon} - \dot{\varepsilon}_e)$) and the other from the energy difference between the two phases $\left(-\frac{\partial \boldsymbol{\mathcal{G}_{ten}}}{\partial \xi_{ten}}\dot{\xi_{ten}}\right)$. It

is assumed that the elongation due to phase transformation is proportional to the maximum transformational strain, ε_{max}, which can be assumed to be in the order of 6% for Ni-Ti. Therefore,

$$\dot{\varepsilon} - \dot{\varepsilon}_e = \varepsilon_{max}\dot{\xi_{ten}} \Rightarrow \varepsilon - \varepsilon_e = \varepsilon_{max}\xi_{ten} \tag{3.11}$$

In the above equation note that, when $\xi_{ten} = 1$, $\varepsilon - \varepsilon_e = \varepsilon_{max}$ and when $\xi_{ten} = 0$, $\varepsilon - \varepsilon_e = 0$. Now substituting equation 3.11 into equation 3.10 gives :

$$\left(\sigma\varepsilon_{max} - \frac{\partial \boldsymbol{\mathcal{G}_{ten}}}{\partial \xi}\right)\dot{\xi_{ten}} = P_{ten}^{inel} \tag{3.12}$$

It is now possible to identify the driving force for the phase transformation in the superelastic response of the SMA:

$$\begin{aligned} \boldsymbol{\mathcal{F}_{ten}} = \sigma\varepsilon_{max} - \frac{\partial \boldsymbol{\mathcal{G}_{ten}}}{\partial \xi_{ten}} \implies \boldsymbol{\mathcal{F}_{ten}}\dot{\xi_{ten}} = P_{ten}^{inel} \\ \text{Hence, } \boldsymbol{\mathcal{F}_{ten}} = \sigma\varepsilon_{max} + \sigma^2\left(\frac{1}{2E_M} - \frac{1}{2E_A}\right) - B(2\xi_{ten} - 1) + b\theta + a \end{aligned} \tag{3.13}$$

It is to be noted here that P_{ten}^{inel} is the macroscopic inelastic power and can be less than zero. The dissipation, $\boldsymbol{\Delta}_{ten}$, is the net macroscopic inelastic work in a closed cycle of state and this is required to be non-negative, i.e,

$$\boldsymbol{\Delta}_{ten} = \oint P_{ten}^{inel}\,\mathrm{d}t \geq 0 \tag{3.14}$$

Further, an expression for the martensitic volume fraction evolution (ξ) can be obtained using expressions 3.7 and 3.11. The volume fraction evolution expression ξ can be obtained from the torque–angle of twist experimental data and the assumed

form of Gibbs potential.

$$\xi_{ten} = \frac{\varepsilon - \dfrac{\sigma}{E_A}}{\dfrac{\sigma}{E_M} - \dfrac{\sigma}{E_A} + 1} \tag{3.15}$$

The experimental stress–strain data can be reduced to its corresponding driving-force – volume fraction plot (to be discussed in section 3.4 later.)

3.2 Torsion Loading Case : Model Development

Shifting focus to a torsional loading case, consider a SMA wire subjected to a torque "T" about its axis or a helical extension SMA spring subjected to force "P" along its axis with "δ" being the corresponding axial displacement. Let,

- "D_m" be the mean coil diameter of the spring in mm
- "d" be the SMA wire diameter in mm.
- "C" denote the spring index.
- "n" be the number of active coils (i.e neglecting the end hooks).

The torque (T) and angle of twist per unit length (ϕ) are directly measured in the case of wire and the same can be computed using equations 2.1 and 2.2 for springs respectively.

For a torsional loading case $U_M^* = \left(\frac{T^2}{2G_M J}\right)$ and $U_A^* = \left(\frac{T^2}{2G_A J}\right)$. Similar to tension loading case, a Gibbs potential per unit reference volume for a pure torsion loading case is assumed to be of the form as shown below, (similar to equation 3.2 discussed earlier)

$$\begin{aligned} \boldsymbol{\mathcal{G}_{tor}} = & \overbrace{-\left(\frac{\xi_{tor} T^2}{2G_M J} + \frac{(1-\xi_{tor})T^2}{2G_A J}\right)}^{1} + \overbrace{B\xi_{tor}(\xi_{tor}-1)}^{2} \\ & + \overbrace{(1-\xi_{tor})(a+b\theta)}^{3} - \overbrace{C\theta(1-\ln\theta)}^{4} \end{aligned} \tag{3.16}$$

where,

- ξ_{tor} is the martensite volume fraction,
- T is the applied torque,
- G_A and G_M are the austenitic and martensitic shear moduli,
- $J = \frac{\pi d^4}{32}$ is the polar moment of inertia
- B, a and b are constants,
- θ is the temperature and
- C is the specific heat

The constant B represents the interaction energy between the austenite and martensite phases while b is the entropy difference between the austenite and martensite phases respectively (see equation 3.18 below). Constant "a" is the internal energy difference between the austenite and martensite phases at 0 K (see equation 3.20 below). The method to identify the above parameters is discussed in Section 6.5.

3.2.1 Establishing Macroscopic Driving Force – Pure Torsion Case

From classical thermodynamics, the entropy is given by,

$$\eta = -\frac{\partial \boldsymbol{\mathcal{G}_{tor}}}{\partial \theta} = -C \ln \theta - (1 - \xi_{tor}) b \tag{3.17}$$

Using above,

$$\left.\begin{aligned} \eta|_{(\xi_{tor}=1)} &= -C \ln \theta \\ \eta|_{(\xi_{tor}=0)} &= -C \ln \theta - b \end{aligned}\right\} \Longrightarrow b = \Delta\eta = \eta|_{(\xi_{tor}=1)} - \eta|_{(\xi_{tor}=0)} \tag{3.18}$$

thus, b is the entropy difference between the austenite and martensite states.

The internal energy, $\exists$, is given by,

$$\begin{aligned}\exists = \boldsymbol{\mathcal{G}_{tor}} + \theta\eta = \boldsymbol{\mathcal{G}_{tor}} - \theta\frac{\partial \boldsymbol{\mathcal{G}_{tor}}}{\partial\theta} = -\left(\frac{\xi_{tor}T^2}{2G_M J} + \frac{(1-\xi_{tor})T^2}{2G_A J}\right) \\ +B\xi_{tor}(\xi_{tor}-1) + (1-\xi_{tor})a - C\theta\end{aligned} \tag{3.19}$$

Using above,

$$\left.\begin{aligned}\exists_A = \exists|_{(\xi_{tor}=0,T=0,\theta=0)} &= a \\ \exists_M = \exists|_{(\xi_{tor}=1,T=0,\theta=0)} &= 0\end{aligned}\right\} \Longrightarrow a = \exists_A - \exists_M \tag{3.20}$$

From the above, the parameter a is the internal energy difference between the two phases at 0 K.

From the Gibbs potential, the thermoelastic part of the angle of twist is given by,

$$\phi_e = -\frac{\partial \boldsymbol{\mathcal{G}_{tor}}}{\partial T} = \frac{\xi_{tor}T}{G_M J} + \frac{(1-\xi_{tor})T}{G_A J} \tag{3.21}$$

Also, the Helmholtz potential ψ, is related to Gibbs potential $\boldsymbol{\mathcal{G}_{tor}}$, by,

$$\psi = \boldsymbol{\mathcal{G}_{tor}} - T\frac{\partial \boldsymbol{\mathcal{G}_{tor}}}{\partial T} \tag{3.22}$$

The difference between the rate of external working ($T\dot{\phi}$) and the rate of change of the Helmholtz potential keeping the temperature fixed ($\dot{\psi}|_\theta$), must be equal to the macroscopic inelastic power (P_{tor}^{inel}). In other words,

$$P_{tor}^{inel} = T\dot{\phi} - \dot{\psi}|_\theta \tag{3.23}$$

Using equations 3.21, 3.22 and upon further simplification,

$$T(\dot{\phi} - \dot{\phi}_e) - \frac{\partial \boldsymbol{\mathcal{G}}_{tor}}{\partial \xi_{tor}} \dot{\xi_{tor}} = P_{tor}^{inel} \tag{3.24}$$

From equation 3.24, it is observed that there are two contributions to the inelastic power, one from the shape change that occurs due to phase transition ($T(\dot{\phi} - \dot{\phi}_e)$) and the other from the energy difference between the two phases $\left(-\frac{\partial \boldsymbol{\mathcal{G}}_{tor}}{\partial \xi_{tor}} \dot{\xi_{tor}}\right)$. The recoverable angle of twist is due to the phase transformation and is proportional to the extent of transformation depending on the axial force and corresponding axial displacement that the spring is subjected too. The maximum angle of twist ϕ_{max} corresponding to a maximum transformational strain that can assumed to be of the order of 6%.

$$\dot{\phi} - \dot{\phi}_e = \phi_{max} \dot{\xi_{tor}} \Rightarrow \phi - \phi_e = \phi_{max} \xi_{tor} \tag{3.25}$$

In the above equation note that, when $\xi_{tor} = 1$, $\phi - \phi_e = \phi_{max}$ and when $\xi_{tor} = 0$, $\phi - \phi_e = 0$. Now substituting equation 3.25 into 3.24 gives:

$$\left(T\phi_{max} - \frac{\partial \boldsymbol{\mathcal{G}}_{tor}}{\partial \xi_{tor}}\right) \dot{\xi_{tor}} = P_{tor}^{inel} \tag{3.26}$$

It is now possible to identify the driving force for the phase transformation in the superelastic response of the SMA springs:

$$\begin{aligned} \boldsymbol{\mathcal{F}_{tor}} = T\phi_{max} - \frac{\partial \boldsymbol{\mathcal{G}_{tor}}}{\partial \xi_{tor}} \implies \boldsymbol{\mathcal{F}_{tor}} \dot{\xi_{tor}} = P_{tor}^{inel} \\ \text{Hence, } \boldsymbol{\mathcal{F}_{tor}} = T\phi_{max} + T^2 \left(\frac{1}{2G_M J} - \frac{1}{2G_A J}\right) - B(2\xi_{tor} - 1) + b\theta + a \end{aligned} \tag{3.27}$$

P_{tor}^{inel} is the macroscopic inelastic power. The rate of mechanical dissipation, $\boldsymbol{\Delta}_{tor}$, is the net macroscopic inelastic work in a closed cycle of state and this is required to

be non-negative as required by the second law of thermodynamics, i.e,

$$\boldsymbol{\Delta}_{tor} = \oint P_{tor}^{inel}\, \mathrm{d}t \geq 0 \tag{3.28}$$

The volume fraction evolution expression ξ_{tor} can be obtained from the torque–angle of twist experimental data and the assumed form of Gibbs potential using equations 3.21 and 3.25.

$$\xi_{tor} = \frac{\phi - \dfrac{T}{G_A J}}{\dfrac{T}{G_M J} - \dfrac{T}{G_A J} + 1} \tag{3.29}$$

The experimental torque–twist data can be reduced to its corresponding driving-force – volume fraction plot (to be discussed in section 3.4 later.)

3.3 Bending Loading Case : Model Development

Now for a pure bending loading case, consider a wire/beam subjected to bending moment "M" with the corresponding curvature denoted by "κ". Both bending moment "M" and curvature (κ) are directly measured experimentally.

For a pure bending case $U_M^* = \left(\frac{M^2}{2E_M I}\right)$ and $U_A^* = \left(\frac{M^2}{2E_A I}\right)$. Similar to tension and torsion loading cases, a Gibbs potential energy per unit reference volume for a pure bending loading case is assumed to be of the form as shown below in equation 3.30. (similar to equations 3.2 and 3.16 discussed earlier)

$$\begin{aligned}\boldsymbol{\mathcal{G}_{bend}} = \overbrace{-\left(\frac{\xi_{bend} M^2}{2E_M I} + \frac{(1-\xi_{bend})M^2}{2E_A I}\right)}^{1} + \overbrace{B\xi_{bend}(\xi_{bend}-1)}^{2} \\ + \overbrace{(1-\xi_{bend})(a+b\theta)}^{3} - \overbrace{C\theta(1-\ln\theta)}^{4}\end{aligned} \tag{3.30}$$

where,

- ξ_{bend} is the martensite volume fraction,
- M is the applied bending moment,
- E_A and E_M are the austenitic and martensitic moduli,
- $I = \frac{\pi d^4}{64}$ is the moment of Inertia
- B, a and b are constants,
- θ is the temperature and
- C is the specific heat

Similar to earlier discussions, the constant "B" represents the interaction energy between the austenite and martensite phases while "b" is the entropy difference between the austenite and martensite phases respectively (see equation 3.32 below). Constant "a" is the internal energy difference between the austenite and martensite phases at 0 K (see equation 3.34 below). The method to identify the above parameters would be described later in section 6.5.

3.3.1 Establishing Macroscopic Driving Force – Pure Bending Case

From classical thermodynamics, the entropy is given by,

$$\eta = -\frac{\partial \boldsymbol{\mathcal{G}_{bend}}}{\partial \theta} = -C \ln \theta - (1 - \xi_{bend})b \tag{3.31}$$

Using above,

$$\left.\begin{aligned} \eta|_{(\xi_{bend}=1)} &= -C \ln \theta \\ \eta|_{(\xi_{bend}=0)} &= -C \ln \theta - b \end{aligned}\right\} \Longrightarrow b = \Delta\eta = \eta|_{(\xi_{bend}=1)} - \eta|_{(\xi_{bend}=0)} \tag{3.32}$$

thus, b is the entropy difference between the austenite and martensite states.

The internal energy, $\exists$, is given by,

$$\begin{aligned}\exists = \boldsymbol{\mathcal{G}_{bend}} + \theta\eta = \boldsymbol{\mathcal{G}_{bend}} - \theta\frac{\partial \boldsymbol{\mathcal{G}_{bend}}}{\partial\theta} = -\left(\frac{\xi_{bend}M^2}{2E_M I} + \frac{(1-\xi)M^2}{2E_A I}\right) \\ +B\xi_{bend}(\xi_{bend}-1) + (1-\xi_{bend})a - C\theta\end{aligned} \tag{3.33}$$

Using above,

$$\left.\begin{aligned}\exists_A = \exists|_{(\xi_{bend}=0, M=0, \theta=0)} &= a \\ \exists_M = \exists|_{(\xi_{bend}=1, M=0, \theta=0)} &= 0\end{aligned}\right\} \Longrightarrow a = \exists_A - \exists_M \tag{3.34}$$

From the Gibbs potential, the thermoelastic part of the total curvature is given by,

$$\kappa_e = -\frac{\partial \boldsymbol{\mathcal{G}_{bend}}}{\partial M} = \frac{\xi_{bend}M}{E_M I} + \frac{(1-\xi_{bend})M}{E_A I} \tag{3.35}$$

Also, the Helmholtz potential ψ, is related to Gibbs potential $\boldsymbol{\mathcal{G}_{bend}}$, by,

$$\psi = \boldsymbol{\mathcal{G}_{bend}} - M\frac{\partial \boldsymbol{\mathcal{G}_{bend}}}{\partial M} \tag{3.36}$$

The difference between the rate of external working ($M\dot{\kappa}$) and the rate of change of the Helmholtz potential keeping the temperature fixed ($\dot{\psi}|_\theta$), must be equal to the macroscopic inelastic power (P^{inel}_{bend}). In other words,

$$P^{inel}_{bend} = M\dot{\kappa} - \dot{\psi}|_\theta \tag{3.37}$$

Using equations 3.35, 3.36 and upon further simplification,

$$M(\dot{\kappa} - \dot{\kappa}_e) - \frac{\partial \boldsymbol{\mathcal{G}_{bend}}}{\partial \xi_{bend}}\dot{\xi_{bend}} = P^{inel}_{bend} \tag{3.38}$$

From equation 3.38, it is observed that there are two contributions to the inelastic power, one from the shape change that occurs due to phase transition ($M(\dot{\kappa} - \dot{\kappa_e})$) and the other from the energy difference between the two phases $\left(-\frac{\partial G}{\partial \xi_{bend}}\dot{\xi_{bend}}\right)$. The maximum transformational strain (κ_{max} in this case)can assumed to be of the order of 6%.

$$\dot{\kappa} - \dot{\kappa_e} = \kappa_{max}\dot{\xi} \Rightarrow \kappa - \kappa_e = \kappa_{max}\xi \tag{3.39}$$

In the above equation note that, when $\xi_{bend} = 1$, $\kappa - \kappa_e = \kappa_{max}$ and when $\xi_{bend} = 0$, $\kappa - \kappa_e = 0$. Now substituting equation 3.39 into equation 3.38 we get,

$$\left(M\kappa_{max} - \frac{\partial \boldsymbol{\mathcal{G}_{bend}}}{\partial \xi_{bend}}\right)\dot{\xi_{bend}} = P^{inel}_{bend} \tag{3.40}$$

It is now possible to identify the driving force for the phase transformation in the superelastic response of the SMA springs:

$$\begin{aligned} \boldsymbol{\mathcal{F}_{bend}} = M\kappa_{max} - \frac{\partial \boldsymbol{\mathcal{G}_{bend}}}{\partial_{bend}} \implies \boldsymbol{\mathcal{F}_{bend}}\dot{\xi_{bend}} = P^{inel}_{bend} \\ \text{Hence, } \boldsymbol{\mathcal{F}_{bend}} = M\kappa_{max} + M^2\left(\frac{1}{2E_M I} - \frac{1}{2E_A I}\right) - B(2\xi_{bend} - 1) + b\theta + a \end{aligned} \tag{3.41}$$

P^{inel}_{bend} is the macroscopic inelastic power. The rate of dissipation, $\boldsymbol{\Delta}_{bend}$, is the net macroscopic inelastic work in a closed cycle of state. In order to satisfy second law of thermodynamics, this quantity must be non-negative i.e,

$$\boldsymbol{\Delta}_{bend} = \oint P^{inel}_{bend}\,\mathrm{d}t \geq 0 \tag{3.42}$$

The volume fraction evolution expression ξ_{tor} can be obtained from the torque–angle of twist experimental data and the assumed form of Gibbs potential using equations 3.35 and 3.39.

$$\xi_{bend} = \frac{\kappa - \dfrac{M}{E_A I}}{\dfrac{M}{E_M I} - \dfrac{M}{E_A I} + 1} \tag{3.43}$$

The experimental moment–curvature data can be reduced to its corresponding driving-force – volume fraction plot (to be discussed in section 3.4 later.)

3.4 Deducing Driving Force and Volume Fraction from Experimental Data for Different Loading Cases

Expressions for driving force for phase transformation and extent of martensite during phase transformation were established for different loading cases (equation sets 3.13 – 3.15 ; 3.27 – 3.29 and 3.41 – 3.43). From the driving force equations 3.13, 3.27 and 3.41, it is evident that the driving force expressions are a function of stress (σ) or torque (T) or bending–moment (M), strain (ε) or angle of twist (ϕ) or curvature (κ), martensitic volume fraction (ξ), and temperature (θ) depending on the loading condition under consideration. The variables $\sigma/T/M$, $\varepsilon/\phi/\kappa$ and θ are nondimensionalized before proceeding further with the derivations. The nondimensionalized variables for different loading cases are summarized below :

Tension Loading Case : $\sigma^* = \sigma/\sigma_{max}$, $\varepsilon^* = \varepsilon/\varepsilon_{max}$, $\theta^* = \theta/\theta_{max}$.

Torsion Loading Case : $T^* = T/T_{max}$, $\phi^* = \phi/\phi_{max}$, $\theta^* = \theta/\theta_{max}$.

Bending Loading Case : $M^* = M/M_{max}$, $\kappa^* = \kappa/\kappa_{max}$, $\theta^* = \theta/\theta_{max}$.

Henceforth, for better readability, the $*$'s will be omitted from the nondimensionalized variables. Experimental results for one particular temperature case are chosen as reference for simulation and establishment of driving force and volume fraction relationships.

For a tension loading case, using expressions 3.15 and 3.13, each experimental data point from stress vs strain plot can be reduced to its corresponding driving-

force – volume fraction plot as shown in figure 3.1 i.e (σ, ε) to $(\boldsymbol{\mathcal{F}_{ten}}, \xi_{ten})$.

For a torsion loading case, using expressions 3.29 and 3.27, each experimental data point from torque vs angle of twist plot can be reduced to its corresponding driving force – volume fraction plot as shown in figure 3.2 and figure 3.3 i.e (T, ϕ) to $(\boldsymbol{\mathcal{F}_{tor}}, \xi_{tor})$.

Similarly, for a pure bending loading condition, using expressions 3.43 and 3.41, each experimental data point from bending vs curvature plot can be reduced to its corresponding driving-force – volume fraction plot as shown in figures 3.4 or 3.5 respectively i.e (M, κ) to $(\boldsymbol{\mathcal{F}_{bend}}, \xi_{bend})$.

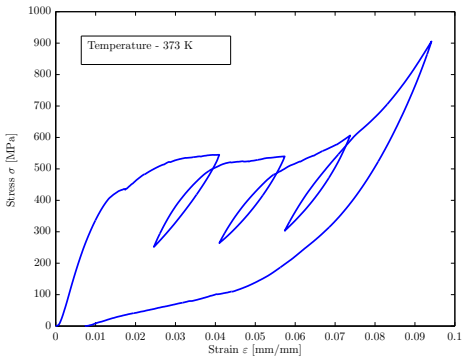

(a) Stress–Strain plot at 373 K.

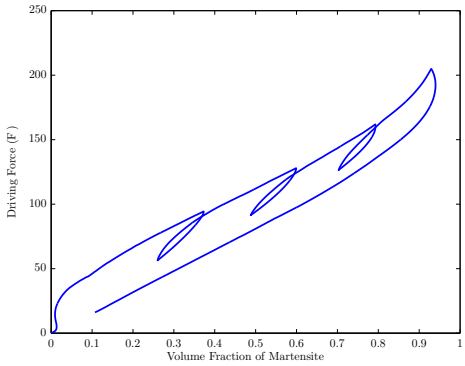

(b) Driving force–volume fraction plot for the stress–strain plot shown

Figure 3.1: Experimental stress–strain data is reduced to driving force–volume fraction plot using thermodynamic principles by using equations 3.15 and 3.13. The flat plateaus of stress – strain plot do not appear on the reduced data plot below.

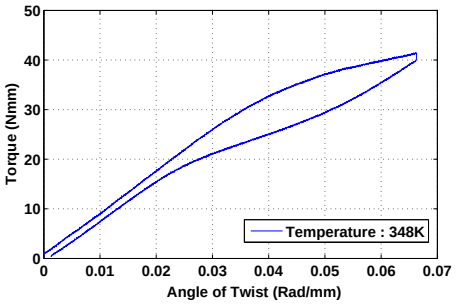

(a) Torque verses angle of twist plot at 348 K.

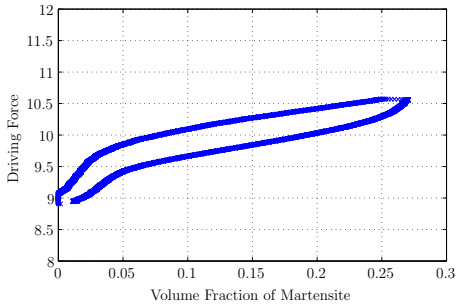

(b) Driving force–volume fraction plot

Figure 3.2: Experimental torque verses angle of twist data is reduced to driving force–volume fraction plot using thermodynamic principles by using equations 3.29 and 3.27.

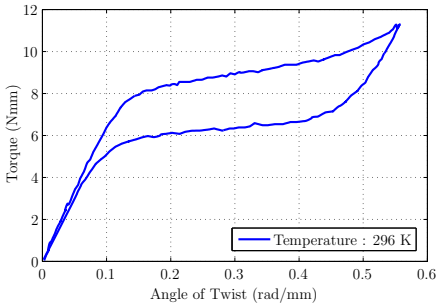

(a) Torque verses angle of twist data at 296 K obtained from [110].

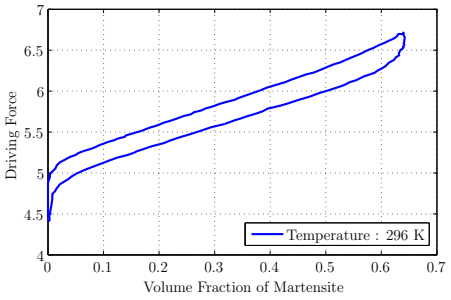

(b) Driving force–volume fraction plot

Figure 3.3: Experimental torque verses angle of twist data is reduced to driving force–volume fraction plot using thermodynamic principles by using using expressions 3.29 and 3.27. Experimental data obtained from [110].

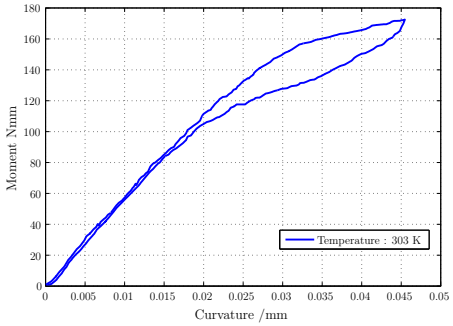

(a) Bending moment verses curvature plot at 303 K [132].

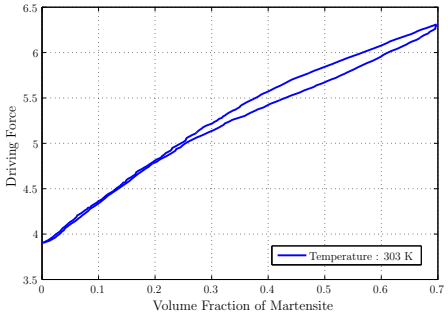

(b) Driving force–volume fraction plot

Figure 3.4: Experimental bending moment verses curvature data is reduced to driving force–volume fraction plot using thermodynamic principles by using equations 3.43 and 3.41. Experimental data obtained for NiTi specimens [132].

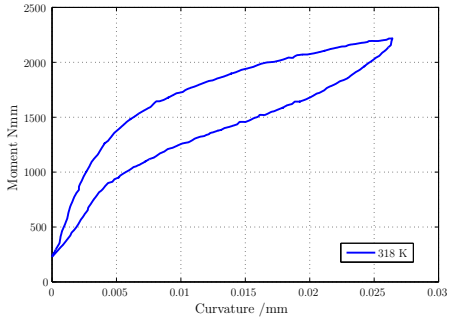

(a) Bending moment verses curvature plot at 318 K [132].

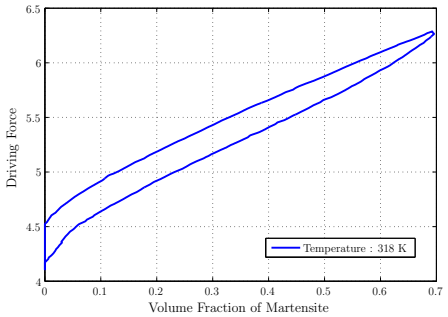

(b) Driving force–volume fraction plot

Figure 3.5: Experimental bending moment verses curvature data is reduced to driving force–volume fraction plot using thermodynamic principles by using equations 3.43 and 3.41. Experimental data obtained for CuZnAl specimen [132].

4. DISCRETE PREISACH MODEL DEVELOPMENT *

The driving force – volume fraction expressions for all loading cases discussed in section 3.4 were a result of employing a thermodynamical framework typically used in modeling phase transforming materials.

Now, if one were to follow a "plasticity like" approach then evolution equations for $\dot{\boldsymbol{\xi}}$ for various transformation cases would be developed by employing different hardening functions. Various mathematical functions like polynomials, exponential or trignometric are developed for capturing different transformation cases (see [85, 86, 89, 99, 108, 109] for examples). However, rather than using a plasticity like approach, in this work, following [64, 76, 90, 104, 157], a discrete Preisach model is employed to capture various driving force – volume fraction relationships ($\boldsymbol{\mathcal{F}}$–$\boldsymbol{\xi}$) developed for different loading conditions. The use of a discrete Preisach approach is quite appropriate with SMAs as phase transformations in SMA are more akin to domain wall switching in magnetism rather than crystallographic slip or flow. The whole SMA structure can be assumed to be a collection of many such domains with each of them discretely switching states depending on the various transformation conditions. Since phase transformations are similar to "domain switching in magnetism", hence use of Preisach models is ideally suitable for capturing hysteresis in phase transformations when compared against the classical plasticity approaches. Such an approach solely focuses on the hysteretic dissipative part of the response

*Reprinted with permission from "Combining Thermodynamic Principles with Preisach models for superelastic SMA Wires" by Doraiswamy, Rao and Srinivasa, *Smart Materials and Structures*, 20, 085032, 2011 [64], Copyright [2014] by IOP.

Reprinted with permission from "A two species thermodynamic Preisach model for the torsional response of SMA wires and springs under superelastic conditions" by Rao and Srinivasa, *International Journal of Solids and Structures*, 50, 887–898, 2013 [90], Copyright [2014] by Elsevier Limited.

and not on the entire reversible thermoelastic response. Such a Preisach approach varies from the conventional Preisach models that are employed to mimic hysteresis where the stress – strain [97] or temperature – strain relationships [95,99] are directly modeled with Preisach elements as discussed in literature review earlier.

Following Doraiswamy et al. [64,104], each hysteron (see figure 4.1) behaves like a non-ideal switch that switches on when the load increases beyond $\boldsymbol{\mathcal{F}}_{forward}$, giving an "output", $\Delta\xi$, and switches off at $\boldsymbol{\mathcal{F}}_{backward}$. With the establishment of the driving force and extent of transformation expressions for various loading cases (equation sets 3.13 – 3.15 , 3.27 – 3.29 , 3.41 – 3.43) , the thresholds for the hysteron are $\boldsymbol{\mathcal{F}}_{forward}$ and $\boldsymbol{\mathcal{F}}_{backward}$ and the output being volume fraction. With the use of large number of hysterons in series that turn on and off at different driving force values, contribution of each hysteron to volume fractions can be obtained. The following algorithm details the process by which the contribution of each hysteron is accumulated to get the total volume fraction of martensite for a given driving force.

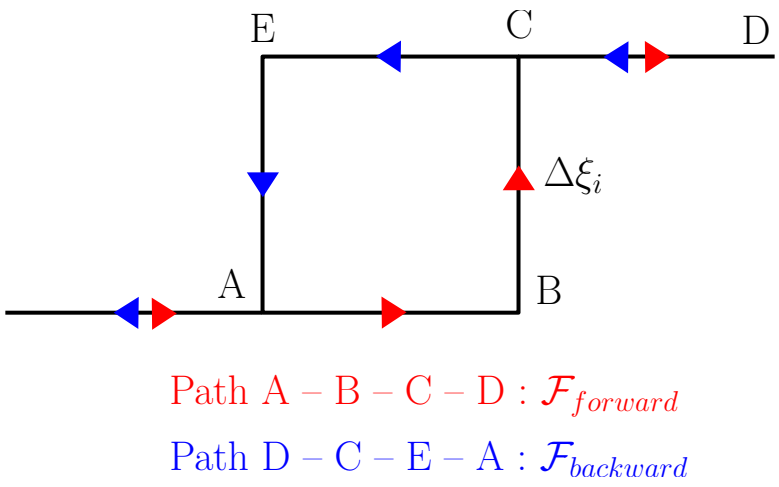

Figure 4.1: Basic hysteretic element or hysteron used in the current discrete Preisach Model. Directions of allowed transformations are represented by the arrows on the hysteron. Each hysteron behaves like a non-ideal switch that switches on when the torque increases beyond $F_{forward}$ with an output of $\Delta\xi_i$ and switches off at $F_{backward}$.

4.1 Preisach Model – Algorithm

The algorithm [1] employed by Doraiswamy et al. [64, 104] for obtaining Preisach parameters is summarized below. The algorithm details the process by which the contribution of each hysteron is accumulated to get the total volume fraction of martensite for a given driving force [64, 104]. The state S_i of the 'i'-th hysteron can take on one of two values: 0 or $\Delta\xi^i$ where $\Delta\xi^i$ is the volume fraction of martensite contributed by the 'i'-th hysteron [64, 104]. At any stage, the extent of transformation, i.e, the volume fraction of martensite evolved, is given by :

$$\xi = \sum_{i=1}^{n} S_i \tag{4.1}$$

The state $S_i^{(n)}$ at time t_n is known and hence the state at t_{n+1} is given by [64, 104] :

$$\text{if } S_i^{(n)} = 0 \;\&\; \boldsymbol{\mathcal{F}}^{(n+1)} > \boldsymbol{\mathcal{F}}^i_{forward} \tag{4.2}$$

$$\text{then } S_i^{(n+1)} = \Delta\xi_i \tag{4.3}$$

$$\text{if } S_i^{(n)} = \Delta\xi_i \;\&\; \boldsymbol{\mathcal{F}}^{(n+1)} < \boldsymbol{\mathcal{F}}^i_{backward} \tag{4.4}$$

$$\text{then } S_i^{(n+1)} = 0 \tag{4.5}$$

$$\text{else } S_i^{(n+1)} = S_i^{(n)} \tag{4.6}$$

At the end of this time step, the $\xi^{(n+1)}$ is then (as in 4.1),

$$\xi^{(n+1)} = \sum_{i=1}^{n} S_i^{(n+1)} \tag{4.7}$$

[1] Special thanks to Dr S. Doraiswamy for his inputs with the Matlab implementation of this Preisach model. More details on this implementation can be found in his Masters thesis [104].

Thus, at the end of the time step t_{n+1}, $\xi^{(n+1)}$ is known, given $\boldsymbol{\mathcal{F}}^{(n+1)}$ and $S_i^{(n)}$ for all the hysterons [64, 104]. For each hysteron, inelastic power δP_{inel}^i is given by,

$$\delta P_{inel}^i = \boldsymbol{\mathcal{F}} \delta\xi \tag{4.8}$$

$$= (\boldsymbol{\mathcal{F}} - \boldsymbol{\mathcal{F}}_{mean})\delta\xi + \mathcal{F}_{mean}\delta\xi \tag{4.9}$$

where $\delta\xi$ is

$$\Delta\xi_i \text{ if } \boldsymbol{\mathcal{F}} > \boldsymbol{\mathcal{F}}_{forward}^i \text{ or}$$
$$-\Delta\xi_i \text{ if } \boldsymbol{\mathcal{F}} < \boldsymbol{\mathcal{F}}_{backward}^i.$$

Therefore, the first term in equation 4.9 is always positive and the second term is positive or negative depending on $\delta\xi$ [64, 104]. The dissipation in a closed cycle of state (i.e sum of δP_{inel}^i over all hysterons) will always be positive as the first term will be positive whereas the sum of second term will be zero [64, 104]. Using the above algorithm, the three parameters $\boldsymbol{\mathcal{F}}_{forward}^i$, $\boldsymbol{\mathcal{F}}_{backward}^i$ and $\Delta\xi^i$ are computed for each hysteron and the driving forces ($\boldsymbol{\mathcal{F}}_{forward}^i$, $\boldsymbol{\mathcal{F}}_{backward}^i$) are assigned in a systematic way as described in figure 4.2 and detailed further in section 4.2 [64, 104]. This greatly simplifies the computation of $\Delta\xi^i$ for each of the hysterons [64, 104].

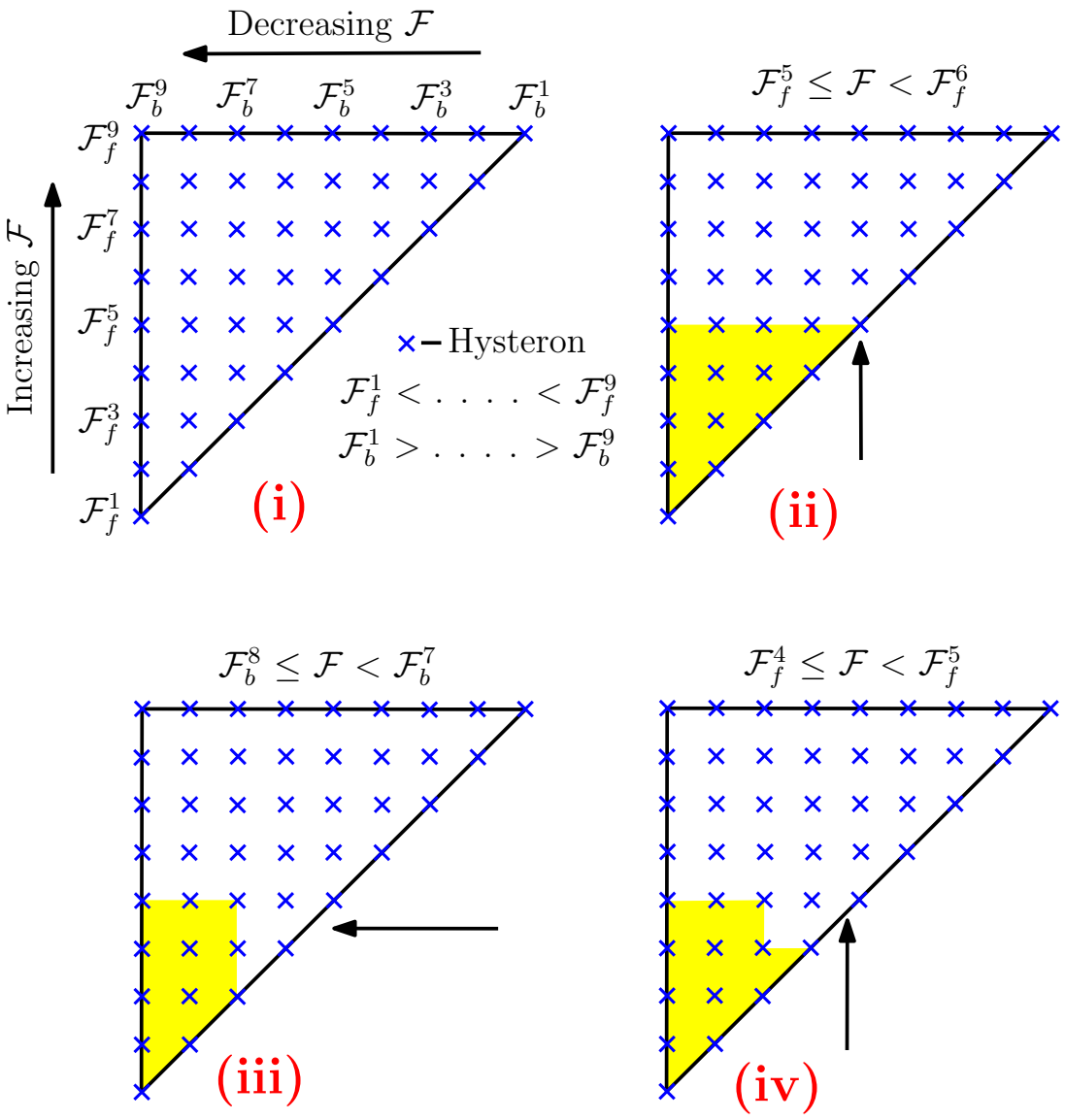

Figure 4.2: (i) : Preisach Triangle - A systematic way for assigning switch on and switch off of the hysterons. The directions of loading (forward) and unloading (backward) sweeps are marked on the figure. Sub figures (ii), (iii), (iv) shows an example for sequencing of states in the Preisach triangle. The colored section shows the triangles that are switched on with the corresponding driving force enforcing the state at the top of the state [64, 104].

4.2 Preisach Triangle

Following Doraiswamy et al. [64, 104], the geometric arrangement of hysterons in a systematic way is with the help of a Preisach triangle as shown in figure 4.2 (i). With known highest and the lowest forward driving force ($\boldsymbol{\mathcal{F}}_{forward}$) values for any loading case, the hysterons with the lowest driving force are positioned at the bottom of the triangle and the highest ones are arranged at the top end of the triangle (refer figure 4.2 (i)). Similarly, for the backward driving force ($\boldsymbol{\mathcal{F}}_{backward}$) hysterons, they are arranged such that they increase from left to right i.e the lowest ones to the left and the highest ones to the right. Further, the hysterons on any particular row have the same $\boldsymbol{\mathcal{F}}_{forward}$ value and similarly the hysterons on any column have the same $\boldsymbol{\mathcal{F}}_{backward}$ value in the triangle (refer figure 4.2 (i)) [64, 104]. Once the $\boldsymbol{\mathcal{F}}_{forward}$ and $\boldsymbol{\mathcal{F}}_{backward}$ values are assigned, the corresponding "output", $\Delta\xi$ for each hysteron needs to be evaluated. By assigning hysterons at specific positions on a Preisach triangle, the three parameters $\boldsymbol{\mathcal{F}}_{forward}$, $\boldsymbol{\mathcal{F}}_{backward}$ and $\Delta\xi$ are automatically estimated. The number of hysterons in a triangle of side n is $\frac{n(n+1)}{2}$ [64, 104].

$\Delta\xi$ for each hysteron can be evaluated by setting up a system of equations where each equation corresponds to the sum of the outputs of all those hysterons that are switched on. By equating these to the volume fraction (ξ) from the data corresponding to the driving force level for each loading case, it is evident that there are $\frac{n(n+1)}{2}$ hysterons, and only $k\left(< \frac{n(n+1)}{2}\right)$ data points (depending on the experimental data). This problem is solved using least squares technique with a non-negativity constraint for the outputs of the hysterons. A **"lsqnonneg"** package from MATLAB® is readily available to compute this [64, 104].

Following Doraiswamy [104], to illustrate this more clearly, an example with a Preisach triangle of side 9 having 45 unknowns is considered as shown in figure 4.2.

If the points are assumed as shown below :

$$\boldsymbol{\mathcal{F}} = \begin{bmatrix} 0 \\ \vdots \\ \boldsymbol{\mathcal{F}_1} \\ \vdots \\ \boldsymbol{\mathcal{F}_2} \\ \vdots \\ \boldsymbol{\mathcal{F}_3} \\ \vdots \end{bmatrix}_{n\times 1} \qquad \xi = \begin{bmatrix} 0 \\ \vdots \\ \xi_1 \\ \vdots \\ \xi_2 \\ \vdots \\ \xi_3 \\ \vdots \end{bmatrix}_{n\times 1}$$

As shown in figure 4.2 (i), the first entry is assigned as 0 and none of the hysterons are switched on. If a state ($\mathcal{F}_f^5 \leq \mathcal{F} < \mathcal{F}_f^6$) shown in figure 4.2 (ii) is assumed and if $\boldsymbol{\mathcal{F}}_1$ be the corresponding driving force, then ξ_1 is the evolved volume fraction a that state [104]. The hysterons contributing to ξ_1 based on the highlighted area in figure 4.2 (ii) and the algorithm described earlier are shown in equation 4.10 [104].

$$\begin{aligned} \Delta\xi_1 = \Delta\xi_{11} + \Delta\xi_{21} + \Delta\xi_{22} + \Delta\xi_{31} + \Delta\xi_{32} + \Delta\xi_{33} + \Delta\xi_{41} + \Delta\xi_{42} \\ + \Delta\xi_{43} + \Delta\xi_{44} + \Delta\xi_{51} + \Delta\xi_{52} + \Delta\xi_{53} + \Delta\xi_{54} + \Delta\xi_{55} \end{aligned} \tag{4.10}$$

where $\Delta\xi_{ij}$ corresponds to the hysteron at the i^{th} row from bottom and j^{th} column from the left [104]. Similarly we can write equations for ξ_2 and ξ_3 corresponding to cases depicted in figures 4.2 (iii) and 4.2 (iv) respectively [104]. In order to evaluate $\Delta\xi$ for each hysteron, a system of equations are setup, where each equation corresponds to sum of all outputs of those hysterons that are switched on [104]. The

entire system can be expressed as follows $Ax = B$.

$$\underbrace{\begin{bmatrix} 0 & & & \cdots & & & 0 \\ & & & \vdots & & & \\ 1 & 1 & \cdots & 1 & 0 & \cdots & 0 \\ & & & \vdots & & & \\ 1 & 1 & & \cdots & & 1 & 1 \end{bmatrix}_{n\times 45}}_{\mathbf{A}} \underbrace{\begin{bmatrix} \Delta\xi_{11} \\ \vdots \\ \Delta\xi_{55} \\ \vdots \\ \Delta\xi_{99} \end{bmatrix}_{45\times 1}}_{\mathbf{x}} = \underbrace{\begin{bmatrix} 0 \\ \vdots \\ \xi_1 \\ \vdots \\ 1 \end{bmatrix}_{n\times 1}}_{\mathbf{B}}$$

It is clear that there are $\frac{n(n+1)}{2}$ hysterons, and only $k\left(< \frac{n(n+1)}{2}\right)$ data points (depending on the experimental data) are available [104]. In this example, the dimensions of A was $k \times 45$ and with $k < \frac{n(n+1)}{2}$, it is not possible to inverse the relationship as $x = A^{-1}b$ [104]. This problem is solved using least squares technique with a non-negativity constraint for the outputs of the hysterons [104].

$$\begin{aligned} &\text{minimize} \parallel Ax - b \parallel \\ \text{subject to} \quad & x_i > 0 \ \forall \ i = 1, \cdots, \frac{n(n+1)}{2} \end{aligned} \tag{4.11}$$

The constrained least square problem is formulated as shown in equation 4.11 with the non-negativity constraint for the outputs of the hysterons computed using **"lsqnonneg"** package from MATLAB® [104]. It must be noted that volume fraction (ξ) data is obtained for each loading case (from figures 3.1b, 3.2b, 3.3b, 3.4b and 3.5b) corresponding to the driving force level [104].

5. MODEL DEVELOPMENT – THREE SPECIES

5.1 Complete Torsion Response

Until now, the discussion was in capturing superelastic responses of SMA components under different loading conditions. In this section, the proposed modeling approach of separating the thermoelastic and dissipative part of the responses is extended to capture both SE and SME effects under torsional loading as depicted in figure 1.6. The goal is to develop a constitutive model for SMA components subjected to torsional loading under both SE and SME effects.

5.1.1 Model Development

The three species considered are austenite and two variants of "detwinned martensite" and the twinned configuration is considered to be of equal proportion of each detwinned martensite variant. It is assumed that M^+ and M^- are the martensite variants under clockwise and anticlockwise twists respectively. Paths (a) – (c) and (a) – (b) in figure 5.1 represents the superelastic effect (austenite – martenite transformations) under clockwise and anticlockwise rotations respectively. Further under no-load conditions, the twinned martensite or self accommodated martensite is an assembly of 50% M^+ & 50% M^-. On application of mechanical loads at low temperatures (below M_f), the twinned martensitic configurations detwin to certain dominant single variant martensite phase either M^+ or M^- depending on the direction of rotation resulting in macroscopic shape change. Paths (d) – (b) or (c) in figure 5.1 represent the twinning response as a part of SME.

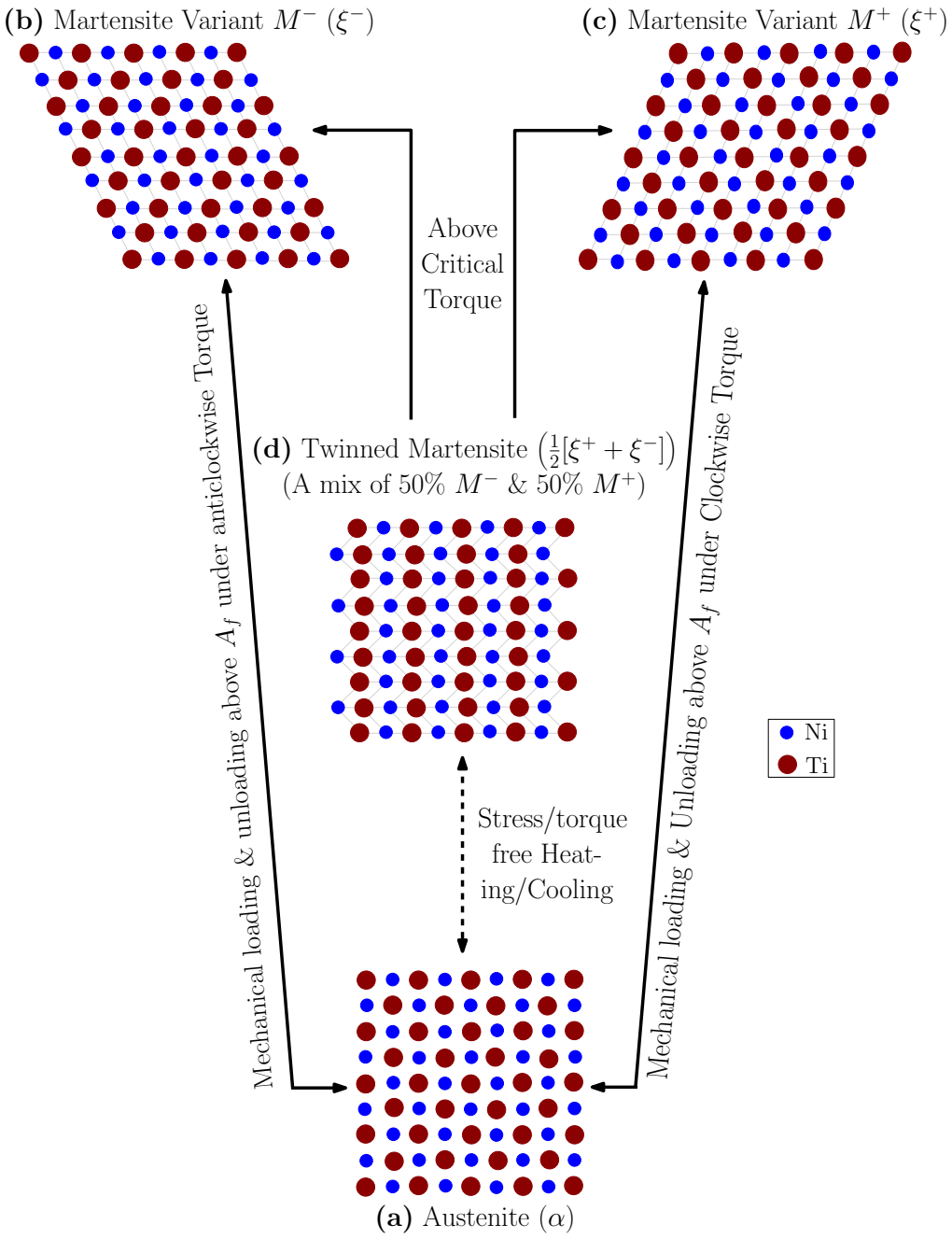

Figure 5.1: **Paths (a) – (c) and (a) – (b)** represent superelastic responses (i.e loading/ unloading operations above A_f) under clockwise and anticlockwise rotations respectively. Below M_f, **Path (d)–(b or c)** represents the twinning response under pure mechanical loading to either M^+ or M^- martensite variants depending on the twisting direction. **Path (a)–(d)** represents stress free thermal cycling between austenite and self accommodated martensite variant. **Path (d)–(b or c) – (a)** represents a typical shape memory cycle depending on the twist direction.

It must be highlighted that the martensite species considered here are related to the crystallographic orientation combinations present at an instant and not to the method by which they were formed. Further, there are also not equivalent to the stress induced and temperature induced components (i.e twinned and detwinned martensite species) as established in earlier literature by Brinson [74]. As shown in figure 5.1, let,

α : Volume fraction of Austenite

ξ^+ : Volume fraction of Detwinned Maternsite M^+

ξ^- : Volume fraction of Detwinned Martensite M^-

Both M^+ and M^- martensite variants are independent of each other and only one variant is dominant in any phase transformation or twinning event as described with various paths highlighted in figure 5.1. The volume fractions of the species and the rate change of volume fractions are connected by equations 5.1a and 5.1b respectively as shown below.

$$\alpha + \xi^+ + \xi^- = 1 \tag{5.1a}$$

$$\dot{\alpha} + \dot{\xi}^+ + \dot{\xi}^- = 0 \tag{5.1b}$$

In this proposed approach, the torque and volume fractions of the three variants are predicted as functions of time given the twist as a function of time. Similar to the two species approach, the model is formulated using a Gibbs potential to capture the measurable macroscopic thermoelastic response and a Preisach model to capture the changes in hysteretic response due to changes in volume fractions.

Consider a SMA component of length (L) subject to a torque (T). Due to this, the SMA component twists and the angle of twist per unit length is ϕ. SMA component here can be a wire, bar or a spring. The SMA component is subjected to a torque T about its axis for wire or bar. In case of spring, the torque can be estimated using the

axial force (P) that the spring is subjected too along its axis as $T = P\left(\frac{D_m}{2}\right)$. With the assumption that the angle of twist across the spring length is uniform, the angle of twist per unit length (ϕ) can be evaluated in terms of the spring displacement (δ) as $\phi = \frac{2\delta}{\pi D_m^2 n}$.

where,

- "D_m" be the mean coil diameter of the spring in mm
- "d" be the SMA wire diameter in mm.
- "C_m" denote the Spring Index.
- "n" be the number of active coils (i.e neglecting the end hooks).

During this process, the SMA undergoes a phase transition and to model this, one can assume the total angle of twist is composed of the thermoelastic part and transformational part as shown in equation 5.2.

$$\phi = \phi_e + \phi_t \implies \dot{\phi} = \dot{\phi}_e + \dot{\phi}_t \tag{5.2}$$

where,

ϕ : Total angle of twist

ϕ_e : Thermoelastic part

ϕ_t : Transformational part

The total transformational rate of twists is assumed to be composed of transformation rate of twists for M^+ and M^- transformations.

$$\dot{\phi}_t = \dot{\phi}_t^+ + \dot{\phi}_t^- \tag{5.3}$$

The transformational rate of twists are assumed to evolve with their respective vol-

ume fractions

$$\begin{aligned} \dot{\phi}_t^+ &= \phi_{max}^+ \dot{\xi^+} \\ \dot{\phi}_t^- &= \phi_{max}^- \dot{\xi^-} \end{aligned} \tag{5.4}$$

where, ϕ_{max}^+ and ϕ_{max}^- are the maximum transformational strains for M^+ and M^- transformations respectively. For NiTi alloys, they can assumed to be of the order of 6% to 8% for both cases. Using equations 5.3 and 5.4 in equation 5.2 results in an equation for total rate of twist as shown below.

$$\dot{\phi} = \dot{\phi}_e + \phi_{max}^+ \dot{\xi^+} + \phi_{max}^- \dot{\xi^-} \tag{5.5}$$

5.1.1.1 The Gibbs Potential - 3 species torsional loading

The Gibbs free energy per unit length is assumed to be a function of the torque (T), operating temperature (θ), the three volume fractions i.e ξ^+, ξ^- and α (introduced in equation 5.1a earlier) as shown in equation 5.6 below:

$$\boldsymbol{\mathcal{G}} := \boldsymbol{\mathcal{G}}(T, \theta, \alpha, \xi^+, \xi^-) \tag{5.6}$$

The internal energy ($\exists$), is related to the Gibbs potential ($\boldsymbol{\mathcal{G}}$), the entropy (η), the temperature (θ) and the angle of twist (ϕ) as shown in equation 5.7 below.

$$\exists = \boldsymbol{\mathcal{G}} + \eta\theta + T\phi \tag{5.7}$$

The rate of mechanical dissipation (Δ), is the net macroscopic inelastic work (χ) in a closed cycle of state which is required to be non-negative by the second law of thermodynamics as shown in expression 5.8b below [65, 158, 159]. 'ρ' is the mass

density (mass per unit volume).

$$\chi = T\dot{\phi} - \rho\dot{\exists} - \rho\dot{\eta}\theta \tag{5.8a}$$

$$\Delta = \oint \chi dt \geq 0 \tag{5.8b}$$

Now using equations 5.6 and 5.7 in equation 5.8a, the inequality is reduced to a form as shown below

$$\begin{aligned} -\left[\phi_e + \rho\frac{\partial \boldsymbol{\mathcal{G}}}{\partial T}\right]\dot{T} - \left[\eta + \rho\frac{\partial \boldsymbol{\mathcal{G}}}{\partial \theta}\right]\dot{\theta} + \left[T\phi^{+}_{max} - \rho\frac{\partial \boldsymbol{\mathcal{G}}}{\partial \xi^{+}}\right]\dot{\xi}^{+} \\ + \left[T\phi^{-}_{max} - \rho\frac{\partial \boldsymbol{\mathcal{G}}}{\partial \xi^{-}}\right]\dot{\xi}^{-} - \left[\rho\frac{\partial \boldsymbol{\mathcal{G}}}{\partial \alpha}\right]\dot{\alpha} = \chi \end{aligned} \tag{5.9}$$

From, the above inequality (equation 5.9), in the absence of phase transformations, the material will behave as a non-dissipative thermoelastic material and that the dissipative response is assumed to be solely due to phase transformations. This then implies that expressions for thermoelastic twist and entropy are obtained as shown below in equations 5.10 and 5.11 respectively.

$$\phi_e = -\rho\frac{\partial \boldsymbol{\mathcal{G}}}{\partial T} \tag{5.10}$$

$$\eta = -\rho\frac{\partial \boldsymbol{\mathcal{G}}}{\partial \theta} \tag{5.11}$$

5.1.1.2 Driving force relations for all transformation cases

Given equations, 5.10 and 5.11, the inequality (equation 5.9), can be further reduced to equation 5.12 as shown below

$$\begin{aligned}\left[T\phi^{+}_{max} - \rho\frac{\partial \boldsymbol{\mathcal{G}}}{\partial \xi^{+}}\right]\dot{\xi}^{+} + \left[T\phi^{-}_{max} - \rho\frac{\partial \boldsymbol{\mathcal{G}}}{\partial \xi^{-}}\right]\dot{\xi}^{-} - \left[\rho\frac{\partial \boldsymbol{\mathcal{G}}}{\partial \alpha}\right]\dot{\alpha} = \chi \\ \Rightarrow \boldsymbol{\mathcal{F}}^{+}\dot{\xi}^{+} + \boldsymbol{\mathcal{F}}^{-}\dot{\xi}^{-} + \boldsymbol{\mathcal{F}}^{\alpha}\dot{\alpha} = \chi\end{aligned} \tag{5.12}$$

where,

Driving Force corresponding to M^{+} is given by $\boldsymbol{\mathcal{F}}^{+} = \left[T\phi^{+}_{max} - \rho\frac{\partial \boldsymbol{\mathcal{G}}}{\partial \xi^{+}}\right]$

Driving Force corresponding to M^{-} is given by $\boldsymbol{\mathcal{F}}^{-} = \left[T\phi^{-}_{max} - \rho\frac{\partial \boldsymbol{\mathcal{G}}}{\partial \xi^{-}}\right]$

Driving Force corresponding to α is given by $\boldsymbol{\mathcal{F}}^{\alpha}$ = - $\left[\rho\frac{\partial \boldsymbol{\mathcal{G}}}{\partial \alpha}\right]$

5.1.1.3 Gibbs potential : assumed form

Until now, the results have been established without specifying a form for the Gibbs potential. A specific form for Gibbs potential per unit reference volume (inspired from [64,65]) motivated by the response characteristics of wire or spring under torsional loading is shown in equation 5.13. It is composed of :

1. a linear combination of the torsional strain energy for all three phases,
2. an interaction term between the martensite variants or between martensite variants and austenite phase,
3. a term related to the heat capacity difference between the martensite variants and austenite phase,
4. a term relating to the heat capacity of the austenite.

$$\boldsymbol{\mathcal{G}} = \overbrace{-\left(\frac{\xi^{+}T^{2}}{2G_{m}J} + \frac{\xi^{-}T^{2}}{2G_{m}J} + \frac{\alpha T^{2}}{2G_{a}J}\right)}^{1} + \overbrace{B\left[\xi^{+}\left(\xi^{+}-1\right) + \xi^{-}(\xi^{-}-1)\right]}^{2} + \overbrace{\left[(1-\xi^{+}) + (1-\xi^{-})\right](a+b\theta)}^{3} - \overbrace{C\theta\,(1-\ln\theta)}^{4} \tag{5.13}$$

where,

- ξ^{+}, ξ^{-} and α are the volume fractions for two martensite variants M^{+}, M^{-} and austenite respectively,
- G_a is the austenitic shear moduli and G_m is the common martensitic shear moduli for the martensite variants ξ^{+} and ξ^{-} respectively
- $J = \frac{\pi d^4}{32}$ is the polar moment of inertia of a solid circular member with diameter "d",
- B, a, b, θ and C are constants.

To reduce model complexity, common parameters G_a, G_m, B, a and b are chosen for both twists. Experimental results suggest that the torsional response of SMA under clockwise and anticlockwise twists are symmetric (for example see figure 4 in [116]). Due to symmetry, the magnitude of these parameters would be the same under both twist directions, however their physical interpretation depends on the twisting direction considered as it was assumed earlier that M^{+} and M^{-} are the martensite variants during clockwise and anticlockwise rotations respectively.

Using equation 5.11, the entropy in terms of Gibbs potential is given by,

$$\eta = -\frac{\partial \boldsymbol{\mathcal{G}}}{\partial \theta} = -C\ln\theta - b\left[(1-\xi^{+}) + (1-\xi^{-})\right] \tag{5.14}$$

In order to find the value of b, which is the "entropy difference between the phases", one can consider several extreme cases :

- For 100% M^+ : $\eta|_{(\xi^+=1,\xi^-=0,\alpha=0)} = -C\ln\theta - b$
- For 100% M^- : $\eta|_{(\xi^+=0,\xi^-=1,\alpha=0)} = -C\ln\theta - b$
- For 100% A : $\eta|_{(\xi^+=0,\xi^-=0,\alpha=1)} = -C\ln\theta - 2b$

From these three cases, according to the model there is a entropy difference between austenite and martensite variants (depending on the twisting direction) because there is a latent heat ($\eta\theta$) difference associated with phase transformations. Since, $M^+ \leftrightarrow M^-$ is a pure twinning event, hence "b" does not play a role for this response. Using the above extreme cases, "b" can be estimated for the following cases.

$$\begin{aligned} b &= [\eta|_{(\xi^+=1,\xi^-=0,\alpha=0)} - \eta|_{(\xi^+=0,\xi^-=0,\alpha=1)}] \text{ or} \\ b &= [\eta|_{(\xi^+=0,\xi^-=1,\alpha=0)} - \eta|_{(\xi^+=0,\xi^-=0,\alpha=1)}] \end{aligned} \tag{5.15}$$

The constant "B" in equation 5.13 represents the interaction energy between the phases or variants i.e interaction energy between austenite and martensite variants (depending on the twisting direction) in case of superelastic effects or between the martensite variants in case of twinning purely due to mechanical loading.

The internal energy in terms of Gibbs potential is given by,

$$\begin{aligned} \exists = \boldsymbol{\mathcal{G}} - \theta\frac{\partial \boldsymbol{\mathcal{G}}}{\partial\theta} = -\left(\frac{\xi^+T^2}{2G_mJ} + \frac{\xi^-T^2}{2G_mJ} + \frac{\alpha T^2}{2G_aJ}\right) + \\ B\left[\xi^+(\xi^+-1) + \xi^-(\xi^--1)\right] + a\left[(1-\xi^+) + (1-\xi^-)\right] - C\theta \end{aligned} \tag{5.16}$$

In order to find the value of a, which is the "internal energy difference between the phases" at 0 K under no load conditions, one can again consider several extreme cases :

- 100% M^+ : $\exists_{M^+} = \exists|_{(\xi^+=1,\xi^-=0,\alpha=0,T=0,\theta=0)} \;=\; a$
- 100 % M^- : $\exists_{M^-} = \exists|_{(\xi^+=0,\xi^-=1,\alpha=0,T=0,\theta=0)} \;=\; a$
- 100% A : $\exists_A = \exists|_{(\xi^+=0,\xi^-=0,\alpha=1,T=0,\theta=0)} \;=\; 2a$

From these three cases, "a" is the internal energy difference between austenite and martensite variants (depending on the twisting direction). Since, $M^+ \leftrightarrow M^-$ is a pure twinning event due to mechanical loading and hence "a" does not play a role during twinning events. Using the above extreme cases, "a" can be estimated for the following cases

$$\left.\begin{array}{rcl} \exists_A &=& 2a \\ \exists_{M^+} &=& a \\ \exists_{M^-} &=& a \end{array}\right\} \Longrightarrow \begin{cases} a = \exists_A - \exists_{M^+} \text{ or} \\ a = \exists_A - \exists_{M^-} \end{cases} \tag{5.17}$$

The method to identify the common model parameters "a", "b" and "B" for both clockwise and anticlockwise rotations would be described later in section 6.5.

5.1.1.4 Establishing driving force expressions for different transformation cases

Using the assumed form of Gibbs potential (equation 5.13), driving force expressions (using equation 5.12) for different species are established below.

The driving force corresponding to M^+ is given by

$$\boldsymbol{\mathcal{F}}^{+} = \left[T\phi^{+}_{max} - \frac{\partial \boldsymbol{\mathcal{G}}}{\partial \xi^{+}}\right] = T\phi^{+}_{max} + \left[\frac{T^2}{2G_m J}\right] - B[2\xi^{+} - 1] + (a + b\theta) \tag{5.18}$$

The driving force corresponding to M^- is given by

$$\boldsymbol{\mathcal{F}}^{-} = \left[T\phi^{-}_{max} - \frac{\partial \boldsymbol{\mathcal{G}}}{\partial \xi^{-}}\right] = T\phi^{-}_{max} + \left[\frac{T^2}{2G_m J}\right] - B[2\xi^{-} - 1] + (a + b\theta) \tag{5.19}$$

The driving force corresponding to α is given by

$$\boldsymbol{\mathcal{F}}^{\alpha} = -\left[\frac{\partial \boldsymbol{\mathcal{G}}}{\partial \alpha}\right] = \left[\frac{T^2}{2G_a J}\right] \tag{5.20}$$

Now the possible transformations among the three species are $A \leftrightarrow M^+$, $A \leftrightarrow M^-$ and $M^- \leftrightarrow M^+$.

Using the above equation sets (5.18, 5.19, 5.20) and equation 5.12, one can obtain driving force relationships for all possible transformation conditions as summarized below

$$k_1 := \mid \boldsymbol{\mathcal{F}}^{+} - \boldsymbol{\mathcal{F}}^{\alpha} \mid = T\phi^{+}_{max} + T^2\left(\frac{1}{2G_m J} - \frac{1}{2G_a J}\right) - B(2\xi^{+} - 1) + b\theta + a \tag{5.21a}$$

$$k_2 := \mid \boldsymbol{\mathcal{F}}^{-} - \boldsymbol{\mathcal{F}}^{\alpha} \mid = T\phi^{-}_{max} + T^2\left(\frac{1}{2G_m J} - \frac{1}{2G_a J}\right) - B(2\xi^{-} - 1) + b\theta + a \tag{5.21b}$$

$$k_3 := \mid \boldsymbol{\mathcal{F}}^{+} - \boldsymbol{\mathcal{F}}^{-} \mid = \boldsymbol{\mathcal{F}}^{M^+ \rightarrow M^-} = T\left[\phi^{+}_{max} - \phi^{-}_{max}\right] - 2B\left[\xi^{+} - \xi^{-}\right] \tag{5.21c}$$

In the above relations, "k_1" and "k_2" represent the driving force expressions for superelastic phase transformations under clockwise and anticlockwise rotations respectively. "k_3" corresponds to twinning events resulting in "self accommodated martensite" variants switching to preferred single variant martenite variants M^+ and M^-. In short, k_1, k_2 and k_3 corresponds to $A \leftrightarrow M^+$, $A \leftrightarrow M^-$ and $M^+ \leftrightarrow M^-$ cases respectively.

From, the above general driving force relationships (equations 5.21a, 5.21b, 5.21c), specific driving force relationships for twinning responses under clockwise and anticlockwise rotations are developed by considering the following important cases below:

- Notice that the driving force for the twinning response (k_3) is temperature independent and depends upon only on the the applied torque and the difference

in the volume fraction of the M^+ and M^- martensite variants. So, if $T = 0$ and ξ^+ and ξ^- are equal then there will be no driving force for twinning as $k_3 = 0$. Also, under stress free conditions, using equation set 5.22 below, $k_1 = k_2$ as $\xi^+ = \xi^-$. Since, the thresholds are the same (i.e $k_1 = k_2$), only an austenitic phase transformation purely due to temperature changes (in absence of any external loads) is possible as there is no driving force for twinning (as $k_3 = 0$). Also, when $T = 0$, according to equation 5.5, $\dot{\phi}_e = 0$ which suggests $\dot{\phi} = 0$ as $\xi^+ = \xi^-$.

$$k_1 =\mid \boldsymbol{\mathcal{F}}^+ - \boldsymbol{\mathcal{F}}^\alpha \mid = -B(2\xi^+ - 1) + b\theta + a \tag{5.22a}$$

$$k_2 =\mid \boldsymbol{\mathcal{F}}^- - \boldsymbol{\mathcal{F}}^\alpha \mid = -B(2\xi^- - 1) + b\theta + a \tag{5.22b}$$

$$k_3 =\mid \boldsymbol{\mathcal{F}}^+ - \boldsymbol{\mathcal{F}}^- \mid = -2B\left[\xi^+ - \xi^-\right] \tag{5.22c}$$

Further, in order to satisfy the volume fraction conservation relationship (see equation 5.1a), if $\xi^+ = \xi^-$ and $k_1 = k_2$, it implies that α and one martensite configuration are present. Under stress free conditions ($T = 0$), this suggests that the possible transformations purely due to temperature changes are between a 50% M^+ & 50% M^- case and austenite. This further emphasizes our earlier assumption of twinned martensite (also referred as self accommodated martensite) configuration being 50% M^+ & 50% M^- as illustrated in figure 5.1.

- With $T \neq 0$ and $\alpha = 0 \rightarrow \xi^+ + \xi^- = 1$ then,

$$k_1 =\mid \boldsymbol{\mathcal{F}}^+ \mid = T\phi^+_{max} + T^2\left(\frac{1}{2G_m J}\right) - B(2\xi^+ - 1) + b\theta + a \tag{5.23a}$$

$$k_2 =\mid \boldsymbol{\mathcal{F}}^{-} \mid = T\phi_{max}^{-} + T^2\left(\frac{1}{2G_mJ}\right) - B(2\xi^{-} - 1) + b\theta + a \tag{5.23b}$$

$$k_3 =\mid \boldsymbol{\mathcal{F}}^{+} - \boldsymbol{\mathcal{F}}^{-} \mid = \boldsymbol{\mathcal{F}}^{M^{+}\rightarrow M^{-}} = T\left[\phi_{max}^{+} - \phi_{max}^{-}\right] - 2B\left[\xi^{+} - \xi^{-}\right] \tag{5.23c}$$

In the above equation sets 5.23c, k_3 represents the driving forces to capture the complete twinning response in both clockwise and anticlockwise rotations. However, since the clockwise and anticlockwise torsion experiments are independent of each other, hence the two martensite species M^{+} and M^{-} are also independent of each other. This suggests that k_3 from equation sets 5.23c can be split to capture individual twinning effects for clockwise (k_3^{+}) and anticlockwise (k_3^{-}) directions respectively as shown in equations 5.24a and 5.24b below. The split twinning events will be between a 50% M^{+} & 50% M^{-} martensite configuration under stress free conditions to either 100% M^{+} or 100% M^{-} depending on the direction of the twist.

$$k_3^{+} = \boldsymbol{\mathcal{F}}^{+} = T\phi_{max}^{+} - 2B\xi^{+} \tag{5.24a}$$

$$k_3^{-} = \boldsymbol{\mathcal{F}}^{-} = T\phi_{max}^{-} - 2B\xi^{-} \tag{5.24b}$$

It must be highlighted that the driving force expressions corresponding to the twinning responses under both rotations are independent of temperature (θ), constants "a" and "b" as it is a pure mechanical response. On the other hand, the driving force expressions corresponding to the superelastic transformations ($A \leftrightarrow M^{+}$ and $A \leftrightarrow M^{-}$ cases) depends upon model constants "a","b" and"B" along with operating temperature "θ" as shown in equations 5.21a 5.21b for clockwise and anticlockwise rotations respectively. In order to capture the shape memory effects under clockwise and anticlockwise twists, the driving force expressions would be a combination of

driving force expressions for the twinning responses and the superelastic responses (with $T = 0$) depending on the twisting direction (i.e equation 5.24a and 5.21a for clockwise twist. Similarly, equation 5.24b and 5.21b for anticlockwise twist.)

5.1.1.5 Establishing volume fraction expressions for different transformation cases

Using the assumed form of Gibbs potential expression 5.13 and using equation 5.10, an expression for elastic part of twist is obtained as shown below

$$\phi_e = -\frac{\partial \boldsymbol{\mathcal{G}}}{\partial T} = \frac{\xi^+ T}{G_m J} + \frac{\xi^- T}{G_m J} + \frac{\alpha T}{G_a J} \tag{5.25}$$

Using the volume fraction conservation relationship (equation 5.1a), the above equation 5.25 is further reduced to special two species cases as shown below.

$$\phi_e|_{\xi^-=0} = \frac{\xi^+ T}{G_m J} + \frac{(1-\xi^+)\, T}{G_a J} \tag{5.26a}$$

$$\phi_e|_{\xi^+=0} = \frac{\xi^- T}{G_m J} + \frac{(1-\xi^-)\, T}{G_a J} \tag{5.26b}$$

$$\phi_e|_{\alpha=0} = \begin{cases} \dfrac{\xi^+ T}{G_m J} + \dfrac{(1-\xi^+)\, T}{G_m J} & \text{or} \\ \dfrac{\xi^- T}{G_m J} + \dfrac{(1-\xi^-)\, T}{G_m J} & \end{cases} \tag{5.26c}$$

As the martensitic species M^+ and M^- are independent of each other, hence the total twist can be separated for clockwise and anticlockwise rotations respectively as shown equation 5.27 below.

$$\phi = \phi^+ + \phi^- \;\Rightarrow\; \dot{\phi} = \dot{\phi^+} + \dot{\phi^-} \tag{5.27}$$

Now using the above equation 5.27 along with the relationship for total rate of twist (equation 5.5)and equation sets (5.26a, 5.26b and 5.26c), simplified equations for

specific two species scenarios can be obtained as shown below.

$$\text{If } \xi^- = 0, \quad \dot{\phi^+} - \dot{\phi}_e|_{\xi^-=0} = \phi^+_{max}\dot{\xi^+} \implies \phi^+ - \phi_e|_{\xi^-=0} = \phi^+_{max}\xi^+ \tag{5.28a}$$

$$\text{If } \xi^+ = 0, \quad \dot{\phi^-} - \dot{\phi}_e|_{\xi^+=0} = \phi^-_{max}\dot{\xi^-} \implies \phi^- - \phi_e|_{\xi^+=0} = \phi^-_{max}\xi^- \tag{5.28b}$$

$$\text{If } \alpha = 0, \quad \dot{\phi} - \dot{\phi_e}|_{\alpha=0} = \phi^+_{max}\dot{\xi^+} + \phi^-_{max}\dot{\xi^-} \tag{5.28c}$$

Again, in equation 5.28c, since M^+ and M^- martensite variants are independent, hence the above equation 5.28c can be split to capture individual twinning effects under clockwise and anticlockwise twisting directions as shown in equation set 5.29a below.

$$\begin{aligned} \text{For clockwise twinning} &\begin{cases} \dot{\phi^+} - \dot{\phi}_e|_{\alpha=0} = \phi^+_{max}\dot{\xi^+} \\ \text{Thus, } \phi^+ - \phi_e|_{\alpha=0} = \phi^+_{max}\xi^+ \end{cases} \\ \text{For anticlockwise twinning} &\begin{cases} \dot{\phi^-} - \dot{\phi}_e|_{\alpha=0} = \phi^-_{max}\dot{\xi^-} \\ \text{Thus, } \phi^- - \phi_e|_{\alpha=0} = \phi^-_{max}\xi^- \end{cases} \end{aligned} \tag{5.29a}$$

The variables torque (T), angle of twist (ϕ) and temperature (θ) are nondimensionalized before proceeding further with the derivations. The nondimensionalized variables are: $T^* = T/T_{max}$, $\phi^{+*} = \phi^+/\phi^+_{max}$ $\phi^{-*} = \phi^-/\phi^-_{max}$, $\theta^* = \theta/\theta_{max}$ for each loading case. Henceforth, for better readability, the $*$'s will be omitted from the nondimensionalized variables.

Equations 5.26a and 5.28a represents a superelastic transformation case $A \rightarrow M^+$ for clockwise twist and the volume fraction of ξ^+ can be determined by equation below

$$\xi^+ = \frac{\phi^+ - \dfrac{T}{G_a J}}{\dfrac{T}{G_m J} - \dfrac{T}{G_a J} + 1} \tag{5.30}$$

Similarly, equations 5.26b and 5.28b represents a superelastic transformation case $A \rightarrow M^-$ for anticlockwise twist and the volume fraction of ξ^- can be determined by equation below

$$\xi^- = \frac{\phi^- - \frac{T}{G_a J}}{\frac{T}{G_m J} - \frac{T}{G_a J} + 1} \tag{5.31}$$

From equations 5.26c and 5.29a, two volume fraction relations for M^+ and M^- representing the martensite twinning for clockwise and anticlockwise rotations respectively can be obtained as shown below. The twinning in both cases is from an assembly of 50% M^+ & 50% M^- martensite species under no-load conditions to M^+ or M^- depending on the twisting direction as discussed with equation 5.22 earlier.

$$\xi^+ = \left(\phi^+ - \frac{T}{G_m J}\right) \tag{5.32a}$$

$$\xi^- = \left(\phi^- - \frac{T}{G_m J}\right) \tag{5.32b}$$

Table 5.1 summarizes the driving force – volume fraction relationship for all possible transformation cases.

Using clockwise and anticlockwise torsion–twist experimental data under both superelastic and twinning conditions, each experimental plot is transformed to their corresponding driving force – volume fraction plots using the relationships summarized in table 5.1. Experimental results for one particular twist and temperature case are chosen as reference for simulation of driving force and volume fraction relationships. Figure 5.2 shows the reduction of the experimental data for twinning response of SMA springs to its corresponding driving force – volume fraction plot. Similarly, figure 5.3 shows the reduction of the experimental data for superelastic responses of SMA wires under clockwise and anticlockwise twists to its corresponding driving

Table 5.1: Summary of driving force–volume fraction relationships for all transformation cases (equation sets 5.21a – 5.30 ; 5.21b – 5.31 ; 5.24a – 5.32a ; 5.24b – 5.32b).

Transformation case	**Driving force & volume fraction expressions**
Superelastic ($A \leftrightarrow M^+$)	$\boldsymbol{\mathcal{F}^{A\leftrightarrow M^+}} = T\phi^+_{max} + T^2\left(\frac{1}{2G_mJ} - \frac{1}{2G_aJ}\right) - B(2\xi^+ - 1) + b\theta + a$
(Clockwise twist)	$\boldsymbol{\xi^+} = \dfrac{\phi^+ - \dfrac{T}{G_aJ}}{\dfrac{T}{G_mJ} - \dfrac{T}{G_aJ} + 1}$
Superelastic ($A \leftrightarrow M^-$)	$\boldsymbol{\mathcal{F}^{A\leftrightarrow M^-}} = T\phi^-_{max} + T^2\left(\frac{1}{2G_mJ} - \frac{1}{2G_aJ}\right) - B(2\xi^- - 1) + b\theta + a$
(Anticlockwise twist)	$\boldsymbol{\xi^-} = \dfrac{\phi^- - \dfrac{T}{G_aJ}}{\dfrac{T}{G_mJ} - \dfrac{T}{G_aJ} + 1}$
Twinning response	$\boldsymbol{\mathcal{F}^+} = T\phi^+_{max} - 2B\xi^+$
(clockwise twist)	$\boldsymbol{\xi^+} = \left(\phi^+ - \dfrac{T}{G_mJ}\right)$
Twinning response	$\boldsymbol{\mathcal{F}^-} = T\phi^-_{max} - 2B\xi^-$
(Anticlockwise twist)	$\boldsymbol{\xi^-} = \left(\phi^- - \dfrac{T}{G_mJ}\right)$

force – volume fraction plot. The driving force – volume fraction plot shown in figure 5.3 is a combination of two driving force – volume fraction plots using equations sets 5.21a – 5.30 and 5.21b – 5.31 for clockwise and anticlockwise rotations respectively. The torque – twist experimental data were non-dimensionlized for establishment of driving force–volume fraction relationships under both rotations with the appropriate sign conventions (clockwise – positive ; anticlockwise – negative).

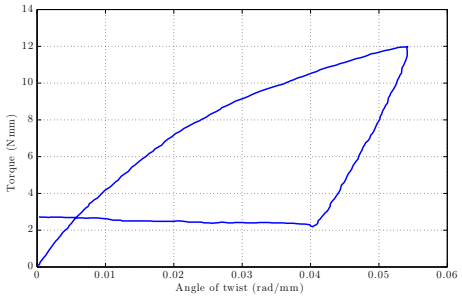

(a) Torque v/s Angle of twist plot at 295 K. Clockwise twist was assumed

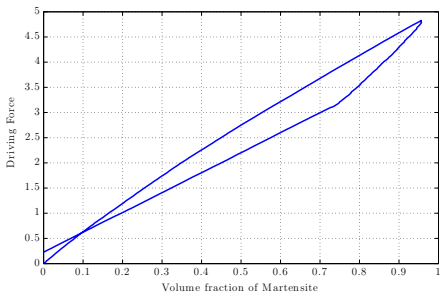

(b) Driving Force–Volume Fraction plot

Figure 5.2: Experimental torque v/s angle of twist data is reduced to driving force–volume fraction plot using thermodynamic principles by using equations developed for twinning response summarized in table 5.1. Clockwise twist was assumed. Experimental data obtained from [113].

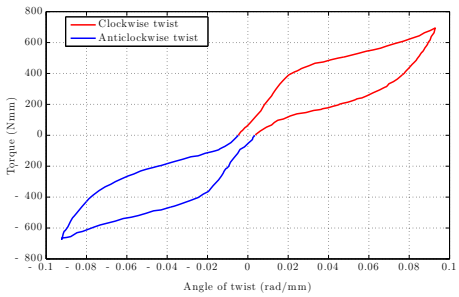

(a) Torque v/s angle of twist data at 297 K for 450^o twist

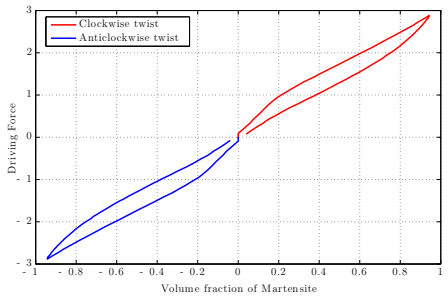

(b) Driving Force–Volume Fraction plot

Figure 5.3: Experimental torque v/s angle of twist data is reduced to driving force–volume fraction plot using thermodynamic principles by using equations developed for superelastic responses summarized in table 5.1. Experimental data obtained from [116].

6. PROTOCOL : MODEL SIMULATIONS AND PREDICTIONS *

Using the two species and three species model formulations discussed in sections 3 and 5, driving force–volume fraction relationships for different loading conditions were developed. The algorithm described in section 4.1 of section 4 was then used to estimate the volume fraction contribution for a given driving force $\mathcal{F}$ under different loading conditions.

The next step in the model prediction is to predict the original experimental data from the $\boldsymbol{\mathcal{F}}$ – $\boldsymbol{\xi}$ plot predicted using the algorithm described in section 4.1. If there are "n" hysterons each contributing ξ_i to the total volume fraction as setup by the Preisach algorithm, then

$$\xi = \sum_{i=0}^{n} \xi_i \tag{6.1}$$

where $\xi_i \ \forall \ \ i = 1, 2, \cdots, n$ represents the volume fraction contribution of those hysterons switched on at this time step.

The following sections below discuss the simulation procedure under different loading conditions and making predictions at different temperatures

6.1 Tension Loading Case - Two Species

6.1.1 Load Controlled Test Protocol

If at time instant t_i, $\sigma(i)$, $\varepsilon(i)$ and $\theta(i)$ are assumed to be known then by using Equation 3.15, $\xi_{ten}(i)$ can be evaluated. In order to compute these variables at time

*Reprinted with permission from "Combining Thermodynamic Principles with Preisach models for superelastic SMA Wires" by Doraiswamy, Rao and Srinivasa, *Smart Materials and Structures*, 20, 085032, 2011 [64], Copyright [2014] by IOP.

Reprinted with permission from "A two species thermodynamic Preisach model for the torsional response of SMA wires and springs under superelastic conditions" by Rao and Srinivasa, *International Journal of Solids and Structures*, 50, 887–898, 2013 [90], Copyright [2014] by Elsevier Limited.

t_{i+1}, it is assumed that $\sigma(i+1)$ is known. $\boldsymbol{\mathcal{F}_{ten}(i+1)}$ can now be computed from equation 3.13 for a known $\xi_{ten}(i)$. Once $\boldsymbol{\mathcal{F}_{ten}(i+1)}$ is evaluated, the Preisach model is used to predict $\xi_{ten}(i+1)$. Now using $\xi_{ten}(i+1)$ and $\sigma(i+1)$ being known, using Equation 3.7, $\varepsilon_e(i+1)$ is established and subsequently $\varepsilon(i+1)$ from equation 3.11. Summarizing the above, the following equations 6.2a and 6.2b below need to be evaluated.

$$\boldsymbol{\mathcal{F}_{ten}^{(n+1)}} = \sigma^{(n+1)} + \left(\sigma^{(n+1)}\right)^2 \left(\frac{1}{2E_M I} - \frac{1}{2E_A I}\right) - B(2\xi_{ten}^{(n)} - 1) + b\theta + a \tag{6.2a}$$

$$\varepsilon^{(n+1)} = \frac{\left(\xi_{ten}^{(n)}\right)\sigma^{n+1}}{E_M I} + \frac{\left(1 - \xi_{ten}^{(n)}\right)\sigma^{n+1}}{E_A I} + \xi_{ten}^{n} \tag{6.2b}$$

6.1.2 Displacement Controlled Test Protocol

If at time instant t_i, $\sigma(i)$, $\varepsilon(i)$ and $\theta(i)$ are known and then $\xi_{ten}(i)$ can be evaluated by using equation 3.15. Here $\varepsilon(i+1)$ is known and $\sigma(i+1)$ needs to be computed. $\boldsymbol{\mathcal{F}_{ten}(i+1)}$ can now be computed using equation 3.13. Now equation 3.15 is used to express σ in terms of ε and ξ_{ten}. The Preisach model is used again to find $\xi_{ten}(i+1)$ from $\boldsymbol{\mathcal{F}_{ten}(i+1)}$. Once $\xi_{ten}(i+1)$ and $\varepsilon(i+1)$ are evaluated, using equation 3.15, $\sigma(i+1)$ is evaluated. Summarizing the above, the following equations below 6.3a and 6.3b need to be evaluated

$$\sigma^{(n+1)} = \frac{\varepsilon^{(n+1)} - \xi_{ten}^{(n)}}{\xi_{ten}^{(n)}\left(\frac{1}{E_M I} - \frac{1}{E_A I}\right) + \frac{1}{E_A I}} \tag{6.3a}$$

$$\boldsymbol{\mathcal{F}_{ten}^{(n+1)}} = \sigma^{(n+1)} + (\sigma^{(n+1)})^2 \left(\frac{1}{2E_M I} - \frac{1}{2E_A I}\right) - B(2\xi_{ten}^{(n)} - 1) + b\theta + a \tag{6.3b}$$

6.2 Torsion Loading Case - Two Species

6.2.1 Load (Torque) Controlled Protocol

If at a time t_i, $T(i)$, $\phi(i)$ and $\theta(i)$ are assumed to be known, then by using Equation 3.29, $\xi_{tor}(i)$ can be evaluated. In order to compute these variables at time t_{i+1}, it is assumed that $T(i+1)$ is known. $\boldsymbol{\mathcal{F}_{tor}(i+1)}$ can now be computed from equation 3.27 for a known $\xi_{tor}(i)$. Once $\boldsymbol{\mathcal{F}_{tor}(i+1)}$ is evaluated, the Preisach model using the algorithm highlighted in Section 4.1 is used to predict $\xi_{tor}(i+1)$. Now being $\xi_{tor}(i+1)$ and $T(i+1)$ being known, using equation 3.21, $\phi_e(i+1)$is established and subsequently $\phi(i+1)$ from 3.25. Summarizing the above, one needs to evaluate equations 6.4a and 6.4b below.

$$T^{(n+1)} = \frac{\phi^{(n+1)} - \xi_{tor}^{(n)}}{\xi_{tor}^{(n)}\left(\frac{1}{G_M J} - \frac{1}{G_A J}\right) + \frac{1}{G_A J}} \tag{6.4a}$$

$$\boldsymbol{\mathcal{F}_{tor}^{(n+1)}} = T^{(n+1)} + (T^{(n+1)})^2\left(\frac{1}{2G_M J} - \frac{1}{2G_A J}\right) - B(2\xi_{tor}^{(n)} - 1) + b\theta + a \tag{6.4b}$$

6.2.2 Displacement (Angle of Twist) Controlled Protocol

If at time t_i, $T(i)$, $\phi(i)$ and $\theta(i)$ are known then by using Equation 3.29 $\xi_{tor}(i)$ can be evaluated. Here $\phi(i+1)$ is known and $T(i+1)$ needs to be computed. $\boldsymbol{\mathcal{F}_{tor}(i+1)}$ is computed using 3.27. Now the Equation 3.29 is used to express T in terms of ϕ and ξ_{tor}. The Preisach model is used again to find $\xi_{tor}(i+1)$ from $\boldsymbol{\mathcal{F}_{tor}(i+1)}$. Once $\xi_{tor}(i+1)$ and $\phi(i+1)$ are evaluated, using Equation 3.29, $T(i+1)$ is evaluated. Summarizing the above, one needs to evaluate equations 6.5a and 6.5b below.

$$T^{(n+1)} = \frac{\phi^{(n+1)} - \xi_{tor}^{(n)}}{\xi_{tor}^{(n)}\left(\frac{1}{G_M I} - \frac{1}{G_A I}\right) + \frac{1}{G_A I}} \tag{6.5a}$$

$$\boldsymbol{\mathcal{F}}_{\boldsymbol{tor}}^{\boldsymbol{(n+1)}} = T^{(n+1)} + (T^{(n+1)})^2 \left(\frac{1}{2G_M I} - \frac{1}{2G_A I}\right) - B(2\xi_{tor}^{(n)} - 1) + b\theta + a \quad (6.5b)$$

6.3 Pure Bending Case - Two Species

6.3.1 Load (Moment) Controlled Protocol

If at time t_i, $M(i)$, $\kappa(i)$ and $\theta(i)$ are assumed to be known then by using equation 3.43, $\xi_{bend}(i)$ can be evaluated. In order to compute these variables at time t_{i+1}, it is assumed that $M(i+1)$ is known. $\boldsymbol{\mathcal{F}_{bend}(i+1)}$ can now be computed from equation 3.41 for a known $\xi_{bend}(i)$. Once $\boldsymbol{\mathcal{F}_{bend}(i+1)}$ is evaluated, the Preisach model is used to predict $\xi(i+1)$. With $\xi_{bend}(i+1)$ and $M(i+1)$ now known, using 3.35 to find $\kappa_e(i+1)$ and hence $\kappa(i+1)$ from equation 3.39. Summarizing the above, one needs to evaluate equations 6.6a and 6.6b below

$$\boldsymbol{\mathcal{F}}_{\boldsymbol{bend}}^{\boldsymbol{(n+1)}} = M^{(n+1)} + (M^{(n+1)})^2 \left(\frac{1}{2E_M I} - \frac{1}{2E_A I}\right) - B(2\xi_{bend}^{(n)} - 1) + b\theta + a \quad (6.6a)$$

$$\kappa^{(n+1)} = \frac{\xi_{bend}^{(n)} M^{n+1}}{E_M I} + \frac{\left(1 - \xi_{bend}^{(n)}\right) M^{n+1}}{E_A I} + \xi_{bend}^{n} \quad (6.6b)$$

6.3.2 Displacement (Curvature) Controlled Protocol

If at time t_i, $M(i)$, $\kappa(i)$ and $\theta(i)$ are known then by using equation 3.43 $\xi_{bend}(i)$ can be evaluated. Here $\kappa(i+1)$ is known and $M(i+1)$ needs to be computed. $\boldsymbol{\mathcal{F}_{bend}(i+1)}$ is computed using 3.41. Now the equation 3.43 is used to express M in terms of κ and ξ_{bend}. The Preisach model is used again to find $\xi_{bend}(i+1)$ from $\boldsymbol{\mathcal{F}_{bend}(i+1)}$. Once $\xi_{bend}(i+1)$ and $\kappa(i+1)$ are evaluated, using equation 3.43, $M(i+1)$ is evaluated. Summarizing the above, one needs to evaluate equations 6.7a and 6.7b below.

$$M^{(n+1)} = \frac{\kappa^{(n+1)} - \xi_{bend}^{(n)}}{\xi_{bend}^{(n)} \left(\frac{1}{E_M I} - \frac{1}{E_A I}\right) + \frac{1}{E_A I}} \quad (6.7a)$$

$$\boldsymbol{\mathcal{F}}_{\boldsymbol{bend}}^{(\boldsymbol{n+1})} = M^{(n+1)} + (M^{(n+1)})^2 \left(\frac{1}{2E_M I} - \frac{1}{2E_A I}\right) - B(2\xi_{bend}^{(n)} - 1) + b\theta + a \quad (6.7b)$$

6.4 Three Species Torsion - Model Simulation

The procedure illustrated in section 6.4.1 below is common for clockwise and anticlockwise superelastic responses as the responses are symmetric. Similarly, a common procedure for clockwise and anticlockwise twinning responses is highlighted in section 6.4.2 below. For convenience, a common volume fraction ξ is employed for discussion in this section. Term ξ here can be ξ^+ or ξ^- depending on the twisting direction. The simulation protocol is same under both twist directions once the corresponding equations are appropriately selected for each case from table 5.1.

6.4.1 Superelastic Responses

6.4.1.1 Load (Torque) Controlled Protocol

If at time t_i, T(i), $\phi(i)$ and $\theta(i)$ are assumed to be known then by using equations 5.30 or 5.31, $\xi(i)$ can be evaluated. In order to compute these variables at time t_{i+1}, it is assumed that T(i+1) is known. $\mathcal{F}(i+1)$ can now be computed from equations 5.21a or 5.21b for a known $\xi(i)$. Once $\mathcal{F}(i+1)$ is evaluated, the Preisach model is used to predict $\xi(i+1)$. With $\xi(i+1)$ and T(i+1) now known, using equations 5.26a or 5.26b, one can find $\phi_e(i+1)$ and hence $\phi(i+1)$ from equations 5.28a or 5.28b.

6.4.1.2 Displacement (angle of twist) controlled protocol

If at time t_i, T(i), $\phi(i)$ and $\theta(i)$ are known then by using equation 5.30 or 5.31 $\xi(i)$ can be evaluated. Here, $\phi(i+1)$ is known and T(i+1) needs to be computed. $\mathcal{F}(i+1)$ is computed using equations 5.21a or 5.21b. Now the equations 5.30 or 5.31 are used to express T in terms of ϕ and ξ. The Preisach model is used again to find $\xi(i+1)$ from $\mathcal{F}(i+1)$. Once $\xi(i+1)$ and $\phi(i+1)$ are evaluated, using equations 5.30 or 5.31, T(i+1) is evaluated.

6.4.2 Twinning Responses

6.4.2.1 Load (Torque) Controlled Protocol

If at time t_i, T(i) and $\phi(i)$ are assumed to be known then by using equations 5.32a or 5.32b, $\xi(i)$ can be evaluated. In order to compute these variables at time t_{i+1}, it is assumed that T(i+1) is known. $\mathcal{F}(i+1)$ can now be computed from equations 5.24a or 5.24b for a known $\xi(i)$. Once $\mathcal{F}(i+1)$ is evaluated, the Preisach model is used to predict $\xi(i+1)$. With $\xi(i+1)$ and T(i+1) now known, using equation set 5.26c, one can find $\phi_e(i+1)$ and hence $\phi(i+1)$ from equation 5.29a depending on the twist direction.

6.4.2.2 Displacement (angle of twist) controlled protocol

If at time t_i, T(i) and $\phi(i)$ are known then by using equation 5.32a or 5.32b $\xi(i)$ can be evaluated. Here $\phi(i+1)$ is known and T(i+1) needs to be computed. $\mathcal{F}(i+1)$ is computed using equations 5.24a or 5.24b. Now the equations 5.32a or 5.32b is used to express T in terms of ϕ and ξ. The Preisach model is used again to find $\xi(i+1)$ from $\mathcal{F}(i+1)$. Once $\xi(i+1)$ and $\phi(i+1)$ are evaluated, using equations 5.32a or 5.32b, T(i+1) is evaluated.

6.5 Parameter Identification

By combining thermodynamics principles and Preisach modeling techniques, the model parameters can be separated into sets of parameters arising from the thermodynamical framework and those from the Preisach models related to hysterons positioning. Section 4.1 discussed the details of obtaining parameters $\boldsymbol{\mathcal{F}}_{forward}$, $\boldsymbol{\mathcal{F}}_{backward}$ and $\Delta\xi$ pertaining to Preisach triangle as represented in figures 4.1 or 4.2 by automatically assigning the hysterons at specific positions on the triangle. The method of obtaining parameters arising from the assumed form of Gibbs potential for different

loading cases from thermodynamical framework will be discussed below.

6.5.1 Tension Loading Case - Two Species

The parameters under consideration E_a, E_m, B, a and b and their corresponding values used for simulation and model predictions are reported in table 6.1. Experimental results of uniaxial tension tests conducted on NiTi wire at temperatures 348, 373 and 398K as illustrated in figure 2.3 are used as reference.

- "E_a" and "E_m" being the austenitic and martensitic elastic moduli can be estimated directly form the tension experimental data by finding the initial slopes of the superelastic response at one particular temperature.

- "B" is the coefficient of the interfacial energy term related to the area of hysteresis (as shown in [65]). Therefore parameter "B" is proportional to the area of hysteresis under stress–strain plot. A value for "B" is chosen in order to obtain a good fit between the model and the experimental hysteresis.

- The computation of entropy difference "b" can justified by the comparing responses at two different temperatures as shown below. If $\boldsymbol{\mathcal{F}}_1$ is the driving force at torque σ_1 and temperature θ_1 and $\boldsymbol{\mathcal{F}}_2$ is the corresponding driving force at torque σ_2 and θ_2 respectively.

$$\boldsymbol{\mathcal{F}}_1 = \frac{\sigma_1^2}{2}\left(\frac{1}{E_M I} - \frac{1}{E_A I}\right) + a + b\theta_1 - B(2\xi_{ten} - 1) + \sigma_1 \varepsilon_{max} \tag{6.8}$$

$$\boldsymbol{\mathcal{F}}_2 = \frac{\sigma_2^2}{2}\left(\frac{1}{E_M I} - \frac{1}{E_A I}\right) + a + b\theta_2 - B(2\xi_{ten} - 1) + \sigma_2 \varepsilon_{max} \tag{6.9}$$

$$\boldsymbol{\mathcal{F}}_1 - \boldsymbol{\mathcal{F}}_2 = \frac{\sigma_1^2 - \sigma_2^2}{2}\left(\frac{1}{E_M I} - \frac{1}{E_A I}\right) + b(\theta_1 - \theta_2) + (\sigma_1 - \sigma_2)\varepsilon_{max} \tag{6.10}$$

The driving force analogous to chemical potential (see [160]) does not change with temperature and therefore $\boldsymbol{\mathcal{F}}_1$ - $\boldsymbol{\mathcal{F}}_2$=0. Using this relation and further

neglecting the terms arising due to modulus differences, we get,

$$b = -\frac{\sigma_1 - \sigma_2}{\theta_1 - \theta_2}\varepsilon_{max}, \tag{6.11}$$

It can be seen that the value of "b" (from table 6.1) matches with the values available in the literature for SMA (see [161]).

- The parameter "a" serves as a datum for the driving force and is computed by setting the driving force to be zero at the stress-free austenite phase i.e.,

$$\mathcal{F}|_{\xi=0,\sigma=0} = a + b\theta + B \tag{6.12}$$

$$a = -b\theta - B \tag{6.13}$$

Table 6.1: Values of thermodynamical parameters employed for model verification for uniaxial tension tests conducted on NiTi wire (see figure 2.3).

Parameters	**Corresponding Values**
E_a	40 GPa
E_m	28 GPa
B	-73 MPa
a	175 MPa
b	-0.2746 MPa/K
θ_1	348 K
θ_2	373 K
θ_2	398 K

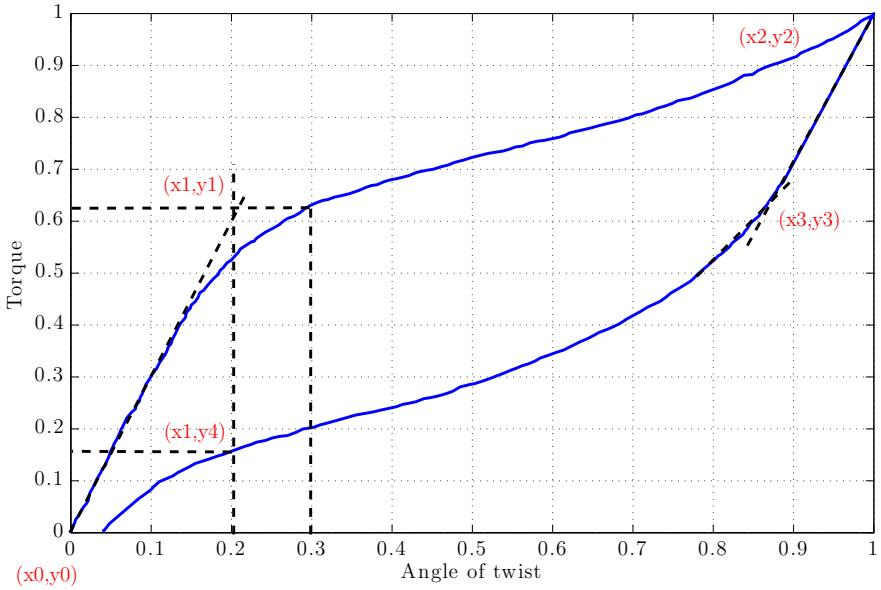

Figure 6.1: Figure shows the critical coordinates determined to estimate model parameters from a superelastic response of a wire (non-dimensionlized data). Experimental data obtained from [116].

6.5.2 Torsion Loading Case - Two Species

In this section, the identification of parameters G_a, G_m, B, a and b arising from the thermodynamical framework (i.e assumed Gibbs potential form in equation 3.16) are discussed.

Doaré et al. [116] performed experiments on SMA wires under different degrees of twist. Experimental data for highest twist is used as reference for model calibration under superelastic conditions and an algorithm to determine these parameters is illustrated below.

The following protocol is employed to determine some critical coordinates used to estimate model parameters from a superelastic torque–twist response of a wire (see figure 6.1).

1. Torque–twist data at one temperature is non-dimensionlized as $T^* = \left(\frac{T}{T_{max}}\right) = y_i$ and $\phi^* = \left(\frac{\phi}{\phi_{max}}\right) = x_i$ for convenience.

2. Using the non-dimesionlized data, define slope $m_i = \left(\frac{y_i - y_{i-1}}{x_i - x_{i-1}}\right)$ and $n_i = \frac{y_i}{x_i}$ for the entire data set. A moving average $m_{avg} = \frac{\sum m_i}{i}$ is established for comparison

3. If $\left(\frac{m_i - m_{avg_{i-1}}}{m_i}\right)$ departs $> 8\%$, break and save the initial data set for modulus evaluation. Following the ASTM standard F2516-07$^{\varepsilon 2}$ [13] for superelastic Ni-Ti materials under tension loading case, the upper plateau strength (UPS) is the corresponding stress value at 3% strain during tension loading of the sample. This approach is extended to the present torque–twist data where the corresponding torque value at 3% shear strain [1] is evaluated. The intersection of the slope of the initial data points till $\left(\frac{m_i - m_{avg_{i-1}}}{m_i}\right)$ departs $> 8\%$ (where it first starts departing linearity) and the torque value at 3% twist is used to determine coordinate (x_1, y_1) as shown in figure 6.1.

4. When $n_i = 1$, the corresponding data point is labeled as co-ordinate as (x_2, y_2). This is the final data point on the loading part of the torque–twist response.

5. Repeat step 2 for the unloading data and when $\left(\frac{m_i - m_{avg_{i-1}}}{m_i}\right)$ departs $> 8\%$, break and save the data set for modulus evaluation. The first point of departure from linearity is used to determine coordinate (x_3, y_3).

6. Using the x_1 co-ordinate from step 2, the corresponding data point on the unloading response is labeled as y_4.

[1] Shear strain (γ) can be related to twist/unit length by the following relation $\gamma = r\phi$ where "r" is the radius of the circular bar.

Using the above protocol the various parameters G_a, G_m, B, a and b are determined as shown below.

- The austenitic and martensitic shear moduli "G_a" and "G_m" can be estimated using the data sets determined in steps 3 and 5. These correspond to the initial loading and final unloading slopes of the torque – angle of twist plot. Similarly for twinning responses,"G_m" can be estimated directly from the the initial slope of the twinning response. In many cases, the shear moduli is evaluated using the elastic moduli with a poisons ratio assumption of around 0.3 as reported in literature (see table 1 in both [108, 109]).

- "B" is the coefficient of the interfacial energy term that relates to the the width of hysteresis area (as shown in [65])."B" is related to the area of hysteresis under torque–angle of twist plot and is estimated as the area of the quadrilateral (x_1, y_1), (x_2, y_2), (x_3, y_3) and (x_1, y_4). For twinning responses, "B" represents the interaction energy between the martensite variants. A value for "B" is chosen in order to obtain a good fit between the model and the experimental hysteresis for twinning responses and partially transformed superelastic responses as observed in case of springs.

- The computation of entropy difference "b" can justified by the comparing responses at two different temperatures as shown below. This discussion is common for both superelastic responses $A \leftrightarrow M^+$ and $A \leftrightarrow M^-$. A common martensite volume fraction ξ [2] is employed for discussion here. If $\mathcal{F}_1$ is the driving force at torque T_1, operating temperature θ_1 and $\mathcal{F}_2$ is the correspond-

[2]Term ξ can be ξ^+ or ξ^- depending on the twisting direction and the corresponding driving force equations can be employed.

ing driving force at torque T_2, operating temperature θ_2.

$$\mathcal{F}_1 = \frac{T_1^2}{2}\left(\frac{1}{G_m J} - \frac{1}{G_a J}\right) + a + b\theta_1 - B(2\xi - 1) + T_1\phi_{max} \tag{6.14}$$

$$\mathcal{F}_2 = \frac{T_2^2}{2}\left(\frac{1}{G_m J} - \frac{1}{G_a J}\right) + a + b\theta_2 - B(2\xi - 1) + T_2\phi_{max} \tag{6.15}$$

$$\mathcal{F}_1 - \mathcal{F}_2 = \frac{T_1^2 - T_2^2}{2}\left(\frac{1}{G_m J} - \frac{1}{G_a J}\right) + b(\theta_1 - \theta_2) + (T_1 - T_2)\phi_{max} \tag{6.16}$$

The driving force for transformation is analogous to chemical potential (see [160, 161]) and is assumed to be independent of temperature and thus $\mathcal{F}_1$ - $\mathcal{F}_2$ = 0. This assumption suggests that driving force – volume fraction plots for different transformation conditions estimated at any twist is independent of temperature as long as they are compared for same extent of transformation (i.e same value of ξ). Using this relation and further neglecting the terms arising due to modulus differences, we get,

$$b = -\frac{T_1 - T_2}{\theta_1 - \theta_2}\phi_{max}, \tag{6.17}$$

In the above relation, T_1 and T_2 are determined by the comparing responses at two different temperatures (θ_1 and θ_2) using the (x_1, y_1) co-ordinates determined in steps 2 and 3.

- The parameter "a" serves as a datum for the driving force and is computed by setting the driving force to be zero at the stress-free austenite phase at a given temperature, i.e.,

$$\mathcal{F}|_{\xi=0,T=0} = a + b\theta + B = 0 \tag{6.18}$$

$$\text{So, } a = -b\theta - B \tag{6.19}$$

The above parameters G_a, G_m, B, a and b are common for both clockwise and anticlockwise twist as the responses are symmetric in nature.

Table 6.2: Values of thermodynamical parameters employed for model verification in case of springs

Parameters	**Corresponding Values**
G_a	14.4 GPa
G_m	10.56 GPa
B	-9.6 Nmm
a	151.34 Nmm
b	-0.38 Nmm/K
θ_1	348 K
θ_2	373 K
θ_3	398 K

6.5.3 Pure Bending Case - Two Species

Similarly, the parameters under consideration E_a, E_m, B, a and b and their corresponding values used for simulation and model predictions are reported in Table 6.3. The parameters are determined keeping the experimental data on pure bending of NiTi wire from Rejzner et al. [132] as reference.

- "E_a" and "E_m" being the austenitic and martensitic elastic moduli can be estimated directly form the tension experimental data by finding the initial slopes of the superleastic response.

- "B" is the coefficient of the interfacial energy term related to the area of hysteresis (as shown in [65]). Therefore parameter "B" is proportional to the area of hysterisis under bending moment verses curvature plot. A value for "B" is chosen in order to obtain a good fit between the model and the experimental hysteresis.

- The computation of entropy difference "b" can justified by the comparing responses at two different temperatures as shown below. If $\mathcal{F}_1$ is the driving force at torque M_1 and temperature θ_1 and $\mathcal{F}_2$ is the corresponding driving force at torque M_2 and θ_2 respectively.

$$\mathcal{F}_1 = \frac{M_1^2}{2}\left(\frac{1}{E_m I} - \frac{1}{E_a I}\right) + a + b\theta_1 - B(2\xi_{bend} - 1) + M_1\kappa_{max} \tag{6.20}$$

$$\mathcal{F}_2 = \frac{M_2^2}{2}\left(\frac{1}{E_m I} - \frac{1}{E_a I}\right) + a + b\theta_2 - B(2\xi_{bend} - 1) + M_2\kappa_{max} \tag{6.21}$$

$$\mathcal{F}_1 - \mathcal{F}_2 = \frac{M_1^2 - M_2^2}{2}\left(\frac{1}{E_m I} - \frac{1}{E_a I}\right) + b(\theta_1 - \theta_2) + (M_1 - M_2)\kappa_{max} \tag{6.22}$$

  Similarly, $\mathcal{F}_1$ - $\mathcal{F}_2$=0 and further neglecting the terms arising due to modulus differences, we get,

$$b = -\frac{M_1 - M_2}{\theta_1 - \theta_2}\kappa_{max}, \tag{6.23}$$

- Similarly, the parameter "a" serves as a datum for the driving force and is computed by setting the driving force to be zero at the stress-free austenite phase i.e.,

$$\mathcal{F}|_{\xi_{bend}=0, M=0} = a + b\theta + B \tag{6.24}$$

$$a = -b\theta - B \tag{6.25}$$

Table 6.3: Values of thermodynamical parameters employed for model verification for pure bending experimental data of NiTi wire [132]

Parameters	**Corresponding Values**
E_a	45 MPa
E_m	35 MPa
B	-1.33 Nmm
a	44.3 Nmm
b	-0.133 Nmm/K
θ_1	323 K
θ_2	303 K

6.5.4 Torsion Case - Three Species

The identification of parameters G_a, G_m, B, a and b arising from the thermodynamical framework (i.e assumed Gibbs potential form in equation 5.13) are discussed. For different driving force–volume fraction relationships summarized in table 5.1, the model parameters are calibrated against the corresponding experimental data under various transformation conditions using a single torque–angle of twist plot for superelastic and twinning responses. The model is preferably calibrated for the maximum extent of transformation and then used to predict responses at lower extents of transformation or at different temperatures.

Doaré et al. [116] performed experiments on SMA wires under different degrees of twist. Experimental data for highest twist is used as reference for model calibration under superelastic conditions. The calibrated parameters are reported in table 6.4.

Aguiar et al. [113] performed experiments on SMA springs under different dead loads which are used as reference for model calibration under twinning responses.

Only modulus G_m and B is of significance here and the corresponding calibrated values are reported in table 6.4.

The procedure for finding parameters for superelastic response is similar to the one illustrated in section 6.5.2. The same algorithm is used to identify parameters G_a, G_m, B, a and b for SE responses.

For twinning responses, "G_m" can be estimated directly from the the initial slope of the twinning response. "B" represents the interaction energy between the martensite variants value for "B" is chosen in order to obtain a good fit between the model and the experimental hysteresis.

The above parameters G_a, G_m, B, a and b are common for both clockwise and anticlockwise twist as the responses are symmetric in nature.

Table 6.4: Values of thermodynamical parameters employed for model verification for springs and wires used for three species thermodyanmic Preisach models

Parameters	**Corresponding Values**	
	Superelastic response (SE)	Twinning response (SME)
G_a	14.5 GPa	-NA-
G_m	11 GPa	11.5 GPa
B	-23.3 Nmm	- 0.2 Nmm
a	163 Nmm	-NA-
b	-0.47 Nmm/K	-NA-
θ_1	297 K	-NA- (295 K)
θ_2	327 K	–

6.6 Note on Parameter "B" for Superelastic and Twinning Responses

From table 6.4, the interaction energy term "B" is significantly larger compared that of twinning responses. This suggests that one requires lesser energy for twinning between martensite variants as compared against phase transformations between austenite and martensite variants associated superelastic phase transformations. Though, SMAs demonstrate large plateau strains (6 to 8%) under both superelastic and twinning responses, experimental evidences under superelastic conditions indicate higher critical stress/torque levels for phase transformation when compared to corresponding critical stresses associated with twinning responses thus emphasising higher interaction energy difference.

Figures 7.32 and 7.33 discussed later shows the experimental results for superelastic and twinning responses for SMA springs and rods respectively. It clearly demonstrates significantly higher plateau stresses/torque levels associated with superelastic responses when compared to twinning responses associated with shape memory response. As discussed in section 1.2.1, plateau stresses **Upper plateau strength (UPS)** and **Lower plateau strength (LPS)** are some of the salient features associated with a typical superelastic response under tension loading case as discussed in the ASTM standard F2516-07$^{\varepsilon 2}$ [13] for superelastic Ni-Ti materials. On similar lines, with twinning responses, the critical stress associated with the onset of flat plateau can be employed for comparison with UPS or LPS associated with superelastic responses. Though, torsional responses of SMA components don't show clear flat plateaus as commonly seen with tension responses, it is still evident that UPS > LPS > plateau stress associated with twinning response. This justifies higher energy values ("B") associated with superelastic phase transformations as compared to twinning response associated with shape memory effects.

6.7 Simulation of Orginal Response for SMA Components

Once the test protocol highlighted in the above sections are selected depending on the transformation case, the model can be used to simulate responses at different temperatures or twists. For prediction of responses of SMA components like wires, rods and springs considered here, a total of "20100 hysterons" which is an equivalent to a Preisach triangle with a side of "200" were employed.

Depending on the choice of the size of the Preisach triangle, the model predictions can do an approximate or a precise prediction by controlling the use of number of Preisach elements used in simulation. An approximate response prediction could be sufficient for design purposes but a more precise prediction might be essential from the control systems standpoint. Such a scheme allows predictions tailored to level of information available and thus saving computational time.

6.8 Model Predictions – Different Strains/Twists/Curvatures or Temperatures

Hysterons generated at one particular twist can be used to predict responses at any other twists (i.e internal loops) without re-computation of any model parameters. This just requires appropriate assumption of strain/twist/curvature or stress/torque/moment vectors during simulation protocol selected for recomputing original relationships as described in previous sections for different loading conditions.

Superelastic responses of SMA are affected by changes in external stimuli (i.e operating temperature) as shown in many experimental evidences (see figure 7 in [72], figure 12 in [156], figure 16 in [142], figure 3 in [105], figure 2 in [162] etc. for examples). The present modeling approach allows us to capture this temperature dependence without re-computation of any model parameters. The inherent assumption here is that the driving force – volume fraction plots for a given extent of trans-

formation (ξ) just translates linearly with changes in operating temperature. This linear relationship is the (a + $b\theta$) terms in the driving force relationships for superelastic responses under different loading conditions. With such an assumption, one can predict responses at different temperatures based on hysterons generated at one particular temperature without the need for changing any model parameters. Thus, it just requires changing temperature value (θ) in during the simulation protocol selected for recomputing original relationship as described in previous sections.

7. RESULTS AND DISCUSSIONS : MODEL SIMULATIONS AND PREDICTIONS *

Using the simulation process discussed in section 6, $\boldsymbol{\mathcal{F}} - \boldsymbol{\xi}$ are estimated from the original experimental data under all loading conditions for a given temperature say θ_1. The prediction of responses at different temperatures (say θ_2 or θ_3) can be achieved by just "changing the temperature term" during the reverse calculations of experimental data from the $\boldsymbol{\mathcal{F}} - \boldsymbol{\xi}$ generated for temperature θ_1. Thus the hysteron parameters have to be estimated only once and they don't have to be recomputed for predictions at different temperatures.

7.1 Tension Loading Results - Two Species

Tension test on wires (see figure 2.3) indicate that the plateau stresses scale linearly with temperature without significant change in hysteresis. The linear assumption ($a + b\theta$ terms in the model) was used to capture the temperature dependence of superelastic responses in SMA tension response. Figure 7.1a shows the simulation using ASTM standard as guidelines as discussed in section 1.2.1 and figure 1.5. The flat upper and lower platues are generally observed in superelastic SMA wires but not in martensite SMA wires that were tested under superelastic conditions. Hence, the model results are quite far from the experimental results since the ASTM standard was primarily developed for superelastic wires. Figure 7.1b shows the model simulation at 373 K compared with the experimental data. Model prediction and

*Reprinted with permission from "Combining Thermodynamic Principles with Preisach models for superelastic SMA Wires" by Doraiswamy, Rao and Srinivasa, *Smart Materials and Structures*, 20, 085032, 2011 [64], Copyright [2014] by IOP.

Reprinted with permission from "A two species thermodynamic Preisach model for the torsional response of SMA wires and springs under superelastic conditions" by Rao and Srinivasa, *International Journal of Solids and Structures*, 50, 887–898, 2013 [90], Copyright [2014] by Elsevier Limited.

experimental results show a close match as the Preisach parameters were chosen to fit the data. The closeness of the fit is an indication of the power of the Preisach approach. The hysterons generated for this result are used to predict responses at different temperatures.

Figure 7.2a and 7.2b shows the model prediction at 348 K and 398 K respectively with the corresponding experimental results used for comparison. The model results are predicted up to 6% strains for both the cases as the the SMA wires are not used for applications $> 6\%$ due to poor fatigue life. Further the predictions of plateau strains is of significant importance for design of superelastic SMA components in civil and biomedical applications.

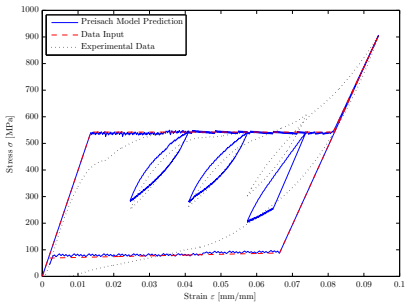

(a) Model prediction using the ASTM standard as guidelines as discussed in section 1.2.1 and figure 1.5.

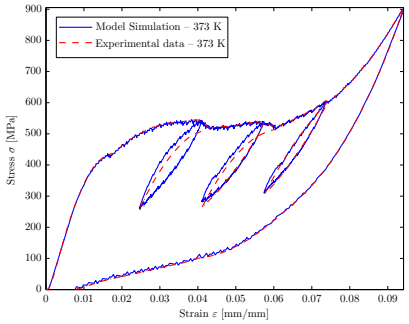

(b) Model prediction and experimental results show a close match as the Preisach parameters were chosen to fit the data. The closeness of the fit is an indication of the power of the Preisach approach.

Figure 7.1: Model simulation using ASTM guidelines and a model simulation of results at 373 K

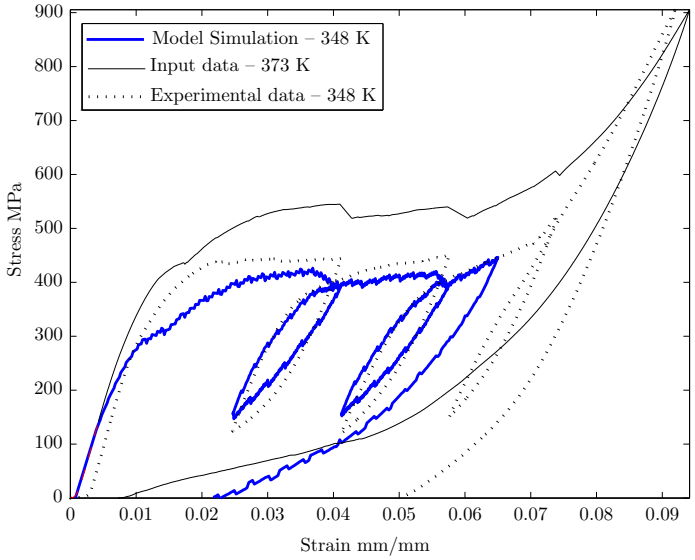

(a) Model prediction for 348 K using the 373 K as input data. Model results show a close match with the experimental results with an average error $\sim 6\%$.

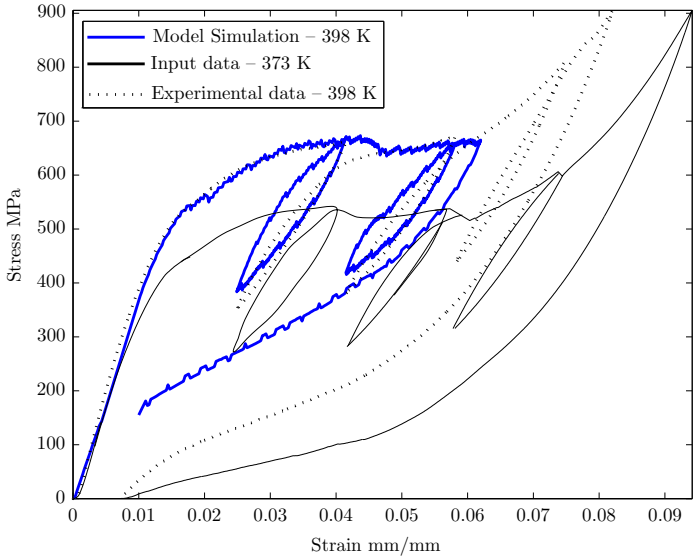

(b) Model prediction for 398 K using the 373 K as input data. Model results show a close match with the experimental results with an average error $\sim 8\%$.

Figure 7.2: Prediction for responses at 348 and 398 K using the hysterons generated at 373 K temperature result. The experimental results for all cases were discussed earlier in 2.3.

7.2 Torsional Loading Results - Two Species

7.2.1 Simulations of SMA Spring and Wire Response Using Complete Torque verses Angle of Twist Data

Figure 7.3 and 7.4 shows the model prediction at 348 K and 296 K respectively with the corresponding experimental results used for comparison. The model shows a good fit with the experimental results and can estimate the hysteresis accurately.

7.2.2 Simulation and Model Predictions of SMA Wire Response at Different Twists

Doarè et al. [116] in their work performed quasi-static tests on 2mm dia SMA wires for three different angle of twists (100, 350 and 450 degrees). The 450^o data was used as reference to calibrate the model with the assumption that it is the maximum possible angle of twist that the sample can encounter without failing. The hysterons generated by the 450^o data are used to predict responses at any other angle of twist without recomputation of any model parameters. Figure 7.13a and 7.13b shows the model predictions at different angles of twist 350 and 225^o twist respectively using the hysterons generated with the 450^o twist. The model predictions show a close match with the experimental results. It must be highlighted from these experiments and model predictions, it is unclear if a fully martensitic wire is obtained at higher twists as there was no elastic deformation of stress induced martensite (SIM) observed in these experiments. Chapman et al. [110] in their work studied the response of three superelastic wires with different diameters under torsion until failure and the results clearly illustrates that one can observe a fully transformed wire response (similar to pure tension responses) under higher degrees of twist (see figures 2 and 3 in [110]).

In order to confirm this point, section 2.3 earlier discussed torsional tests on SMA wires under large twist. Figures 7.5, 7.6, 7.7, 7.8, 7.9, 7.10, 7.11, 7.12 shows

simulation results that used the entire experimental data for model calibration in each of the test cases discussed in section 2.3. The use of Preisach model results in a jagged nature of the response as shown in the results. The Preisach parameters were chosen to calibrate the model and the strength of such an approach is evident here with the model simulations showing a close match with the experimental data. The outer loops, complex internal loops and RPM predictions were accurately captured in all the simulations when compared with its corresponding experimental data. The model is preferably calibrated at the maximum angle of twist and then used to predict responses at lower twists. In subsequent subsections, these model simulations are used to predict responses with more complex internal loops as discussed in section 2.3 earlier.

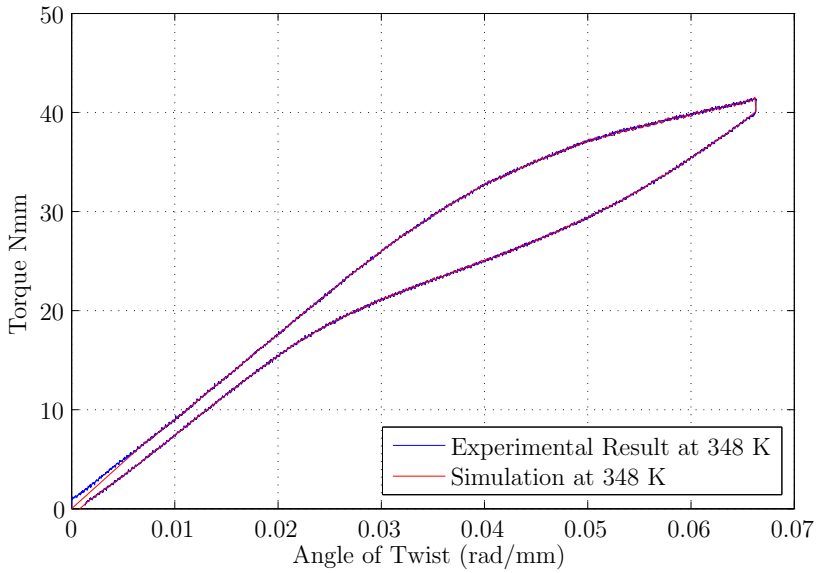

Figure 7.3: Model prediction for the superelastic response of SMA spring at 348 K. Model prediction and experimental results show a good match. This is not surprising since the Preisach parameters were chosen to fit the data. However the closeness of the fit is an indication of the power of the Preisach approach.

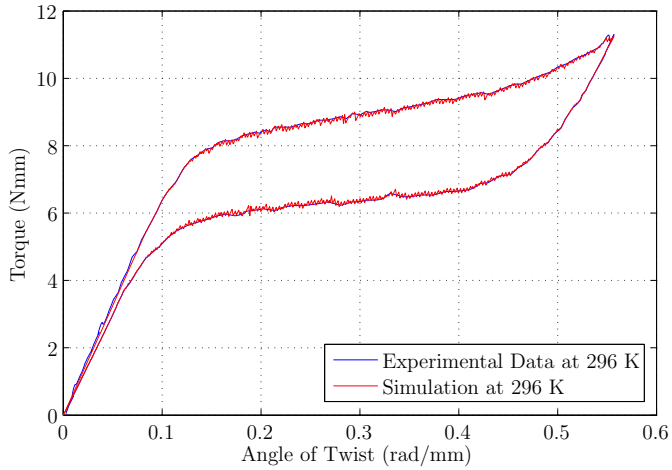

Figure 7.4: Model prediction for the superelastic response of SMA wire tested at 296 K showing a good match. Experimental results at 296 K were obtained from [110]. The jaggedness of the model simulation is due to the fact that a discrete Preisach model was used.

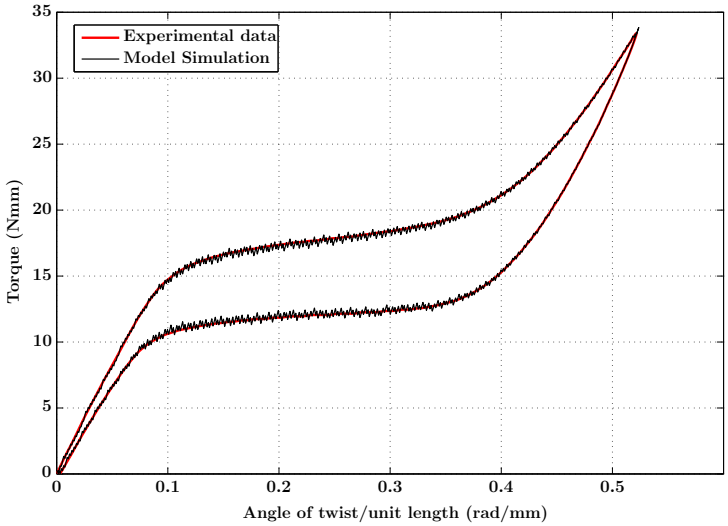

Figure 7.5: Figure showing the data that is used for model calibration. All model predictions discussed in section 7.2.2.1 uses the hysterons generated for this outer loop response.

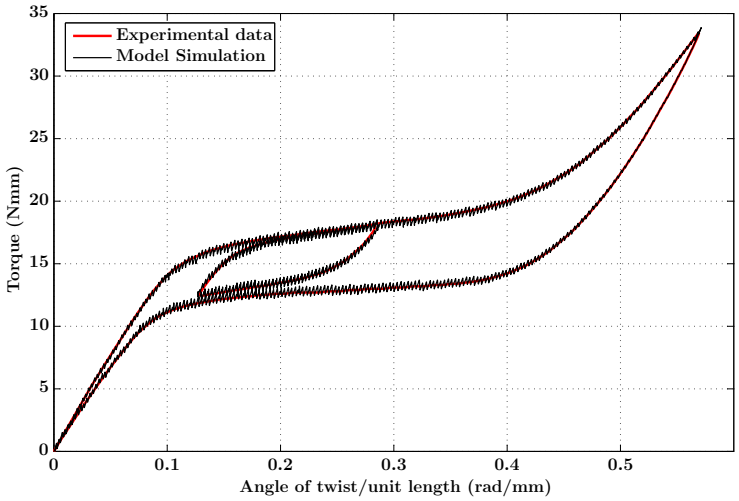

Figure 7.6: Simulation for a hysteretic response with one large internal loops during loading cycle. All model predictions discussed in section 7.2.2.2 uses the hysterons generated for this experimental data containing the outer loop with one internal loop during the loading cycle.

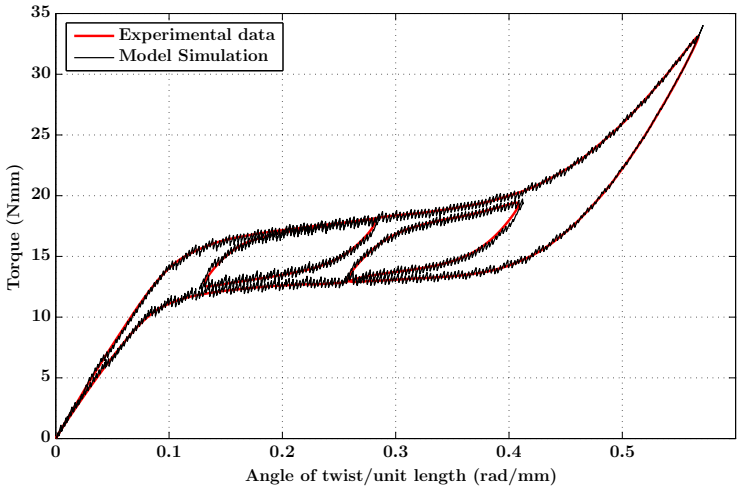

Figure 7.7: Simulation for a hysteretic response with an internal loop during the loading and unloading cycle. All model predictions discussed in section 7.2.2.3 uses the hysterons generated for this entire outer loop and internal loops during the loading and unloading stages.

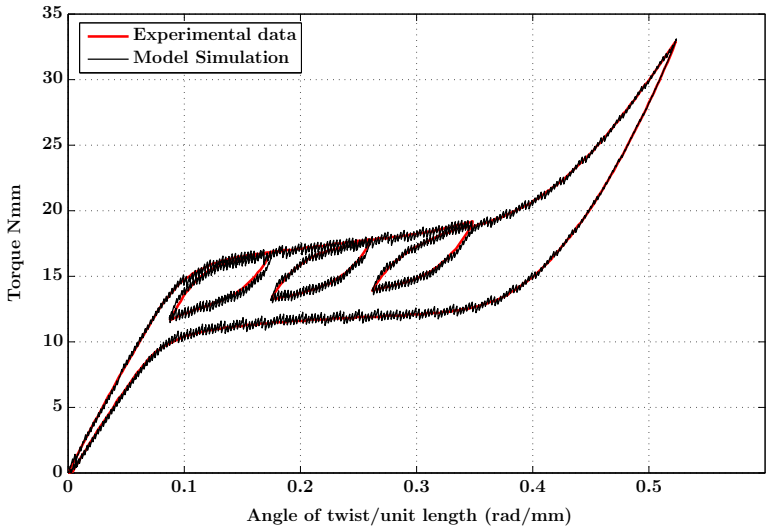

Figure 7.8: Simulation for a hysteretic response with three large internal loops during loading cycle. The jaggedness in the response is due to the discrete nature of the Preisach model

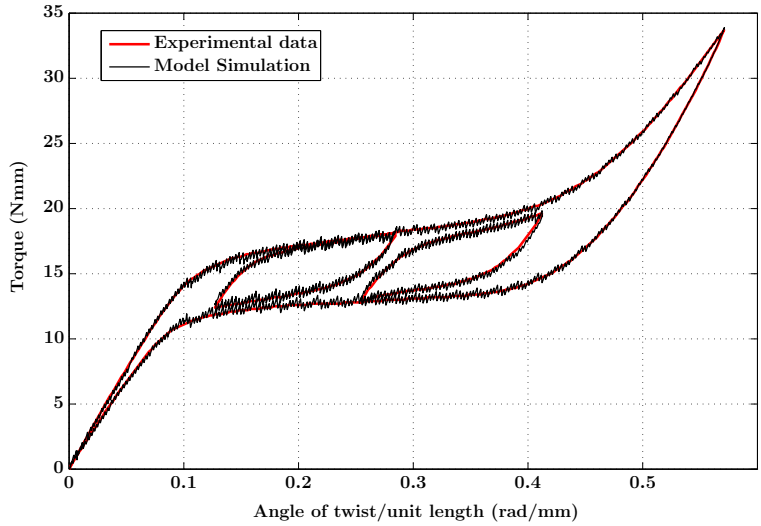

Figure 7.9: Simulation for a hysteretic response that compares internal loops during loading and unloading part of the response. Again, the simulation is a close fit when compared to the experimental data.

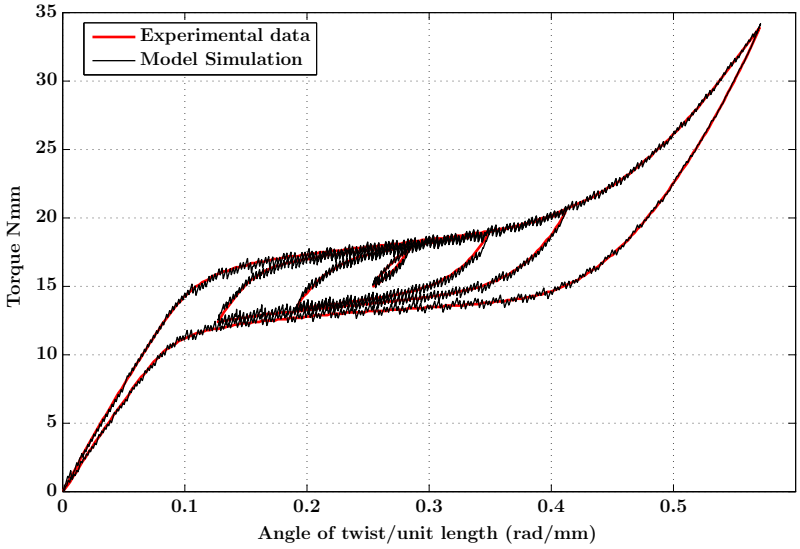

Figure 7.10: Simulation of complex internal loops during loading cycles. The RPM effects are well captures by the Preisach model.

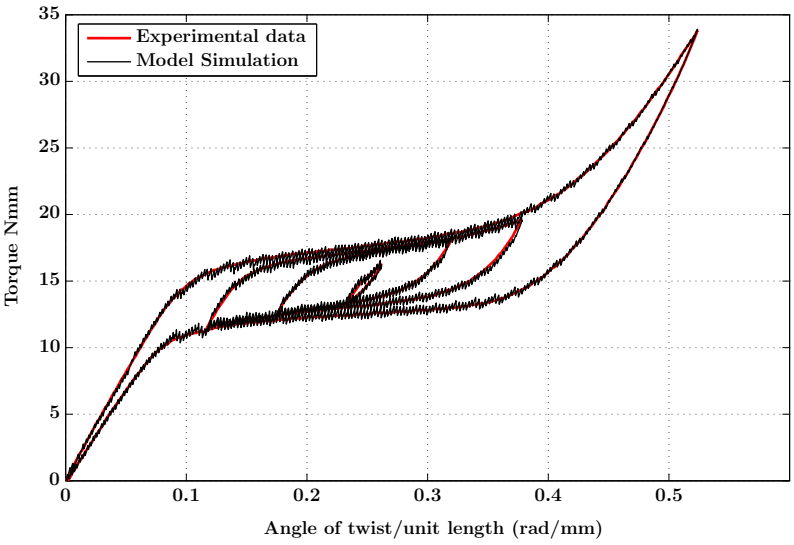

Figure 7.11: Simulation of complex internal loop during unloading cycles. The RPM effects are well captures by the Preisach model.

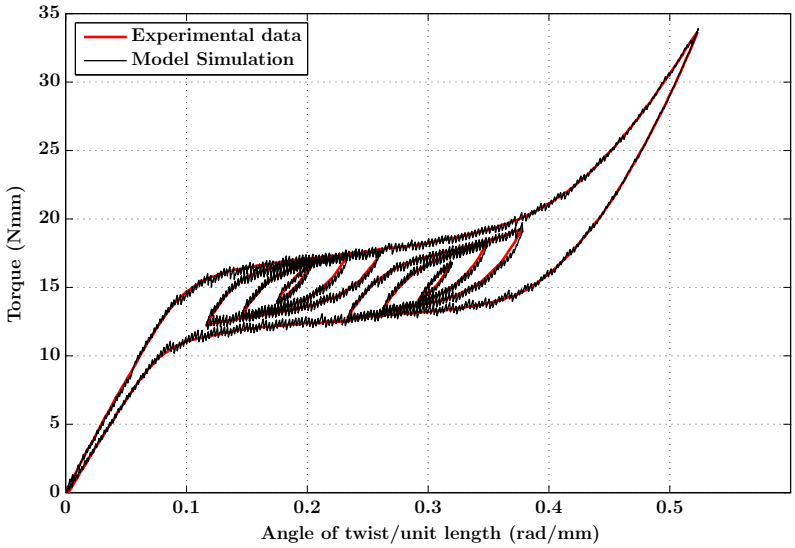

Figure 7.12: Simulation of a response having complex internal loops during both loading and unloading cycles. The strength of the Presiach model is clearly demonstrated here with a close fit with the experimental data.

7.2.2.1 Model Predictions using simple load unload outer loop response as input data

The model can also be used to predict responses at different^o of twists. In predictions shown in figures 7.14, 7.15, 7.16 and 7.17 some examples of model predictions are demonstrated. The predictions show a close match with the outer and inner loop with reasonable predictions. In all the predictions, the model is calibrated for the outer loop response of a simple loading and unloading case upto 1800^o maximum twist as shown in figure 7.5. The Preisach elements from this calibrated response is used to predict responses for different cases as shown in figures 7.15 7.16 and 7.17. The predictions closely captured the outer loop responses and captured the simple and complex internal loops (including RPM) especially during the loading stage with reasonable fidelity.

7.2.2.2 Model Predictions using the entire outer loop with one internal loop during the loading cycle as input data

Some model predictions that use the entire outer loop with one internal loop during the cycle as shown in figure 7.6 is employed for predicting more complex responses. This input data uses an additional internal loop information in additional to the outer loop as discussed in the earlier section 7.2.2.1. Figures 7.18, 7.19 and 7.20 show some model predictions using this input data. The model predictions captured the outer loop responses and captured the simple and complex internal loops (including RPM) with a closer match to the experimental data as compared to those discussed in section 7.2.2.1 that used only the outer loop for model calibration. Thus, the Preisach model is capable of predicting the complete inner response with only outer loop data, although the use of a single inner loop for calibration improves the predictions. The internal loops during the unloading stages of the model predictions didn't exactly match the experimental data as the model input data used only the outer loop and loading cycle internal loop data. Hence, the outer loop and loading cycle internal loops were predicted with reasonable fidelity.

7.2.2.3 Model Predictions using the entire outer loop and one internal loop under loading and unloading stage as input data.

Figures 7.21 and 7.22 show some model predictions with complex internal loops using the entire outer loop with internal loops during the loading and unloading sages of the response as input data (as shown in figure 7.7). It is clear that these model predictions are a close match to the experimental data when compared to earlier predictions discussed in section 7.2.2.1 or 7.2.2.2 as more information that included one big internal loop during loading and unloading stages along with outer loop was used for model predictions. This thus suggests that the choice of number of Preisach

elements and the input data used for model calibration can result in approximate or precise predictions and thus allowing predictions tailored to the level of information available [90].

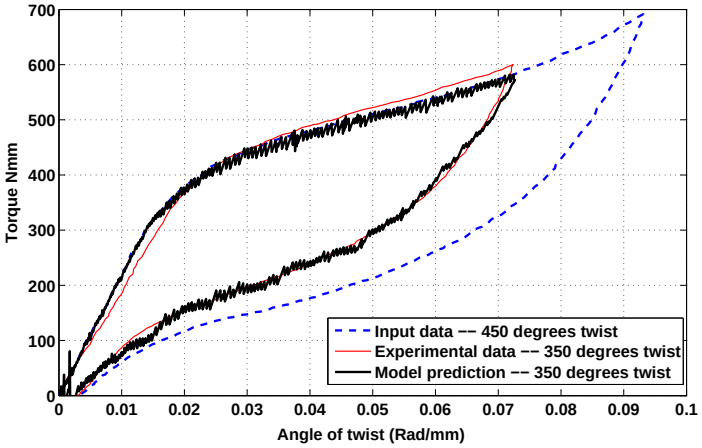

(a) Model prediction for 350^o twist using 450^o twist as input data. Model results show a close match with the experimental results with an average error $\sim 6.5\%$.

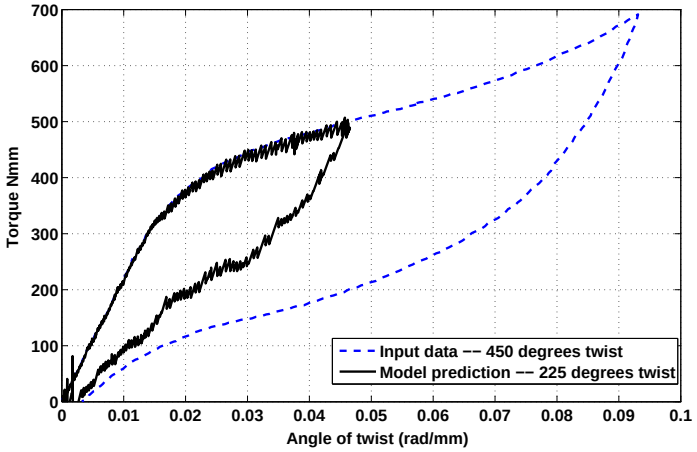

(b) Model prediction for 225^o twist using 450^o twist as input data.

Figure 7.13: Prediction for responses at 350 and 225^o twist using the hysterons generated at 450 degrees twist. The experimental results for all cases were obtained from [116].

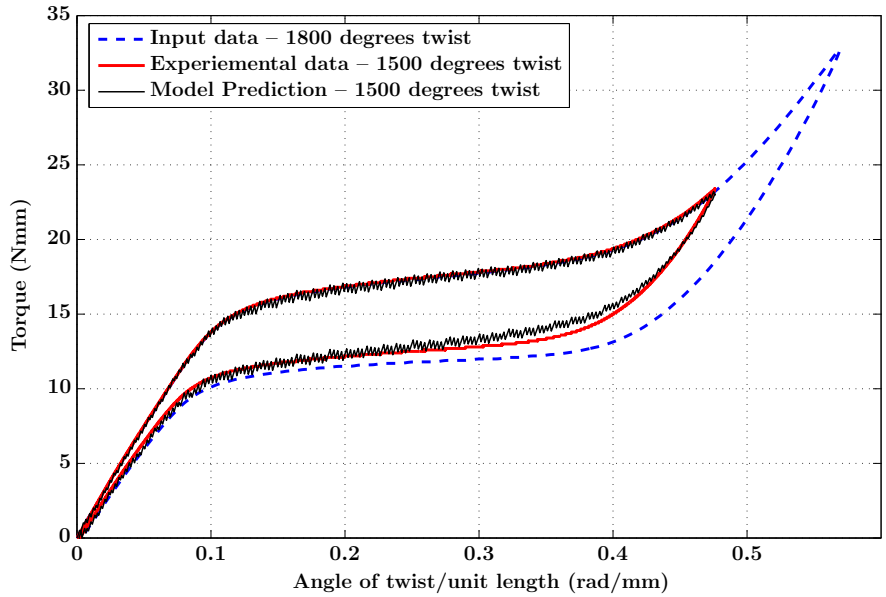

(a) Prediction of 1500^otwist using 1800 twist data using the input data as shown in figure 7.5.

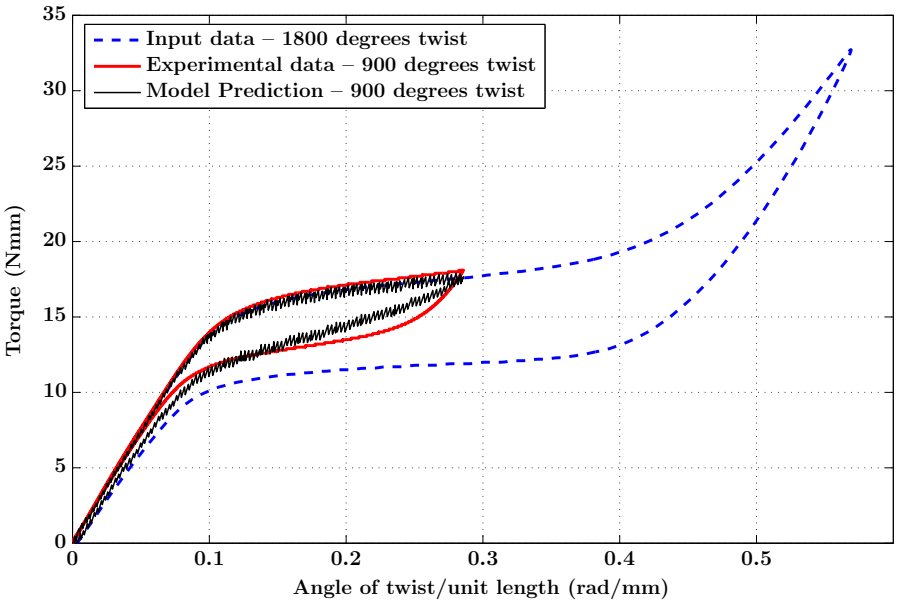

(b) Prediction of 900^otwist using 1800 twist data using the input data as shown in figure 7.5.

Figure 7.14: Figures show the prediction of lower twists 1500^o and 900^o using the hysterons generated with the 1800^o data as shown in figure 7.5. The predictions show a close match with the experimental data and the outer loop is well predicted.

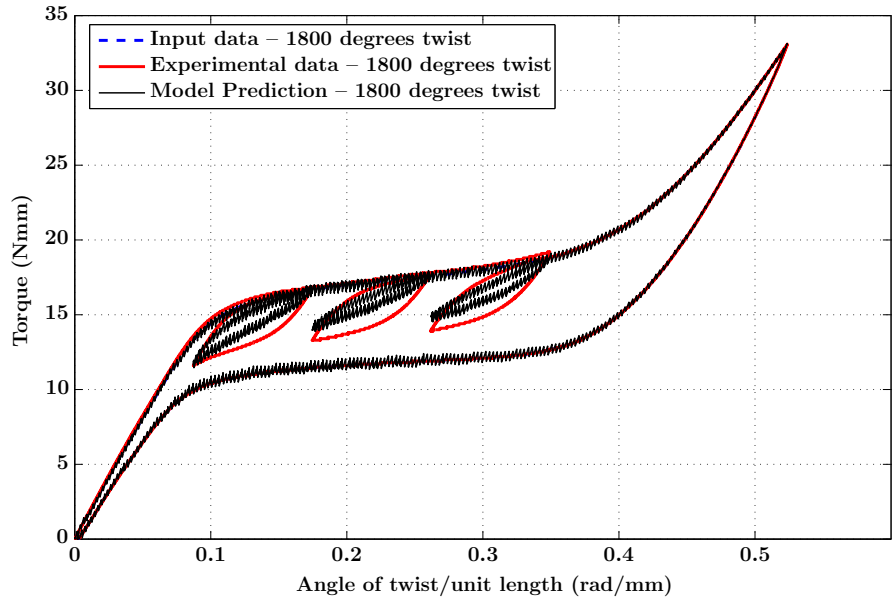

(a) Prediction of 1800^o twist with three loops during the loading cycle using the input data as shown in figure 7.5.

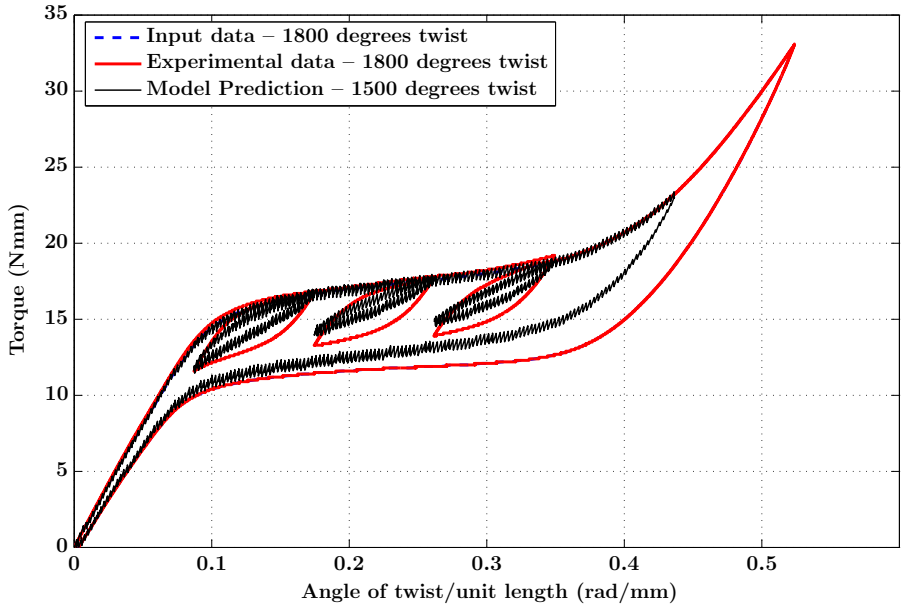

(b) Prediction of 1500^o maximum twist with three loops during the loading cycle using the input data as shown in figure 7.5.

Figure 7.15: Figures show the prediction of 1800 and 1500^o twist using the hysterons generated with the 1800^o outer loops data of the simple load and unload case as shown in figure 7.5. Using minimum information, complex responses involving internal loops are predicted and the results show a close fit with outer loops and a good RPM prediction.

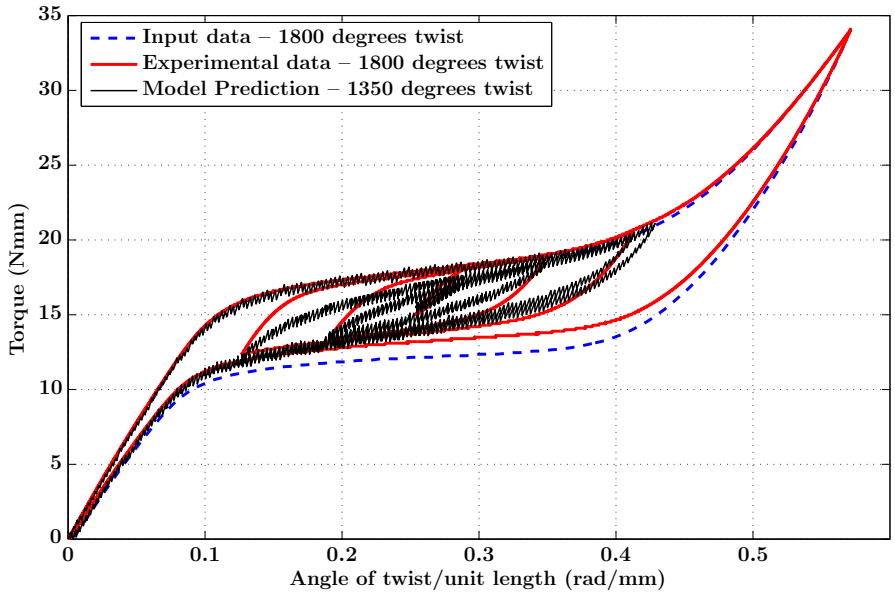

(a) Prediction of 1350^omaximum twist with a complex loading loop using the input data as shown in figure 7.5.

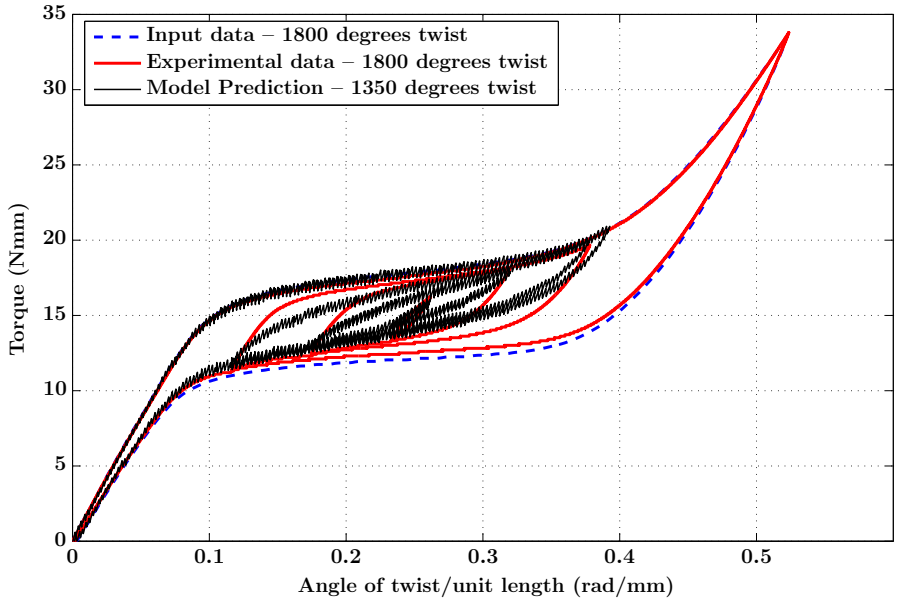

(b) Prediction of 1350^omaximum twist with complex unloading loop using the input data as shown in figure 7.5.

Figure 7.16: Figures show the prediction of 1350^o maximum twist for complex loop under loading and unloading cases using the hysterons generated with the 1800^o outer loops data of the simple load and unload case as shown in figure 7.5. The outer loops are well represented and the complex loops with RPM prediction match well with the experimental data.

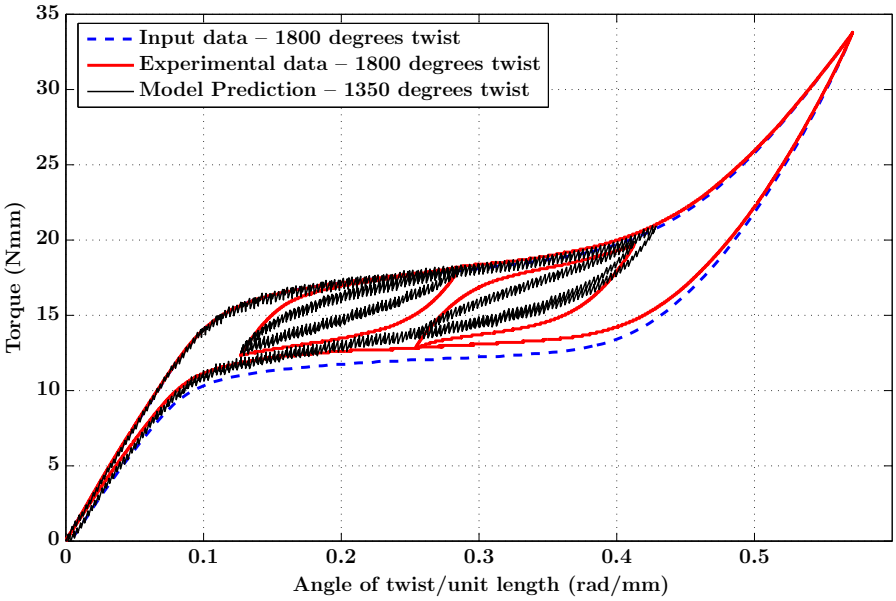

(a) Prediction of 1350^o maximum twist with big internal loops during loading and unloading cycles using the input data as shown in figure 7.5.

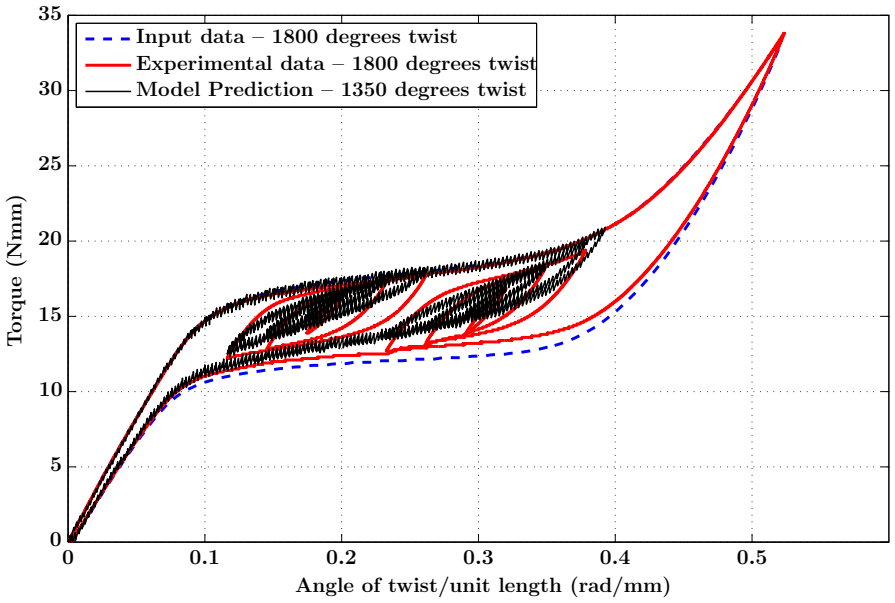

(b) Prediction of 1350^o maximum twist with complex loading and unloading loop using the input data as shown in figure 7.5.

Figure 7.17: Figures show the prediction of 1350^o maximum twist for two different cases that contain simple and complex loops using the hysterons generated with the outer loops data of the simple load and unload case as shown in figure 7.5. The outer loops are well represented and the complex loops with RPM prediction match well with the experimental data.

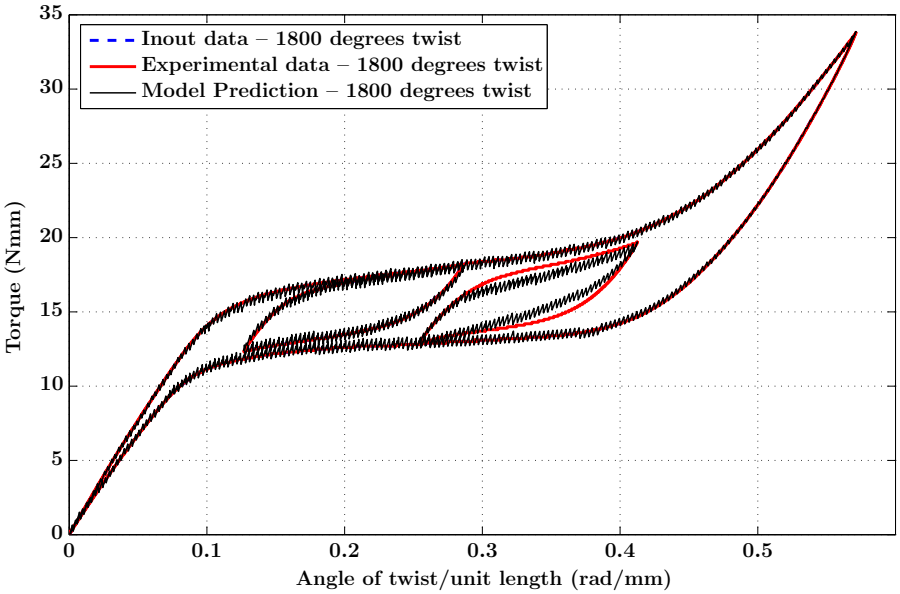

(a) Prediction of 1800^o twist with big internal loops during loading and unloading cycles using the input data as shown in figure 7.6.

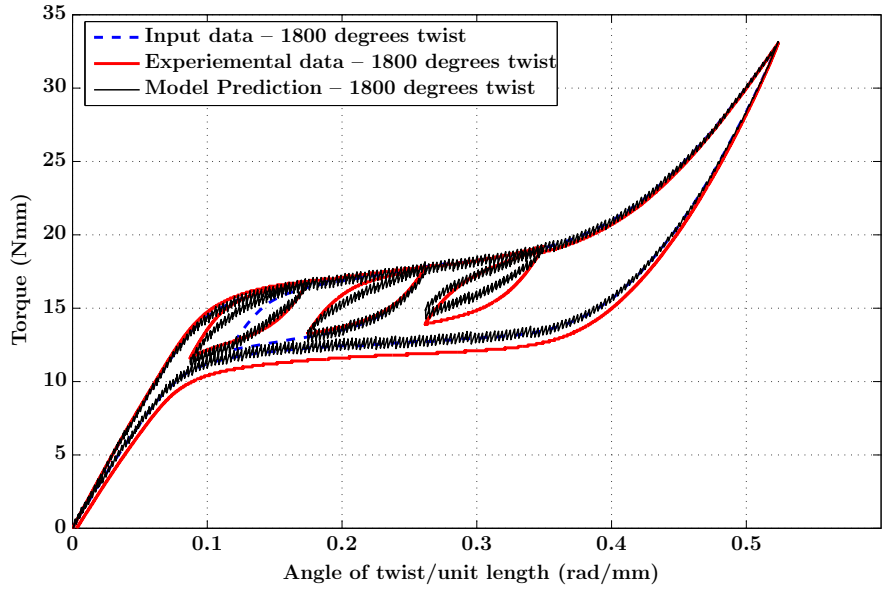

(b) Prediction of 1800^o maximum twist with three loops during the loading cycle using the input data as shown in figure 7.6.

Figure 7.18: Figures show the prediction of 1800^o twist for two different cases with two and three internal loops using the hysterons generated with the outer loop and one internal loop data as shown in figure 7.6. Using the outer loop and one internal loop information, complex responses involving more internal loops are predicted with the results show a close match to the experimental data.

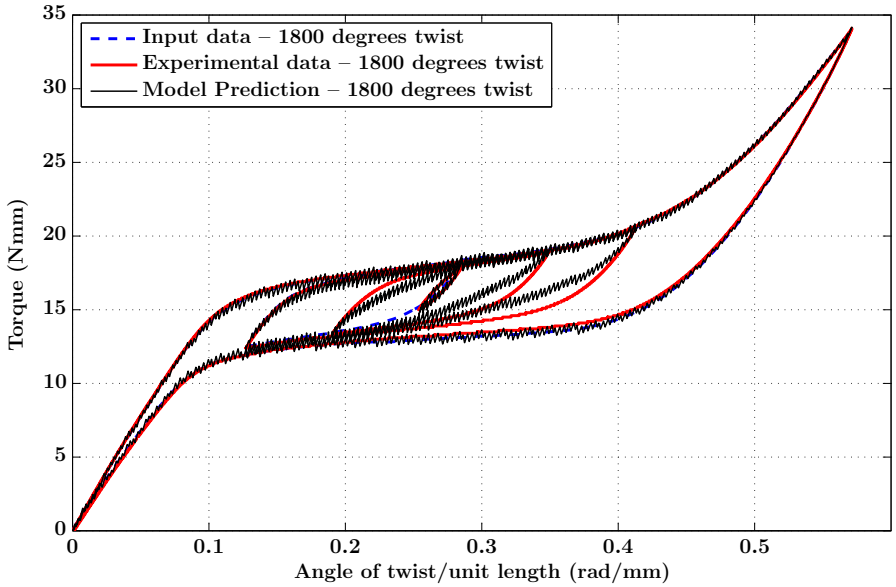

(a) Prediction of 1800^o twist with complex loop during the loading cycle using the input data as shown in figure 7.6.

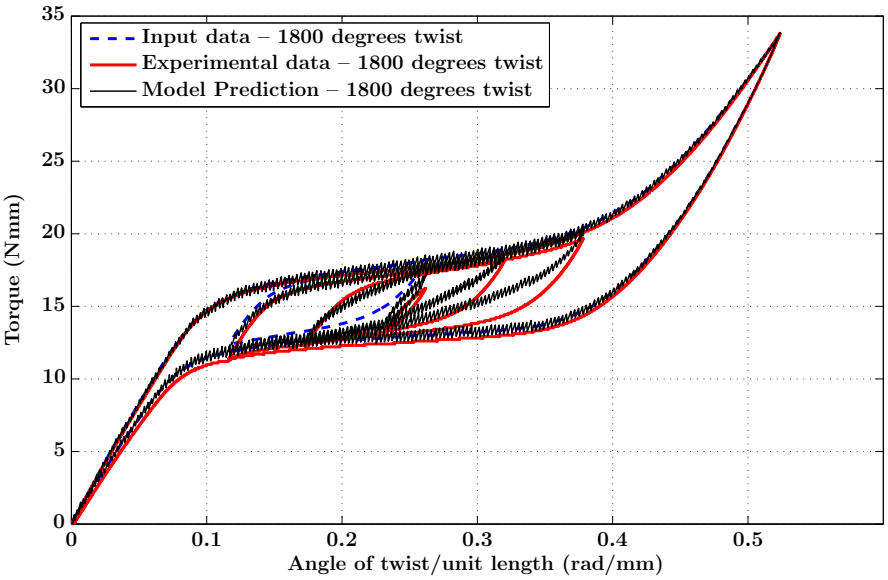

(b) Prediction of 1800^o maximum twist with complex loop during the unloading cycle using the input data as shown in figure 7.6.

Figure 7.19: Figures show the prediction of 1800^o twist for two different cases with two and three internal loops using the hysterons generated with the outer loop and one internal loop data as shown in figure 7.6. Using the outer loop and one internal loop information, complex loop responses were predicted and compared against the experimental data.

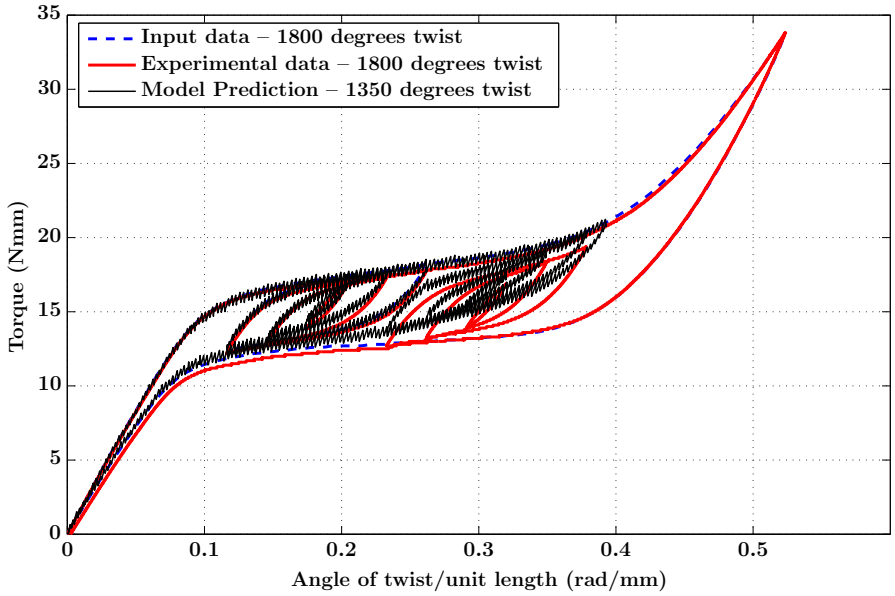

(a) Prediction of 1350^o twist with complex loops during loading and unloading cycles using the input data as shown in figure 7.6.

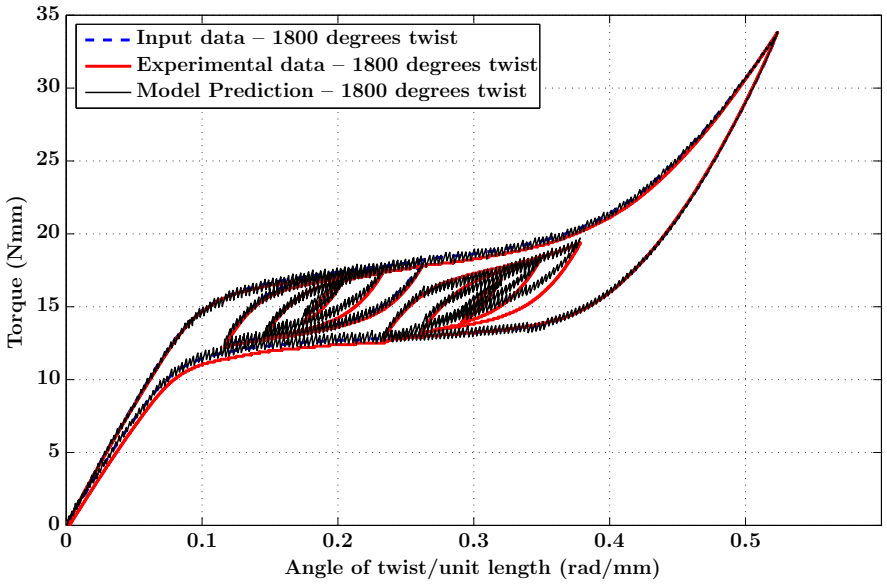

(b) Prediction of 1800^o twist with complex loops during loading and unloading cycles using the input data as shown in figure 7.6.

Figure 7.20: Figures show the prediction of 1350 and 1800^o maximum twist using the hysterons generated with the outer loop and one internal loop data as shown in figure 7.6. Using the outer loop and one internal loop information, complex loops under loading and unloading legs of the response were predicted and compared against the experimental data.

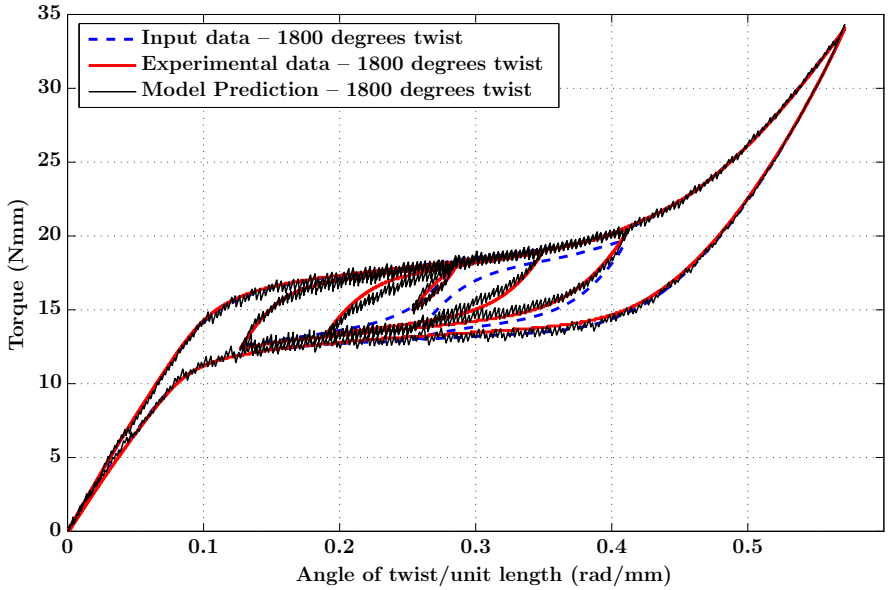

(a) Prediction of 1800^o twist with complex loop during the loading cycle using the input data as shown in figure 7.7.

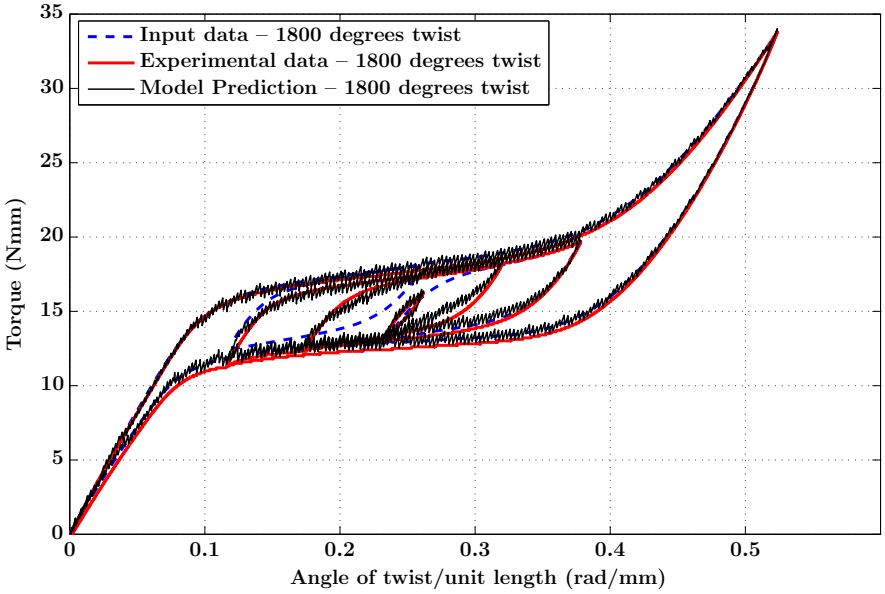

(b) Prediction of 1800^o twist with complex loop during the unloading cycle using the input data as shown in figure 7.7.

Figure 7.21: Figures show the prediction of complex loops for loading and unloading cases with 1800^o maximum twist using the hysterons generated with the outer loop and internal loop during loading and unloading stages as shown with full data simulation discussed in figure 7.7.

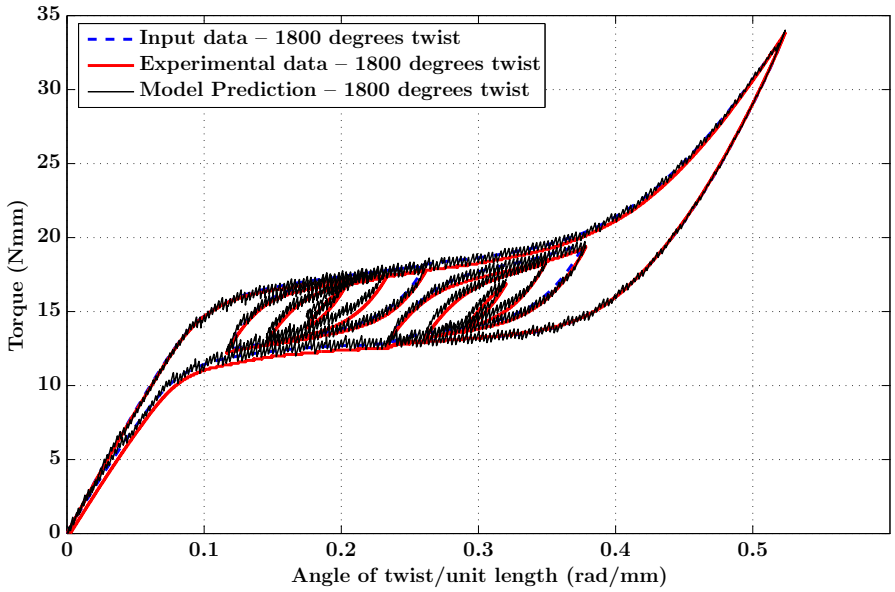

(a) Prediction of 1800^o twist using the input data as shown in figure 7.7.

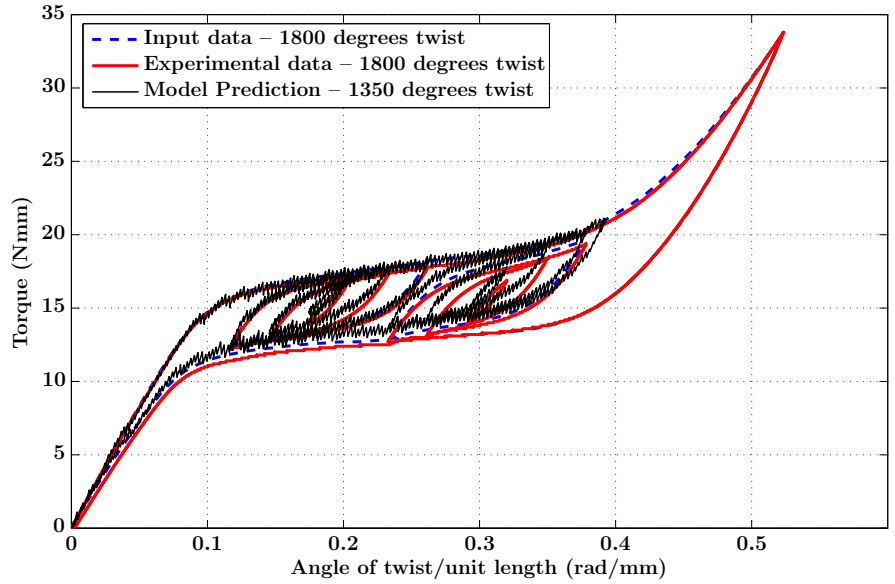

(b) Prediction of 1350^o twist using the input data as shown in figure 7.7.

Figure 7.22: Figures show the prediction of 1800^o and 1350^o maximum twist using the hysterons generated with the outer loop and internal loop during loading and unloading stages as shown with full data simulation discussed earlier in figure 7.7. The predictions are a close match to the experimental data when compared to earlier predictions as more information that included one big internal loop during loading and unloading stages along with outer loop was used for model predictions.

7.2.3 Simulation and Model Predictions for SMA Components (Wires and Springs) at Different Temperatures

The linear assumption ($a + b\theta$ terms in the model) was used to capture the temperature dependence of superelastic responses in SMA tension response. This assumption is extended for the torsion loading case for prediction of responses at different temperatures. Hence, it was assumed that the driving force doesn't change with temperature if compared for the "same extent of transformations (ξ_{tor})". The driving force expressions are estimated for the same martensitic volume fraction ξ_{tor} at two different temperatures θ_1 and θ_2.

7.2.3.1 Simulation and model predictions for SMA spring response at different temperatures

Figures 7.23a and 7.23b shows the model prediction at temperatures 348 and 398 K using the hysterons generated with the 373 K results as the data input. The predictions doesn't match exactly due to the fact that extent of transformation at 373 K is different when compared to that in case of 348 or 398 K results. The springs undergo only partial transformation from austenite to SIM at different temperatures above A_f. As seen in the experimental results from figure 2.5a, the higher the temperature above A_f, the lesser is the transformation from austenite to SIM and thus lesser is hysteresis area when compared against the same maximum deformation (75 mm) of the spring. The model predictions for different temperatures could match exactly if the superelastic responses at different temperatures are compared for the "same extent of transformation" for each temperature case. The model predictions at different temperatures would be over or under estimated based on the choice of temperature that is used to generate the hysterons for prediction. It has to be noted that hysteron parameters in this current estimation do not have to recomputed to

predict the response at different temperatures. If one needs to predict the hysteresis exactly for a partially transformed case then one would have to recompute the hysterons for the each temperature case.

7.2.3.2 Simulation and model predictions for SMA wire response at different temperatures

Figures 7.24a and 7.24b shows the model prediction at temperatures 297 and 338 K using the hysterons generated with the 297 K results as the data input. The experimental results at both temperatures were conducted at a frequency of 0.01 Hz obtained from [116]. The greater extent of transformation in the case of wires is evident from the estimation of driving force–volume fraction plot as shown in figure 3.3b when compared against corresponding estimation for springs as shown in figure 3.2b. Parameters need not be recomputed for predicting response at different temperatures as the same hysterons generated in the 297 K were used to estimate the response at 338 K. With higher temperature above A_f, the higher is the critical torque required for transformation and thus lesser is the transformation from austenite to SIM when compared against the same maximum deformation (450^o twist). The model predictions at higher temperatures doesn't match exactly as the "extent of transformation" is different in each case due to the fact both the tests were unloaded after 450^o twist [116]. Hence exact prediction of hysteresis could not be possible for such a case.

7.2.4 Simulation of SMA Wire Response for Different Diameters

The model was also used to predict the torsional response of two different wire diameters using the response for one diameter results as input. Chapman et al. [110] in their recent work reported experimental data for NiTi wires under torsion for three different diameters (viz. 0.018", 0.02" and 0.023") under isothermal conditions at

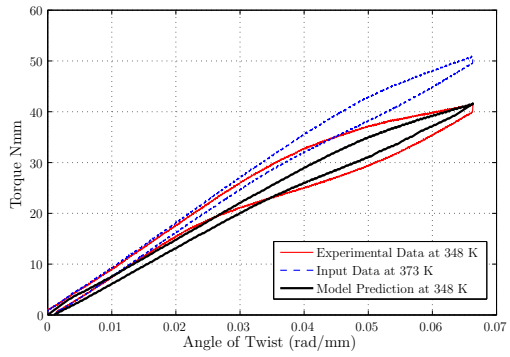

(a) Model prediction for 348 K compared with the corresponding experimental data.

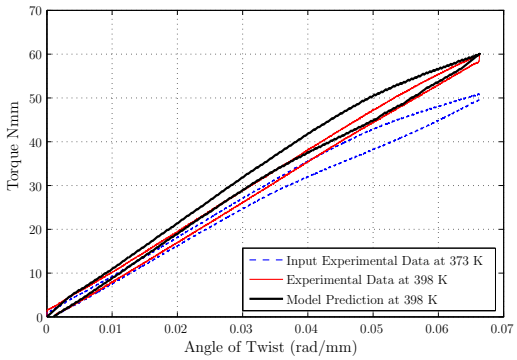

(b) Model prediction for 398 K compared with the corresponding experimental data.

Figure 7.23: Prediction for responses at temperatures 348 and 398 K using the hysterons generated from 373 K. The prediction does not match exactly due to the fact that extent of transformation at 373 K is different when compared to that in case of 348 or 398 K results. (details in section 7.2.3.1). The average error for this case was 8.7% and 5.2% for 348 and 398 K predictions respectively using hysterons generated from 373 K trial.

296 K as shown in figure 3 of [110]. Model prediction for diameters 0.018" and 0.023" using the model prediction at 0.02" results. Only the term "G_aJ" and "G_mJ" were changed depending on the diameter of wire chosen for prediction and the remaining model parameters were unchanged for predicting response. Figures 7.25a and 7.25b shows the model predictions for 0.018" and 0.023" dia case using hysterons generated in the 0.02" dia and the results show a close match. It must be pointed out that in the experimental results reported by Chapman et al. for three different diameters the "unloading point" selected is different for each diameter case. They claim to have selected the "unloading points" as "limits of transformation region" for each diameter case by testing each wire diameter specimen until failure [110]. If one assumes complete transformation for each case, the elastic deformation of stress induced martensite (SIM) would be different as the unloading points chosen are

different for each diameter case (evident in figure 2 from their work [110]). This would mean that the net hysteresis area when compared for the three diameters are different. So the use of same hysterons might not predict the hysteresis exactly unless "extent of transformation" in each case is the same.

Prediction of the results at different diameters is just an added feature of this model in addition to prediction of responses at different temperatures. It must be noted that predicting the torsional responses of different wire diameters using the response of one wire diameter is based on the assumption that the topology of the wire considered are the same. If a hollow and a solid wire with "equal polar moment of inertia" were loaded to the same torque, then the "extent of transformation" in the hollow wire would be greater compared to the solid wire as the untransformed austentic core (due to really small shear strains) in hollow wire is no longer an issue at higher torque levels. Hence the predicting responses for the same material at different diameters can be generalized if the topology of the specimen is the same and the specimens are subjected to the same "extent of transformation". Due to paucity of available experimental data on pure torsion for different wire diameters, only one case discussed in the paper was verified.

Torsional response of hollow SMA tubes/springs have also been of interest lately due the possibility that "hollow springs" could be a great way to harness SME/SE effects as they could be heated or cooled internally (see [18, 163–169] for more discussions on hollow SMA springs/tubes and their applications).

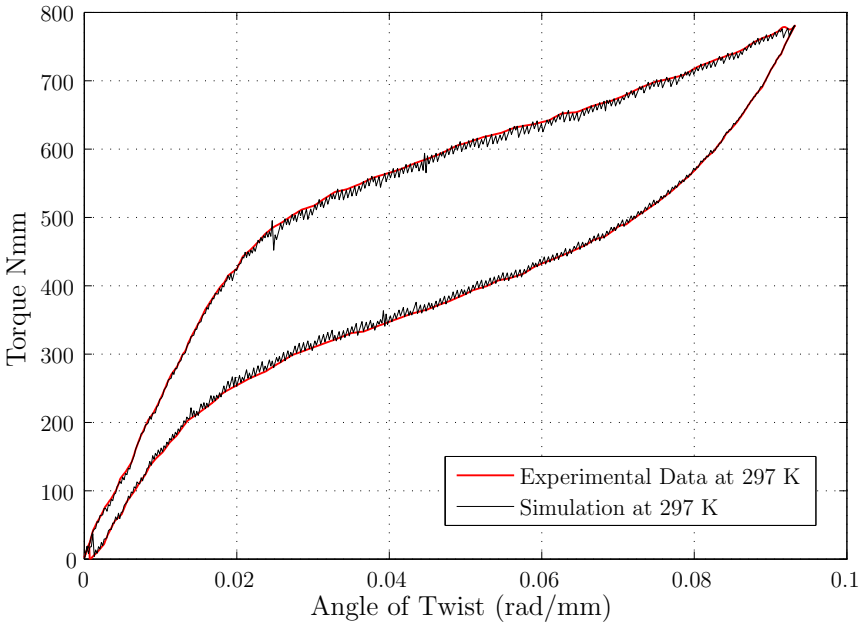

(a) Model simulation for 297 K using the input data at 297 K.

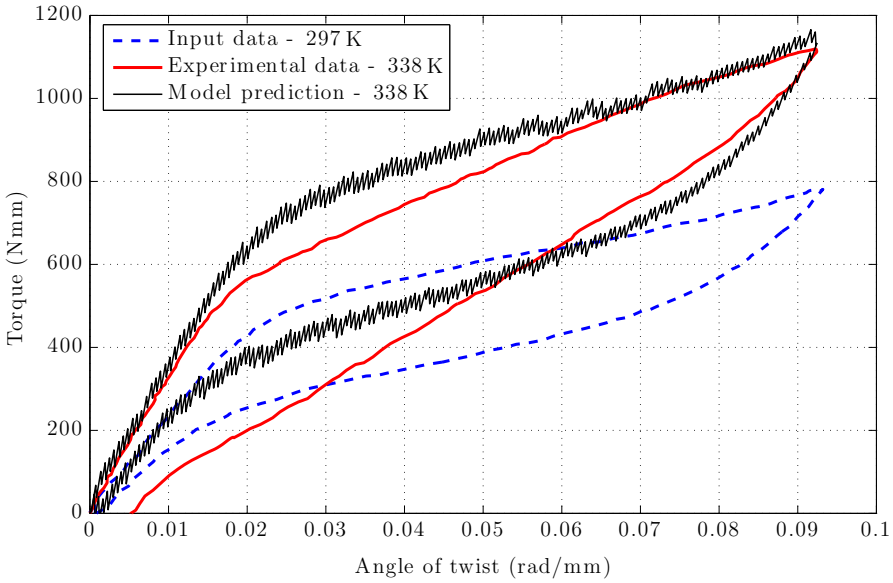

(b) Model prediction for 338 K using the input data at 297 K.

Figure 7.24: Prediction for responses at 338 K using the hysterons generated at 297 K. The results for both temperatures were obtained from [116]. The average error for this case was around 19%.

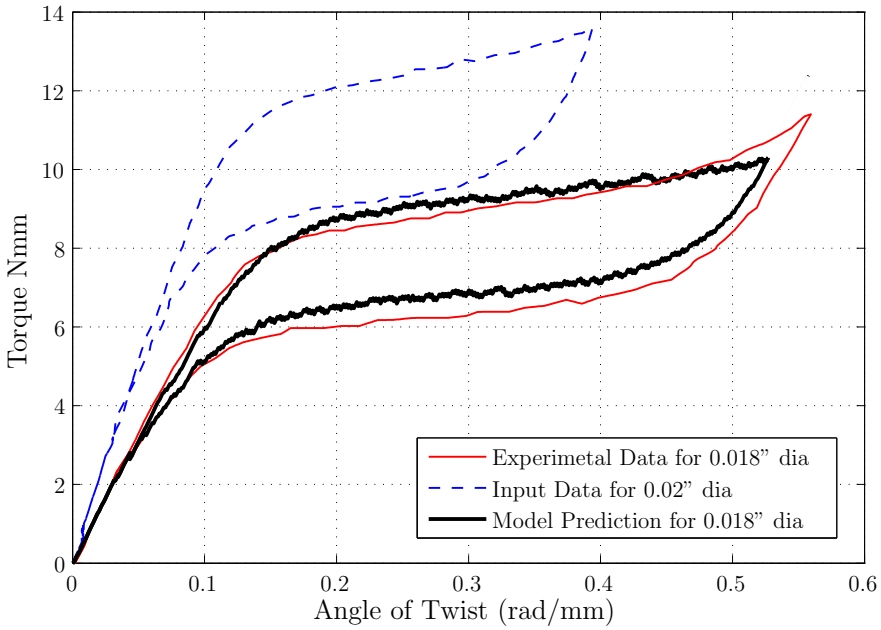

(a) Model prediction for 0.018" diameter using the input data for 0.02" diameter results.

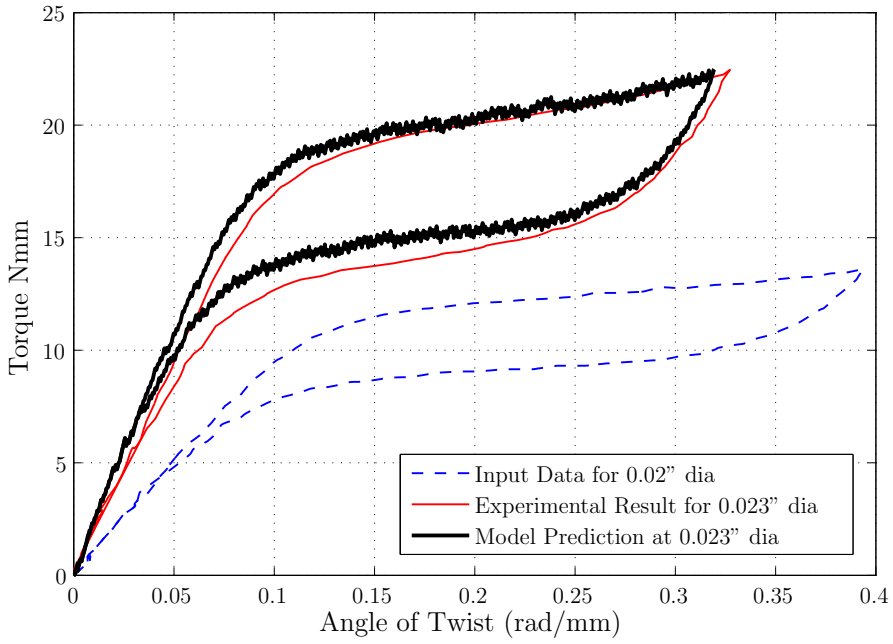

(b) Model prediction for 0.023" diameter using the input data for 0.02" diameter results.

Figure 7.25: Prediction for responses at different diameters 0.018" and 0.023" using the hysterons generated at 0.02". The experimental results for all cases were obtained from [110]. Model results show a close match with the experimental results with an average error $\sim 7\%$ for both cases.

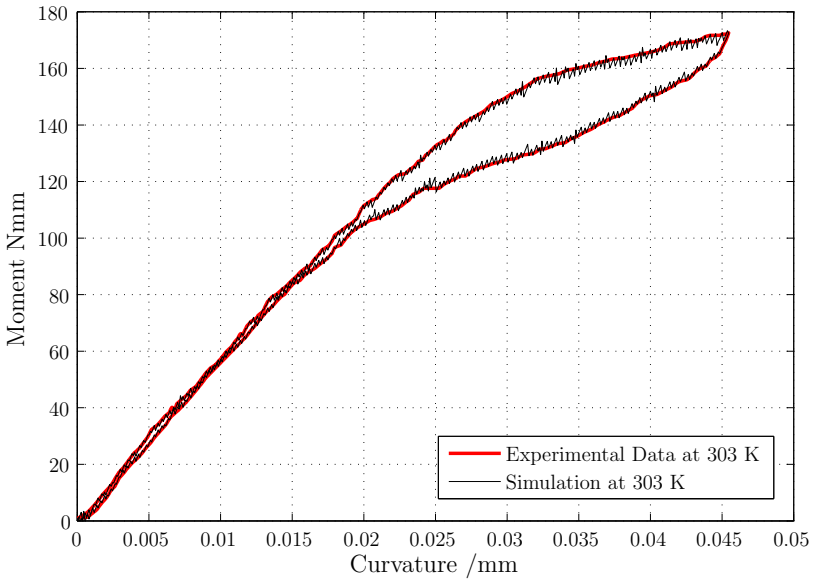

Figure 7.26: Model prediction for the superelastic response of NiTi SMA wire at 303 K. Model prediction and experimental results show a close match. The close match of simulation results shows the power of Preisach model since the Preisach parameters were chosen to fit the data. Experimental results at 303K were obtained from [132].

7.3 Pure Bending Results - Two Species

7.3.1 Simulations of NiTi SMA Wire and CuZnAl SMA Beam Response Using Bending Moment verses Curvature Data

Figure 7.26 shows the model simulation predictions as compared with experimental results at 303 K conducted on NiTi wire. Figure 7.27 shows the model simulation results at 308 K for CuZnAl beam as compared with the corresponding experimental results. The model shows a good fit with the experimental results and can estimate the hysteresis accurately for both NiTi and CuZnAl results. The close match of simulation results shows the power of Preisach model since the Preisach parameters were chosen to fit the data. The jaggedness in the response is due to employment of

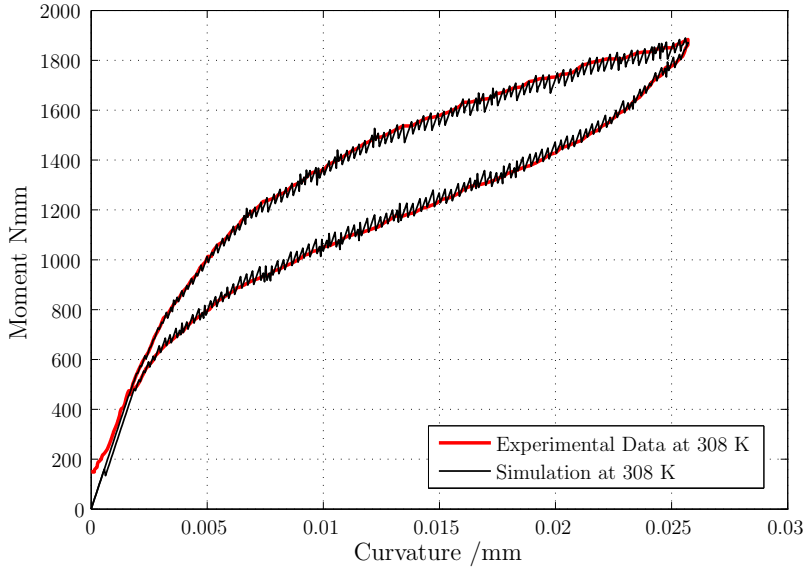

Figure 7.27: Model prediction for the superelastic response of CuZnAl SMA beam tested at 308 K showing a good match. The jaggedness in the response is due to employment of a discrete Preisach model in simulation. Experimental results at 308 K were obtained from [132].

a discrete Preisach model in simulation.

7.3.2 Prediction of Pure Bending Response of NiTi SMA Wire Response at Different Temperatures

Figure 7.28a and figure 7.28b shows the model prediction at temperatures 323 K and 303 K using the hysterons generated with the 323 K results as the data input. The hysteron parameters in this current estimation do not have to recomputed to predict the response at different temperatures. It is evident from the experimental results, that the higher the temperature above A_f, the lesser is the transformation from austenite to SIM and thus lesser is hysteresis area when compared against the same maximum curvature $\kappa = 0.045\ mm^{-1}$ as reported by Rejzner et al. [132]. The NiTi wires undergo only a partial transformation from austenite to SIM at different

temperatures above A_f and thus the "extent of transformation" at 323 K is different when compared to that of 303 K result. The model predictions for different temperatures could match exactly if the superelastic responses at different temperatures are compared for the "same extent of transformation" for each temperature case. The model predictions at different temperatures would be over or under estimated based on the choice of temperature that is used to generate the hysterons for prediction. If one needs to predict the hysteresis exactly for a partially transformed case then one would have to recompute the hysterons for the each temperature case as described earlier in section 7.3.1.

7.3.3 Prediction of Pure Bending Response of CuZnAl SMA Beam Response at Different Temperatures

Figure 7.29a and figure 7.29b shows the model prediction at temperatures 298 K and 308 K using the hysterons generated with the 318 K results as the data input. It is observed from the reported experimental results at 318K and 308K, that the specimen is subjected to a finite bending moment even at zero curvature (see figure 7 in [132]). This affects the predictions as the observed elastic behavior in CuZnAl case is much smaller when compared to NiTi case. This can be observed in 298 K predictions, where the elastic part of the response is over-predicted. Further, the maximum applied curvature was in the range of 0.027 to 0.03 mm^{-1} for different temperature trials reported by Rejzner et al. [132]. This suggests that the "extent of transformation" is different for each temperature case and hence resulting in over or under prediction of the hysteresis based on the trial (318 K experimental results in this case) chosen to generate the hysterons for prediction of responses at other temperatures.

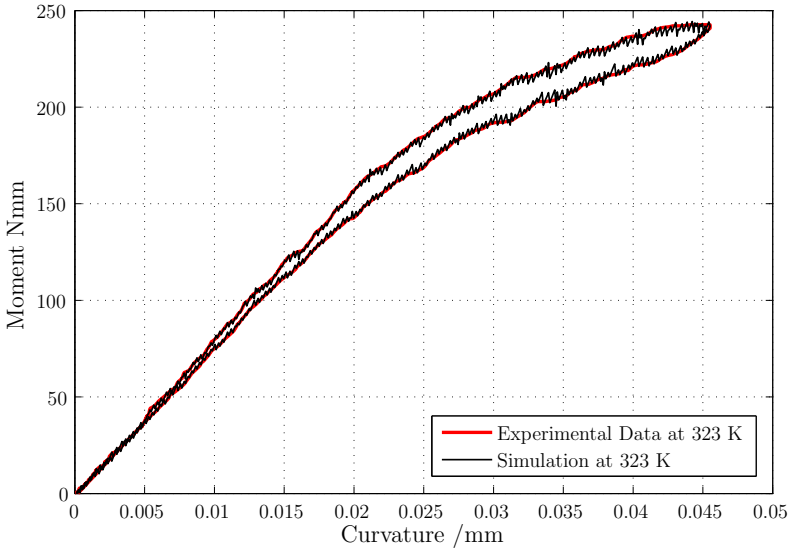

(a) Model prediction for 323 K compared with the corresponding experimental data at 323 K.

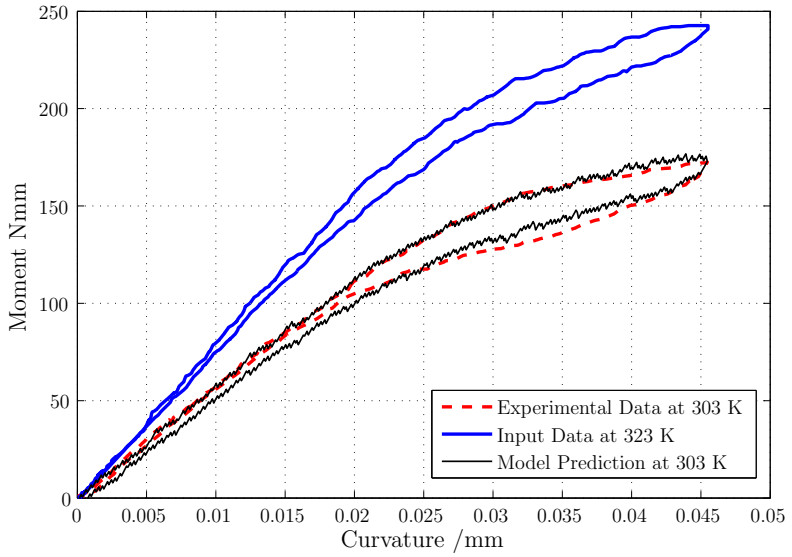

(b) Model prediction for 303 K compared with corresponding experimental results using the data at 323 K as input. The average error for this case between the model predictions and experimental results was $\sim 8\%$.

Figure 7.28: Prediction for responses at temperatures 323 and 303 K for a NiTi Specimen using the hysterons generated from 323 K. It must be noted that the extent of transformation at 323 K is different when compared to that in case of 303 K. The results for both temperatures were obtained from [132] (details in section 7.3.2).

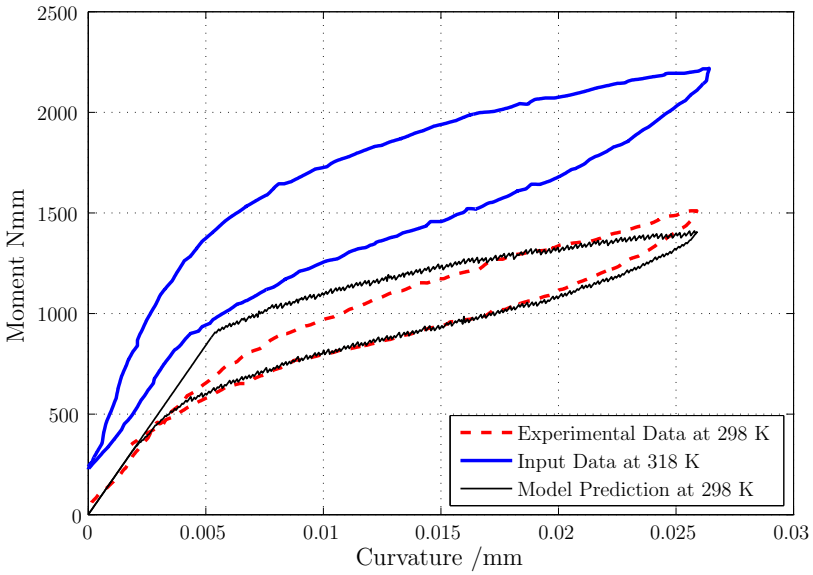

(a) Model prediction for 298 K using the input data at 318 K.

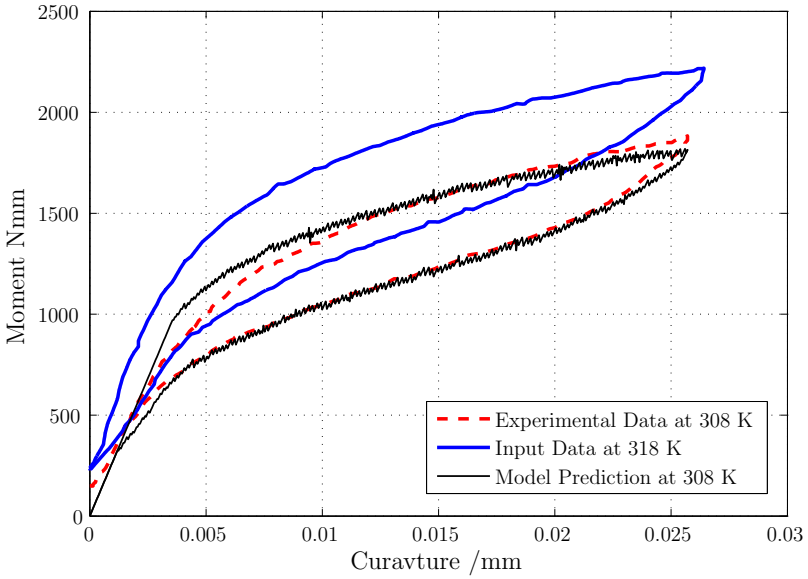

(b) Model prediction for 308 K using the input data at 318 K.

Figure 7.29: Prediction for responses for a CuZnAl specimen at temperatures 298 and 308 K using the hysterons generated at 318 K. The average error for both cases between the model predictions and experimental results was $\sim 16\%$. The results for both temperatures were obtained from [132].

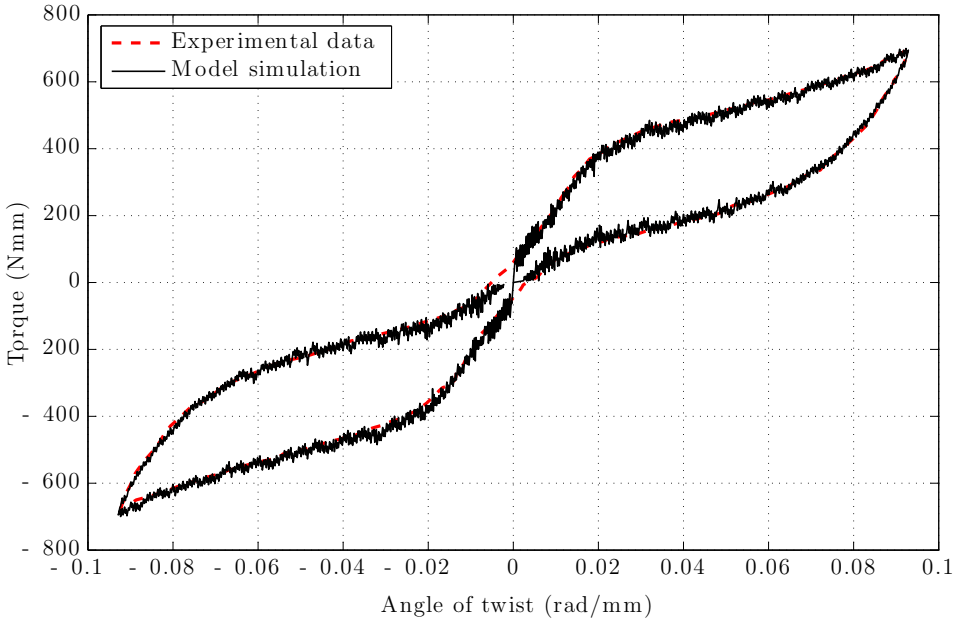

Figure 7.30: Model simulation for the superelastic response of SMA wire at 297 K under clockwise and anticlockwise twists. The simulation closely matches the experimental results demonstrating the power of Preisach approach. Experimental results were obtained from [116].

7.4 Torsion Results - Three Species

7.4.1 Simulations of SMA Spring and Wire Response Using Complete Torque verses Angle of Twist Data

Figure 7.30 shows the model simulation for the superelastic response of SMA wire at 297 K subjected to clockwise and anticlockwise twists. Figure 7.31 shows the model prediction for a twinning response of SMA spring tested at 295 K. The simulation closely matches the experimental results demonstrating the power of Preisach approach. The jaggedness in the response is due to the use of a discrete Preisach model.

The model was used to simulate responses of SMA components like springs, wires,

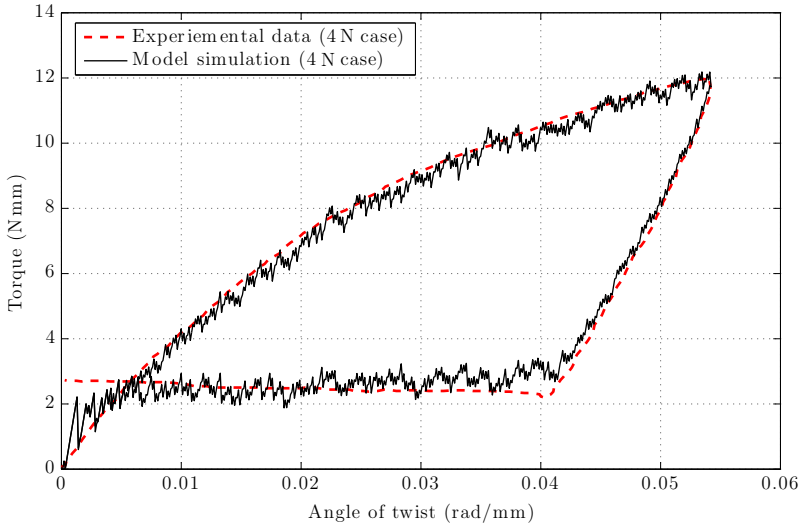

Figure 7.31: Model simulation for the twinning response of SMA spring tested at 295 K showing a good match. The jaggedness in the response is due to the use of a discrete Preisach model. Experimental results were obtained from [113].

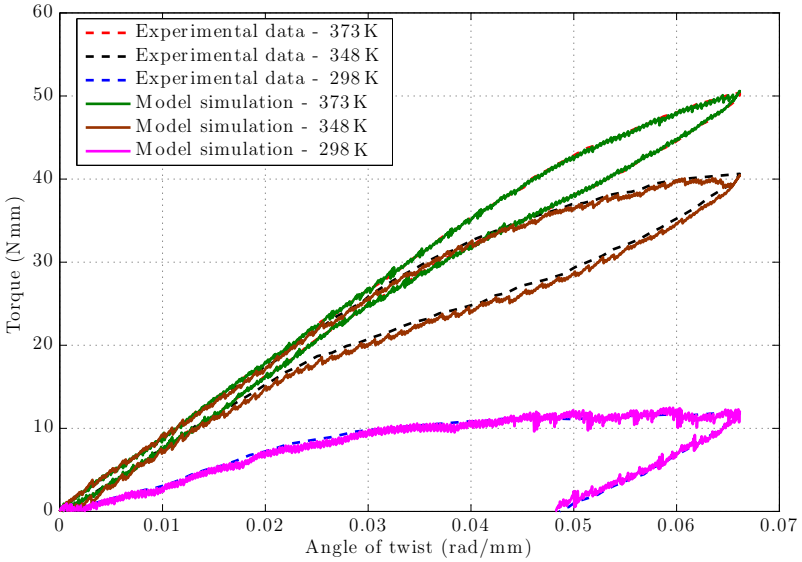

Figure 7.32: Model simulation for superelastic responses at different temperatures and twinning responses of SMA springs shown in a single plot. Simulation results are compared with corresponding experimental results and show a close match. Clockwise twist was assumed for all cases.

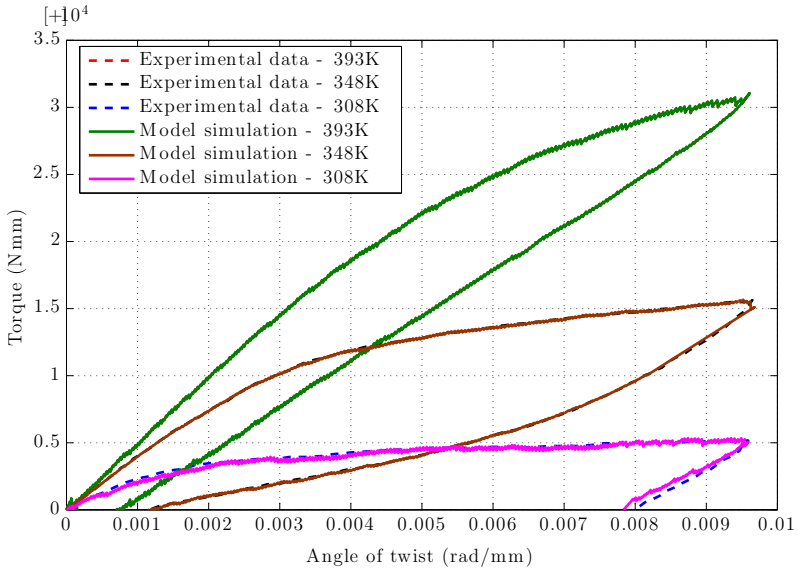

Figure 7.33: Model simulation for superelastic responses at different temperatures and twinning responses of SMA rods depicted in a single plot. Simulation results show a close match when compared with corresponding experimental results. Experimental results were obtained from [162] and clockwise twist was assumed for all cases.

rods at different temperatures for superelastic and twinning responses. Figure 7.32 shows model simulations for torsional response of SMA springs as compared with their experimental results. Figure 7.33 shows model simulations for torsional response of SMA rods compared with their experimental results. The advantages of formulating the model directly in terms of experimentally measurable quantities torque – twist is evident, as the model can be used to simulate torsional responses of SMA components with the predictions closely matching experimental results and thus showing the strength of Preisach approach under various test conditions.

7.4.2 Prediction of Responses of SMA Wires and Springs at Different Twists

Doaré et al. [116] performed quasi-static tests on superelastic wires at 297 K under clockwise and anticlockwise twists for different angles of twist – 100, 350 and 450^o

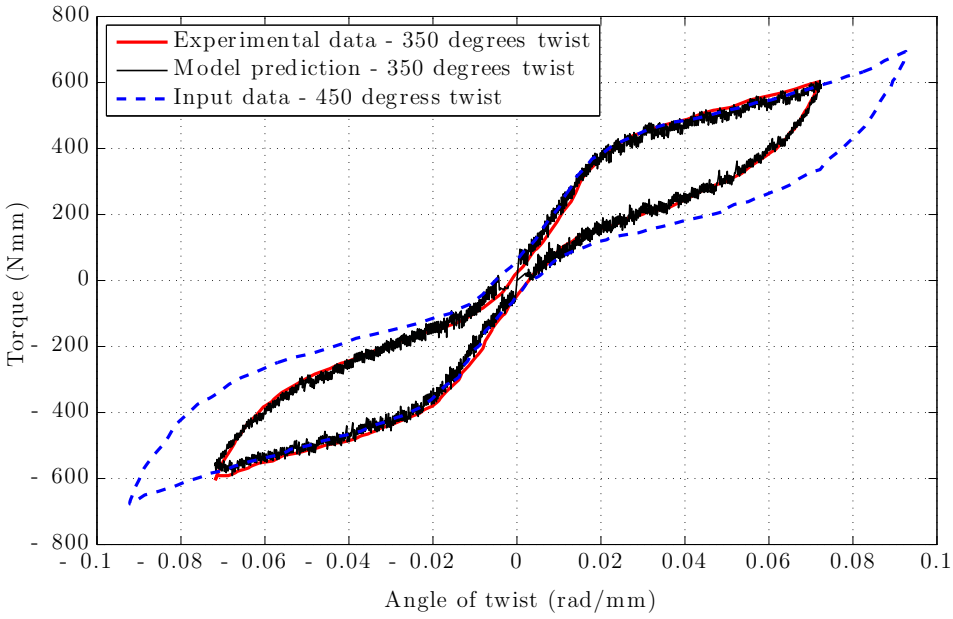

Figure 7.34: Model predictions for the superelastic response of SMA wire at 297 K under clockwise and anticlockwise twists for 350^o twist. The model input are the hysterons generated at the 450^o as shown in figure 7.30. Model predictions show a close match with the experimental results with an average error of 6%. Experimental results were obtained from [116].

twist. For predicting responses at different twists, the model is preferably calibrated at the maximum angle of twist and then used to predict responses at any lower twists. Figure 7.34 shows the model predictions at 350^o twist under clockwise and anticlockwise directions using the hysterons generated at 450^o twist. The assumption here was that 450^otwist data used for model calibration is the maximum possible twist encountered by sample without failure. As discussed earlier, since under torsional loading a fully transformed case is not possible due to really small shear strains at the core, thus such an assumption of maximum possible twist is made. However, specimens with a hollow cross-section can undergo complete transformation as the untransformed core is no longer an issue. Due to paucity of available experimental data on hollow cross-sections, the discussion is restricted to solid wires and springs

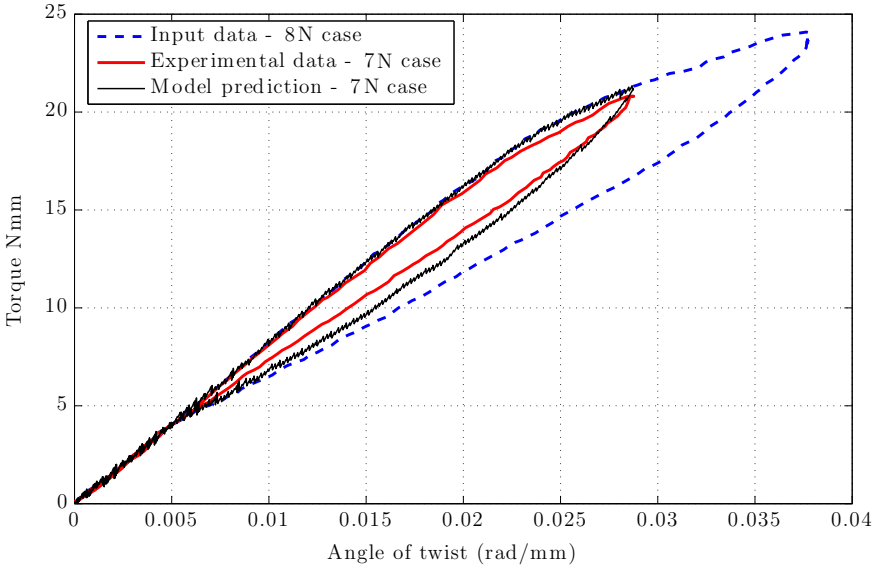

Figure 7.35: Model predictions for the superelastic response of SMA spring under 7 N load. The model input are the hysterons generated for 8 N case. Model predictions show a close match with the experimental results. The average error for this case was about 6.5%. Experimental results were obtained from [113].

here.

Aguiar et al. [113] performed quasi-static experiments on SMA extension springs under constant load conditions. Figure 7.35 shows the model prediction for superelastic responses of SMA spring at 7 N using the hysterons generated for 8 N case as input. Model predictions show a close match with the experimental results. Similarly, as shown in figure 7.36, the model was used to predict twinning responses of SMA spring at 295 K under 3.5 N load using the hysterons generated at 4 N as input.

In all the cases, none of the model parameters are recomputed as discussed in section 6.8 earlier. Simulation of both superelastic and shape memory responses of SMA components enables designers to use them for stroke estimation for SMA components when used as thermal actuators in many applications.

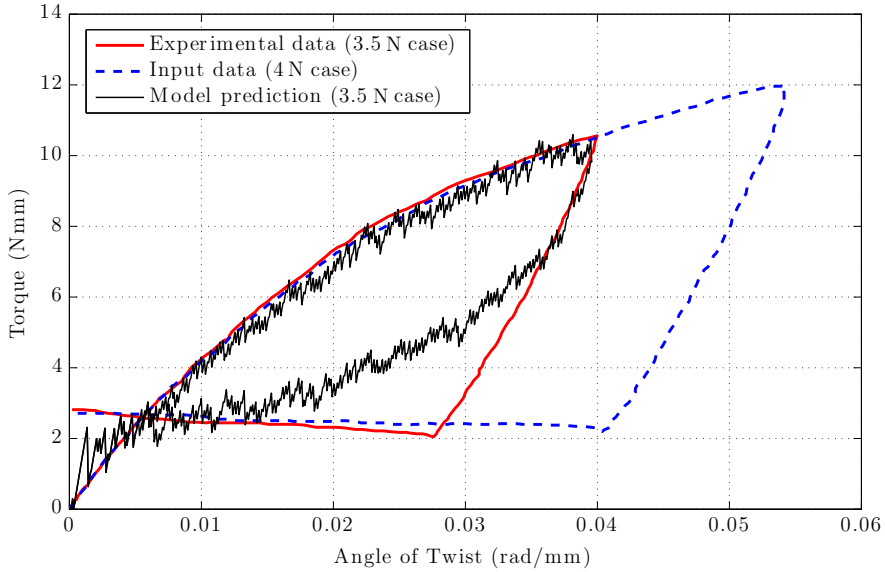

Figure 7.36: Model predictions for the twinning response of SMA spring at 295 K under 3.5 N load. The model input are the hysterons generated at 4 N as shown in figure 7.31. The average error for this case was about 14.8%. Experimental results were obtained from [113].

7.4.3 Prediction of Complete Superelastic Responses of SMA Wire at Different Operating Temperature

Figure 7.37 shows model prediction for an SMA wire at 338K using the hysterons generated at 297K as shown in figure 7.30. None of the model parameters are recomputed as discussed in section 6.8 earlier.

It is evident from the result that the model predictions don't show an exact match when compared against their corresponding experimental results. This is due to the partially transformed cases associated with torsional loading cases as discussed in section 7.2.3.1 and 7.2.3.2. One could achieve a fully transformed case for SMA components with hollow cross-sections as small shear strains at the core (i.e untransformed austentic core in case of superelastic responses) is no longer an issue. Model predictions at different temperatures for a hollow cross-section could possibly

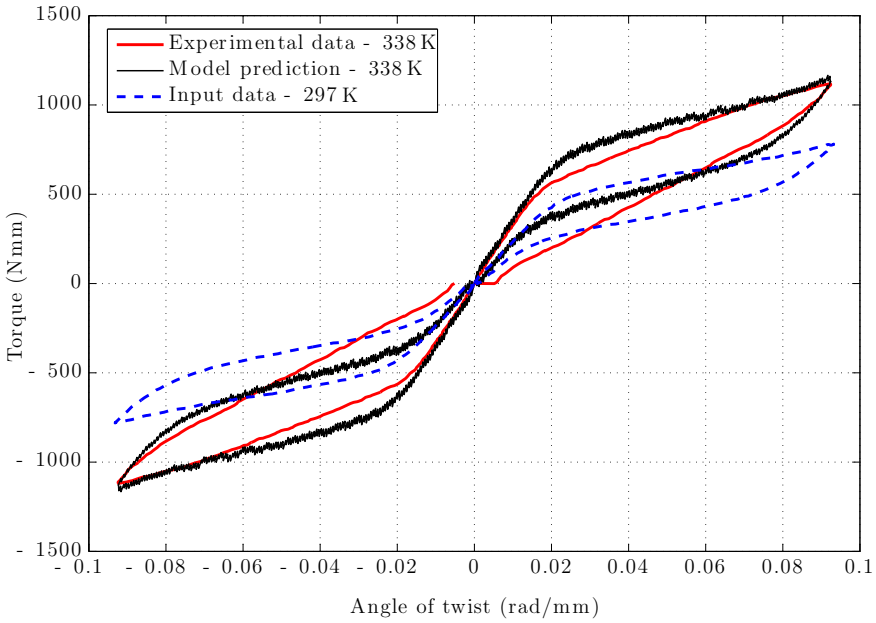

Figure 7.37: Model predictions for superelastic response of SMA wire at 338 K using the hysterons generated at 297 K under clockwise and anticlockwise twists as shown in figure 7.30. The average error for this case was around 19%. Experimental results were obtained from [116].

be compared for a fully transformed case. However, due to paucity of experimental data on hollow cross-sections, the discussion was restricted with SMA components having solid cross-sections [90].

7.5 Average Error Estimation : Model Prediction verses Experimental Results

In pure torsion and bending tests, the quantity "extent of transformation" is not experimentally measured and here this quantity is estimated using the torque–angle of twist data or bending moment–curvature data as shown in section 3.4 i.e using driving force – martensitic volume fraction expressions for the respective loading case. Given the test conditions and the fact that model predictions are based on hysterons generated from one experimental result as input data, an average error between the model predictions and the corresponding experimental results were estimated for

each case. The average errors were estimated using the trapezoidal integration rule (**trapz** command in MATLAB®).

$$\text{Average error} = \sqrt{\frac{\int(\text{Model value} - \text{experimental value})^2\, dx}{\left(\int \text{Experimental value}\right)^2\, dx}} \tag{7.1}$$

The average error is an estimate for that specific case as the model predictions could be different depending on the hysterons generated for predictions (i.e the choice of initial experimental data as input). The average error for each of model predictions discussed in this work are highlighted in figures 7.13a, 7.23, 7.24, 7.25,7.28b, 7.29,7.34, 7.35, 7.36, 7.34 and 7.37.

8. FUNCTIONAL DEGRADATION OF SMA COMPONENTS

8.1 Motivation and Literature Review - Functional Fatigue of SMA

With growing applications of SMA components in different engineering applications, the issue of material performance over its designed life is of great concern to researchers lately. As pointed out as Eggeler et al. [170] numerous factors can influence the fatigue life of SMA. Factors include material chemical composition, material impurity (i.e particle size distribution), type of loading, applied load magnitude, extent of deformation or plateau strains, processing conditions, defect accumulation, accumulated plastic deformation, microstructure and operating temperature being a few to list [170]. Over the years, numerous experimental data concerning SMA fatigue under superelastic conditions and thermal cycling (mimicking shape memory effects) have been reported. Most of the focus has been in understanding fatigue behaviour of SMA wires (see [171–173] for detailed reviews) under tension with some attention towards bending – rotating tests of SMA wire (see [170, 174–176] etc. for more discussions) and functional fatigue of actuator springs (see [177–180] etc. for more discussions).

Eggeler et al. [170] in their famous work subdivide SMA fatigue into two categories namely "structural fatigue" and "functional fatigue" (see figure 8.1). SMAs failing like other engineering material due to repeated high cyclic mechanical loads is classified under "structural fatigue" which is generally accompanied by defect accumulation, crack initiation (normally micro-structure controlled and growth - geometry dependent) [170, 181]. However, unlike classical material systems, SMAs are also sensitive to operating temperature fluctuations and interaction of SIM (stress induced martensite) as observed in the case of repeated SE cycles with "cyclic strain

and fatigue damage accumulation" that critically affects the phase transformation abilities [170, 181].

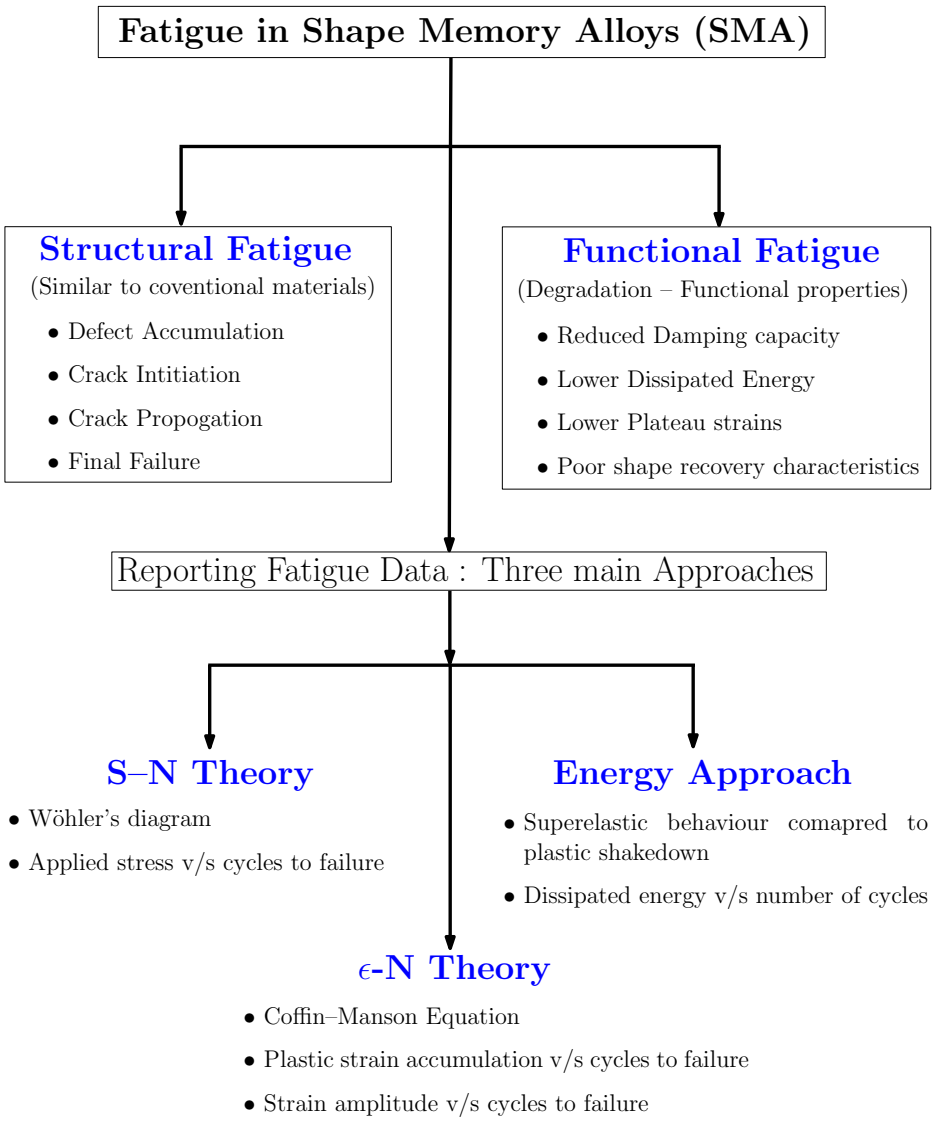

Figure 8.1: Figure describes classification of SMA fatigue into two categories namely "structural fatigue" and "functional fatigue" by Eggeler et al. [170, 181]. It also lists the three traditional approaches (theories) of reporting fatigue data in SMA literature primarily devoted for capturing superelastic effects (mostly mechanical loading effects with temperature being an external control parameter).

The traditional approach of reporting fatigue data in most of the SMA literature (see figure 8.1) is using any of the traditional fatigue theories listed below :

1. **S-N theory** or Wöhler's diagram to capture "applied stress verses cycles to failure" plots (see [182–187] for examples).

2. **ε-N theory** that plot "strain amplitude verses cycles to failure" or employ "Coffin–Manson (modified Coffin–Manson approaches in some cases)" under low cycle fatigue cases to obtain "plastic strain accumulation verses cycles to failure" relationships (see [188–193] etc. for examples).

3. **Energy approach** that develop relationships between dissipated energy verses number of cycles under stabilized superelastic effects. Superelastic behaviour is compared to plastic shakedown for these analysis (see [194–198] for examples).

Such empirical theories solely focus on mechanical loading effects with temperature being a external control parameter. Generally with such theories, relationships are developed for each temperature case (see figure 14 in [182], figure 2 in [176], figure 7 in [199] for illustrations) and are limited to analysing superelastic effects. Given the fact that thermomechanical responses of SMA are sensitive to operating temperature fluctuations under superelastic conditions, such traditional theories are incapable of capturing functional degradation under coupled thermomechanical cycling of SMA components.

To capture such complex thermomechanical responses, theories considering both mechanical and thermal effects in a single framework must be employed rather than modifying classical fatigue theories developed for pure mechanical loading cycles. In conventional materials like steel or aluminum, such an approach appears to be fruitful. For example, Naderi, Khonsari and co-workers have discussed a thermodynamic approach of using the entropy produced over specimen lifetime subjected to

fatigue tests to analyze material degradation [200, 201]. Their approach considered the Clausius–Duhem inequality to discuss the rate of volumetric entropy generation that includes "mechanical dissipation due to plastic deformation, non-recoverable internal energy and thermal dissipation owing to heat conduction" [201, 202]. Using this inequality, a quantity described as total entropy gain or fracture fatigue entropy (FFE) is developed by integrating the inequality from time $t = 0$ to the time of failure $t = t_f$ [201–203]. They proposed that FFE is material dependent but independent of geometry, load and frequency in their discussion with material systems like metals (stainless steel, aluminum) and some composite laminate systems like woven glass/epoxy [201, 204]. The temperature fluctuations considered were a resultant of plastic deformation of the material and further a "relationship between normalized cycles to failure and normalized entropy generation" is assumed to be linear to predict fatigue life of the material (see equation 5.3 in [201]). In classical materials (like most metals and alloys), the surface temperature rise at higher stresses is a resultant of hysteresis heating and several polynomial, exponential relationships to capture this temperature rise over material life have been proposed (see figure 1 [205] for a summary of several such efforts). In most of these efforts, the mechanical and thermal effects are decoupled and such simple relationships work well with classical materials [205–207]. Though such approaches have a strong thermodynamic base, developing relationships for surface temperature rise or capturing the "rate of volumetric entropy generation" for SMA can get quite cumbersome given the complex hysteretic thermomechanical nature of SMA responses that are temperature dependent. Further, in SMAs the mechanical and thermal effects are coupled and influence the component functionality together. Hence, developing relationships for plastic strain energy per cycle that capture both mechanical and thermal loading effects can get quite tricky (see equation 4 in [203, 207] for some examples that

consider only mechanical loading for aluminum and Stainless steel materials).

Motivated by Knosari & co-workers, an effort to develop a thermodynamically based approach for characterizing functional degradation in SMA where phase transitions and associated irreversibility add an additional degree of complexity that is not present in conventional materials is undertaken here. The approach presented here is capable of overcoming the limitations of the FFE approach and traditional S-N or ε-N theories for analyzing functional fatigue of SMAs.

Following the approach highlighted in section 3 which employs a two species Gibbs potential based formulation to separate the thermoelastic and the dissipative part of the entire SMA component response is employed here. The models were formulated directly using experimentally measurable quantities like torque–twist or moment–curvature with the intention of developing relationships directly at the component level. Using thermodynamic principles, relationships for "driving force for the phase transformation" and "extent of phase transformation" were established.

The driving force relationships would capture both mechanical and thermal loading effects in the same framework with the ability to capture both shape memory and superelastic effects using a single formulation. Hence, a plot of driving force verses no. of cycles would play the role of a traditional S-N curve. This quantity would be equivalent to the thermodynamical force for onset of phase transformations which are directly responsible for the functionality of SMA components (shape changing capability and large recoverable strains).

In case of thermally activated SMA components (mimicking shape memory effects), a drop in driving force amplitude would directly correspond to material loosing its ability to undergo phase transformations which directly corresponds to loss in functionality of SMA component. In case of superelastic effects, a relationships of "driving force for the phase transformation" and "extent of phase transformation"

can also be used to analyze shakedown effects under repeated SE cycles as these relationships capture the pure dissipative part of the SE response. Designers can use this approach as a guideline for analyzing functional degradation of SMA components used as thermal actuators or damping elements under both shape memory and superelastic conditions.

The application of this approach requires two steps

1. Use of a model to convert thermomechanical cycles to driving force for phase transformation versus extent of transformation (i.e volume fraction of martensite).

2. Using experimental data to plot these modified variables as a function of no. of cycles (i.e driving force amplitude verses no of cycles).

The driving force for transformation and volume fraction of martensite expressions developed for tension and torsion loading cases in section 3 are provided below for convenience.

The driving force for the phase transformation in the superelastic response of the SMA components under tension is shown in equation 8.1. Similarly, expression for the martensitic volume fraction evolution (ξ_{ten}) using expressions 3.7 and 3.11 is shown in 8.2 below.

$$\begin{aligned} \boldsymbol{\mathcal{F}_{ten}} = \sigma\varepsilon_{max} - \frac{\partial \boldsymbol{\mathcal{G}_{ten}}}{\partial \xi_{ten}} \implies \boldsymbol{\mathcal{F}_{ten}}\dot{\xi_{ten}} = P_{ten}^{inel} \\ \text{Hence, } \boldsymbol{\mathcal{F}_{ten}} = \sigma\varepsilon_{max} + \sigma^2\left(\frac{1}{2E_M} - \frac{1}{2E_A}\right) - B(2\xi_{ten} - 1) + b\theta + a \end{aligned} \tag{8.1}$$

$$\xi_{ten} = \frac{\varepsilon - \dfrac{\sigma}{E_A}}{\dfrac{\sigma}{E_M} - \dfrac{\sigma}{E_A} + 1} \tag{8.2}$$

The driving force for the phase transformation for the superelastic response of the

SMA components under pure torsion is shown in equation 8.3. The volume fraction evolution expression ξ_{tor} obtained using equations 3.21 and 3.25 is shown in equation 8.4.

$$\begin{aligned} \boldsymbol{\mathcal{F}_{tor}} &= T\phi_{max} - \frac{\partial \boldsymbol{\mathcal{G}_{tor}}}{\partial \xi_{tor}} \implies \boldsymbol{\mathcal{F}_{tor}}\dot{\xi_{tor}} = P_{tor}^{inel} \\ \text{Hence, } \boldsymbol{\mathcal{F}_{tor}} &= T\phi_{max} + T^2\left(\frac{1}{2G_M J} - \frac{1}{2G_A J}\right) - B(2\xi_{tor} - 1) + b\theta + a \end{aligned} \tag{8.3}$$

$$\xi_{tor} = \frac{\phi - \dfrac{T}{G_A J}}{\dfrac{T}{G_M J} - \dfrac{T}{G_A J} + 1} \tag{8.4}$$

This two step procedure with experiments carried on SMA springs will be an illustration of this approach.

8.2 Highlights : Driving Force – Volume Fraction Relationships

Some highlights of using such a thermodynamic based approach to determine Driving force – volume fraction relationships are summarized below [64, 90]:

- There is a greater connection with the thermodynamics of the response and an added capability of simulating both load and displacement controlled experiments in a single modeling framework.

- It is not necessary to use different approaches for stress and temperature driven phase changes observed with SMA response as the driving force expression captures both the mechanical and thermal loading in the same framework i.e torque (T) and operating temperature (θ) here.

- Driving force expressions 8.1 or 8.3 are the equivalent of thermodynamical force for onset of phase transformation effect which is directly responsible for the functionality of SMA component. A drop in driving force corresponds

to material loosing functionality i.e material is no longer transforming and performing its intended function. Hence, this quantity can used as a parameter to analyze the functional degradation of SMA components.

- The volume fraction relationship can help us estimate the extent of transformation using the torque and twist as input data. This is particularly useful in torsional loading cases as the SMA components are partially transformed. This is due to the fact that the shear strains tends to zero at the core of the specimen crosssection as the wire twists under torsion [90, 116]. The possibility of a fully transformed case is possible only the angle of twist asymptomatically reaches infinity at the core prior to the component failure [90, 116]. Doaré et al. [116] have reported experimental results on SMA wire subjected to different degrees of twist (100, 350 and 450^o twist) to illustrate this point of partial transformation (see figure 4 in [116].) in real world applications.

- A driving force – volume fraction plot that solely captures the dissipative part of the response can also be used to analyze shakedown effects observed with typical superleastic responses associated with SMAs. This can substitute "Energy approach" that develop relationships between dissipated energy verses number of cycles under stabilized superelastic effects by comparing SE behaviour to plastic shakedown.

- With the model formulation in terms of stress–strain or torque–twist, designers can use the model to analyze component behaviour directly as the model can use the sensor data as inputs. Though this approach is restricted to specifically analysing SMA components under tension or torsion loading case, it could be extremely useful for designers in analysing the functional degradation of SMA components.

8.3 Thermomechanical Fatigue Tests

The following section describes the details of the test rig and test protocol designed to capture the functional degradation effects. The entire test rig is entirely using LabVIEW® software (see figure 8.4) to execute user defined thermomechanical tests on SMA components like NiTi extension springs.

8.3.1 Experimental Setup Description

The custom built test rig consists of an assembly of the following parts procured from various suppliers (see figure 8.2) :

- Test Frame parts custom fabricated by 80-20 Inc®
- SM–100N load cells and strain gauge transducer amplifier (SGA) supplied by Interface Force Inc®.
- Programmable power supplies PMC 5–18A and PAS 20–18A from Kikusui America Inc®.
- Data acquisition systems (DAQ), model USB 2416–4AO from Measurement Computing® and NI-myDAQ from National Instruments®
- Brushless DC muffin fans Model OD1225–12HB from Knight Electronics (Orion Fans)
- Triple Output power supply CPS 250 from Tektronix for controlling muffin fan speed
- End hooks and extension rods from Mark–10®

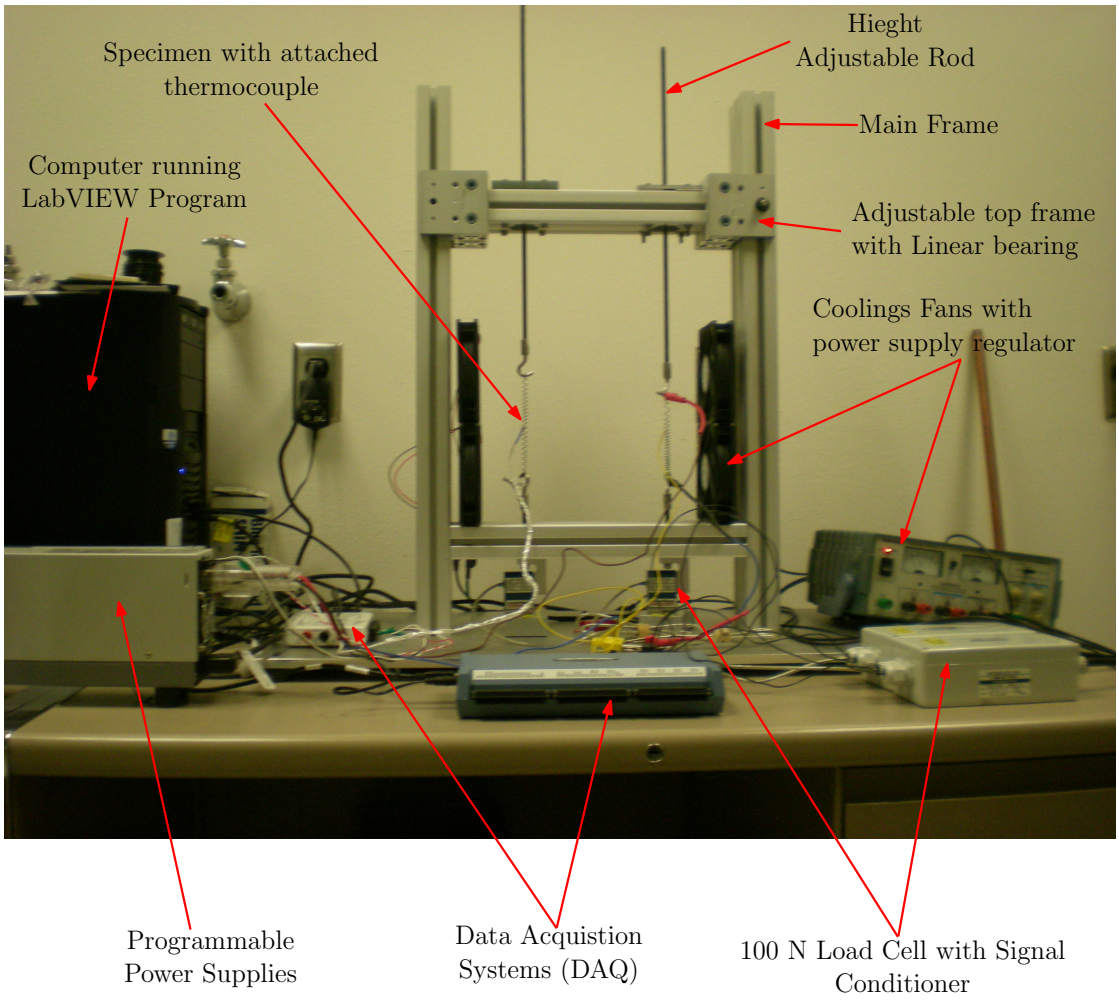

Figure 8.2: Custom built thermomechanical fatigue test rig controlled entirely using LabVIEW® software to execute user defined thermomechanical test protocols. More details of the setup in section 8.3.1.

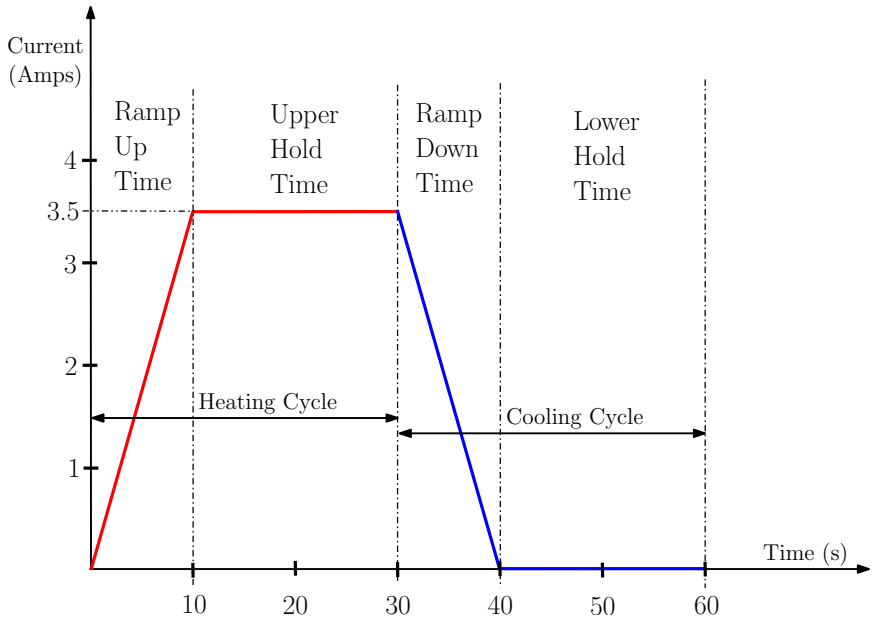

Figure 8.3: Thermal cycle adopted to simulate shape memory effect to ensuring complete M↔A transformations. More details in section 8.3.2.

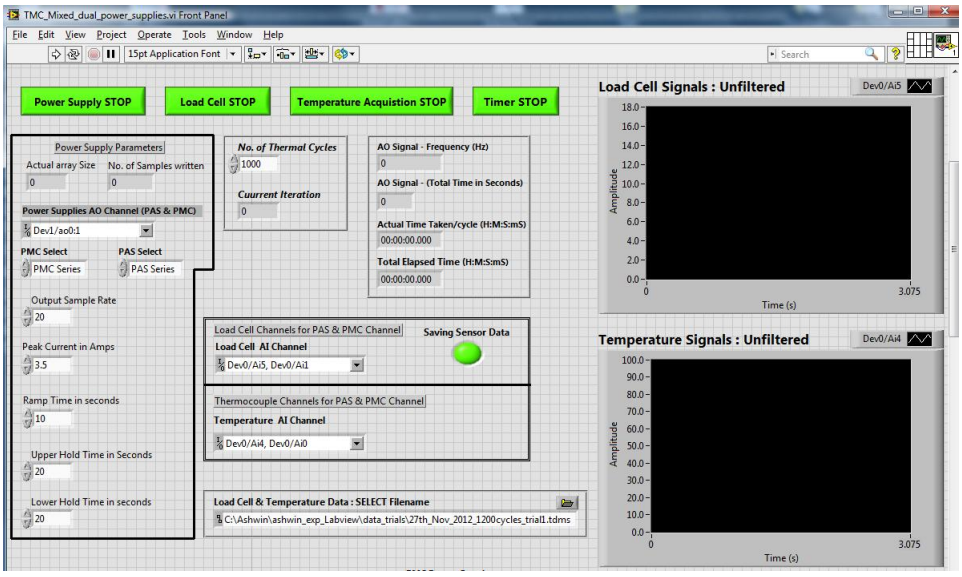

Figure 8.4: Snapshot of LabVIEW® program front panel used to create user defined thermomechanical cycles as described in figure 8.3. More details on the LabVIEW® program are available in Appendix A.

The test frame consists of two vertical columns mounted on a base plate. A movable upper crosshead supported by a linear bearing attachment and a lower fixed crosshead are positioned between the two vertical columns as shown in 8.2. The upper frame is supported by a linear bearing attachment for proper positioning on the vertical column based on specimen gauge length selected. Height adjustable extension rods with end hooks are employed for positioning specimen. The load cells are positioned between the lower frame and the base plate with the load cell axis co-linear with specimen loading axis. The load cell's output is connected to the strain gauge transducer amplifiers (SGA) for a 0–10 V analog input (AI) control as suggested by supplier (see section A for more details). The output from SGA are connected to a differential AI channels of DAQ for continuous measurements using LabVIEW® software. Programmable power supplies were employed for resistive heating of the test specimen (i.e passing DC through the specimen) with the test leads connected between the hooks holding the test specimen (see section A for more details). The power supplies are programmed to run in a "constant current mode (CC)" using an 0–10 V external voltage source as defined by user in the LabVIEW® program. DC muffin fans are employed for specimen cooling controlled by constant voltage external power supply. "K-type" thermocouples were used to continuously record specimen temperature as a function of time using DAQ and LabVIEW® program. More details on the LabVIEW program are available in A.

8.3.2 Thermal Cycle Definition

In order to simulate shape memory effect, a thermal cycle as shown in figure 8.3 is employed to ensure (M→A) and (A→M) transformations. A thermal cycle of $60s$ is divided into two segments – a $30s$ heating cycle followed by a $30s$ cooling cycle. Due to high resistance of Ni-Ti, cooling fans are employed for forced convection cooling of

specimen especially during the cooling cycle. Using these thermal cycles repeatedly, one can simulate SME and capture the functional degradation of the test specimen held under constant deformation. The breakup of the heating and cooling cycles are given below :

1. **Ramp Up Time** - A part of the heating cycle where a peak current of 3.5 amps is reached in a time interval of $10s$. The peak current is selected such that the temperature of the specimen is well above A_f to ensure complete (M→A) transformation.

2. **Upper Hold Time** - A part of heating cycle where a hold time of $20s$ is provided at the peak current of 3.5 amps to ensure complete (M→A) transformation of the test specimen.

3. **Ramp Down Time** - A part of cooling cycle where a gradual drop from 3.5 back to 0 amps is achieved. This segment is the mirror of ramp up time.

4. **Lower Hold Time** - A part of cooling cycle where a hold time of $20s$ is employed to ensure the temperature of the specimen is below M_f to ensure complete (A→M) transformation.

8.3.3 Material and Test Methodology

SMA actuator extension springs were obtained from Images SI Inc with composition details of 55.91 % Nickel, balance Titanium with trace elements $< 0.25\%$ as provided by supplier [208]. The SMA wire was 30 to 40% cold worked before shape setting it into extension springs. The transformation temperature of interest A_f as reported by the supplier was around 325 K. The spring specifications are as follows.

- Mean coil diameter of the spring "D_m" = 5.5 mm

- Wire diameter "d" = 0.754 mm
- Spring Index "C_m" = 7.3
- Free length "L_f" = 26.8 mm
- Number of active coils "n" = 20.

The springs were predeformed to 75 or 100 mm stroke and held between the hooks as shown in figure 8.2. The springs are subjected to repeated thermal cycles as defined in figure 8.3. For every cycle, load cell and thermocouple sensor readings are continually recorded as a function of time using the data acquisition system (DAQ) and LabVIEW® program. The predefromed springs are martensitic at the start of the test. During the heating cycle, the springs contract thus generating a recovery force which is measured by load cell continuously. The springs relax back to their original predeformed configuration at the end of the cooling cycle.

8.4 Results and Discussions

The same driving force – volume fraction relationship expressions can be used to analyze functional degradation of components under both shape memory and superelastic effects.

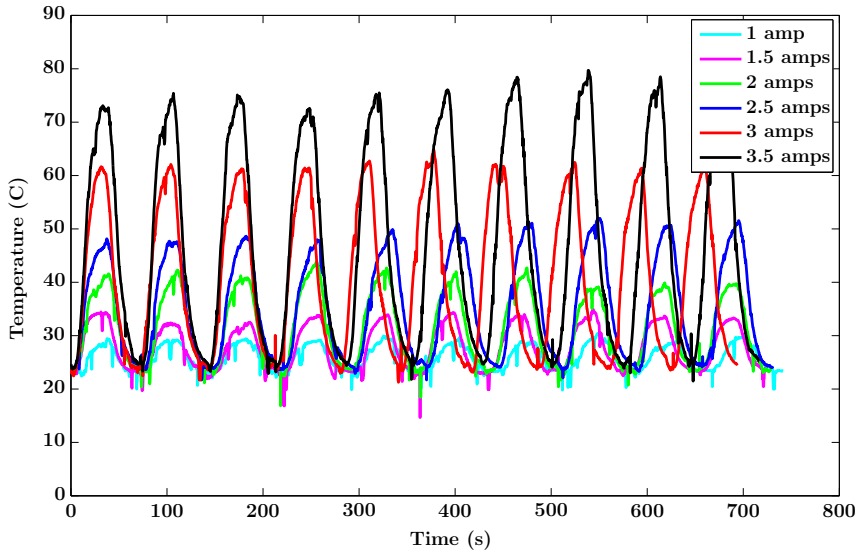

(a) Thermal cycles at different currents peak current using profile described in figure 8.3. Plot showing temperature vs. time for 10 thermal cycles.

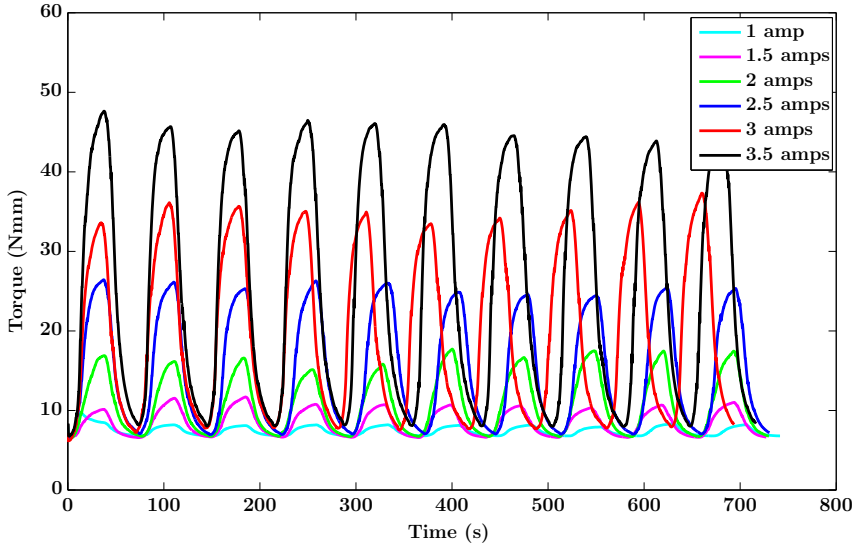

(b) The equivalent torque vs time plots for 10 thermal cycles. Clear increase in peak recovery/pull forces with increasing currents.

Figure 8.5: SMA spring $S1$ was predeformed to 75 mm stroke and thermally cycled at different peak currents. Corresponding temperature vs time ; torque vs time plots are shown in the subfigures.

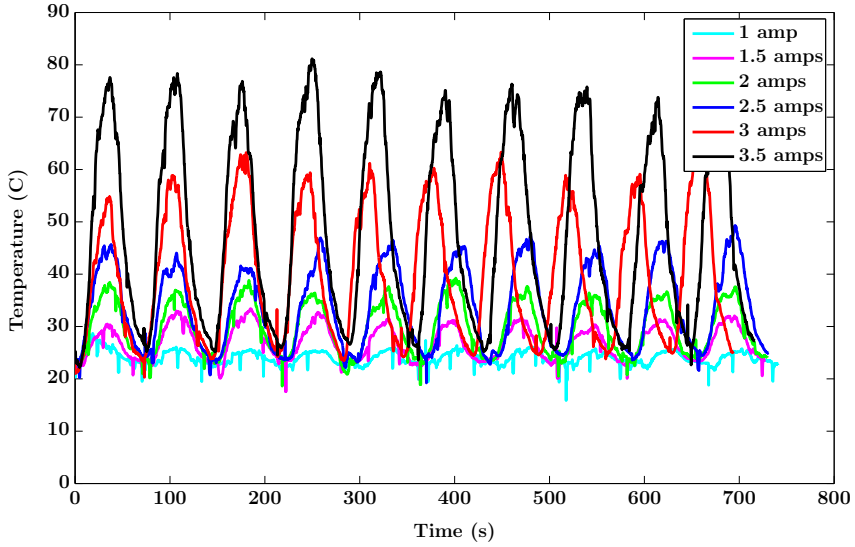

(a) Thermal cycles at different currents peak current using profile described in figure 8.3. Plot showing temperature vs. time for 10 thermal cycles.

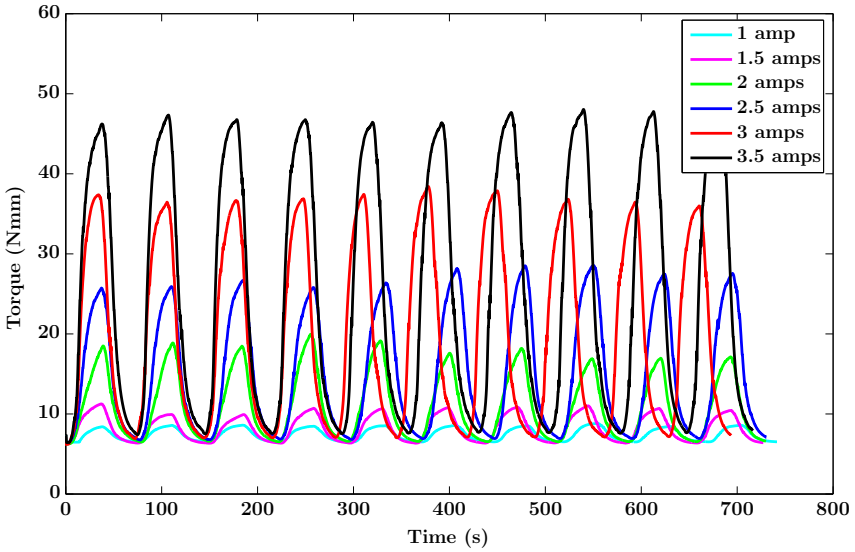

(b) The equivalent torque vs time plots for 10 thermal cycles. Clear increase in peak recovery/pull forces with increasing currents.

Figure 8.6: SMA spring $S2$ was predeformed to 75 mm stroke similarly to the one described in 8.5 and thermally cycled at different peak currents. Corresponding temperature vs time ; torque vs time plots are shown in the subfigures.

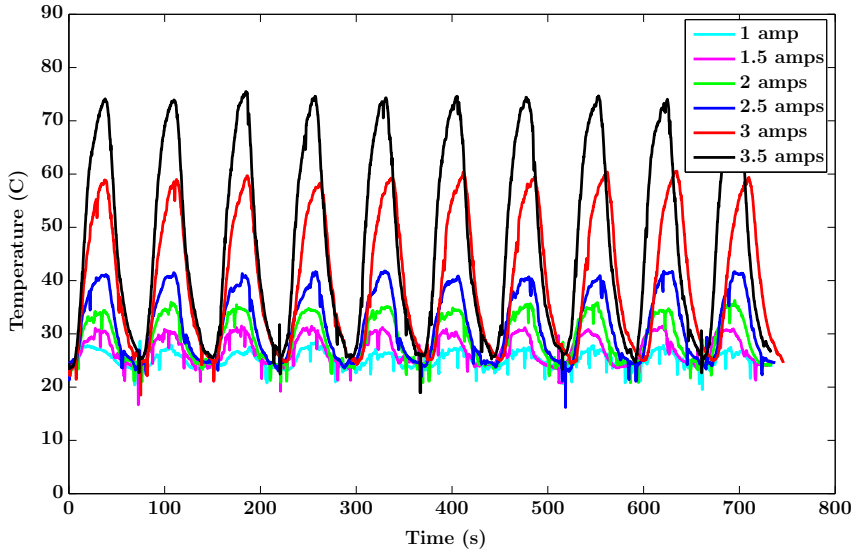

(a) Thermal cycles at different currents peak current using profile described in figure 8.3. Plot showing temperature vs. time for 10 thermal cycles.

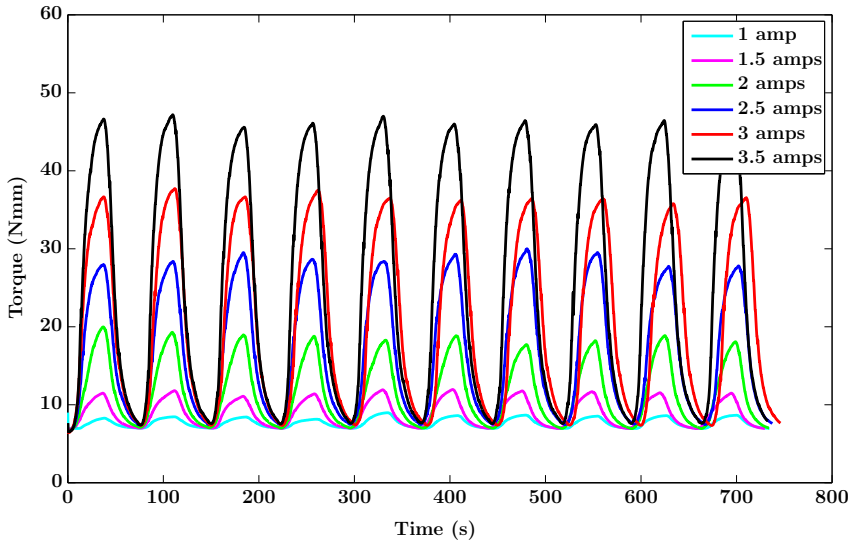

(b) The equivalent torque vs time plots for 10 thermal cycles. Clear increase in peak recovery/pull forces with increasing currents.

Figure 8.7: SMA spring $S3$ was predeformed to 100 mm stroke and thermally cycled at different peak currents. Corresponding temperature vs time ; torque vs time plots are shown in the subfigures.

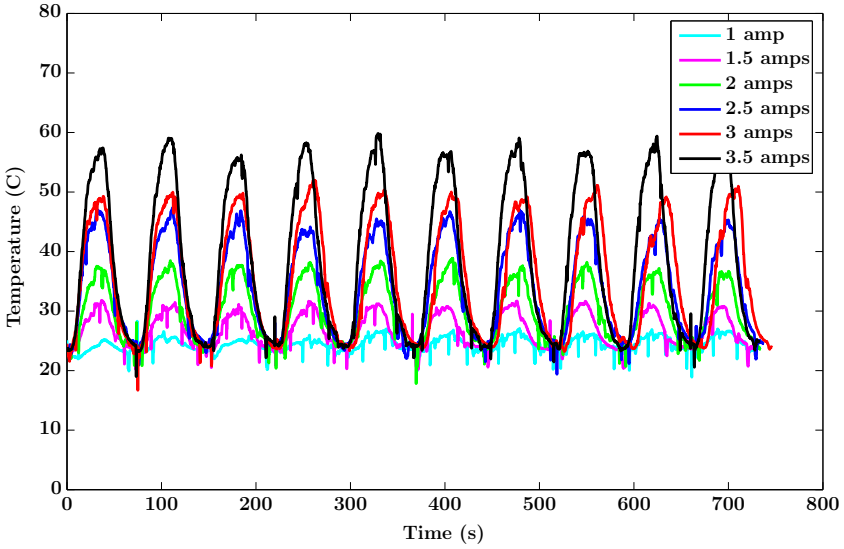

(a) Thermal cycles at different currents peak current using profile described in figure 8.3. Plot showing temperature vs. time for 10 thermal cycles.

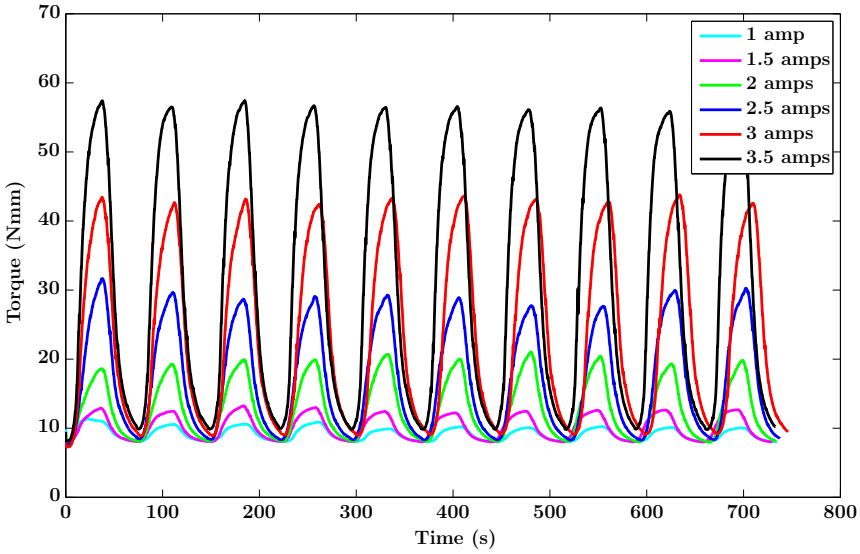

(b) The equivalent torque vs time plots for 10 thermal cycles. Clear increase in peak recovery/pull forces with increasing currents.

Figure 8.8: SMA spring $S4$ was predeformed to 100 mm stroke similarly to the one described in 8.7 and thermally cycled at different peak currents. Corresponding temperature vs time ; torque vs time plots are shown in the subfigures.

8.4.1 Response of SMA Spring Under Thermomechanical Loading

Predeformed springs were used to study the SMA spring recovery/pull force response for 10 repeated thermoemchanical cycles as described in figure 8.3 with different peak currents. Two springs were predeformed to 75 mm stroke and two other springs were predeformed to 100mm stroke. All these springs were subjected to thermal cycles described in figure 8.3 with different peak currents of 1 amp, 1.5 amps, 2 amps, 2.5 amps, 3 amps and 3.5 amps. These different currents cause resistive heating and the springs reach different temperatures. If the temperatures reach A_s, it causes the predeformed springs to transform to austenite and generate a recovery force. With higher currents/temperatures, one would expect higher recovery pull forces.

Figures 8.5 and 8.6 show the SMA springs $S1$ and $S2$ predeformed to 75 mm stroke and subjected to different peak currents. The corresponding temperature vs time ; torque vs time plots indicate clear increase in peak recovery/pull forces with increasing currents.

Figures 8.7 and 8.8 show the corresponding plots for predeformed springs $S3$ and $S4$ with 100 mm stroke.

8.4.2 Thermal Cycling of SMA Springs – Mimicking SME

The sensor data collected over the specimen lifetime of the tested samples are used as inputs in equation 8.3 to capture the driving force variation for further analysis. Figure 8.9 shows the driving force variation over thermal cycles defined in 8.3 for one sample predeformed for 75 mm stroke. Figure shows the driving force drop over number of cycles indicating loss of functionality. It is also clear the driving force amplitude for each cycle reduces with increasing number cycles. This has been illustrated in figure 8.10 where the driving force amplitude against the number of

cycles.

In order to understand this further, multiple samples were tested with the same starting driving force. The driving force is a combination of load and temperature. Multiple combinations of load and temperature can lead to a common starting driving force. Using results in section 8.4.1, two combinations of load–temperature were selected to conduct repeated cyclic tests (solid and broken lines representing different combinations). All these tests were overlapped on the same plot to analyze the degradation trend. Figure 8.12 shows a semilog plot of driving force vs number of cycles with different spring samples starting with relatively same driving force amplitude. Samples with same starting driving force amplitudes show reasonably similar pattern in functional degradation over number of thermomechanical cycles.

The quantity driving force would be the thermodynamical force equivalent for onset of phase transformations which are directly responsible for the functionality of SMA components (shape changing capability and large recoverable strains). Hence a drop in driving force amplitude would directly correspond to material loosing its ability to undergo phase transformation which directly corresponds to loss in functionality of SMA component. Since multiple combinations of load and temperature can yield with same driving force amplitude, this quantity could be a true representation of the phase transforming ability and subsequently capturing damage in SMA components. Since this quantity capture both the mechanical and thermal effects in a single framework, hence, this quantity can be used by designers as a guideline for analyzing functional degradation of SMA components. For example, designers can fix a threshold where if the driving force amplitude drops to 80% of its initial value then the component has lost its functionality and needs replacement. This plot can be useful in designing SMA components like springs, wires or tubes in automotive, aerospace and biomedical applications that use them as thermal actuators due to

their ability to deliver large working strokes [8, 18, 24, 26, 50, 56–58].

8.4.3 Shakedown Analysis – SE

Eggeler and co-workers [170, 209] conducted repeated pull-pull superelastic tests on SMA flat specimens at 294 K. Driving force – volume fraction expressions 8.1 – 8.2 or 8.3 – 8.4 can used to capture the pure dissipative part of the superelastic response as the thermoelastic part was separated out. Figure 8.11 shows the stress–strain converted to corresponding driving force – volume fraction plots that capture pure dissipative part of the superelastic response. The figure clearly shows a decrease in driving force – volume fraction area with increasing cycles demonstrating the shakedown effects and which directly corresponds to reduced dissipative ability of the SMA component. This plot can be particularly useful for designers in analyzing functionality of SMA components like large SMA springs, beams that are employed as damping elements in bridges, buildings and also in seismic resisting systems due to their excellent energy dissipation and re-centering capabilities [20, 43–46, 55].

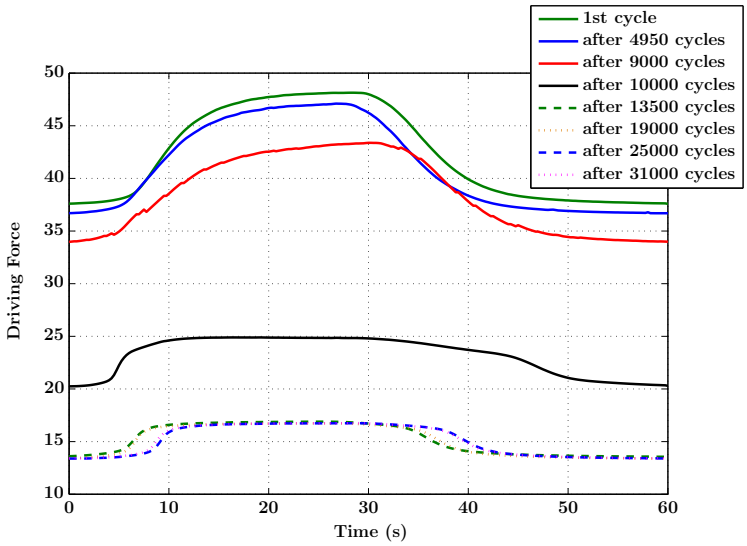

Figure 8.9: Driving Force variation over thermal cycles defined in figure 8.3. The drop in driving force drop over number of cycles clearly indicating loss of functionality. The amplitude also reduces with increasing cycles.

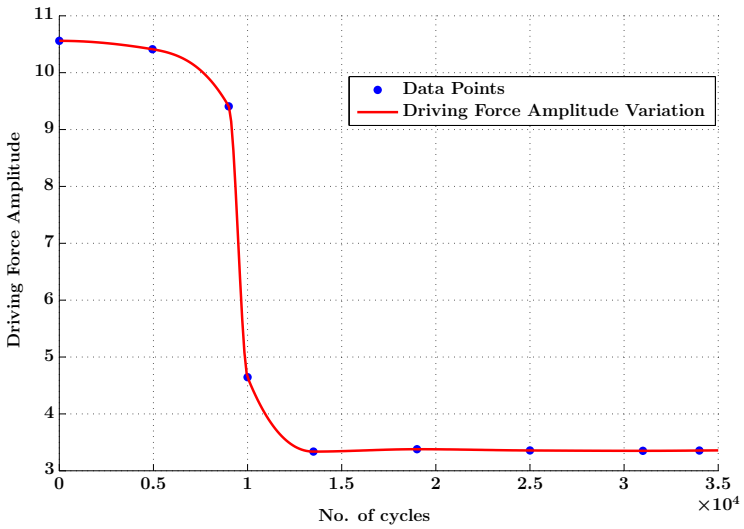

Figure 8.10: Driving Force amplitude as a function of cycles that can used to analyze functional degradation of SMA components. A drop of Driving force indicates that the material is no longer transforming and loosing its functionality.

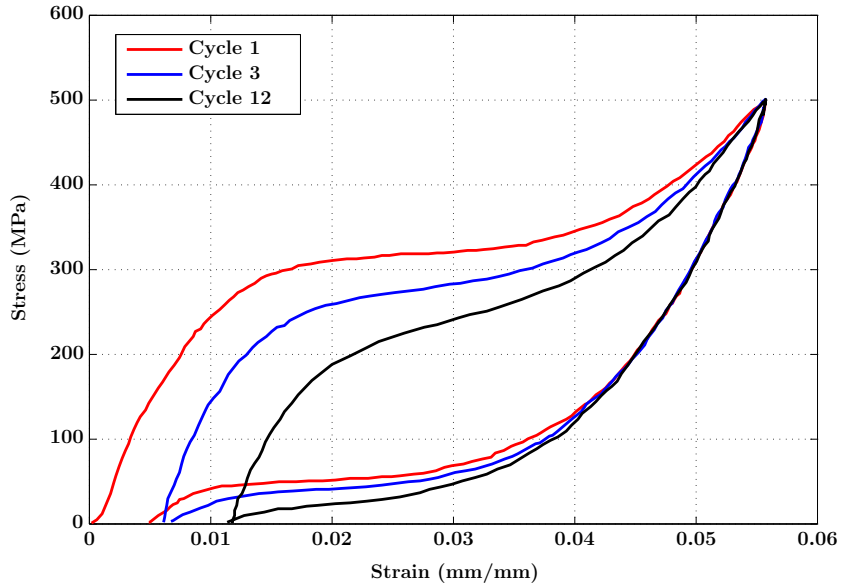

(a) Stress–strain data for 12 deformation cycles.

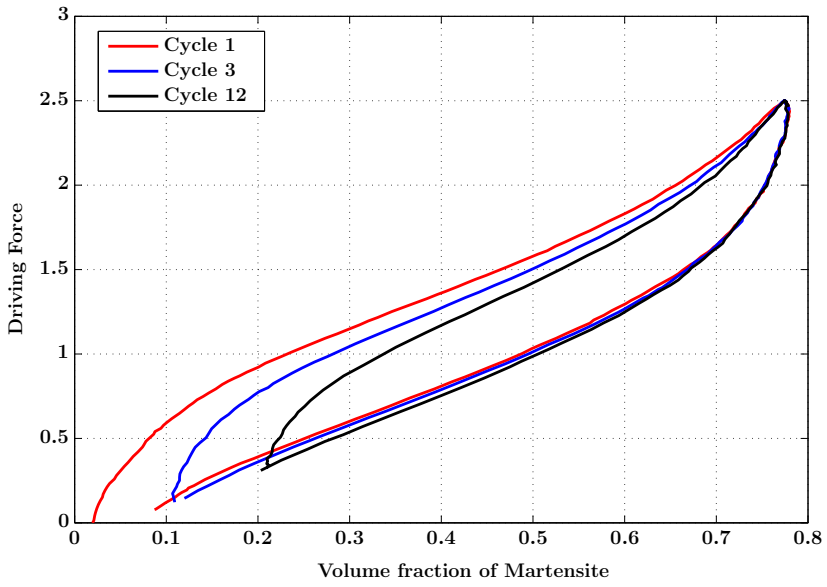

(b) Corresponding Driving force – volume fraction plot capturing pure dissipative part

Figure 8.11: Figure shows stress–strain converted to corresponding driving force – volume fraction plots using equation set 8.1 and 8.2 that capture pure dissipative part of the superelastic response. Figure clearly shows a decrease in driving force – volume fraction area with increasing cycles which directly corresponds to reduced dissipative ability of the SMA component. Experimental data obtained from [170, 209].

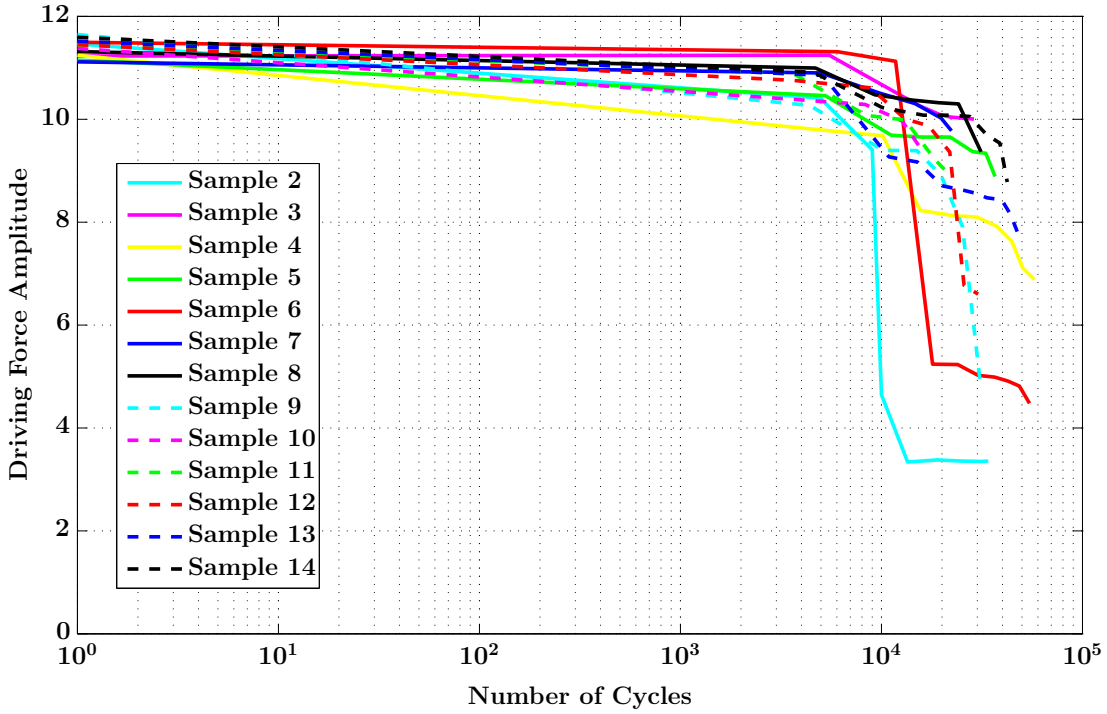

Figure 8.12: Figure shows the functional degradation of various samples starting relatively at the same driving force amplitude. The solid lines indicate one particular combination of load and temperature case. The dotted lines indicate another combination load–temperature combination with the same starting driving force amplitude. Samples with same starting driving force amplitudes show reasonably similar pattern in functional degradation over number of thermomechanical cycles.

9. SUMMARY AND CONCLUSIONS

9.1 Experiments on SMA Components Like Wires and Springs

- Thermally responsive SMA demonstrate interesting properties like superelasticity (SE) where typically exhibit complex, nonlinear hysteretic response and understanding their coupled thermomechanical responses is of critical importance for both researchers and application developers.

- SMA component responses are also affected by alloy composition, thermomechanical processing history, changes in operating temperature and loading rates.

- SMA components are tested under tension (wires) and torsional (wires and springs) loading cases with the purpose of elucidating the internal loop responses both during loading and unloading. The effect of operating temperature is also investigated.

- These experiments also allows designers to get an insight into behavior of internal loops and analyze "return point memory (RPM) or sink point memory (SPM)" aspects of the hysteretic response. RPM and SPM play an important role in design as it provides important information on the ability of SMA components to return back to its original unloading point upon completion of a smaller hysteretic loop. SMA components showing a "good RPM/SPM characteristics" is indicative of minimal residual/irreversible deformations after they were subjected to repeated complete or partial transformations during applications.

- From an application standpoint, improved understanding of torsional responses

under partial or fully transformed cases with internal loops is of particular importance as in many cases the entire response is utilized and only a partial internal loop might be of significance

9.2 Conclusions for Two Species Thermodynamic Preisach Approach

- The goal of this work was in developing simple strength of materials based models and tools for superelastic shape memory alloys (SMA) under tension, torsion and bending loading conditions.

- The key idea here is of separating the thermoelastic and the dissipative part of the hysteretic response using Gibbs potential and thermodynamic principles. The dissipative part of the response is accounted for using a discrete Preisach model. Such an approach combines the physics and elegance of the thermodynamic based approach with the algorithmic efficiency/simplicity of the Preisach model and thus providing an effective way in predicting complex hysteretic responses of SMA components like wires, beams and springs.

- The models are constructed based directly on experimentally measurable quantities like torque and angle of twist, bending moment–curvature etc., rather than solving for non-homogeneous shear stresses, strains directly across the wire cross-section (especially for torsion and bending loading cases).

- The modeling approach can simultaneously include both thermal and mechanical loading in the same framework with the capability of simulating both load and displacement controlled experiments. Further, it allows for easy handling of temperature variations observed in superelastic responses of SMA in addition to capturing complex internal loops. The model predictions were used

to predict SMA component responses at different operating temperatures or twists.

- The use of a discrete Preisach model to capture the hysteretic part of the response, one can do an approximate or a precise prediction by controlling the use of number of Preisach elements and the input data used for model calibration. This way one doesn't have to choose different functions for simulating approximate or fine predictions and thereby saving computational time.

- The modeling approach can capture complex hysterestic responses with multiple internal loops with ease. In addition, it can capture temperature dependence of responses with reasonable ease.

- An approximate response prediction could be beneficial for design purposes but a more precise prediction is essential from the control systems standpoint. Prediction of torque v/s angle of twist, moment verses curvature responses of SMA components directly could greatly facilitate designers in designing components for various engineering applications.

9.3 Conclusions for Three Species Thermodynamic Preisach Approach – Capturing the Complete Torsional Response

- Extending the two species thermodynamic Preisach modeling approach, a model to capture the complete torsional response of SMA components like wires, rods and springs under both superelastic and shape memory effects is formulated by combining thermodynamics principles along with discrete Preisach models.

- The key idea was in employing a three species Gibbs potential based formulation to separate the thermoelastic response from its dissipative response for both superelastic and twinning responses.

- The three species considered were austenite and two martensite variants under clockwise and anticlockwise rotations thus enabling the prediction of responses under both twisting directions.

- The proposed approach allows a greater connection with the thermodynamics of the response and an added capability of simulating both load and displacement controlled experiments in a single modeling framework.

- The model results were compared with experimental results for wires, bars and springs showing a close match with an average error being $< 15\%$ for most predictions.

9.4 Conclusions for Thermodynamic Force Approach for Analyzing Functional Degradation of SMA Components

- With growing applications of SMA, the issue of material performance over its designed life is of great concern to researchers lately. In order to analyze SMA component performance under coupled thermomechanical effects, theories considering both mechanical and thermal effects in a single framework must be employed rather than modifying classical fatigue theories developed for capturing pure mechanical loading effects. This approach can substitute traditional fatigue theories like S–N or ε–N which primarily use mechanical loading effects with temperature being an external control parameter.

- Using the modeling approach earlier, relationships for "thermodynamic driving force for the phase transformation" and "extent of phase transformation" were employed depending on the loading scenario. The thermodynamic driving force is the equivalent of thermodynamical force for onset of phase transformation effect which is directly responsible for the functionality of SMA component.

- A custom designed thermomechanical fatigue test rig was used perform user defined repeated thermomechanical tests on SMA springs. The data from these tests serve both to calibrate the model and establish "thermodynamic driving force for the phase transformation" and "extent of phase transformation" relationships for SMA springs.

- A drop in driving force corresponds to material loosing functionality i.e material is no longer transforming and performing its intended function. Hence, this quantity can used as a parameter to analyze the functional degradation of SMA components. Further, the volume fraction relationship can help us estimate the extent of transformation (i.e amount of martensite) and a drop from its initial value corresponds to portions (islands) of material not contributing into phase transformation.

- A driving force – volume fraction plot that solely captures the dissipative part of the response can also be used to analyze shakedown effects observed with typical superelastic responses associated with SMAs. This can substitute "Energy approach" that develop relationships between dissipated energy verses number of cycles under stabilized superelastic effects by comparing SE behavior to plastic shakedown.

- Designers can set appropriate driving force thresholds and use this approach as a guideline for analyzing functional degradation of SMA components used as thermal actuators or damping elements under both shape memory and superelastic conditions.

10. RECOMMENDATIONS AND FUTURE WORK

The following topics need attention

10.1 Experimental Data on SMA Components

1. SMA demonstrate complex, nonlinear hysteretic responses under different loading conditions. SMA components under pure bending with complex internal loops is not well understood. SMAs tend to demonstrate tension–compression asymmetry as the martensite variants under compression are different than those formed under tension loading cases. For this, better understanding of SMA component responses under compression and bending are important.

2. SMA components might be subjected to combined loading cases (like tension–torsion). Internal loop responses under these combined loading cases must be investigated for different SMA geometries (wires, tubes and rods) to better understand their hysteretic responses. The present literature mainly focuses on outer loop response for wires and tubes.

3. Many operating conditions can influence the mechanical response of SMA components. Factors like material composition, operating temperature, type of heating like air/water/oil/resistive (direct or indirect), rate of heating/cooling, loading rates etc. could influence the overall hysteretic response. Researchers might need prior information for the effect of such factors while designing SMA components that are subjected to repeated loading and unloading cycles under different application scenarios.

4. With regard to SMA springs in particular, additional geometry factors like wire diameter, wire topology(tube/solid), spring index and coil angles also

affect their mechanical response. The role of these factors must be accounted by designers and investigated in depth.

5. The prior thermomechanical processing history, heat treatment conditions like shape setting temperature, heating/cooling rates, heating/cooling techniques and soaking times also greatly affect the mechanical properties of SMAs. Experimental data investigating such factors would play a pivotal role in better designing SMA components for engineering applications.

10.2 Extension of Thermodynamic Preisach Modeling Approach

1. The thermodynamic Preisach approach provides an effective way to capture complex hysteretic responses with the effect the operating temperature being easily accounted for in the model. Extending this modeling approach to capture combined loading effects, loading rates with complex internal loops could greatly help designers investigate more complex design cases.

2. Finite element implementation of thermodynamic Preisach models under different loading cases with standard FE packages like ANSYS® or ABAQUS® could help designers in analyzing SMA components under different loading cases easily.

3. Integrating these models with commercial multibody dynamic packages like MSC ADAMS® could help designers simulates mechanisms that use SMA components like wires, springs or rods. These simulations could give first hand information on the feasibility studies of mechanisms.

10.3 Analyzing Functional Degradation of SMA Components

1. The issue of material performance over its designed life is of great concern to researchers. As pointed out by Eggeler et al. [170], factors such as material

chemical composition, material impurity (i.e particle size distribution), type of loading, applied load magnitude, extent of deformation or plateau strains, processing conditions, defect accumulation, accumulated plastic deformation, microstructure and operating temperature affect the fatigue life of SMA components. Experiments investigating each of these factors could help designers better predict the fatigue life of SMA components before catastrophic unintended failures during service

2. Using these advanced experimental results, damage models that allow better understanding of functional degradation of SMA components must be developed. These models could provide useful information to designers.

10.4 Designing SMA Compenents for Applications

Given the complex nature of SMA component response, designing SMA devices for different application is not a trivial task. It is not possible to design SMA actuators without integrating SMA material behavior, mechanics (models) and design (mechanisms) knowledge. Developing design philosophies that allow better understanding of their coupled thermomechanical responses is of critical importance for both researchers and application developers. SMA components tend to show poor fatigue life's at strains $> 3\%$, hence clever linear to rotary mechanisms, stroke amplification mechanisms could greatly help application developers.

REFERENCES

[1] D. Lagoudas, *Shape memory alloys: modeling and engineering applications*. Springer– Verlag, Spring Street, New York, New York, 2008.

[2] P. Ghosh, A. Rao, and A. R. Srinivasa, "Design of multi-state and smart-bias components using shape memory alloy and shape memory polymer composites," *Materials & Design*, vol. 44, pp. 164 – 171, Feb 2013.

[3] L. A. Momoda, *The future of engineering materials: Multifunction for performance – Tailored structures*, vol. 34. The Bridge : National Academy of Engineering, 2004.

[4] H. Janocha, *Adaptronics and smart structures: basics, materials, design, and applications*. Springer – Verlag Berlin Heidelberg, New York, 1999.

[5] T. Okano, "Molecular design of temperature-responsive polymers as intelligent materials," *Responsive Gels: Volume Transitions II*, vol. 110, pp. 179–197, 1993.

[6] J. Leng, X. Lan, Y. Liub, and S. Dua, "Shape memory polymers and their composites: Stimulus methods and applications," *Progress in Materials Science*, vol. 56, no. 7, pp. 1077–1135, 2011.

[7] N. Ganesh, S. Maniprakash, L. Chandrasekaran, S. Srinivasan, and A. Srinivasa, "Design and development of a sun tracking mechanism using the direct sma actuation," *Journal of Mechanical Design*, vol. 133, p. 075001, 2011.

[8] D. Stoeckel, "Shape memory actuators for automotive applications," *Materials & Design*, vol. 11, no. 6, pp. 302–307, 1990.

[9] A. K. Noor, "Computational structures technology: leap frogging into the twenty-first century," *Computers & Structures*, vol. 73, no. 1, pp. 1–31, 1999.

[10] M. Naraghi, "Multifunctional materials - aero 606 course notes," Fall 2012.

[11] J. Shaw, C. Churchill, and M. Iadicola, "Tips and tricks for characterizing shape memory alloy wire: Part 1–differential scanning calorimetry and basic phenomena," *Experimental Techniques*, vol. 32, no. 5, pp. 55–62, 2008.

[12] A. S. F2004-05R10, "Standard test method for transformation temperature of nickel-titanium alloys by thermal analysis," *ASTM International, West Conshohocken, PA*, 2010.

[13] A. S. F. 2007e2, "Standard test method for tension testing of nickel-titanium superelastic materials," *ASTM International, West Conshohocken, PA*, 2007.

[14] W. Huang, Z. Ding, C. Wang, J. Wei, Y. Zhao, and H. Purnawali, "Shape memory materials," *Materials Today*, vol. 13, no. 7-8, pp. 54–61, 2010.

[15] J. McNichols and J. Cory, "Thermodynamics of nitinol," *Journal of Applied Physics*, vol. 61, no. 3, pp. 972–984, 1987.

[16] J. Van Humbeeck, "Shape memory alloys: a material and a technology," *Advanced Engineering Materials*, vol. 3, no. 11, pp. 837–850, 2001.

[17] C. Wayman, "Shape memory and related phenomena," *Progress in Materials Science (UK)*, vol. 36, pp. 203–224, 1992.

[18] D. Hartl and D. Lagoudas, "Aerospace applications of shape memory alloys," *Proceedings of the Institution of Mechanical Engineers, Part G: Journal of Aerospace Engineering*, vol. 221, no. 4, p. 535, 2007.

[19] B. Sutapun, M. Tabib-Azar, and M. Huff, "Applications of shape memory alloys in optics," *Applied Optics*, vol. 37, no. 28, pp. 6811–6815, 1998.

[20] G. Song, N. Ma, and H. Li, "Applications of shape memory alloys in civil structures," *Engineering Structures*, vol. 28, no. 9, pp. 1266–1274, 2006.

[21] J. Van Humbeeck, "Non-medical applications of shape memory alloys," *Materials Science and Engineering: A*, vol. 273, pp. 134–148, 1999.

[22] L. Machado and M. Savi, "Medical applications of shape memory alloys," *Brazilian Journal of Medical and Biological Research*, vol. 36, no. 6, pp. 683–691, 2003.

[23] D. Lagoudas, O. K. Rediniotis, and M. M. Khan, "Applications of shape memory alloys to bioengineering and biomedical technology," in *Proceedings of the 4th International Workshop on Scattering Theory and Biomedical Applications, Perdika, Greece,(Oct. 1999)*, pp. 195–207, 2000.

[24] T. Duerig, A. Pelton, and D. Stöckel, "An overview of nitinol medical applications," *Materials Science and Engineering: A*, vol. 273, pp. 149–160, 1999.

[25] D. Mantovani, "Shape memory alloys: Properties and biomedical applications," *JOM Journal of the Minerals, Metals and Materials Society*, vol. 52, no. 10, pp. 36–44, 2000.

[26] N. Morgan, "Medical shape memory alloy applications–the market and its products," *Materials Science and Engineering: A*, vol. 378, no. 1, pp. 16–23, 2004.

[27] F. El Feninat, G. Laroche, M. Fiset, and D. Mantovani, "Shape memory materials for biomedical applications," *Advanced Engineering Materials*, vol. 4, no. 3, pp. 91–104, 2002.

[28] R. Bogue, "Shape-memory materials : A review of technology and applications," *Assembly Automation*, vol. 29, no. 3, pp. 214–219, 2009.

[29] F. Gil, J. Manero, and J. Planell, "Relevant aspects in the clinical applications of niti shape memory alloys," *Journal of Materials Science: Materials in Medicine*, vol. 7, no. 7, pp. 403–406, 1996.

[30] C. Manhartsberger and W. Seidenbusch, "Force delivery of ni-ti coil springs," *American journal of orthodontics and dentofacial orthopedics*, vol. 109, no. 1, pp. 8–21, 1996.

[31] F. Miura, M. Mogi, Y. Ohura, and M. Karibe, "The superelastic japanese niti alloy wire for use in orthodontics part iii. studies on the japanese niti alloy coil springs," *American Journal of Orthodontics and Dentofacial Orthopedics*, vol. 94, no. 2, pp. 89–96, 1988.

[32] I. Spinella, E. Dragoni, and F. Stortiero, "Modeling, prototyping, and testing of helical shape memory compression springs with hollow cross section," *Journal of Mechanical Design*, vol. 132, p. 061008, 2010.

[33] S. Drake, D. Wayne, J. Powers, and K. Asgar, "Mechanical properties of orthodontic wires in tension, bending, and torsion," *American Journal of Orthodontics*, vol. 82, no. 3, pp. 206–210, 1982.

[34] F. Miura, M. Mogi, Y. Ohura, and H. Hamanaka, "The super-elastic property of the japanese niti alloy wire for use in orthodontics," *American Journal of Orthodontics and Dentofacial Orthopedics*, vol. 90, no. 1, pp. 1–10, 1986.

[35] S. Kapila and R. Sachdeva, "Mechanical properties and clinical applications of orthodontic wires," *American Journal of Orthodontics and Dentofacial Orthopedics*, vol. 96, no. 2, pp. 100–109, 1989.

[36] J. Von Fraunhofer, P. Bonds, and B. Johnson, "Force generation by orthodontic coil springs.," *The Angle Orthodontist*, vol. 63, no. 2, p. 145, 1993.

[37] R. Schneevoigt, A. Haase, V. Eckardt, W. Harzer, and C. Bourauel, "Laboratory analysis of superelastic niti compression springs," *Medical Engineering & Physics*, vol. 21, no. 2, pp. 119–125, 1999.

[38] S. Thompson, "An overview of nickel–titanium alloys used in dentistry," *International Endodontic Journal*, vol. 33, no. 4, pp. 297–310, 2000.

[39] A. Maganzini, A. Wong, and M. Ahmed, "Forces of various nickel titanium closed coil springs," *The Angle Orthodontist*, vol. 80, no. 1, pp. 182–187, 2010.

[40] L. Petrini and F. Migliavacca, "Biomedical applications of shape memory alloys," *Journal of Metallurgy*, vol. 2011, 2011.

[41] J. Ryhänen, "Biocompatibility evolution of nickel-titanium shape memory alloy," *Academic Dissertation, Faculty of Medicine, University of Oulu, Oulu, Finland.[Links]*, 1999.

[42] FDA, "United states food and drug administartion," 2012. `http://www.fda.gov/`.

[43] M. Speicher, D. Hodgson, R. DesRoches, and R. Leon, "Shape memory alloy tension/compression device for seismic retrofit of buildings," *Journal of Materials Engineering and Performance*, vol. 18, no. 5, pp. 746–753, 2009.

[44] S. Saadat, J. Salichs, M. Noori, Z. Hou, H. Davoodi, I. Bar-On, Y. Suzuki, and A. Masuda, "An overview of vibration and seismic applications of niti shape memory alloy," *Smart Materials and Structures*, vol. 11, p. 218, 2002.

[45] R. DesRoches and B. Smith, "Shape memory alloys in seismic resistant design and retrofit: a critical review of their potential and limitations," *Journal of Earthquake Engineering*, vol. 8, no. 3, pp. 415–429, 2004.

[46] J. Wilson and M. Wesolowsky, "Shape memory alloys for seismic response modification: a state-of-the-art review," *Earthquake Spectra*, vol. 21, p. 569, 2005.

[47] M. Alam, M. Youssef, and M. Nehdi, "Utilizing shape memory alloys to enhance the performance and safety of civil infrastructure: a review," *Canadian Journal of Civil Engineering*, vol. 34, no. 9, pp. 1075–1086, 2007.

[48] L. Janke, C. Czaderski, M. Motavalli, and J. Ruth, "Applications of shape memory alloys in civil engineering structures–overview, limits and new ideas," *Materials and Structures*, vol. 38, no. 5, pp. 578–592, 2005.

[49] Y. Mo, G. Song, and K. Otero, "Development and testing of a proof-of-concept smart concrete structure," *Proceeding of Smart Structures Technologies and Earthquake Engineering*, 2004.

[50] I. Chopra, "Status of application of smart structures technology to rotorcraft systems," *Journal of the American Helicopter Society*, vol. 45, no. 4, pp. 228–252, 2000.

[51] G. Brook, "Applications of titanium-nickel shape memory alloys," *Materials & Design*, vol. 4, no. 4, pp. 835–840, 1983.

[52] G. Song, D. Patil, C. Kocurek, and J. Bartos, "Applications of shape memory alloys in offshore oil and gas industry: a review," *Proc. Earth and Space 2010–Engineering, Science, Construction, and Operations in Challenging Environments (Honolulu, HI, USA, 14–17 March 2010)*, vol. 366, 2010.

[53] R. DesRoches and M. Delemont, "Seismic retrofit of simply supported bridges using shape memory alloys," *Engineering Structures*, vol. 24, no. 3, pp. 325–332, 2002.

[54] M. Indirli, M. G. Castellano, P. Clemente, and A. Martelli, "Demo-application of shape memory alloy devices: the rehabilitation of the s. giorgio church bell tower," in *SPIE's 8th Annual International Symposium on Smart Structures and Materials*, pp. 262–272, International Society for Optics and Photonics, 2001.

[55] K. Williams, G. Chiu, and R. Bernhard, "Adaptive-passive absorbers using shape-memory alloys," *Journal of Sound and Vibration*, vol. 249, no. 5, pp. 835–848, 2002.

[56] A. Bellini, M. Colli, and E. Dragoni, "Mechatronic design of a shape memory alloy actuator for automotive tumble flaps: A case study," *Industrial Electronics, IEEE Transactions*, vol. 56, no. 7, pp. 2644–2656, 2009.

[57] R. Loewy, "Recent developments in smart structures with aeronautical applications," *Smart Materials and Structures*, vol. 6, p. R11, 1997.

[58] A. Razov and A. Cherniavsky, "Applications of shape memory alloys in space engineering: past and future," *European Space Agency - Publications ESA SP*, vol. 438, pp. 141–146, 1999.

[59] A. Khandelwal and V. Buravalla, "Models for shape memory alloy behavior: An overview of modeling approaches," *The International Journal of Structural Changes in Solids*, vol. 1, no. 1, pp. 111–148, 2011.

[60] R. Abeyaratne and J. Knowles, "On the driving traction acting on a surface of strain discontinuity in a continuum," *Journal of the Mechanics and Physics of Solids*, vol. 38, no. 3, pp. 345–360, 1990.

[61] J. Ball and R. James, "Fine phase mixtures as minimizers of energy," *Archive for Rational Mechanics and Analysis*, vol. 100, no. 1, pp. 13–52, 1987.

[62] F. Falk, "Model free energy, mechanics, and thermodynamics of shape memory alloys," *Acta Metallurgica*, vol. 28, no. 12, pp. 1773–1780, 1980.

[63] F. Falk, "One-dimensional model of shape memory alloys," *Archives of Mechanics*, vol. 35, no. 1, pp. 63–84, 1983.

[64] S. Doraiswamy, A. Rao, and A. Srinivasa, "Combining thermodynamic principles with preisach models for superelastic shape memory alloy wires," *Smart Materials and Structures*, vol. 20, p. 085032, 2011.

[65] K. Rajagopal and A. Srinivasa, "On the thermomechanics of shape memory wires," *Zeitschrift fur Angewandte Mathematik und Physik*, vol. 50, pp. 459–496, 1999.

[66] K. Tanaka and S. Nagaki, "A thermomechanical description of materials with internal variables in the process of phase transitions," *Archive of Applied Mechanics*, vol. 51, no. 5, pp. 287–299, 1982.

[67] K. Tanaka and R. Iwasaki, "A phenomenological theory of transformation superplasticity," *Engineering Fracture Mechanics*, vol. 21, no. 4, pp. 709–720, 1985.

[68] K. Tanaka, "A thermomechanical sketch of shape memory effect: one-dimensional tensile behavior," *Res Mechanica*, vol. 2, no. 3, pp. 59–72, 1986.

[69] K. Tanaka, T. Hayashi, Y. Itoh, and H. Tobushi, "Analysis of thermomechanical behavior of shape memory alloys," *Mechanics of Materials*, vol. 13, no. 3, pp. 207–215, 1992.

[70] Y. Sato and K. Tanaka, "Estimation of energy dissipation in alloys due to stress-induced martensitic transformation," *Res Mech.*, vol. 23, no. 4, pp. 381–393, 1988.

[71] V. Buravalla and A. Khandelwal, "Phenomenological modeling of shape memory alloys," in *AIP Conference Proceedings*, vol. 1029, p. 104, 2008.

[72] C. Liang and C. Rogers, "One-dimensional thermomechanical constitutive relations for shape memory materials," *Journal of Intelligent Material Systems and Structures*, vol. 1, no. 2, pp. 207–234, 1990.

[73] C. Liang and C. Rogers, "A multi-dimensional constitutive model for shape memory alloys," *Journal of Engineering Mathematics*, vol. 26, no. 3, pp. 429–443, 1992.

[74] L. Brinson, "One-dimensional constitutive behavior of shape memory alloys: thermomechanical derivation with non-constant material functions and redefined martensite internal variable," *Journal of Intelligent Material Systems and Structures*, vol. 4, no. 2, pp. 229–242, 1993.

[75] A. Bekker and L. Brinson, "Phase diagram based description of the hysteresis behavior of shape memory alloys," *Acta Materialia*, vol. 46, no. 10, pp. 3649–3665, 1998.

[76] A. Rao and A. Srinivasa, "A three species model for simulating torsional response of shape memory alloy components using thermodynamic principles and discrete preisach models," *Mathematics and Mechanics of Solids*, vol. (In Press, 2014).

[77] D. Lagoudas, J. Boyd, and Z. Bo, "Micromechanics of active composites with sma fibers," *Journal of Engineering Materials and Technology*, vol. 116, p. 337, 1994.

[78] R. Abeyaratne and J. Knowles, "A continuum model of a thermoelastic solid capable of undergoing phase transitions," *Journal of the Mechanics and Physics*

of Solids, vol. 41, no. 3, pp. 541–571, 1993.

[79] F. Auricchio and J. Lubliner, "A uniaxial model for shape-memory alloys," *International Journal of Solids and Structures*, vol. 34, no. 27, pp. 3601–3618, 1997.

[80] F. Auricchio, R. Taylor, and J. Lubliner, "Shape-memory alloys: macromodelling and numerical simulations of the superelastic behavior," *Computer Methods in Applied Mechanics and Engineering*, vol. 146, no. 3, pp. 281–312, 1997.

[81] B. Raniecki, C. Lexcellent, and K. Tanaka, "Thermodynamic models of pseudoelastic behaviour of shape memory alloys," *Archiv of Mechanics, Archiwum Mechaniki Stosowanej*, vol. 44, pp. 261–284, 1992.

[82] B. Raniecki and K. Tanaka, "On the thermodynamic driving force for coherent phase transformations," *International Journal of Engineering Science*, vol. 32, no. 12, pp. 1845–1858, 1994.

[83] S. Leclercq and C. Lexcellent, "A general macroscopic description of the thermomechanical behavior of shape memory alloys," *Journal of the Mechanics and Physics of Solids*, vol. 44, no. 6, pp. 953–957, 1996.

[84] J. Boyd and D. Lagoudas, "A thermodynamical constitutive model for shape memory materials. part i. the monolithic shape memory alloy," *International Journal of Plasticity*, vol. 12, no. 6, pp. 805–842, 1996.

[85] M. Qidwai and D. Lagoudas, "Numerical implementation of a shape memory alloy thermomechanical constitutive model using return mapping algorithms," *International Journal Numerical Methods in Engineering*, vol. 47, no. 6, pp. 1123–1168, 2000.

[86] R. Mirzaeifar, R. DesRoches, and A. Yavari, "Analysis of the rate-dependent coupled thermo-mechanical response of shape memory alloy bars and wires in tension," *Continuum Mechanics and Thermodynamics*, pp. 1–23, 2011.

[87] Z. Bo, *Consitutive Modeling of shape memory alloys*. PhD thesis, Texas A&M University, College Station, TX, 1996.

[88] Z. Bo and D. Lagoudas, "Thermomechanical modeling of polycrystalline smas under cyclic loading, part i: Theoretical derivations," *International Journal of Engineering Science*, vol. 37, no. 9, pp. 1089–1140, 1999.

[89] M. Qidwai and D. Lagoudas, "On thermomechanics and transformation surfaces of polycrystalline niti shape memory alloy material," *International Journal of Plasticity*, vol. 16, no. 10, pp. 1309–1343, 2000.

[90] A. Rao and A. Srinivasa, "A two species thermodynamic preisach model for the torsional response of shape memory alloy wires and springs under superelastic conditions," *International Journal of Solids and Structures*, vol. 50, no. 6, pp. 887–898, 2013.

[91] X. Tan and J. Baras, "Modeling and control of hysteresis in magnetostrictive actuators," *Automatica*, vol. 40, no. 9, pp. 1469–1480, 2004.

[92] S. Dutta and F. Ghorbel, "Differential hysteresis modeling of a shape memory alloy wire actuator," *Mechatronics, IEEE/ASME Transactions*, vol. 10, no. 2, pp. 189–197, 2005.

[93] D. Hughes and J. Wen, "Preisach modeling of piezoceramic and shape memory alloy hysteresis," *Smart Materials and Structures*, vol. 6, p. 287, 1997.

[94] M. Khan and D. Lagoudas, "Modeling of shape memory alloy pseudoelastic spring elements using preisach model for passive vibration isolation," in *Pro-*

ceedings of SPIE, vol. 4693, pp. 336–47, 2002.

[95] A. Ktena, D. Fotiadis, P. Spanos, and C. Massalas, "A preisach model identification procedure and simulation of hysteresis in ferromagnets and shape-memory alloys," *Physica B: Condensed Matter*, vol. 306, no. 1, pp. 84–90, 2001.

[96] A. Ktena, D. Fotiadis, P. Spanos, A. Berger, and C. Massalas, "Identification of 1d and 2d preisach models for ferromagnets and shape memory alloys," *International Journal of Engineering Science*, vol. 40, no. 20, pp. 2235–2247, 2002.

[97] J. Ortín, "Preisach modeling of hysteresis for a pseudoelastic cu-zn-al single crystal," *Journal of Applied Physics*, vol. 71, no. 3, pp. 1454–1461, 1992.

[98] G. Webb, D. Lagoudas, and A. Kurdila, "Hysteresis modeling of sma actuators for control applications," *Journal of Intelligent Material Systems and Structures*, vol. 9, no. 6, p. 432, 1998.

[99] Z. Bo and D. Lagoudas, "Thermomechanical modeling of polycrystalline smas under cyclic loading, part iv: Modeling of minor hysteresis loops," *International Journal of Engineering Science*, vol. 37, no. 9, pp. 1205–1249, 1999.

[100] F. Falk, "Ginzburg-landau theory and solitary waves in shape memory alloys," *Zeitschrift für Physik B Condensed Matter*, vol. 54, no. 2, pp. 159–167, 1984.

[101] F. Preisach, "Über die magnetische nachwirkung," *Zeitschrift für Physik A Hadrons and Nuclei*, vol. 94, no. 5, pp. 277–302, 1935.

[102] I. Mayergoyz and S. O. service), *Mathematical models of hysteresis and their applications*. Elsevier, Boston, Massachusetts, 2003.

[103] I. Mayergoyz, "Mathematical models of hysteresis," *Magnetics, IEEE Transactions on*, vol. 22, no. 5, pp. 603–608, 1986.

[104] S. Doraiswamy, "Discrete preisach model for the superelastic response of shape memory alloys," Master's thesis, Texas A&M University, 2010.

[105] J. Shaw, "Simulations of localized thermomechanical behavior in a niti shape memory alloy," *International Journal of Plasticity*, vol. 16, no. 5, pp. 541–562, 2000.

[106] H. Tripolt, C. Burstone, P. Bantleon, and W. Manschiebel, "Force characteristics of nickel-titanium tension coil springs," *American Journal of Orthodontics and Dentofacial Orthopedics*, vol. 115, no. 5, pp. 498–507, 1999.

[107] H. Tobushi and K. Tanaka, "Deformation of a shape memory alloy helical spring (analysis based on stress-strain-temperature relation)," *JSME International Journal. Series 1, Solid Mechanics, Strength of Materials*, vol. 34, no. 1, pp. 83–89, 1991.

[108] R. Mirzaeifar, R. DesRoches, and A. Yavari, "A combined analytical, numerical, and experimental study of shape-memory-alloy helical springs," *International Journal of Solids and Structures*, 2010.

[109] R. Mirzaeifar, R. DesRoches, and A. Yavari, "Exact solutions for pure torsion of shape memory alloy circular bars," *Mechanics of Materials*, vol. 42, no. 8, pp. 797–806, 2010.

[110] C. Chapman, A. Eshghinejad, and M. Elahinia, "Torsional behavior of niti wires and tubes: Modeling and experimentation," *Journal of Intelligent Material Systems and Structures*, vol. 22, no. 11, pp. 1239–1248, 2011.

[111] C. Liang and C. Rogers, "Design of shape memory alloy springs with applications in vibration control," *Journal of Vibration and Acoustics*, vol. 115, p. 129, 1993.

[112] C. Liang and C. Rogers, "Design of shape memory alloy springs with applications in vibration control," *Journal of Intelligent Material Systems and Structures*, vol. 8, no. 4, pp. 314–322, 1997.

[113] R. Aguiar, M. Savi, and P. Pacheco, "Experimental and numerical investigations of shape memory alloy helical springs," *Smart Materials and Structures*, vol. 19, p. 025008, 2010.

[114] A. Paiva, M. Savi, A. Braga, and P. Pacheco, "A constitutive model for shape memory alloys considering tensile-compressive asymmetry and plasticity," *International Journal of Solids and Structures*, vol. 42, no. 11-12, pp. 3439–3457, 2005.

[115] M. Savi and A. Paiva, "Describing internal subloops due to incomplete phase transformations in shape memory alloys," *Archive of Applied Mechanics*, vol. 74, no. 9, pp. 637–647, 2005.

[116] O. Doaré, A. Sbarra, C. Touzé, M. Moussa, and Z. Moumni, "Experimental analysis of the quasistatic and dynamic torsional behaviour of shape memory alloys," *International Journal of Solids and Structures*, 2011.

[117] W. Brantley, W. Augat, C. Myers, and R. Winders, "Bending deformation studies of orthodontic wires," *Journal of Dental Research*, vol. 57, no. 4, p. 609, 1978.

[118] I. Lopez, J. Goldberg, and C. Burstone, "Bending characteristics of nitinol wire.," *American Journal of Orthodontics*, vol. 75, no. 5, p. 569, 1979.

[119] A. Goldberg, J. Morton, and C. Burstone, "The flexure modulus of elasticity of orthodontic wires," *Journal of Dental Research*, vol. 62, no. 7, pp. 856–858, 1983.

[120] M. Asgharnia and W. Brantley, "Comparison of bending and tension tests for orthodontic wires," *American Journal of Orthodontics*, vol. 89, no. 3, pp. 228–236, 1986.

[121] H. Walia, W. Brantley, and H. Gerstein, "An initial investigation of the bending and torsional properties of nitinol root canal files," *Journal of Endodontics*, vol. 14, no. 7, pp. 346–351, 1988.

[122] S. Khier, W. Brantley, and R. Fournelle, "Bending properties of superelastic and nonsuperelastic nickel-titanium orthodontic wires," *American Journal of Orthodontics and Dentofacial Orthopedics*, vol. 99, no. 4, pp. 310–318, 1991.

[123] R. Tonner and N. Waters, "The characteristics of super-elastic ni-ti wires in three-point bending. part l: The effect of temperature," *The European Journal of Orthodontics*, vol. 16, no. 5, pp. 409–419, 1994.

[124] J. Oltjen, M. Duncanson Jr, J. Ghosh, R. Nanda, and G. Frans Currier, "Stiffness-deflection behavior of selected orthodontic wires," *The Angle Orthodontist*, vol. 67, no. 3, pp. 209–218, 1997.

[125] H. Nakano, K. Satoh, R. Norris, T. Jin, T. Kamegai, F. Ishikawa, and H. Katsura, "Mechanical properties of several nickel-titanium alloy wires in three-point bending tests," *American Journal of Orthodontics and Dentofacial Orthopedics*, vol. 115, no. 4, pp. 390–395, 1999.

[126] P. Wilkinson, P. Dysart, J. Hood, and G. Herbison, "Load-deflection characteristics of superelastic nickel-titanium orthodontic wires," *American Journal of*

Orthodontics and Dentofacial Orthopedics, vol. 121, no. 5, pp. 483–495, 2002.

[127] F. Parvizi and W. Rock, "The load/deflection characteristics of thermally activated orthodontic archwires," *The European Journal of Orthodontics*, vol. 25, no. 4, pp. 417–421, 2003.

[128] P. Garrec and L. Jordan, "Stiffness in bending of a superelastic ni-ti orthodontic wire as a function of cross-sectional dimension," *The Angle Orthodontist*, vol. 74, no. 5, pp. 691–696, 2004.

[129] M. Sakima, M. Dalstra, and B. Melsen, "How does temperature influence the properties of rectangular nickel–titanium wires?," *The European Journal of Orthodontics*, vol. 28, no. 3, pp. 282–291, 2006.

[130] T. Bartzela, C. Senn, and A. Wichelhaus, "Load-deflection characteristics of superelastic nickel-titanium wires," *The Angle Orthodontist*, vol. 77, no. 6, pp. 991–998, 2007.

[131] B. Berg, "Bending of superelastic wires, part i: Experimental aspects," *Journal of Applied Mechanics*, vol. 62, p. 459, 1995.

[132] J. Rejzner, C. Lexcellent, and B. Raniecki, "Pseudoelastic behaviour of shape memory alloy beams under pure bending: experiments and modelling," *International Journal of Mechanical Sciences*, vol. 44, no. 4, pp. 665–686, 2002.

[133] A. Wick, O. Vöhringer, and A. Pelton, "The bending behavior of niti," *Journal de Physique. IV*, vol. 5, no. 8, pp. C8–789, 1995.

[134] B. Raniecki, J. Rejzner, and C. Lexcellent, "Anatomization of hysteresis loops in pure bending of ideal pseudoelastic sma beams," *International Journal of Mechanical Sciences*, vol. 43, no. 5, pp. 1339–1368, 2001.

[135] S. Marfia, E. Sacco, and J. Reddy, "Superelastic and shape memory effects in laminated shape-memory-alloy beams," *AIAA journal*, vol. 41, no. 1, pp. 100–109, 2003.

[136] T. Atanacković and M. Achenbach, "Moment – curvature relations for a pseudoelastic beam," *Continuum Mechanics and Thermodynamics*, vol. 1, no. 1, pp. 73–80, 1989.

[137] A. Eshghinejad and M. Elahinia, "Exact solution for bending of shape memory alloy superelastic beams," *ASME Conference Proceedings*, vol. 2011, no. 54723, pp. 345–352, 2011.

[138] R. Mirzaeifar, R. DesRoches, A. Yavari, and K. Gall, "A closed form solution for superelastic shape memory alloy beams subjected to bending," in *Proceedings of SPIE*, vol. 8342, p. 83421O, 2012.

[139] K. Rajagopal and A. Srinivasa, "On the bending of shape memory wires," *Mechanics of Advanced Materials and Structures*, vol. 12, no. 5, pp. 319–330, 2005.

[140] F. Auricchio and E. Sacco, "Thermomechanical modelling of a superelastic shape-memory wire under cyclic stretching–bending loadings," *International Journal of Solids and Structures*, vol. 38, no. 34, pp. 6123–6145, 2001.

[141] P. Purohit and K. Bhattacharya, "On beams made of a phase-transforming material," *International Journal of Solids and Structures*, vol. 39, no. 13, pp. 3907–3929, 2002.

[142] J. A.Shaw and S. Kyriakides, "Thermomechanical aspects of niti," *Journal of the Mechanics and Physics of Solids*, vol. 43, no. 8, pp. 1243–1281, 1995.

[143] S.Miyazaki, K.Otsuka, and Y.Suzuki, "Transformation pseudoelasticity and deformation behaviour in a t-50.6 at.-% ni alloy," *Scripta METALLURGICA*, vol. 15, pp. 287–292, 1981.

[144] Y. Huo and I. Müller, "Nonequilibrium thermodynamics of pseudoelasticity," *Continuum Mechanics and Thermodynamics*, vol. 5, no. 3, pp. 163–204, 1993.

[145] C. Lexcellent and H. Tobushi, "Internal loops in pseudoelastic behaviour of ti-ni shape memory alloys: Experiment and modelling," *Meccanica*, vol. 30, no. 5, pp. 459–466, 1995.

[146] Y. Liu, Z. Xie, J. Van Humbeeck, and L. Delaey, "Asymmetry of stress–strain curves under tension and compression for niti shape memory alloys," *Acta Materialia*, vol. 46, no. 12, pp. 4325–4338, 1998.

[147] I. Müller and S. Seelecke, "Thermodynamic aspects of shape memory alloys," *Mathematical and Computer Modelling*, vol. 34, no. 12, pp. 1307–1355, 2001.

[148] M. Dolce and D. Cardone, "Mechanical behaviour of shape memory alloys for seismic applications 2. austenite niti wires subjected to tension," *International Journal of Mechanical Sciences*, vol. 43, no. 11, pp. 2657–2677, 2001.

[149] J. Ortín and L. Delaey, "Hysteresis in shape memory alloys," *International Journal of Non-Linear Mechanics*, vol. 37, no. 8, pp. 1275–1281, 2002.

[150] Y. Matsuzaki, K. Funami, and H. Naito, "Inner loops of pseudoelastic hysteresis of shape memory alloys: Preisach approach," in *SPIE's 9th Annual International Symposium on Smart Structures and Materials*, pp. 355–364, International Society for Optics and Photonics, 2002.

[151] R. DesRoches, J. McCormick, and M. Delemont, "Cyclic properties of superelastic shape memory alloy wires and bars," *Journal of Structural Engineering*,

vol. 130, no. 1, pp. 38–46, 2003.

[152] T. Ikeda, F. A. Nae, H. Naito, and Y. Matsuzaki, "Constitutive model of shape memory alloys for unidirectional loading considering inner hysteresis loops," *Smart materials and Structures*, vol. 13, no. 4, p. 916, 2004.

[153] M. K. Kumar, K. Sakthivel, S. Sivakumar, C. L. Rao, and A. Srinivasa, "Thermomechanical modeling of hysteresis in smas using the dissipationless reference response," *Smart Materials and Structures*, vol. 16, no. 1, p. S28, 2007.

[154] O. Heintze and S. Seelecke, "A coupled thermomechanical model for shape memory alloys–from single crystal to polycrystal," *Materials Science and Engineering: A*, vol. 481, pp. 389–394, 2008.

[155] I. Müller, "Pseudo-elastic hysteresis in shape memory alloys," *Physica B: Condensed Matter*, vol. 407, no. 9, pp. 1314–1315, 2012.

[156] K. Otsuka and X. Ren, "Physical metallurgy of ti–ni-based shape memory alloys," *Progress in Materials Science*, vol. 50, no. 5, pp. 511–678, 2005.

[157] A. Rao, "Modeling bending response of shape memory alloy wires/beams under superelastic conditions – a two species thermodynamic preisach approach," *The International Journal of Structural Changes in Solids*, vol. 5, pp. 1–26, 2013.

[158] A. Green and P. Naghdi, "On thermodynamics and the nature of the second law," *Proceedings of the Royal Society of London. A. Mathematical and Physical Sciences*, vol. 357, no. 1690, pp. 253–270, 1977.

[159] A. Nallathambi, S. Doraiswamy, A. Chandrasekar, and S. Srinivasan, "A 3-species model for shape memory alloys," *The International Journal of Structural Changes in Solids*, vol. 1, no. 1, pp. 149–170, 2011.

[160] H. Callen, *Thermodynamics and an Introduction to Thermostatistics*. John Wiley & Sons, Hoboken, New Jersey, 2nd edition ed., 1985.

[161] Z. Bo, D. C. Lagoudas, and D. Miller, "Material characterization of sma actuators under nonproportional thermomechanical loading," *Journal of Engineering Materials and Technology*, vol. 121, no. 1, pp. 75–85, 1999.

[162] H. Prahlad and I. Chopra, "Modeling and experimental characterization of sma torsional actuators," *Journal of Intelligent Material Systems and Structures*, vol. 18, no. 1, pp. 29–38, 2007.

[163] A. Baz, K. Iman, and J. McCoy, "Active control of flexible space structures using the nitinol shape memory actuators," tech. rep., DTIC Document, 1987.

[164] A. Keefe and G. Carman, "Thermomechanical characterization of shape memory alloy torque tube actuators," *Smart Materials and Structures*, vol. 9, p. 665, 2000.

[165] I. Spinella and E. Dragoni, "Analysis and design of hollow helical springs for shape memory actuators," *Journal of Intelligent Material Systems and Structures*, vol. 21, no. 2, pp. 185–199, 2010.

[166] C. Chapman, Z. Karbaschi, M. Elahinia, and M. Tabesh, "Torsional behavior of shape memory alloy tubes for biomedical applications," ASME, 2010.

[167] M. Takahashi, "Shape memory alloy actuator," Sept. 7 2010. US Patent 7,788,921.

[168] A. Spaggiari, I. Spinella, and E. Dragoni, "Design of a telescopic linear actuator based on hollow shape memory springs," *Journal of Materials Engineering and Performance*, vol. 20, no. 4, pp. 489–496, 2011.

[169] E. Khan and S. Srinivasan, "A new approach to the design of helical shape memory alloy spring actuators," *Smart Materials Research*, vol. 2011, 2011.

[170] G. Eggeler, E. Hornbogen, A. Yawny, A. Heckmann, and M. Wagner, "Structural and functional fatigue of niti shape memory alloys," *Materials Science and Engineering: A*, vol. 378, no. 1, pp. 24–33, 2004.

[171] N. Morgan and C. Friend, "A review of shape memory stability in niti alloys," *Le Journal de Physique IV*, vol. 11, no. PR8, 2001.

[172] E. Hornbogen, "Review thermomechanical fatigue of shape memory alloys," *Journal of Materials Science*, vol. 39, no. 2, pp. 385–399, 2004.

[173] S. Robertson, A. Pelton, and R. Ritchie, "Mechanical fatigue and fracture of nitinol," *International Materials Reviews*, vol. 57, no. 1, pp. 1–37, 2012.

[174] H. Tobushi, T. Hachisuka, S. Yamada, and P. Lin, "Rotating bending fatigue of a tini shape memory alloy wire," *Mechanics of Materials*, vol. 26, no. 1, pp. 35–42, 1997.

[175] M. de Azevedo Bahia, R. Fonseca Dias, and V. Buono, "The influence of high amplitude cyclic straining on the behaviour of superelastic niti," *International Journal of Fatigue*, vol. 28, no. 9, pp. 1087–1091, 2006.

[176] S. Miyazaki, K. Mizukoshi, T. Ueki, T. Sakuma, and Y. Liu, "Fatigue life of ti–50 at.% ni and ti–40ni–10cu (at.%) shape memory alloy wires," *Materials Science and Engineering: A*, vol. 273, pp. 658–663, 1999.

[177] H. Tobushi, Y. Ohashi, T. Hori, and H. Yamamoto, "Cyclic deformation of tini shape-memory alloy helical spring," *Experimental Mechanics*, vol. 32, no. 4, pp. 304–308, 1992.

[178] H. Tamura, K. Mitose, and Y. Suzuki, "Fatigue properties of ti-ni shape memory alloy springs," *Journal de Physique. IV*, vol. 5, no. 8, pp. C8–617, 1995.

[179] C. Grossmann, J. Frenzel, V. Sampath, T. Depka, A. Oppenkowski, C. Somsen, K. Neuking, W. Theisen, and G. Eggeler, "Processing and property assessment of niti and niticu shape memory actuator springs," *Materialwissenschaft und Werkstofftechnik*, vol. 39, no. 8, pp. 499–510, 2008.

[180] C. Grossmann, J. Frenzel, V. Sampath, T. Depka, and G. Eggeler, "Elementary transformation and deformation processes and the cyclic stability of niti and niticu shape memory spring actuators," *Metallurgical and Materials Transactions A*, vol. 40, no. 11, pp. 2530–2544, 2009.

[181] K. Ramaiah, C. Saikrishna, V. Ranganath, V. Buravalla, and S. Bhaumik, "Fracture of thermally activated niti shape memory alloy wires," *Materials Science and Engineering: A*, vol. 528, no. 16, pp. 5502–5510, 2011.

[182] S. Miyazaki, "Thermal and stress cycling effects and fatigue properties of ni–ti alloys," *Butterworth-Heinemann, Engineering Aspects of Shape Memory Alloys(UK)*, pp. 394–413, 1990.

[183] K. Melton and O. Mercier, "Fatigue of niti thermoelastic martensites," *Acta Metallurgica*, vol. 27, no. 1, pp. 137–144, 1979.

[184] G. Mammano and E. Dragoni, "Functional fatigue of shape memory wires under constant-stress and constant-strain loading conditions," *Procedia Engineering*, vol. 10, pp. 3692–3707, 2011.

[185] G. Kang, Q. Kan, C. Yu, D. Song, and Y. Liu, "Whole life transformation ratchetting and fatigue of superelastic niti alloy under uniaxial stress-controlled

cyclic loading," *Materials Science and Engineering: A*, vol. 535, pp. 228–234, 2012.

[186] T. Ataalla, M. Leary, and A. Subic, "Functional fatigue of shape memory alloys," *Sustainable Automotive Technologies 2012*, pp. 39–43, 2012.

[187] G. Scirè Mammano and E. Dragoni, "Functional fatigue of ni-ti shape memory wires under various loading conditions," *International Journal of Fatigue*, 2012.

[188] O. Bertacchini, D. Lagoudas, F. Calkins, and J. Mabe, "Thermomechanical cyclic loading and fatigue life characterization of nickel rich niti shape-memory alloy actuators," in *The 15th International Symposium on: Smart Structures and Materials & Nondestructive Evaluation and Health Monitoring*, pp. 692916–692916, International Society for Optics and Photonics, 2008.

[189] O. Bertacchini, D. Lagoudas, and E. Patoor, "Thermomechanical transformation fatigue of tinicu sma actuators under a corrosive environment–part i: Experimental results," *International Journal of Fatigue*, vol. 31, no. 10, pp. 1571–1578, 2009.

[190] D. Lagoudas, D. Miller, L. Rong, and P. Kumar, "Thermomechanical fatigue of shape memory alloys," *Smart Materials and Structures*, vol. 18, no. 8, p. 085021, 2009.

[191] A. Figueiredo, P. Modenesi, and V. Buono, "Low-cycle fatigue life of superelastic niti wires," *International Journal of Fatigue*, vol. 31, no. 4, pp. 751–758, 2009.

[192] A. Runciman, D. Xu, A. Pelton, and R. Ritchie, "An equivalent strain/coffin–manson approach to multiaxial fatigue and life prediction in superelastic nitinol medical devices," *Biomaterials*, vol. 32, no. 22, pp. 4987–4993, 2011.

[193] C. Maletta, E. Sgambitterra, F. Furgiuele, R. Casati, and A. Tuissi, "Fatigue of pseudoelastic niti within the stress-induced transformation regime: a modified coffin–manson approach," *Smart Materials and Structures*, vol. 21, no. 11, p. 112001, 2012.

[194] Z. Moumni, A. Van Herpen, and P. Riberty, "Fatigue analysis of shape memory alloys: energy approach," *Smart Materials and Structures*, vol. 14, no. 5, p. S287, 2005.

[195] Z. Moumni, W. Zaki, H. Maitournam, *et al.*, "Cyclic behavior and energy approach to the fatigue of shape memory alloys," *Journal of Mechanics of Materials and Structures*, vol. 4, no. 2, pp. 395–411, 2009.

[196] H. Soul, A. Isalgue, A. Yawny, V. Torra, and F. Lovey, "Pseudoelastic fatigue of niti wires: frequency and size effects on damping capacity," *Smart Materials and Structures*, vol. 19, no. 8, p. 085006, 2010.

[197] C. Dunand-Châtellet and Z. Moumni, "Experimental analysis of the fatigue of shape memory alloys through power-law statistics," *International Journal of Fatigue*, vol. 36, no. 1, pp. 163–170, 2012.

[198] A. Gloanec, G. Bilotta, and M. Gerland, "Deformation mechanisms in a tini shape memory alloy during cyclic loading," *Materials Science and Engineering: A*, vol. 564, 2013.

[199] K. Wilkes, P. Liaw, and K. Wilkes, "The fatigue behavior of shape-memory alloys," *JOM Journal of the Minerals, Metals and Materials Society*, vol. 52, no. 10, pp. 45–51, 2000.

[200] M. Khonari and M. Amiri, *Introduction to Thermodynamics of Mechanical Fatigue*. CRC Press, 6000 Broken Sound Parkway, Boca Raton, Florida, 2012.

[201] M. Naderi, M. Amiri, and M. Khonsari, "On the thermodynamic entropy of fatigue fracture," *Proceedings of the Royal Society A: Mathematical, Physical and Engineering Science*, vol. 466, no. 2114, pp. 423–438, 2010.

[202] M. Amiri and M. Khonsari, "On the role of entropy generation in processes involving fatigue," *Entropy*, vol. 14, no. 1, pp. 24–31, 2011.

[203] M. Naderi and M. Khonsari, "An experimental approach to low-cycle fatigue damage based on thermodynamic entropy," *International Journal of Solids and Structures*, vol. 47, no. 6, pp. 875–880, 2010.

[204] M. Naderi and M. Khonsari, "Thermodynamic analysis of fatigue failure in a composite laminate," *Mechanics of Materials*, vol. 46, pp. 113–122, 2012.

[205] M. Amiri and M. Khonsari, "Life prediction of metals undergoing fatigue load based on temperature evolution," *Materials Science and Engineering: A*, vol. 527, no. 6, pp. 1555–1559, 2010.

[206] G. Fargione, A. Geraci, G. La Rosa, and A. Risitano, "Rapid determination of the fatigue curve by the thermographic method," *International Journal of Fatigue*, vol. 24, no. 1, pp. 11–19, 2002.

[207] M. Amiri and M. Khonsari, "Rapid determination of fatigue failure based on temperature evolution: Fully reversed bending load," *International Journal of Fatigue*, vol. 32, no. 2, pp. 382–389, 2010.

[208] N. springs, "Images si inc.." Website. `http://www.imagesco.com/nitinol/expansion-spring.html`.

[209] A. Heckmann and E. Hornbogen, "Microstructure and pseudo-elastic low-cycle high amplitude fatigue of niti," in *Journal de Physique IV (Proceedings)*, vol. 112, pp. 831–834, 2003.

[210] Interfaceforce, "Strain gage transducer manual," *Interface Advanced Force Measurement*, 2012.

[211] I. A. F. Measurement, "Company website," 2012. http://www.interfaceforce.com/index.php/.

APPENDIX

EXPERIMENTAL SET-UP DETAILS

LOAD CELL CONNECTIONS

The load cells contain a full-bridge wheatstone bridge circuit with each leg having a resistance of 350 ohms. As shown in figure A.1, the preferred excitation voltage across the terminal is 10 VDC and the corresponding strain gauge output is tapped and supplied to J2 terminal of the signal conditioner (also known as SGA - strain gauge amplifier). The role of the signal conditioner is in converting the strain gauge input (i.e output of load cell) to a voltage or current output as desired. The output from the signal conditioner is fed to the data acquisition system as a 0-10V analog input signal. Following the procedure provided by supplier [210], the 100N load cells are calibrated for a 0-10V DC signal and the load cell responses are recorded as a function of time in the LabVIEW® program. Here the calibration factor is 10(i.e 0V is equivalent to 0N and 10V is equivalent to 100N). Further details on Load cell construction and calibration procedures can be found at suppliers website [211]

POWER SUPPLY CONNECTIONS

For PMC 18-5A power supply, the settings on the front panel for all the switches are shown in figure A.2 to ensure external user control. Connections between pins #15 and #17 of the J2 connector located on the back panel of the power supply are made to the positive and the ground terminals of the data acquisition system (DAQ) respectively. An analog output channel is selected for this connection between J2 connector and DAQ to ensure functioning of the power supply under constant current(CC) mode under an external voltage source 0-10V as shown in figure A.2.

For PAS 20-18A power supply, the "CONFIG" settings on the front panel are set to "0100" for a constant current model functioning under an external voltage source 0-10V. Connections between pins #1 and #5 of the J1 connector located on the back panel of the power supply are made to the positive and the ground terminals of the data acquisition system (DAQ) respectively. An analog output channel of the DAQ is selected for this connection between J1 connector and DAQ to ensure functioning of the power supply under constant current(CC) mode under an external voltage source 0-10V as shown in figure A.3.

LABVIEW® CODE DESCRIPTION

Figure A.4 and A.5 shows the entire LabVIEW® code used to execute user defined thermomechanical cycles on SMA springs.

The important aspects of the LabVIEW® program are :

1. **Analog Output Signal** – A thermal cycle created by user as shown in figure 8.3 is exported as a an Analog Output (AO) signal from the LabVIEW® code. The AO signal here is same for both the power supplies. The power supplies are programmed to run in a "Constant Current Mode (CC)" using an 0–10V external voltage source as defined by user in the LabVIEW® program. Once the user input the required times for different sectors of the thermal signal, then LabVIEW® build an array for the entire signal and exports it as a 0–10V AO signal to the power supplies. The power supplies respond to this signal and deliver the requires current in CC mode.

2. **Analog Input Signals** – For every thermal cycle as shown in figure 8.3, the data acquisition acquires Analog Input (AI) signals from the sensors i.e Load Cells and thermocouples as a function of time. The load cells are calibrated to provide voltages 0 to 10V for the corresponding load acquisitions. The

thermocouples provide a continuous realtime surface temperature information of the springs.

3. **Data Analysis** – Sometimes the acquired data might need some filtering depending on the background noise present in the experimental setup/data acquisition system. Appropriate filters might be selected to attenuate the noise and acquire useful data. For this study a band pass filter of 55Hz was used to cliff off frequency information greater than 60Hz resulting due to AC supply. However, the raw unfiltered data was used for all calculations.

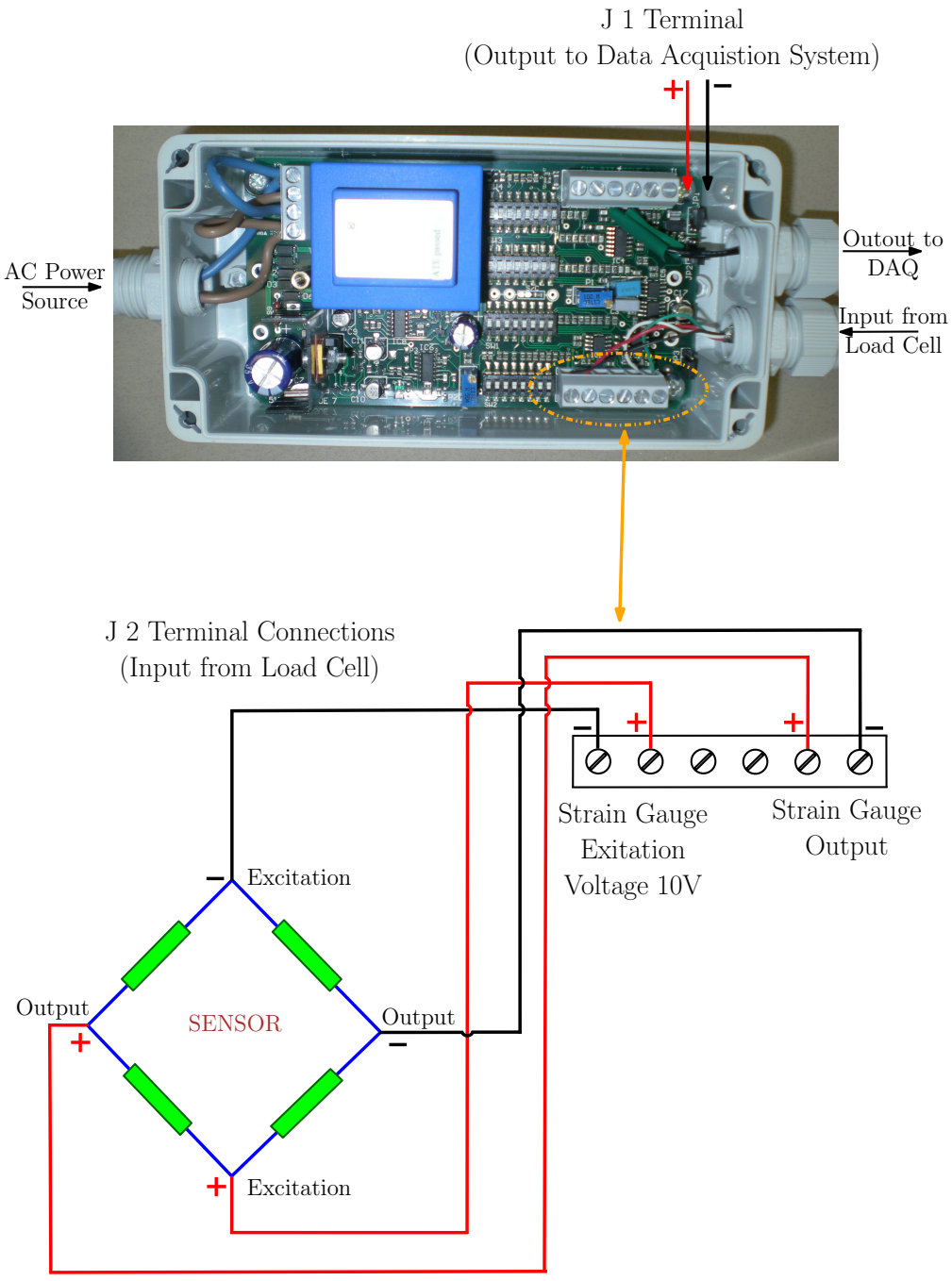

Figure A.1: 100N Load Cell : Diagram showing connections between load cell and strain gauge transducer amplifier (SGA). Output from SGA is exported to DAQ as an Analog Input Channel

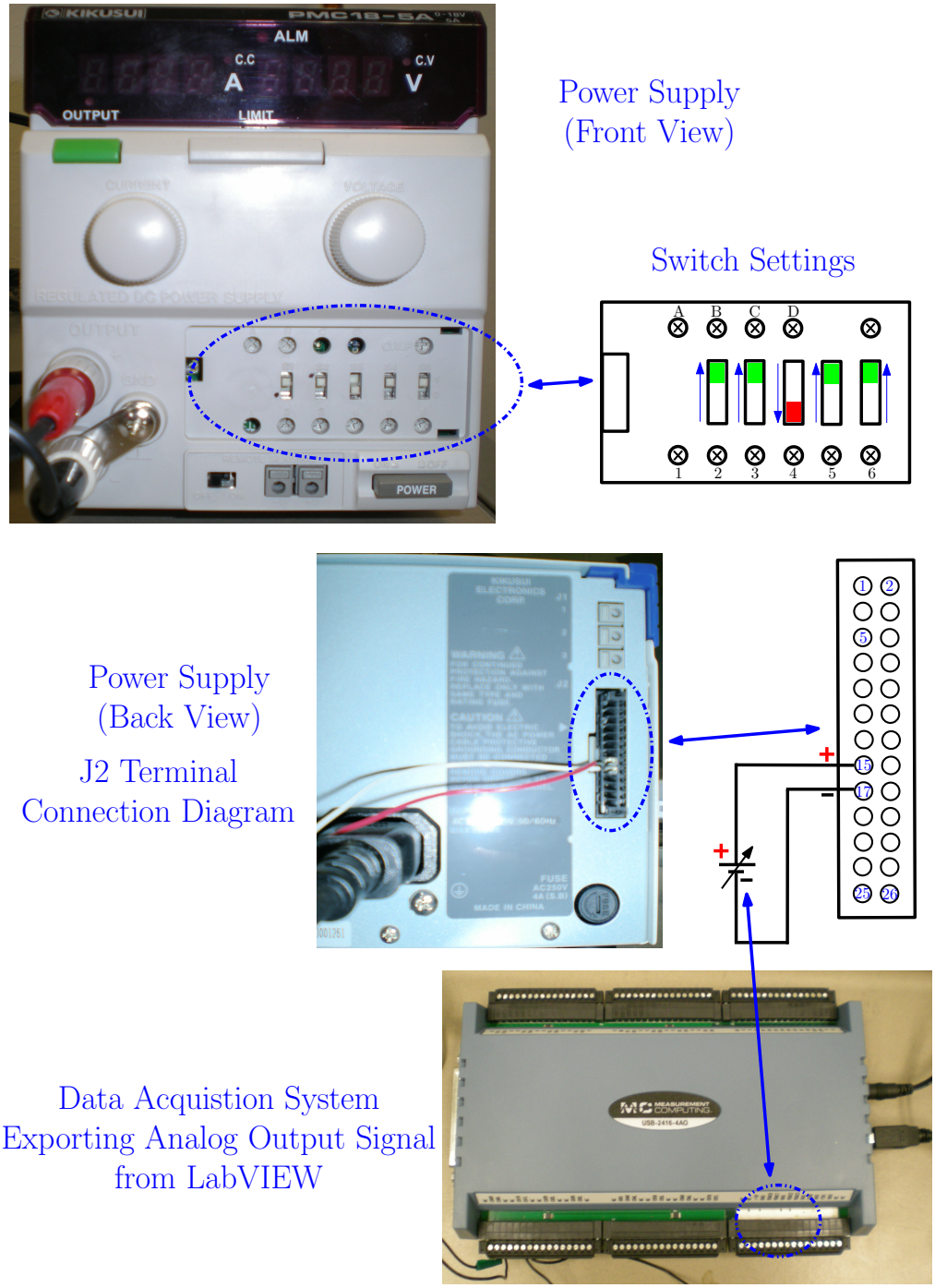

Figure A.2: PMC 18-5A Power Supply : J1 terminal switch settings and J2 terminal wiring diagram for a CC mode operation with connections to DAQ. LabVIEW® program directs the power supply through an analog output channel connection between DAQ and power supply.

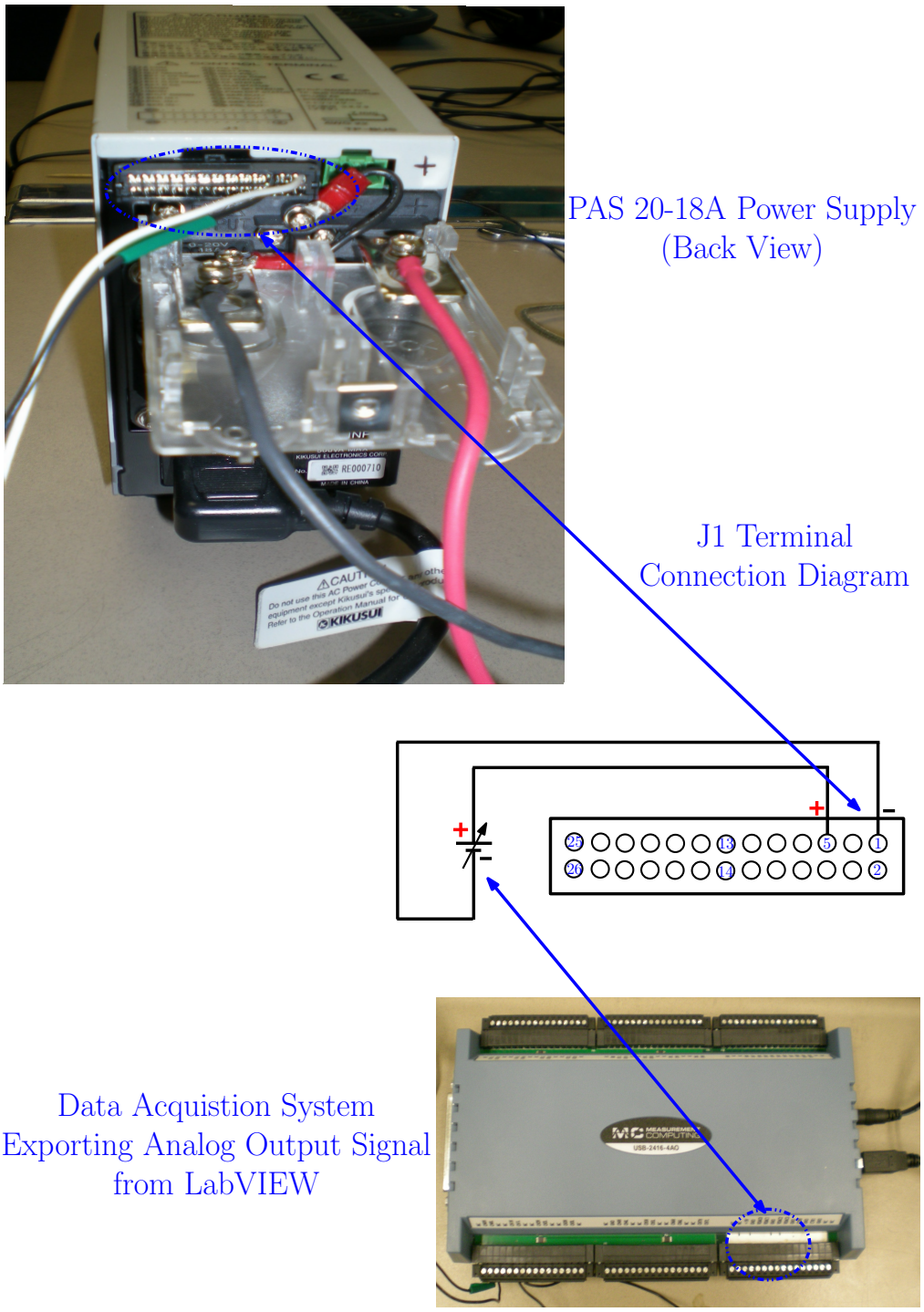

Figure A.3: PAS 20-18A Power Supply : J1 terminal wiring diagram for a CC mode operation with connections to DAQ. LabVIEW® program directs the power supply through an analog output channel connection between DAQ and power supply.

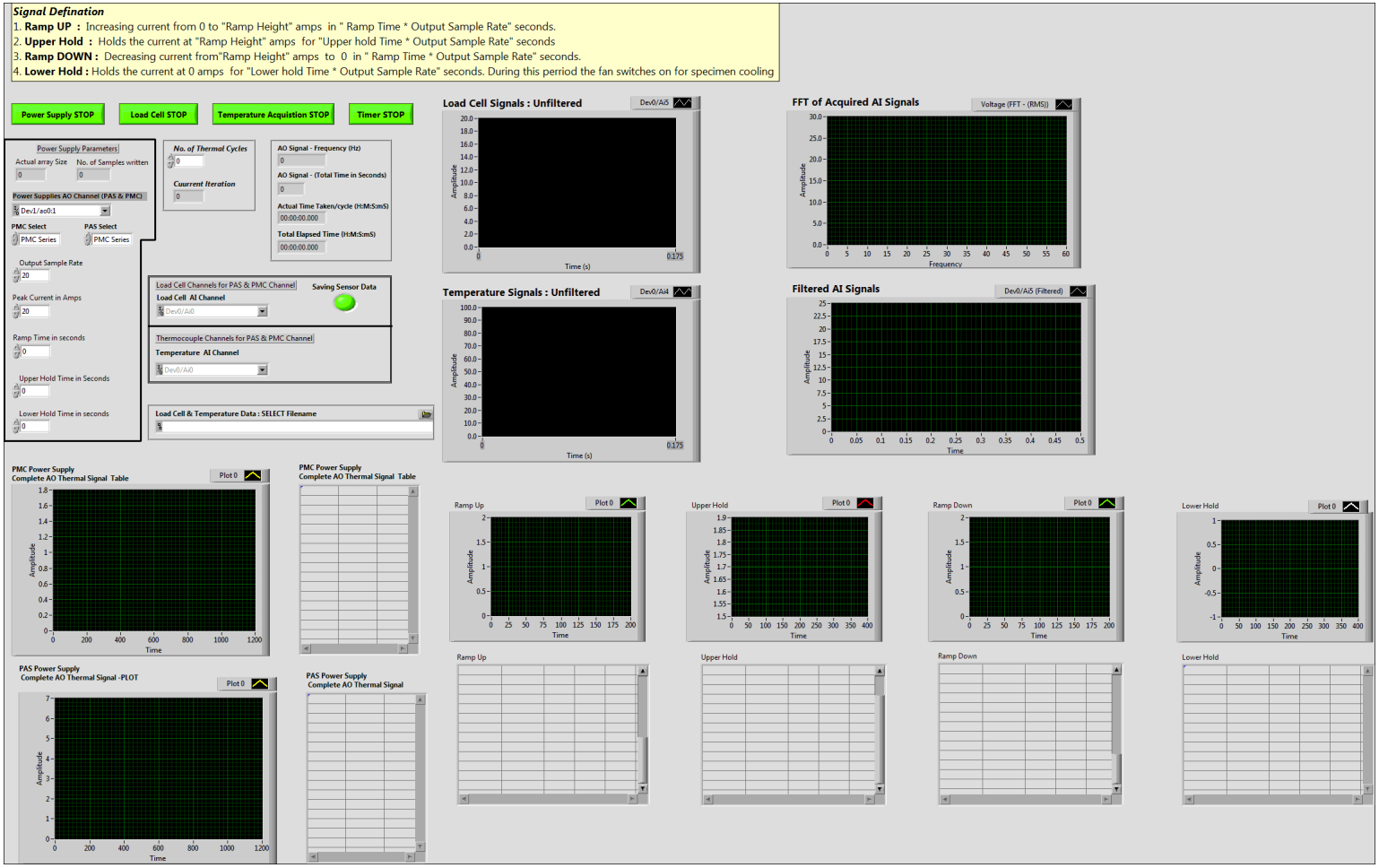

Figure A.4: Figure shows the front panel of the LabVIEW® code which allows user to define the thermal signal and record sensor data.

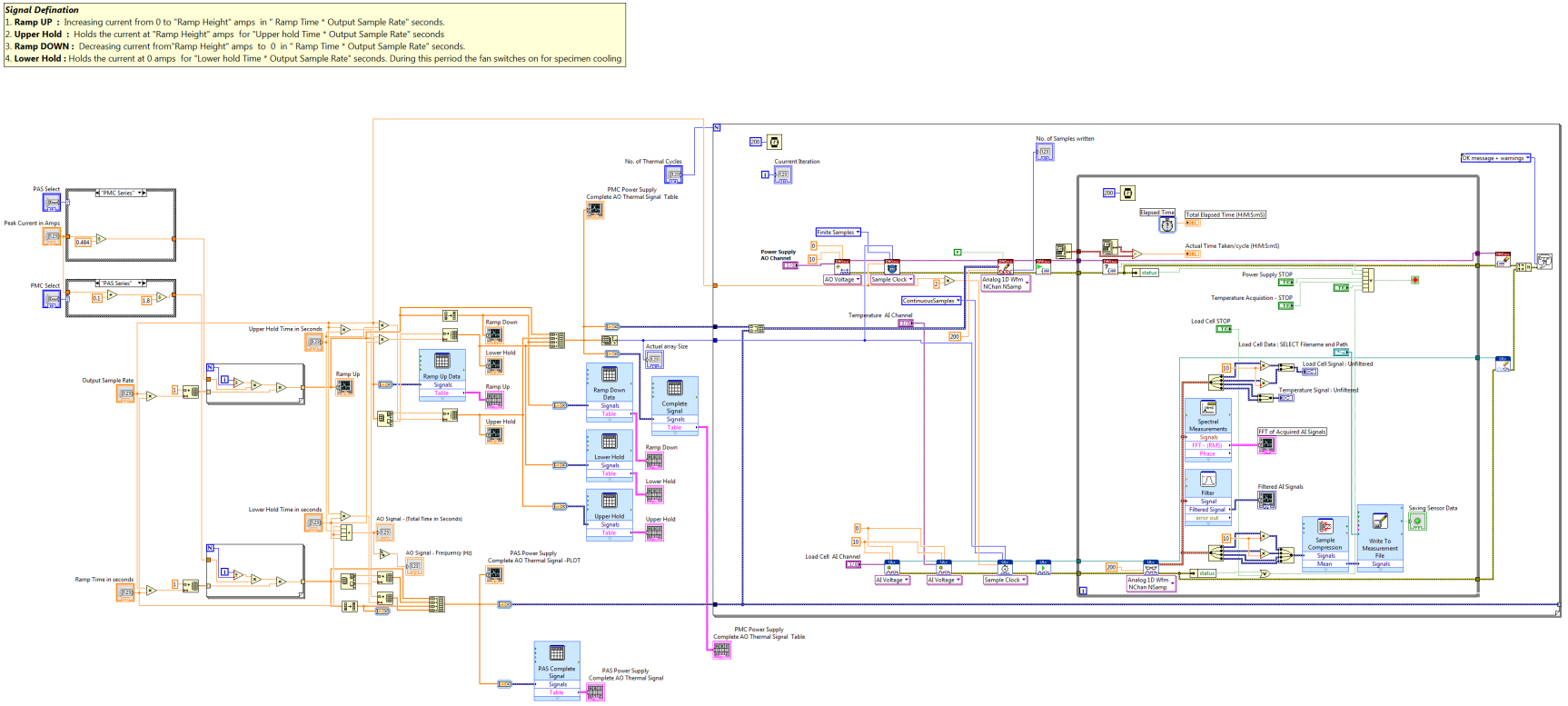

Figure A.5: Figure shows the block diagram for the entire LabVIEW® code used to execute user defined thermomechanical cycles on SMA components.